UNIVERSITY OF CALIFORNIA, SAN DIEGO

Ultrasonic Methods for Rail Inspection

A dissertation in partial satisfaction of the requirements for the degree
Doctor of Philosophy

in

Structural Engineering

by

Robert Ronald Phillips

Committee in charge:

Professor Francesco Lanza di Scalea, Chair
Professor Farhat Beg
Professor Vlado Lubarda
Professor Michael D. Todd
Professor Chia-Ming Uang

2012

The Dissertation of Robert Ronald Phillips is approved, and it acceptable in quality and form for publication on microfilm and electronically:

Chair

University of California, San Diego

2012

DEDICATION

To all the people who take the risk to return to school and improve their knowledge and life.

EPIGRAPH

Great moments are made from great opportunities.

Herb Brooks

TABLE OF CONTENTS

LIST OF FIGURES

LIST OF TABLES

ACKNOWLEDEMENTS

My greatest thanks go to Dr. Francesco Lanza di Scalea for his confidence and support than guided me to graduate school and the pursuit of a doctoral degree. When I sat in his undergraduate course SE163 Non-destructive Evaluation and was told that material properties can be determined without destroying a test sample I was intrigue and captivated. By the second week of the class I started asking him for an undergraduate researcher position in his research group. I thank him for taking a chance on me and allowing me to learn and advance technologies in the field of non-destructive evaluation and structural health monitoring. Over the last six years he has always supported me and without his guidance I would not be where I am today. But I feel that the bond we have built together has become more than just a student teacher relationship and I proud to call him friend with a bond that will be with me for the rest of my life.

When I think back to my journey that brought me back to school to achieve a higher degree, I have to think what spark me to pursue the discipline of Structural Engineering. Since high school, I had a fascination when architecture and buildings, but I had never considered the mechanics of the structure. I have to thank my bother Chuck for the book *Why Buildings Stand Up* by Mario Salvadori he gave me as a gift one Christmas. The book motivated and directed me to structural engineering as before I had not realized that my fascination was not in the form of the buildings but the mechanics.

Without the support of my former employer Matt Short at Flashback Stage Lighting, I would not have been able to return to school. Despite an investment of over 10 years of training and employment, Matt understood my desire to expand my horizons and gave me his full support. Trying to support myself while studying was extremely difficult, and Matt gave me the flexibility in my job duties to make it possible.

As a re-entry student, I returned to higher education through the California community college system. I found the teachers at Grossmont College in El Cajon to be engaged and motivated to inspire students. One inspired me more than any other, despite the fact the he had the highest expectation for his students than any other did. Dennis Collins was not a PhD, but he taught such a high level that all his students called him Dr. Collins. Because he challenged my abilities, he inspired me to learn more and because of that he expanded my understanding of the physical world that benefits me to this day. I seriously doubt without his demands on me to expand my abilities I would be at the level of education that I am at today.

A special acknowledgement goes to the faulty of the Structural Engineering department at the University of California, San Diego. Their teaching skills prepared me for graduate school and expanded my understanding of both the theoretical and practical aspects of engineering in general. Dr. Frieder Sieble, Dr. Chi-Ming Uang, Dr. Micheal Todd, and Dr Yeal D. Van Einde in particular comes to mind when I think back on my studies of structural engineering as an undergraduate student.

A special thanks goes to those that came though my research group as the University of California, San Diego. The two people that give me the fondest memories and remain good friends today are Dr. Ivan Bartoli and Dr. Stefano Coccia. Both of these gentlemen became my mentors and I believe in the bond we made and hope that it will continue for the rest of my life. Several other past participants come to mind as well. Dr. Alessandro Marzani had a kindred spirit for science and a drive to get answers that is inspirational. Dr. Salvatore Salamore made the difficult work seem effortless and his optimism was endless. Dr. Ankit Srivastava despite his laid back persona has a brilliance that I was honored to have experienced firsthand.

Thanks to all my current colleagues in the NDE/SHM laboratory at the University of California, San Diego. Dr. Claudio Nucera, Jeff Tippman, Xuan “Peter” Zhu, Stefano Mariani, and Thompson Nguyen have challenged me both as a researcher and expanded by teaching abilities. Additionally I want to recognize the staff of the Powell laboratories on campus. In particle Paul Greco, Dr. Christopher Latham, and Alex Sherman their help and assistance has invaluable in my execution of the experiments throughout my research career at the University of California, San Diego.

VITA

2007	Bachelor of Science, University of California, San Diego
2006-2009	Research Assistant, University of California, San Diego
2009	Master of Science, University of California, San Diego
2009-2012	Research Assistant, University of California, San Diego
2012	Doctor of Philosophy, University of California, San Diego

Publications

Journal Articles

1. Phillips, R., Zhu, X., and Lanza di Scalea, F., "The Influence of Stress on Electro-mechanical Impedance Measurements in Rail Steel," Materials Evaluation, vol. 70(10), pp. 1213-1218, 2012.

2. Coccia, S., Phillips, R., Bartoli, I., Salamone, S., Lanza di Scalea, F., Fateh, M., and Carr, G., "UCSD/FRA Non-contact Ultrasonic Guided Wave System for Rail Inspection: An Update," Journal of the Transportation Research Board, Transportation Research Board of the National Academies No. 2261, pp. 143-147, 2011.

3. Salamone, S., Bartoli, I., Phillips, R., Nucera, C., and Lanza di Scalea, F., "Health Monitoring of Prestressing Tendons in Post-Tensioned Concrete Bridges," Journal of the Transportation Research Board, Transportation Research Record no. 2220, pp. 21-27, 2011.

4. Bartoli, I., Salamone, S., Phillips, R., Lanza di Scalea, F. and Sikorsky, C., "Use of Interwire Ultrasonic Leakage to Quantify Loss of Prestress in Multiwire Tendons," ASCE Journal of Engineering Mechanics, 137(5), pp. 324-333, 2011

5. Rizzo, P., Cammarata, M., Bartoli, I., Lanza di Scalea, F., Salamone, S., Coccia, S. and Phillips, R., "Ultrasonic Guided Wave-based Monitoring of Rail Head: Laboratory and Field Tests," Advances in Civil Engineering - Special Issue on Structural Health Monitoring for Civil Structures: From the Lab to the Field, vol. 2010, Art. ID 291293, pp. 1-13, 2010 (invited).

6. Bartoli, I., Phillips, R., Coccia, S., Srivasatava, A., Lanza di Scalea, F., Fateh, M. and Carr, G., "Stress Dependence of Ultrasonic Guided Waves in Rails," Journal of the Transportation Research Board, Transportation Research Record no. 2159, pp. 91-97, 2010.

7. Coccia, S., Salamone, S., Bartoli, I., Phillips, R., Lanza di Scalea, F., Fateh, M. and Carr, G., "Non-contact Ultrasonic Guided Wave Detection of Rail Defects," Journal of the Transportation Research Board, Transportation Research Record, no. 2117, pp. 77-84, 2009.

8. Bartoli, I., Salamone, S., Phillips, R., Lanza di Scalea, F., Coccia, S., and Sikorsky, C., "Monitoring Prestress Level in Seven-wire Prestressing Tendons by Inter-wire Ultrasonic Wave Propagation," Journal of Advances in Science and Technology – Embodying Intelligence in Structures and Integrated Systems, 56, pp. 200-205, 2008.

Refereed Conference Proceedings

1. Nucera C., Phillips R., Lanza di Scalea F., Fateh M., Carr G., "A wayside system for in-situ measurement of rail neutral temperature by nonlinear ultrasonic guided waves," Proceedings of the ASME 2012 RTD Fall Conference (RTDF 2012), October 16-18, 2012, Omaha, Nebraska

2. Nucera C., Phillips R., Lanza di Scalea F., Fateh M., Carr G., "A wayside system based on ultrasonic guided waves for the measurement of NT in CWR," Proceedings of the AREMA 2012 Annual Conference and Exposition, Chicago, IL, Sept 16-19, 2012.
3. Coccia, S., Phillips, R., Bartoli, I., Salamone, S., Lanza di Scalea, F., Fateh, M., and Carr, G., "UCSD/FRA Non-contact Ultrasonic Guided Wave System for Rail Inspection: An Update," CD- ROM Proceedings of the 90th Annual Meeting of the Transportation Research Board, Washington, DC, January 2011.

4. Salamone, S., Bartoli, I., Phillips, R., Nucera, C., and Lanza di Scalea, F., "Health Monitoring of Prestressing Tendons in Post-Tensioned Concrete Bridges," CD-ROM Proceedings of the 90th Annual Meeting of the Transportation Research Board, Washington, DC, January 2011.

5. Bartoli, I., Phillips, R., Coccia, S., Srivastava, A., Lanza di Scalea, F., Fateh, M. and Carr, G., "Stress Dependence of Ultrasonic Guided Waves in Rails," CD-ROM Proceedings of the 89th Annual Meeting of the Transportation Research Board, Washington, DC, January 2010.

6. Coccia, S., Bartoli, I., Phillips, R., Salamone, S., Lanza di Scalea, F., Fateh, M., and Carr, G., "UCSD/FRA Ultrasonic guided-Wave System for Rail Inspection," Proceedings of the American Railway Engineering and Maintenance-of-Way Association (AREMA) Annual Conference, Chicago, IL, September 20-23, 2009.

7. Coccia, S., Salamone, S., Phillips, R., Lanza di Scalea, F., and Fateh, M., "Non-contact Ultrasonic Guided Wave Detection of Rail Defects," CD-ROM Proceedings of the 88th Annual Meeting of the Transportation Research Board, Washington, DC, January 11-15, 2009.

Other Conference Proceedings

1. Coccia, S., Phillips, R., Nucera, C., Bartoli, I., Salamone, S., Lanza di Scalea, F., Fateh, M. and Carr, G., "UCSD/FRA Non-contact Ultrasonic Guided-wave System for Rail Inspection: An Update," Proceedings of SPIE (International Society for Optical Engineering) Smart Structures/NDE Annual International Symposium – Sensors and Smart Structures Technologies for Civil, Mechanical and Aerospace Systems, M. Tomizuka, C.B. Yun, V. Giurgiutiu, J. Lynch, eds., San Diego, CA, Vol. 7981, pp. 7981131-8, 2011.

2. Phillips, R., Nucera, C., Coccia, S., Bartoli, I., Fateh, M. and Carr, G., "Monitoring Thermal Stresses and Incipient Buckling in Continuous-Welded Rail: Results from the UCSD/FRA/BNSF Large-scale Laboratory Test Track," Proceedings of SPIE (International Society for Optical Engineering) Smart Structures/NDE Annual International Symposium – Sensors and Smart Structures Technologies for Civil, Mechanical and Aerospace Systems , M. Tomizuka, C.B. Yun, V. Giurgiutiu, J. Lynch, eds., San Diego, CA, Vol. 7981, pp. 79813T1-6, 2011.

3. Salamone, S., Bartoli, I., Nucera, C., Phillips, R. and Lanza di Scalea, F., "Health Monitoring of Prestressing Tendons in Post-tensioned Concrete Structures," Proceedings of SPIE (International Society for Optical Engineering) Smart Structures/NDE Annual International Symposium – Sensors and Smart Structures Technologies for Civil, Mechanical and Aerospace Systems, M. Tomizuka, C.B. Yun, V. Giurgiutiu, J. Lynch, eds., San Diego, CA, Vol. 7981, pp.7981221-10, 2011.

4. Bartoli, I., Coccia, S., Phillips, R., Srivastava, A., Lanza di Scalea, F., Salamone, S., Fateh, M. and Carr, G., "Stress Dependence of Guided Waves in Rails," Proceedings of SPIE (International Society for Optical Engineering) Smart Structures/NDE 17th Annual International Symposium – Health Monitoring of Structural and Biological Systems, San Diego, CA, Vol. 7650, pp. 765021-1-10, March 2010.

5. Salamone, S., Bartoli, I., Phillips, R., Nucera, C., Srivastava, A., Lanza di Scalea, F., and Sikorsky, C., "Stress Monitoring by Ultrasonic Guided Waves in Prestressing Tendons for Post- tensioned Concrete Structures," Proceedings of the 5th European Workshop on Structural Health Monitoring, F. Casciati and M. Giordano, eds., Sorrento, Italy, pp. 258-263, June 28 - July 4, 2010.

6. Bartoli, I., Phillips, R., Coccia, S., Lanza di Scalea, F., Salamone, S., Marzani, A., Fateh, M. and Carr, G., "Ultrasonic Guided Waves in Continuously Welded Rails for Buckling Prediction," Proceedings of the 5th European Workshop on Structural Health Monitoring, F. Casciati and M. Giordano, eds., Sorrento, Italy, pp. 1235-1240, June 28 - July 4, 2010.

7. Salamone, S., Bartoli, I., Phillips, R., Nucera, C., Lanza di Scalea, F., Sikorsky, C. and Tamutus, T., "Health Monitoring of Prestressing Tendons in Post-tensioned Concrete Structures," CD- ROM Proceedings of the ASNT Conference on NDE/NDT for Highways and Bridges: Structural Materials Technology, New York, NY, pp. 401-408, August 16-20, 2010.

8. Nucera, C., Salamone, S., Bartoli, I., Phillips, R., Lanza di Scalea, F. and Sikorsky, C., "Nonlinear Ultrasonic Guided Waves for Stress Monitoring in Prestressing Tendons for Post- tensioned Concrete Structures," CD-ROM Proceedings of the ASNT Conference on NDE/NDT for Highways and Bridges: Structural Materials Technology, New York, NY, pp. 409-417, August 16-20, 2010.

9. Bartoli, I., Coccia, S., Phillips, R., Srivastava, A., Lanza di Scalea, F., Salamone, S., Fateh, M. and Carr, G., "Stress Dependence of Guided Waves in Rails," Proceedings of SPIE (International Society for Optical Engineering) Smart Structures/NDE 17th Annual International Symposium – Health Monitoring of Structural and Biological Systems, San Diego, CA, Vol. 7650, pp. 765021-1-10, March 2010.

10. Bartoli, I., Nucera, C., Phillips, R., Salamone, S., Srivastava, A., Lanza di Scalea, F., Coccia, S., and Sikorsky, C., ""Stress Monitoring in Prestressing Tendons for Post-tensioned Concrete Structures by Nonlinear Ultrasonic Guided Waves," Proceedings of 17th International Workshop on Structural Health Monitoring, F-K. Chang, ed., Stanford University, September 9-11, pp. 2115-2122, 2009.

11. Coccia, S., Phillips, R., Baertoli, I., Salamone, S., Lanza di Scalea, F., Fateh, M. and Carr, G., "Ultrasonic Guided Wave Detection of Rail defects: Prototype Development and Field Testing for the Federal Railroad Administration," Proceedings of 7th International Workshop on Structural Health Monitoring, F-K. Chang, ed., Stanford University, September 9-11, pp. 255-262, 2009.

12. Bartoli, I., Salamone, S., Di Leo, P., Mezzanotte, M., Lanza di Scalea, F., Rhymer, J., Phillips, R., Ajovalasit, A. and D'Acquisto, L., "Impact Force Identification and Location on Isotropic and Composite Panels," Proceedings of 7th International Workshop on Structural Health Monitoring, F-K. Chang, ed., Stanford University, September 9-11, pp. 1902-1909, 2009.

13. Coccia, S., Bartoli, I., Phillips, R., Lanza di Scalea, F., Fateh, M. and Carr, G., "Non-contact Ultrasonic Detection of Rail Defects," Proceedings of the Transportation Research Board (TRB) 11th Joint Light Rail Conference, Los Angeles, CA, April 19-22, 2009.

14. Bartoli, I., Nucera, C., Srivastava, A., Salamone, S., Phillips, R., Lanza di Scalea, F., Coccia, S. and Sikorsky, C., "Nonlinear Ultrasonic Guided Waves for Stress Monitoring in Prestressing Tendons for Post-tensioned Concrete Structures," Proceedings of SPIE (International Society for Optical Engineering) Smart Structures/NDE 16th Annual International Symposium - Sensors and Smart Structures Technologies for Civil, Mechanical and Aerospace Systems, M. Tomizuka, ed., San Diego, CA, Vol. 7292, pp. 7292711-72927112, 2009

15. Lanza di Scalea, F., Bartoli, I., Salamone, S., Phillips, R., and Sikorsky, C., "Monitoring Prestress Level in Seven-wire Prestressing Tendons by Inter-wire Ultrasonic Wave Propagation," Proceedings of 3rd International Conference on Smart Materials, Structures, and Systems (CIMTEC), Catania, Italy, June 8-13, 2008.

16. Bartoli, I., Phillips, R., Lanza di Scalea, F., Salamone, S., Coccia, S, and Sikorsky, C., "Load Monitoring in Multi-wire Strands by Interwire Ultrasonic Measurements," Proceedings of SPIE (International Society for Optical Engineering) Smart Structures and Materials and NDE for Health Monitoring and Diagnostics – Sensors and Smart Structures Technologies for Civil, Mechanical and Aerospace Structures, M. Tomizuka, ed., San Diego, California, Vol. 6932, pp.6932091-69320912, 2008.

17. Bartoli, I., Lanza di Scalea, F., Phillips, R., Sorrivi, E. And Sikorsky, C., "Health Monitoring of Prestressing Tendons by Ultrasonic Waves and Embedded Sensors," Proceedings of 6th International Workshop on Structural Health Monitoring: Quantification, Validation and Implementation-K. Chang, ed., Stanford University, September 11-13, pp. 476-482, 2007

18. Bartoli, I., Marzani,A., Lanza di Scalea, F., Rizzo, P., Viola, E., Sorrivi, E., and Phillips, R. "SAFE Modeling of Waves for the Structural Health Monitoring of Prestressing Tendons," Proceedings of SPIE (International Society for Optical Engineering) Smart Structures and Materials and NDE for Health Monitoring and Diagnostics – Health Monitoring of Structural and Biological Systems, San Diego, California, Vol. 6532, pp. 65320D1-65320D12, 2007.

Technical Reports

1. Coccia, S., Phillips, R., Bartoli, I., Salamone, S., Rizzo, P., Lanza di Scalea, F., "On-line High-speed Rail Defect Detection – Part II ," Technical Report No. DOT/FRA/ORD-12/02, Department of Transportation/ Final Report to the Federal Railroad Administration, 2012

2. Coccia, S., Bartoli, I., Phillips, R., Rizzo, P., Salamone, S., and Lanza di Scalea, F., "On-line High-speed Rail Defect Detection – Part II," Technical Report No. SSRP-10/03 to the Federal Railroad Administration, University of California, San Diego, 2010.

3. Bartoli I., Salamone S., Phillips R., Nucera C., Lanza di Scalea F., "Health Monitoring to detect failure of prestressing (PS) cables in segmental box-girder bridges," Technical Report No. 090938 to the California Department of Transportation, University of California, San Diego, 2009.

4. Lanza di Scalea, F., Bartoli, I., Coccia, S., Salamone, S., and Phillips, R., "Automated Measurement of Stress in Continuous Welded Rail (CWR)," Letter Report to the Federal Railroad Administration, University of California, San Diego, 2009.

5. Coccia, S., Bartoli, I., Phillips, R., Salamone, S. and Lanza di Scalea, F., "Noncontact Rail Defect Detection: Fourth Field Test," Technical Report No. SSRP-09/04 to the Federal Railroad Administration, University of California, San Diego, 2009.

6. Nucera, C., Bartoli, I., Salamone, S., Phillips, R., and Lanza di Scalea, F., "Nonlinear Ultrasonics for Health Monitoring of Prestressing Tendons," Letter Report to the California Department of Transportation, University of California, San Diego, 2008.

7. Bartoli, I., Sorrivi, E., Lanza di Scalea, F., and Phillips, R., "Health Monitoring of Prestressing Cables: Literature Review and Wave Propagation Results," Technical Report No. SSRP-07/14 to the California Department of Transportation, University of California, San Diego, 2007.

Patents

9. Lanza di Scalea, F. and Phillips R., "Characterization of surface cracks in rail," US Provisional Patent Appl. 61/595,574, filed Feb 6, 2012.

10. Lanza di Scalea, F., Nucera C., Phillips R., Coccia S., "Stress detection in rail," US Provisional Patent Appl. 61/558,353 filed Nov. 10, 2011.

ABSTRACT OF THE DISSERTATION

Ultrasonic Methods for Rail Inspection

By

Robert Ronald Phillips

Doctor of Philosophy in Structural Engineering

University of California, San Diego, 2012

Professor Francesco Lanza di Scalea

Between January 2002 and January 2012, over 6,500 derailments due to internal defects and track misalignments, known as sunkinks, occurred in the US, with associated ~ 1 billion dollars of direct and indirect cost to the railroad industry. Internal defects in rails are the result of manufacturing defects and rail wear. Current rail inspection methods have well known limitations that prevent them from detecting all of the critical flaws with minimum false positive rates. Safety Recommendations issued by the National Transportation Safety Board (NTSB) following the disastrous train derailments at Superior, WI in 1992 and Oneida, NY in 2007, among others, reiterated the need to improve current rail inspection methods. Sunkinks are the result of excessive compressive thermal loads developed in Continuous Welded Rail (CWR) in hot weather. In order to monitor the possibility of a sunkink, the rail industry

necessitates of a reliable method to indicate the level of thermal stress in the rail in a nondestructive and practical manner. Both the Federal Railroad Administration and the railroads are still searching for such method for in-situ thermal stress measurement in rails. is not the search

The goal of this dissertation is to improve the state of the art of ultrasonic wave propagation in waveguides, with specific applications to: (1) improving internal defect detection in rails, and (2) measuring thermal loads in rails.

On the first application (defect detection), a prototype has been developed using non-contact means of generating and detecting guided waves in rails. Specifically, the prototype uses a pulsed laser for wave generation and air-coupled sensors for wave detection. The system also employs real-time statistical processing of the ultrasonic measurements that maximizes the sensitivity to defects while minimizing false positives. The prototype was field tested with excellent results in terms of defect detection reliability.

On the second application (thermal stress measurement), the techniques of guided-wave velocity change and Electro-Mechanical Impedance (EMI) changes have been explored. The wave velocity change is traditionally used in the field of bulk waves (acousto-elasticity). The extension to guided waves is not obvious. The EMI method is conventionally used to detect structural defects close to the probing transducer by measuring the coupled transducer-structure electrical impedance. The EMI method is less used to measure load levels in the structure. A model has been developed to predict the electro-mechanical response of a piezoelectric transducer

mounted on a structure subjected to quasi-static loads. Experimental validation has been performed at UCSD's Large-Scale Rail Buckling Testbed, a unique 70ft-long track of CWR that was constructed at UCSD's Powell Labs for this project. Both techniques of guided-wave velocity measurements and EMI measurements have shown to have some promise, once the effects of temperature alone are compensated for.

1. Introduction

1.1 Introductory discussion and motivation for research

U. S. Federal Railroad Administration safety statistics for 2002-2012 [1] show that track failures from rail, joint bars, anchoring and rail geometry account for 6501 accidents at a cost of over one billion dollars. Three particular track failures account for 25% of total incidents and 41% of the reported damage cost. Transverse defects that include wear and manufacturing impurity fissures are the primary cause of the accidents. The second leading cause comes from detail fractures that are developed as a result of surface shelling. Changes in the rail geometry due to constrained thermal expansion, known in the rail industry as sunkinks, are the third leading cost.

Perhaps the greatest concern for derailments is, aside from the cost, the high potential of collateral damage from the release of hazardous material carried by the train. One such example occurred in New Brighton, Pennsylvania on October of 2006. The derailment of 20 tank cars released ethanol into a river and surrounding soil in addition to the evacuation of a seven-block region for 2 days. Such accidents can be costly, environmentally devastating, and disrupt innocent lives [2].

For defect detection in rail, the most common methods are contact ultrasonics and magnetic induction [3]. While contact ultrasonic testing has been used since the 1960’s with some reliability, the method does have its flaws. Conventionally, the

ultrasonic method is performed with liquid filled wheel probes in a pulse-echo configuration from the top of the rail head. In this approach, speeds are limited by the need for contact and limits of the wheels capacity to resist centripetal forces. Additionally, the pulse-echo method can be masked by surface flaking and shelling, that prevent the ultrasonic beam from reaching internal defects below the surface condition. The magnetic induction methods have more limitations. Magnetic induction is highly sensitive to lift-off distance of the transducers and surface obstructions. With an aging transportation infrastructure, increases in tonnage, and rail safety concerns, a method that overcomes the limitations of current methods has been explored in this dissertation. The method with the most promise is the use of ultrasonic guided waves as reported in recent literature [4-6].

On the rail thermal buckling (sunkink) issue, the primary concern of railroad maintenance engineers is to know the state of thermal stress in the rail at any given moment. More specifically, the parameter of interest is the rail Neutral Temperature (NT), or the rail temperature corresponding to zero thermal stress. Methods used currently to determine the rail neutral temperature *in-situ* are strain gauging, static stiffness, and magnetic permutation [7-9]. Despite having some proven reliability, all of these methods have serious limitations. Strain gauging is a decades old method, and it requires cutting the rail in order to establish the zero-stress (reference) point for the gage. The static stiffness method (VERSE) is also intrusive to the service schedules as it requires unanchoring of several feet of rail. The magnetic permutation

measurements have yet to be proven to be reliable. A new method that is nonintrusive and reliable is in high demand in rail engineering.

Proposed in this dissertation are methods based on ultrasonic measurements to address the concerns of the rail industry and Federal Railroad Administration vis-à-vis the two above mentioned issues: (1) detection rail defects, including internal defects and surface defect, and (2) measurement of the rail thermal stresses (or rail neutral temperature). Within this work, a non-contact ultrasonic using ultrasonic guided waves system (based on laser generation and air-coupled detection) has been packaged into a prototype and tested in the field showing better performance than the industry standard [6]. This system is expanded to include a method for surface characterization using surface guided waves. Finally, the method of Electro-Mechanical Impedance (EMI) was used for the potential determination of the rail neutral temperature [10].

1.2 Outline of dissertation

In this dissertation the emphasis is on the ultrasonic methods used to monitor the health and condition of rail tracks. The dissertation extends the work by the UCSD NDE & SHM laboratory on the investigation of guided waves for defect detection.

Chapter 2 discusses the motivation behind the research presented in thesis dissertation. An overview of the challenges in the inspection of rail inspections is discussed. The reasoning for the improvement in defect detection and rail neutral temperature measurements are described.

Chapter 3 describes the type and origin of the railhead defects that are targeted in this study. A summary of the history of rail inspection in the United States and an overview of railhead defects is given. The problems encountered in the detection methods are discussed. A review of the current methods used by the rail industry is presented.

Chapter 4 covers the Semi Analytical Finite Element (SAFE) numeric method for the solution to the wave equation for wave guides. Advantages and disadvantages of the method for rail defect detection and rail neutral temperature measurements are presented through the SAFE results. Advancement to the method is achieved by modeling the wave propagating modes for loaded wave guides.

Chapter 5 the Electromechanical Impedance (EMI) analytic model is derived. The piezoelectric and mechanical properties are presented for the EMI technique. The analytic model for the mechanical and electrical response of piezoelectric wafers is given. In the evaluation of the EMI behavior a unique method for stress measurements is identified.

Chapter 6 gives the development and result of the rail defect detection through ultrasonic guided waves. A unique part of the research is the improvements in the development of a prototype using a laser/air-coupled ultrasonic technique. The results of blond test performed for the Federal Railroad Administration overseen by Herzog Rail Services and the Volpe National Transportation Systems Center.

Chapter 7 gives the results of the experiment involved in the proof of concept for the EMI as an advancement the measurement on *in-situ* stresses. From the proof of concept results, continued testing was performed to evaluate the EMI method as a new tool for rail neutral temperature determination.

Chapter 8 summarizes the conclusions and recommendations for future work.

2. Problem Statement

2.1 Internal Rail Flaws

The onset of rail defects is influenced be many factors. Generally, the sources of rail defects fall into three categories [3]. Defect origins are classified as rail wear, manufacturing defects and improper use or handling. The Federal Railroad Administration *Track Inspector Rail Defect Reference Manual* reviews the identification of defect orgins [11].

Defects generated from rail wear and rolling contact fatgiue include, but are not limited to, bolt hole cracks, vertical split head, and detail fractures. Manfufacting defects are onset by impurities in the material and hydrogen bubbles occuring in the cooling process. Break burns and base fractures are examples of defects from improper use and handing. While not not all defects are critial, the detection of them may require operational restrictions. To be consired noncritial, the defect cannot affect the safe operations of the trains or the structural integrity of the track.

Upon detection of an internal defect, remedial action is directed by federal regulations. From Title 49 Code of Federal Regulations (CFR) Part 212,the table found in § 213.337 and shown in Figure 2-1 prescribes the remedial actions required for the various types of rail defects. If the defective rail is not replaced or removed from service, the owner of the track must take the remedial action prescribed in the table, which is designated by one or more of the following notes[12]:

A. Assign person designated under §213.305 to visually supervise each operation over defective rail.

A2. Assign person designated under §213.305 to make visual inspection. That person may authorize operation to continue without visual supervision at a maximum of 10 m.p.h. for up to 24 hours prior to another such visual inspection or replacement or repair of the rail.

B. Limit operating speed over defective rail to that as authorized by a person designated under §213.305(a)(1)(i) or (ii). The operating speed cannot be over 30 m.p.h.

C. Apply joint bars bolted only through the outermost holes to defect within 20 days after it is determined to continue the track in use. Limit operating speed over defective rail to 30 m.p.h. until joint bars are applied; thereafter, limit speed to 50 m.p.h. When a search for internal rail defects is conducted under §213.339 and defects are discovered which require remedial action C, the operating speed shall be limited to 50 m.p.h., for a period not to exceed 4 days. If the defective rail has not been removed from the track or a permanent repair made within 4 days of the discovery, limit operating speed over the defective rail to 30 m.p.h. until joint bars are applied; thereafter, limit speed to 50 m.p.h.

D. Apply joint bars bolted only through the outermost holes to defect within 10 days after it is determined to continue the track in use. Limit operating speed over the

REMEDIAL ACTION

Defect	Length of defect (inch)		Percent of rail head cross-sectional area weakened by defect		If defective rail is not replaced, take the remedial action prescribed in note
	More than	But not more than	Less than	But not less than	
Transverse fissure			70 100	5 70 100	B. A2. A.
Compound fissure			70 100	5 70 100	B. A2. A.
Detail fracture Engine burn fracture Defective weld			25 80 100	5 25 80 100	C. D. [A2] or[E and H]. [A] or [E and H].
Horizontal split head Vertical split head Split web Piped rail Head web separation	1 2 4 (1)	2 4 (1)	 (1)	 	H and F. I and G. B. A.
Bolt hole crack	½ 1 1½ (1)	1 1½ (1)	 (1)	 	H and F. H and G. B. A.
Broken base	1 6	6 	 	 	D. [A] or [E and I].
Ordinary break					A or E.
Damaged rail					D.
Flattened rail	Depth > 3/8 and Length > 8				H.

(1) Break out in rail head.

Figure 2-1: Remedial Actions in the presence of known defects (Title 49 CFR § 213.337)

defective rail to 30 m.p.h. or less as authorized by a person designated under §213.305(a)(1)(i) or (ii) until joint bars are applied; thereafter, limit speed to 50 m.p.h.

E. Apply joint bars to defect and bolt in accordance with §213.351(d) and (e).

F. Inspect rail 90 days after it is determined to continue the track in use.

G. Inspect rail 30 days after it is determined to continue the track in use.

H. Limit operating speed over defective rail to 50 m.p.h.

I. Limit operating speed over defective rail to 30 m.p.h.

Statistics related to accident reports in U.S. annually are available through the Federal Railroad Administration Office of Safety and Analysis. The reported data gives the total count of accidents, type of incident, cost of the damage, and the occurrence of any casualties. Data related to rail defects are found under the category of T-Rail, Joint Bars and Rail Anchoring found at **http://safetydata.fra.dot.gov/OfficeofSafety /Default.aspx.** Table 2.1 list the top 5 causes, by cost of damage, reported for January 2011- January 2012 of the previously mentioned category. Costs of rail failures include cost of inspection, loss of business confidence, train delays, cost of remedial and preemptive treatments, and consumer support. The table list the type of defect, and in the second column shows the ranking and percentage of the total accidents for the category. In the last column, the cost of the damage is listed. From this category of accident causes, the top five in cost account for 56.7% of the total accidents for the category that contains 23 different causes defined by the Federal Railroad Administration.

Table 2.1: FRA Office of Safety T-Rail, Joint Bars, Rail Anchoring (top 5 Damage Cost Accident Causes data for January 2002- January 2012)

Type of Defect	% of Total Accidents	Reported Damage Costs ($)
Detail Fracture (Shelling/Head Check)	14.6 (2nd Highest)	148,874,377
Transverse/Compound Fissure	24.6 (Highest)	144,942,128
Vertical Split Head	12.1 (3rd Highest)	46,515,206
Broken Weld (Field)	2.0 (10th Highest)	37,435,067
Bolt Hole or Crack	3.4 (6th Highest)	29,090,304
Total	**56.7**	**406,857,082**

Table 2.2: FRA Office of Safety T-Rail, Joint Bars, Rail Anchoring (top 5 Damage Cost Accident Causes data for January 2011- January 2012)

Type of Defect	% of Total Accidents	Reported Damage Costs ($)
Detail Fracture (Shelling/Head Check)	21.8 (Highest)	15,079,399
Transverse/Compound Fissure	15.9 (2nd Highest)	8,319,632
Vertical Split Head	13.5 (3rd Highest)	5,713,913
Broken Weld (Field)	0.4(18th Highest)	142,204
Bolt Hole or Crack	4.4 (8th Highest)	3,588,606
Total	**56.0**	**32,843,754**

2.2 Neutral Temperature/Buckling FRA Statistics

To have some idea of the significance of the detail fracture (shelling/head check), transverse/compound fissure and vertical split head type defects, the data for the year 2011 is shown in

Table 2.2. These three types of defect still account for the top three causes of accidents. Also, the top five damage cost causes for the ten year period still account for 56% of total accidents.

Maintaining rail track geometry is a continuous challenge to the rail operators throughout the world. The dynamics of trains passing tonnage on the rail bed and the environment continually alter the geometry of the rail. The focus in the studies presented here are on the effect of temperature and the loading imposed on the rail by temperature variation. Sunkink is the result of the thermal load imposed on a section of continuous welded rail due to the normal heating of the ambient temperature. Conversely, rail breaks occur in cold weather as the temperature drops.

(a) Sunkink misalignment (b) Sunkink buckling

Figure 2-2: Sunkink of Rail (a) Sunkink misalignment (b) Sunkink Buckling

According to FRA statistics, sunkink was the cause of 103 derailments between January 2002 and January 2012, accounting for 21% of the derailments in the track geometry category. Moreover, of the $40M total cost of derailments over 50% was caused by track geometry faults. Between January 2011 and January 2012, fifty-eight derailments were caused by the phenomenon known has sunkink in the rail industry. The severity of sunkink ranges from a rail misalignment, as shown in Figure 2-2, to complete rail buckling, shown in Figure 2-2 b. In very recent history, a derailment just outside of Chicago on July 4th 2012 resulted in two fatalities and it was cause by a thermally-buckled rail.

When the rail is installed into service, it is in a stress free condition at the installation temperature. The rail temperature corresponding to zero thermal stress is known in the rail industry as the rail neutral temperature. As the rail is cooled or heated to a temperature different than the rail neutral temperature, it absorbs tensile forces or compressive forces, respectively These forces are defined by the common equation:

$$P = A\sigma = -\alpha EA\Delta T = -\alpha EA\left(T - T_N\right) \qquad \textbf{2.1}$$

where α is the coefficient of thermal expansion of the rail steel, E is Young's modulus of elasticity, A is the cross sectional area of the rail, T is the current rail temperature, and T_N is the rail neutral temperature.

The major concern to rail owners is the excessive compressive force leading to the sunkink and buckling.

Continuous welded rail in the United States is typically installed at temperatures between 90^{o}F and 110 ^{o}F. Over time, due to a variety of causes such as rail settlement and maintenance, the rail neutral temperature can be reduced to a range of 50 ^{o}F to 70 ^{o}F. Depending on the cross sectional area of a rail, an increase in rail temperature of 1^{o}F will increase the compressive force by 2.5 kips. Considering that on a hot summer day the rail temperatures will exceed the ambient temperature by 30^{o}F, the resulting temperature of the rail will range between 140^{o}F to 160^{o}F. The increase in compressive force of ~250 kips can then lead to a buckling failure.

3. Rail Defects and Review of Rail Inspection Methods

3.1 Structural Rail Defects

Several conditions results in structural defects in rail. Normally the defects originate from the manufacturing process, cyclical loading, impact from rolling stock, rail wear and plastic flow. Extensive maintenance and inspection programs have been developed over several decades to extend the life of the rail in service. Inspection methods have developed from simple visual inspection to laser/air-coupled ultrasonic inspection. Maintenance programs involve surface cleaning to rejuvenate rail profiles through rail grinding.

Rail defects are classified into longitudinal defects, extending along the vertical plane, and transverse defects extending along the transverse plane. Any progressive defect with a transverse separation is considered a transverse defect. Figure 3-1 is visual representation to define the previously mentioned terminology.

Steel is essentially iron and carbon. However, in order to create a workable material, several other materials are required in the manufacturing process. As an example, 1 ton of steel takes 1 $^{1}/_{3}$ tons of iron ore, $^{2}/_{3}$ ton of coal, $^{1}/_{5}$ ton of limestone, ¼ ton of iron and/or steel scrap, 165 tons of water, and 8 tons of air. The rail is manufactured in a four-step process. First. from the raw materials the molten steel is produced. Then the molten material is cast into lingots or continuous blooms. Next, a rolling process is

performed to obtain the appropriate cross section of rail. Finally, the finishing is done by cooling, straightening, and cutting to the proper length.

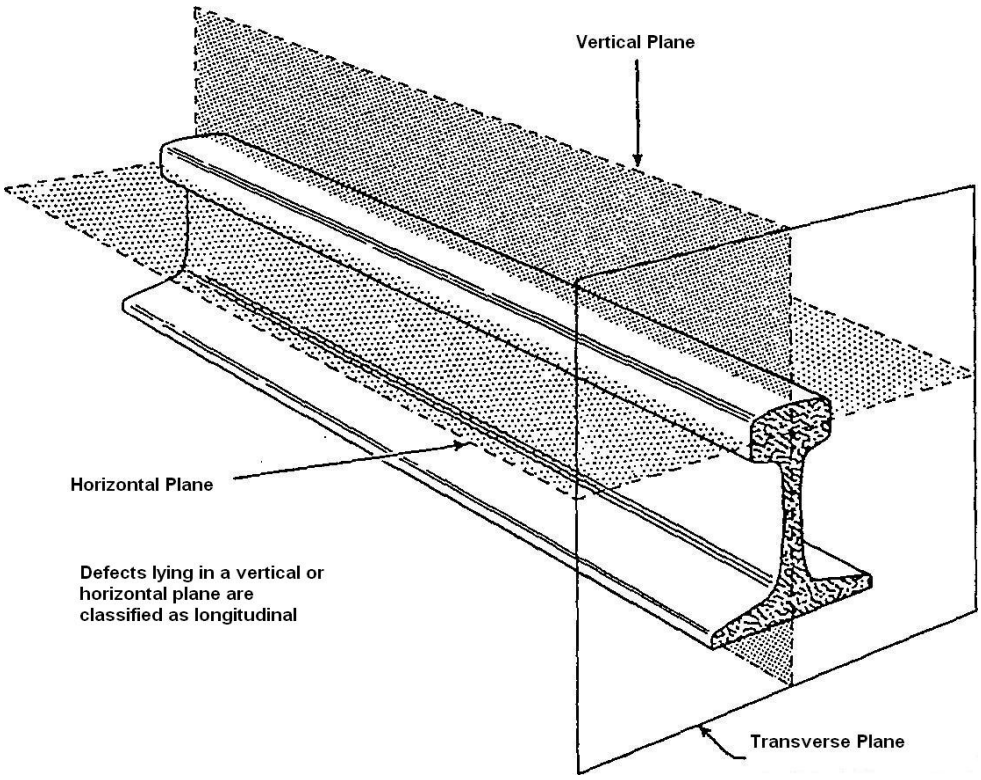

Figure 3-1: Identifications of terminology for rail defect orientations.

3.1.1 Manufacturing Defects

In this manufacturing process, it is possible for impurities, such as a carbon particle, to become trapped in the formed cross section. Such impurities can produce fissures and traverse defects such as that shown in Figure 3-2.The position of the inclusion can be anywhere across the cross section, but the defect created will be a transverse defect.

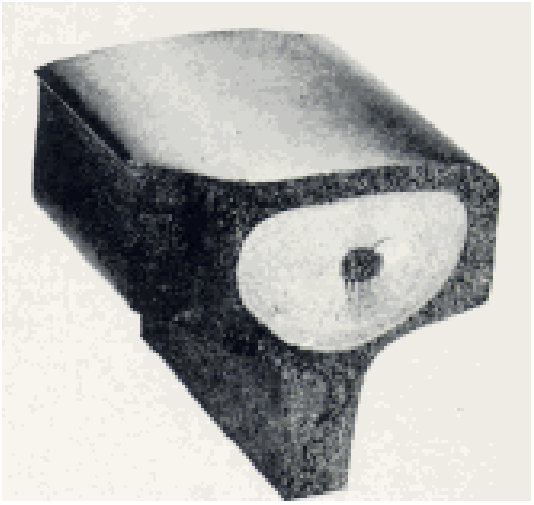

Figure 3-2: Transverse defect due to impurity inclusion.

The trapping of hydrogen bubbles during the cooling process creates the other most common manufacturing defect. The fissure produced by the hydrogen bubble creates a transverse defect that has a slow growth rate. An example of such a defect is shown in Figure 3-3

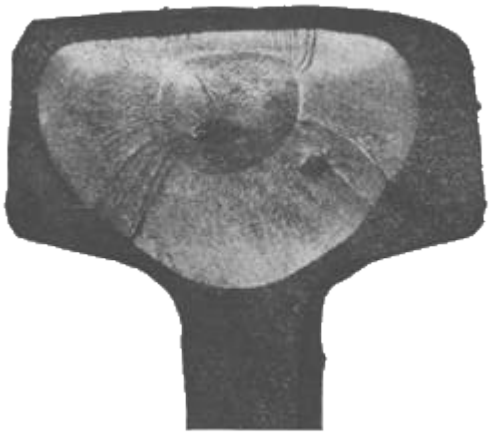

Figure 3-3: Slow growth transverse fissure generated by hydrogen bubble in manufacturing.

3.1.2 Rail Loading and Stressing Defects

Rail loading at the rail/wheel interface is a complex scenario that involves a static load, a dynamic load and an impact load acting vertically on the rail head. On level tangent track, the static load of a 160 ton, 8 wheel railcar would be 20 ton. The static load is highly influenced by track section curvature and super-elevation. The train speed results in the additional dynamic loading. Car/truck interaction with the track geometry results in the vertical dynamic loading. An additional loading over the static loading and dynamic loading is the impact loading resulting from flat spots in wheels and significant railhead irregularity.

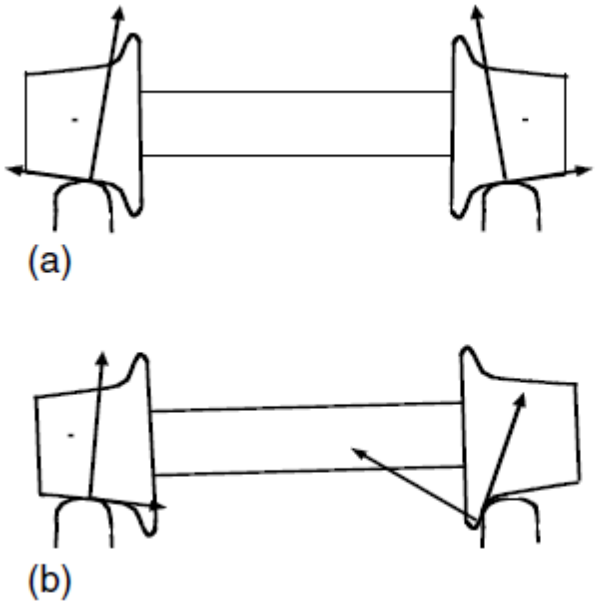

Figure 3-4: Normal and Lateral Force from Wheel-Rail Interaction:(a) Level Track (b) Track with Super Elevation.[13]

Figure 3-4 shows the free body diagram of the vertical and transverse force vectors of the wheel/rail interface, for both a level track and track in a curve that has a super

elevation. It is seen that the forces acting on the railhead in a super elevation vary significantly between the high rail and the low rail. These vertical and transverse forces act essentially on the strong axis of the rail, and they contribute to the growth of rail defects.

In addition to the overstressing initiation of defect, rail wear and rolling contact fatigue create a surface condition that is detrimental to current ultrasonic test methods and leads to more internal defects. The rail/wheel interface is a complex loading scenario which is complicated by the rail geometry. While widely understood by using Hertz contact theory resulting in an ellipsoidal contact, the point of contact and area of contact is heavily influenced by the track geometry [14-19]. Figure 3-5 shows that the contact surface is larger than that seen in the high rail, however the high rail contact surface occur at the critical gauge corner..

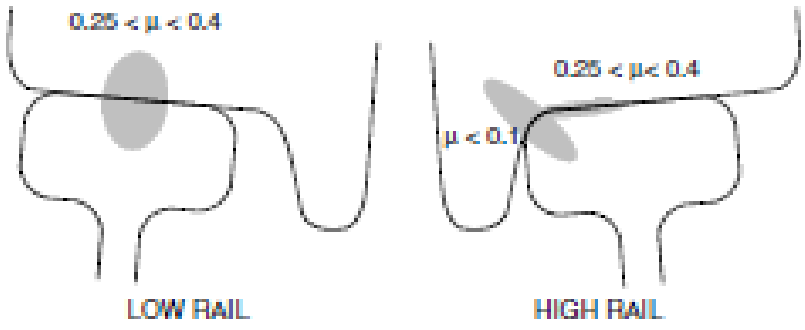

Figure 3-5: Wheel/Rail Contact of Low Rail and High Rail [20]

Additionally, the gage width of the train car wheel set is narrower than that of the track and this difference induces a behavior known as hunting, as seen is Figure 3-6. This figure shows that, on a tangent section of track, the train car will wander laterally

within the rail's gage width. The hunting behavior places the contact point randomly between those seen in the low/high rail situation found in sections of rail in a curve [13, 20].

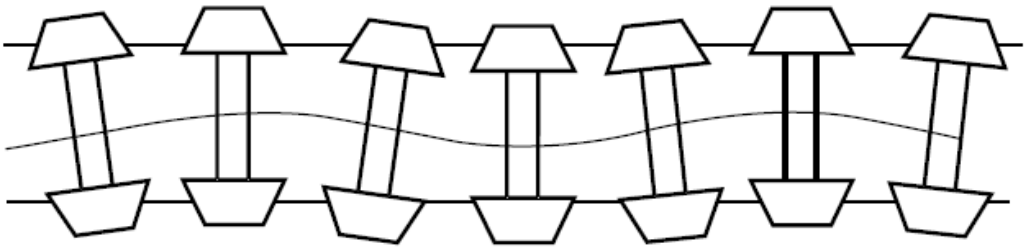

Figure 3-6: Kinematic Oscillation of Wheelset (Hunting)[13]

The strain deformation within the rail due to the contact forces is shown in Figure 3-7: Contact patch pressure and forces causing surface and internal elastic deformation of the rail [21]. It is clear that the strain imposed on the rail from the wheel/rail interface is greatest near the surface, although internal strains also develop.

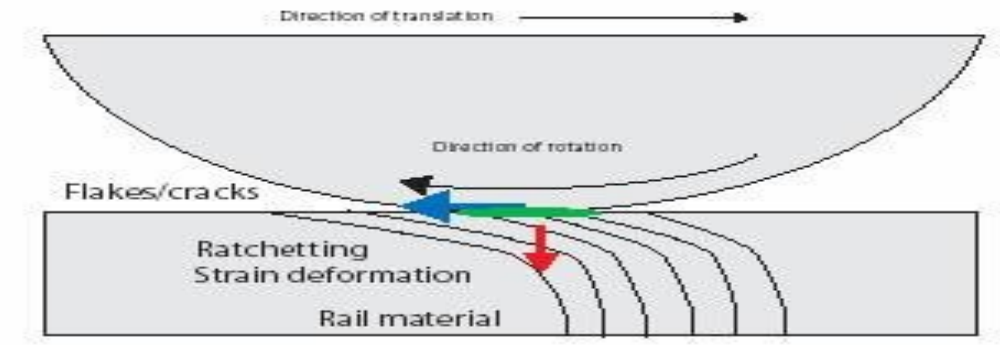

Figure 3-7: Contact patch pressure and forces causing surface and internal elastic deformation of the rail [21]

As stated previously, the greatest concern is at the rail gauge corner. As seen in Figure 3-8, when the wheel flange is in contact with the rail, the highest stress level is concentrated at the gage corner.

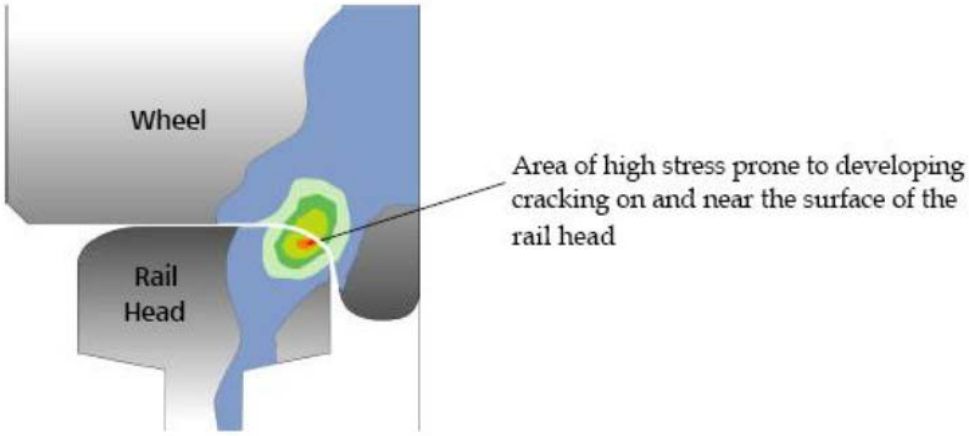

Figure 3-8: Contact stresses at gage corner on tight curved track[21]

The large surface deformation and fatigue of the rail steel lead to a variety of surface defects which in turn initiate internal defects. One cause of initiation and growth of internal defects is the hydraulic effect of water penetration into the surface penetrating crack [21, 22]. In both seasons the hydraulic effect is damaging to the rail. In the summer, water becomes trapped and as an incompressible fluid turns the top surface of the shallow angle crack into a level, thus adding a moment in the stress field. In the winter, the entrapped water expands at night as temperatures drop below freezing and expands the crack.

At the rail surface, there are four types of conditions that are of concern as some surface conditions will turn down and become transverse defects. The largest

contributor to masking of modern ultrasonic methods is a shelling defect, an example of which is shown in Figure 3-9. Shelling generally occurs in the high rail found in a curved section of rail. Head checking is more commonly found in a tangent section of track as the condition is generated by the fatigue of the friction and loading of the rail/wheel interface. Figure 3-10 shows a case of head checking.

Figure 3-9: Rail Surface Shelling.

Head checking is the case that will lead to the onset of surface flacking. In the case of head checking, the frictional forces and the onset of surface hardening from the rail/wheel interface initiate plastic flow between the head checking pits on the surface. As seen in Figure 3-11, the condition of the rail can quickly go from a pitted surface to an area covered with the flaking of the steel surface. Once the onset of flaking has begun, the same problem that occurs in shelling will manifest itself.

Figure 3-10: Rail Head Checking

Figure 3-11: Rail Surface Checking and Flaking

An extreme case of head checking, as shown in Figure 3-12, is classified as head spalling. The onset of spalling occurs at the site of a brake burn. Brake burns are the result of hard braking that results in slip friction condition. Spalling is seen on the top

surface of the rail head and is not as much of a concern to the ultrasonic inspection method, since the rail corners are not generally masked by the surface condition[23].

Figure 3-12: Rail Surface Spalling

All the previously mentioned surface defects have the potential to turn downward into the head of the rail and create a transverse defect. In Figure 3-13, the vectors of the surface crack growth and the downward branch are illustrated. The typical traverse defect formed from the downward branch is the Tache Oval. In the case of a defect formed from the surface condition, the location of the Tache Oval is found to be at the edge of the gage corner, commonly referred to as a detail fracture. An example of this type of defect formed under the shell in the near surface of the rail head is shown in Figure 3-14a. As a comparison, in Figure 3-14b the same transverse defect is shown when formed in the absence of the surface shelling. In the juxtaposition of the two gauge corner defects, the presence of the shell acts as a barrier to the path of an

ultrasonic source. It is this barrier that is the challenge to improving ultrasonic rail inspection methods

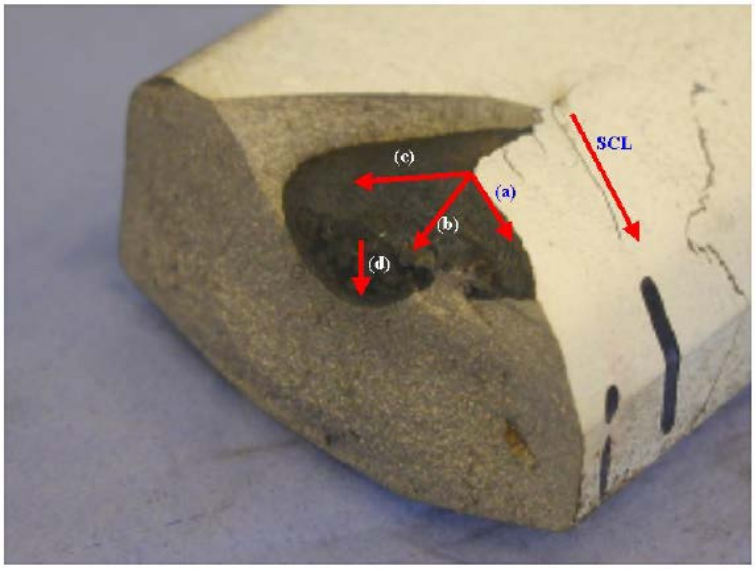

Figure 3-13: Features of RCF crack growth – BR113A 1986 rail, Grade 220 [49]. "SCL" is surface crack length, 'a', 'b', and 'c' are the initial directions of crack growth. 'd' is the downward branch of the crack leading to rail failure.

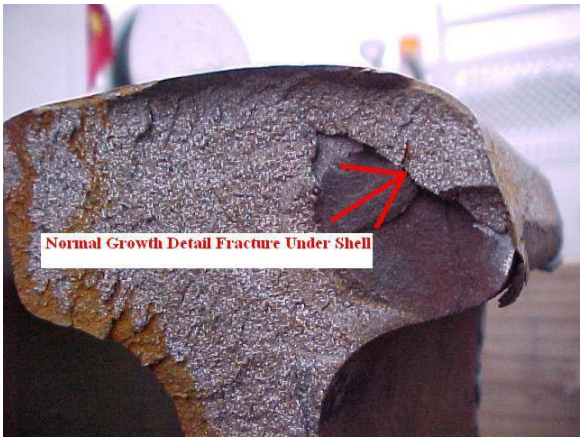

(a) Detail fracture (Tache Oval) under shelling (b) Detail Fracture with no Shelling

Figure 3-14: Gage Corner detail Fracture: (a) Detail Fracture Under Shelling (b) Detail Fracture with no Shelling

3.1.3 Current Rail Defect Detection Methods

After seeing an increased number of disastrous train derailments, Dr. Elmer Sperry in 1923 took it upon himself to develop a nondestructive testing system for rail inspection. By 1928 Dr. Sperry had built an inspection car and had in service on the Wasbash Railway in Montpelier, Ohio and Clark Junction, Ind., under a commercial contract. One of Sperry's inspection cars detected a large transverse fissure and recommended the rail be removed and replaced. Although annoyed by the recommendation, the section of rail was removed and taken to Dr. Sperry for further inspection. Upon breaking the rail and displaying the size of the defect and the ability of the rail inspection cars, the railroads were convinced that the testing was worthwhile. By 1930 Sperry's service fleet numbered 10 cars [24].

In the first Sperry inspection cars, the inspection method was through magnetic induction and the method is still in practice today. The method is based on the principles of electromagnetism. A heavy current is induced in the rail to be inspected via brushes in contact with the rail. Search coils are moved through the magnetic field and perturbations of the field identify defects in the rail [25]. A schematic of the system components are displayed in Figure 3-15. The contact brushes required by this technique are often considered cumbersome. Other disadvantages of the induction methods are the required small lift-off of the core from the rail head surface, and the pronounced sensitivity to electromagnetic noise. Rail inspection systems based on induction methods are also sensitive to the presence of joints, bars and holes in the rail, resulting in false detections that need to be purged from the results

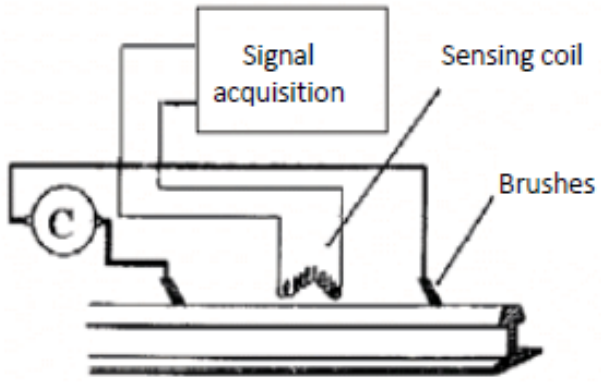

.

Figure 3-15: Components of Induction Inspection System

The most common method for rail inspections today remains ultrasonic testing, that consists of scanning the rail through ultrasonic beams and detect the return of reflected and scattered energy using ultrasonic transducers [26]. Traditionally, the transducers are

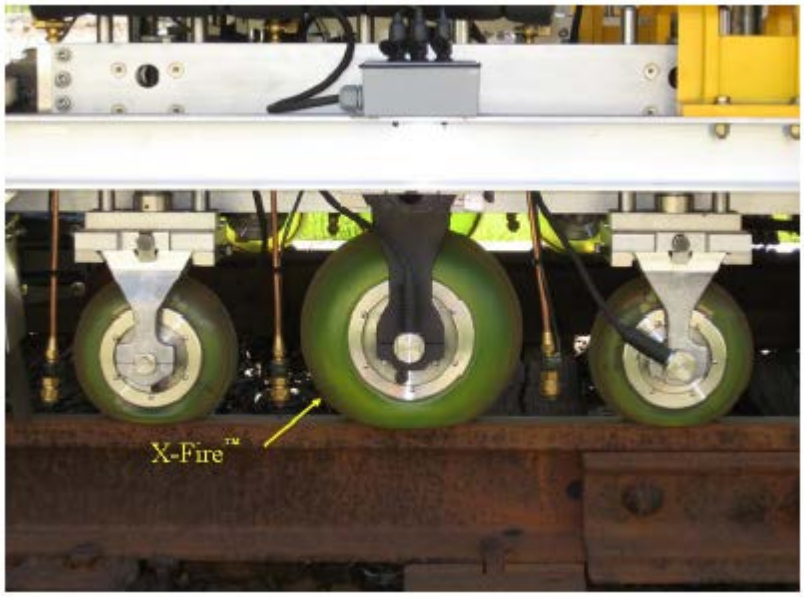

Figure 3-16: Ultrasonic Wheel Test System

mounted in a liquid filled wheel or on a sled, as a coupling medium is needed to transmitted and receive the ultrasonic signals. An example of the ultrasonic wheel system is shown in Figure 3-16.

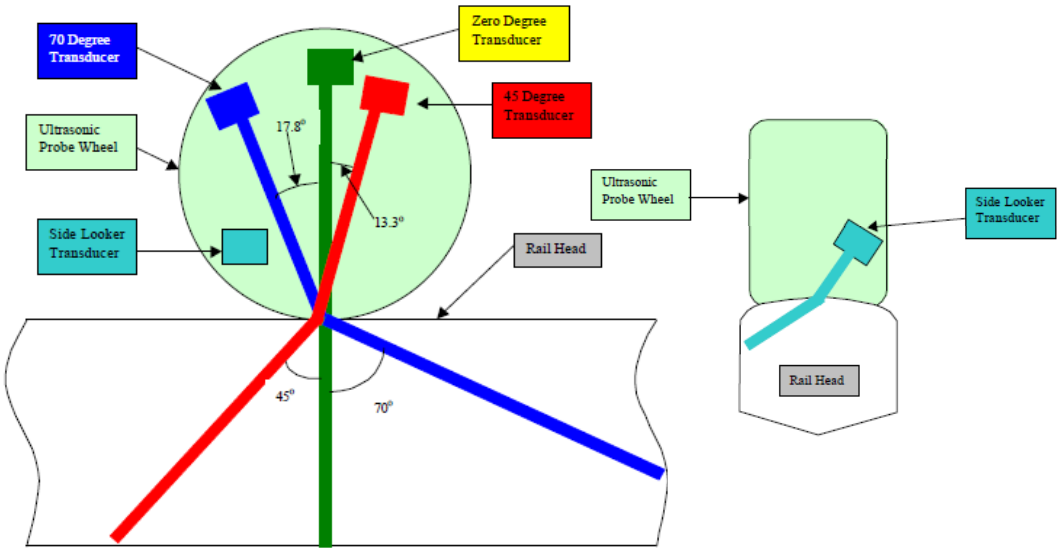

Figure 3-17: Common Transducer Configuration in Inspection Wheel

In order to cover the rail cross section, multiple transducers are installed within the liquid filled wheel. The number of transducers mounted in the wheel can be a few as two, and as many as twelve. In order to target specific areas of the rail cross section, the transducers are mounted at fixed angles determined by Snell's law. The most common configuration, see Figure 3-17, holds six transducers. The transducers have orientations to generate ultrasonic beams propagating at normal incidence 0^o, 45^o and 70 from the normal to the rail surface. The 0^o transducer is mounted at 0^o exciting a bulk wave targeting defects in the web and horizontal defects in the head. Mounted at 13.3^o , a

bulk wave that propagates at 45^o to the normal targeting bolt hole defects, defective welds, and add additional coverage to the web. Normally, three transducers are mounted at 17.8^o producing a bulk wave that propagating at 70^o to the normal directing to wave to reflect of the internal transverse defects that grow at an angle of 20^o to the normal. Additionally, a side looking transducer is mounted at 17.8^o to generate beams transverse to the plane of the track to identify vertical discontinuities and the gauge corner. The presence of a defect is determined be the amplitude of the reflections and arrival times [27]. While the inspection area of the ultrasonic waves of covering the whole railhead, there are several drawbacks to the method such as [28]: is capable

- Inspection vehicles have limited inspection speeds [27]. Reported operating speed are between 25 and 45 mph however, these reported speeds are the theoretical maximum speeds achievable by the inspection vehicle. In the United States the Federal Railroad Administration mandates a stop and verify policy, thus upon identification of a defect location the inspection vehicle and the rail is hand inspected to verify the existence and size of the defect. Stop and verify policies reduce average operating speeds to less than 10 mph. Even at the theoretical max speeds, the inspection service is disruptive to normal operating timetables.
- Shallow surface cracks such as head checking, flaking and shelling shadow the inspection area [3]. Deeper defects go undetected as the shallow surface defects shadow the defect by reflecting the beam energy of the ultrasonic waves.
- Reportedly the current systems find 65% to 80% of the actual defects. Having a missed rate of 20% to 35% is not optimum. In addition the masking due to rail

surface defects, ultrasonic wheels are susceptible to surface conditions. Materials and debris on the rail surface have adverse effects to ultrasonic signals. Grease, icing and even leaves can mask the ultrasonic signals.

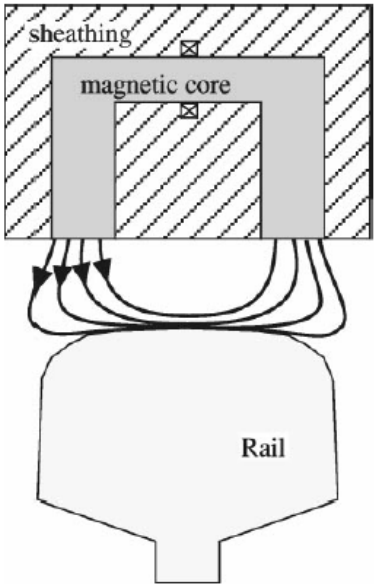

Figure 3-18: Eddy-Current Sensor Magnetic Field Pattern

In order to address the speed limitations of the current contact methods, noncontact inspection techniques are beginning investigated. One such method is an induction method based on eddy-currents [29]. In Figure 3-18, the orientation of the magnetic field from the eddy-current sensor is shown. The method works by inducing a magnetic field transverse to the travelling direct of the rail and measures variations in the active and reactive components of the magnetic field. While the greatest benefit of the system is that it can operate at regular operating trains speed, the defects that it is affective at detects are limited to the surface and very shallow internal defects. Perhaps the largest limitation of the eddy current method is the limited lift off distance. In order to achieve

consistent measurements, the lift off distance cannot be greater than 2-4 mm and, if this distance is achieved, the depth of the field penetration is limited to 4-6 mm.

Table 3.1: Advantages and Disadvantages of Current Rail Inspection Methods

Inspection Technique	Advantages	Disadvantages
Contact induction	Reliable for detect of surface defects	Limited test speeds. Contact required. Unreliable in internal defect detection. Sensitivity to electromagnetic noise. Sensitivity to joints, joint bars, and bolt holes
Traditional Ultrasonic Wheel	Well established Reliable for many internal and surface defects	Transverse defects under shelling are masked by shell Limited test speed. Contact required.
Eddy Current	Reliable for detect of surface defects. Noncontact deployment. High speed testing	Unreliable in internal defect detection. Limited sensor lift-off. Sensitivity to electromagnetic noise. Sensitivity to joints, joint bars, and bolt holes
Ultrasonic guided wave	Potentially reliable for surface and internal defects. Potentially reliable for the detection of defects under shelling. High speed testing. Noncontact deployment	Reliability needs testing in full field deployment. Equipment costs are prohibitive.

Over the last decade, the most promising noncontact technique to develop is ultrasonic guided wave. In particular, laser induced ultrasonic waves to which the advancements are covered extensively in the dissertation. Several studies have

advanced this technology and shown it to be a very effective method for the location of internal transverse defect, including those under shelling and other surface conditions [6, 30-34]. In the application of the method, a laser induces an ultrasonic guided wave by the ablation of the rail surface. The corresponding propagated signal in received by air-coupled piezoelectric transducers. More detail of the method and its performance is covered in section 6 of this dissertation. Table 3.1 summarizes the advantages and disadvantages of the current methods of rail inspection for internal transverse defects.

3.2 Rail Neutral Temperature and Buckling

Measurements of the rail neutral temperature are a difficult undertaking in a nondestructive manner. Current methods require cutting of the rail or are invasive by the requirement of unfastening the rail in order to make measurements. The greatest challenge is that the neutral temperature is not a constant over time. There are several factors that cause the neutral temperature to change over time. making a record of the installation unreliable.

Changes to the ballast conditions such as consolidations will shift the neutral temperature. Even the derogation of the ties affects the neutral temperature as the environment through wind, rain, and sun break down the tie and reducing the lateral resistance of the tie. Also with the dynamic of train traffic, the rail is stressed and it may slip from the fasteners. Another factor is track alignment, as over time the ties slip laterally and the rail is no longer held straight and true to the original installation.

3.2.1 Current Method for Rail Neutral Temperature

Current methods for the measure of the rail neutral temperature cover a wide range of physical phenomenon that are affect by changes in stress. Many techniques have been investigates in the last several decades .Two common treads with the current state of the art systems are either some form of destructive action or small windows for accurate measurements.

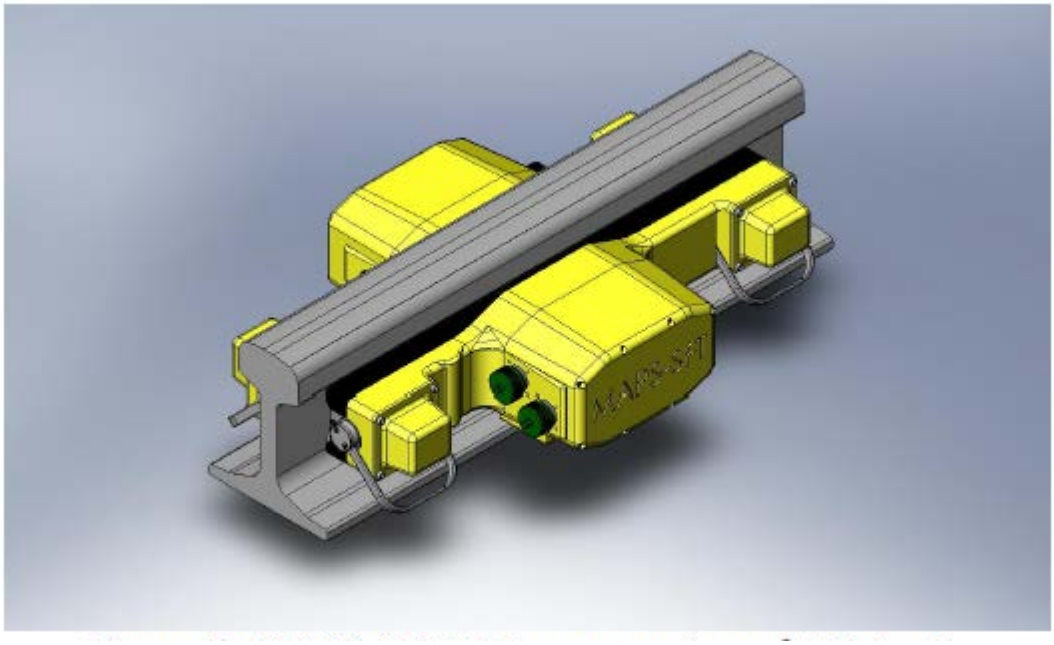

Figure 3-19: MAPS-SFT HUs on Section of 113A rail

The MAPS-SFT™ stress measurement system is manufactured by MAPS Technology Ltd. In the United Kingdom. The MAPS-SFT™ system is based on knowledge of Barkhausen Emission, Magnetoacoustic Emission, and Directional Effective Permeability applied to a multi-parameter magnetic system [35]. The original

system was developed for biaxial stress measurement in industrial plant components. Based on a design to measure residual stress, the system has limited measurement accuracy of 10-20 MPa. Consider that for every 1^{o}C, a straight piece of rail will produce 2-4 MPa of stress. With this limitation, accurate measurements have to be taken very close to the rail neutral temperature. As a wayside device, as shown in Figure 3-19, it is nonintrusive.

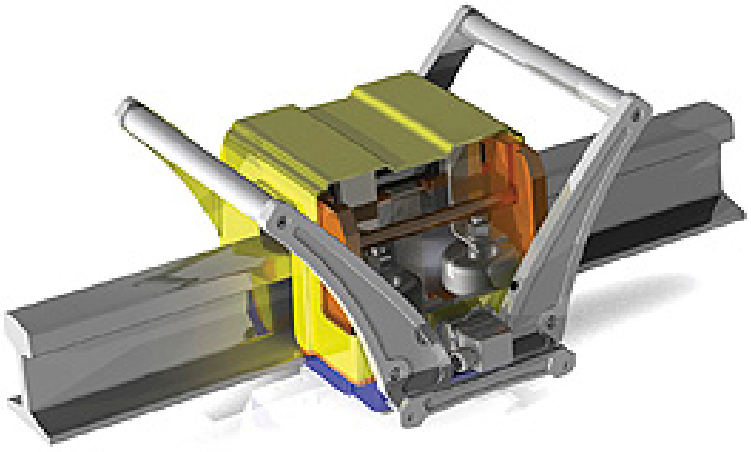

Figure 3-20: Rail Stress Test B.V.

Grontmij out of Europe operates the Rail Stress Test B.V., Figure 3-20, system that is based on the magneto-elastic effect a phenomenon identified by Villari in 1865 [36-38]. The Villari effect is the measure of difference in the magnetic field caused by the stress in the rail. A 360^{o} magnetic field is imposed on the contour of the rail and the intensity of the field to achieve a known magneto-elastic state measures the stress state of the rail. However, the metallurgic composition of the rail has a large effect on the measurements. In order to overcome the metallurgic variations of the rail section, a calibration must be taken at the measurement point and measurements must taken at the

same point in order to be accurate. The system is currently operated in the field and the accuracy and reliability continue to improve.

Both MAP-SFT and Rail Stress Test B.V. are not intrusive techniques. Conversely, the VERSE device is far more intrusive [39], see Figure 3-21. While the device does not require any destructive action, it does require unfastening of ~ 100 feet of rail. The unfastened length is lifted to determine the force required to displace it by a set amount. Once the force for the required displacement is known, the stress free temperature (neutral temperature) is back calculated. The VERSE measurement must be taken with the rail in a tensile state, and its accuracy is compromised in a track with a radius

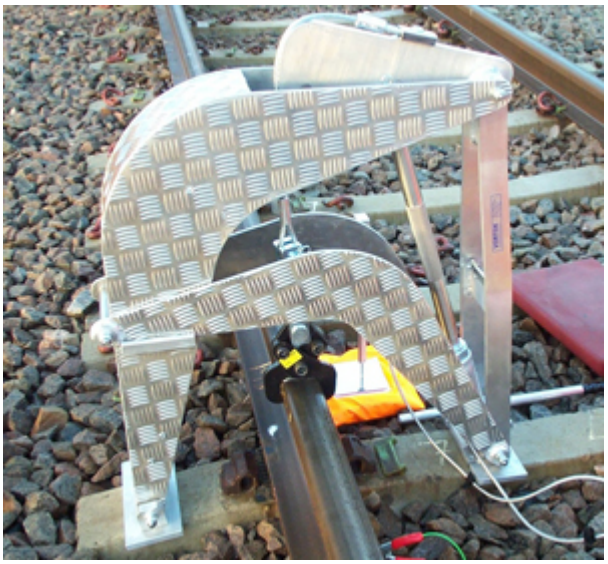

Figure 3-21: VERSE Device

Another nondestructive method for rail stress measurement in the D'Stresen method. In Figure 3-22, the D'Stresen system is shown from a field test conducted at the Transportation Technology Center in Pueblo Colorado[9, 40]. The system is configured with a rigid frame that holds a shaker and four accelerometers to measure

the accelerations of the rail. The acceleration amplitudes are measuring the dynamic resonance of a 90 Hz torsional mode of vibration in the rail. While there is no need to unfasten the rail, the accuracy of the system is susceptible to tie to tie variations of the fasteners. The system also has the advantage that the measurement can be taken in both tension and compressive stress states, however the knowledge that it is in either tension or compression has to be known prior to the measurement. Do to the limitations of the system the method can only be an “estimator” of the rail neutral temperature.

Figure 3-22: D’Stresen Measurement System

While not extremely common, another technique consists of the installation of an inclusion at the rail neutral axis, and the measurement of the dilation of the inclusion over time to determine the stress state of the rail [41, 42]. Figure 3-23 shows the instrumented 8 mm inclusion after beginning installed when the rail was in a stress-free state. The fact that the inclusion must be inserted while the rail is stress free means that

the installation takes place when the rail is installed or the rail must be cut and then welded back in. Despite the destructive drawback, the system is trusted to be accurate.

Figure 3-23: Stress Measurement by Inclusion Dilation Device

Surely the most trusted method for rail stress measurement is the application of strain gauges on the neutral axis. The method has been used and proven for several decades [43, 44]. Widely used throughout the world, a configuration of four strain gauges in a full Wheatstone bridge is used to measure the stress in the rail. The typical installation is shown in Figure 3-24. In order to be accurate the strain gauges must be installed when the rail is stress free. Thus the application of the gauges is during rail installation or the rail is cut allowed to relax and the weld back together. Over time, the

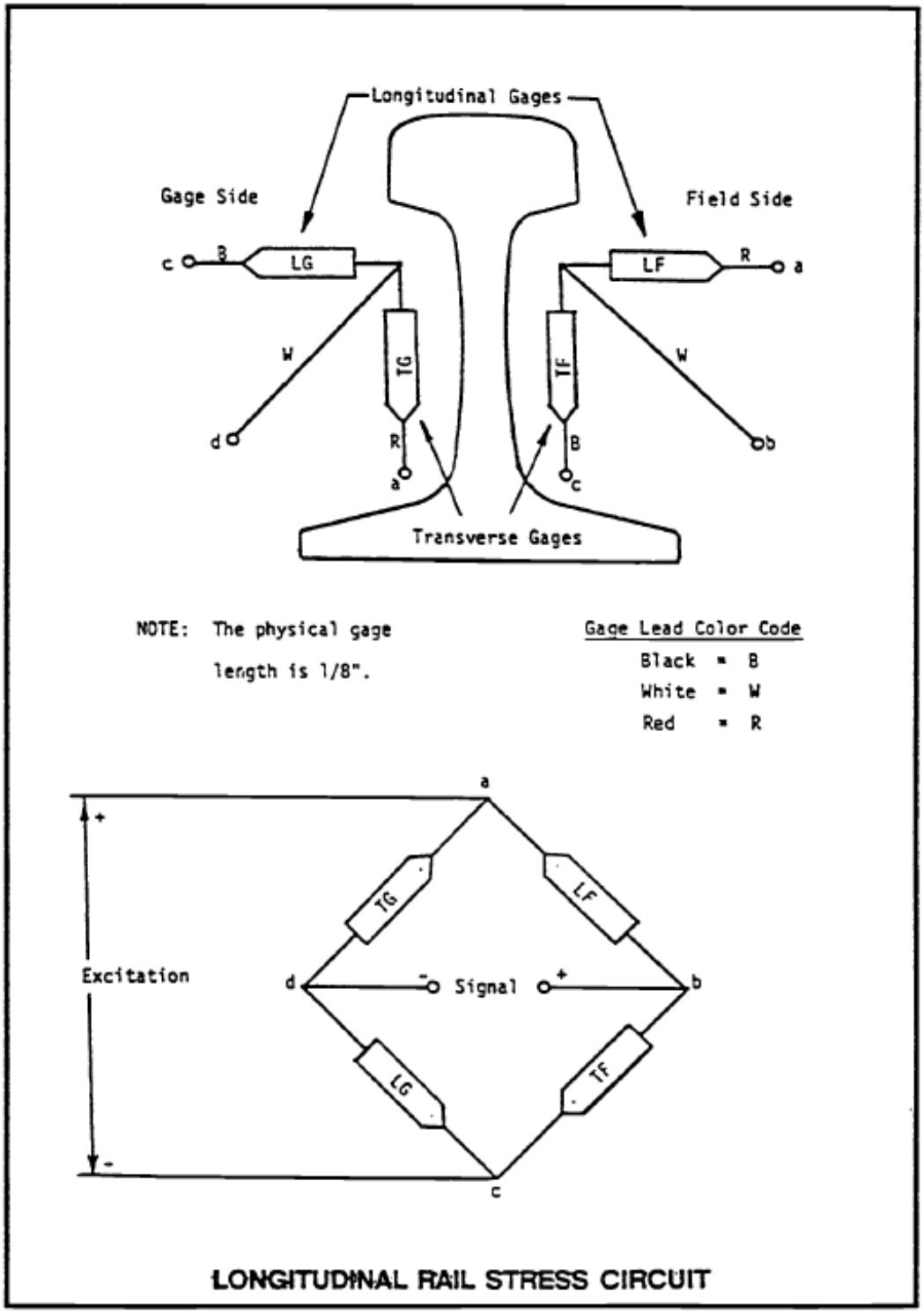

Figure 3-24: Longitudinal Rail Stress Circuit

measuring method has be streamlined to the point that hard wires and contiuous montiroing stations are no longer needed. The Salient Systems solution uses a battery operated device that contains a themocouple a wireless device to upload the data [45]. The device as installed is shown in Figure 3-25.

Figure 3-25: Salient Systems Wireless Strain Measurement Devices

4. Modeling of Guided Wave Propagation in Loaded Solids

4.1 Introduction to Guided Waves

When one visualizes a wave propagating in water, the wave moves away from its source until all the energy is lost in the medium. A similar phenomenon in an earthquake as the ground motion moves away from its source and dissipates in the unbounded medium. Guided waves have a much different behavior because the wave is propagating in a medium with boundaries and undergoes multiple. While the analog of a wave propagating in water is used, the interaction with boundaries causes dispersion (wave velocity depends on frequency) and multimode behavior (multiple vibrating modes can exists simultaneously

Figure 4-1: Energy in Waveguide [46]

A plate in which two of the dimensions are much larger than the three is considered a waveguide, as the smallest dimension holds the wave energy within a defined space as seen in Figure 4-1. Other types of waveguides include bars, rods, pipes, and rails, where one dimension dominates the other.

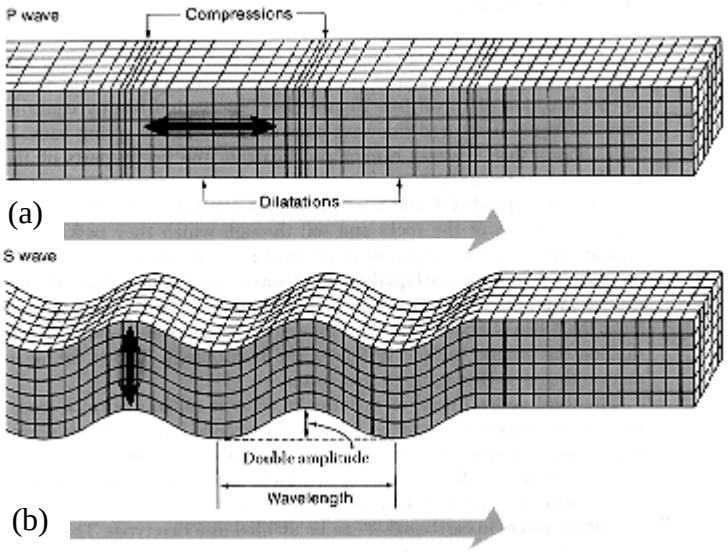

Figure 4-2: P Wave and S Wave Propagation

The generation of guided wave starts is the propagation of two fundamental waves. The first fundamental waves are the result of a compressive longitudinal bulk wave known as a P-wave see Figure 4-2a. The second fundamental wave is the shear bulk wave as seen in Figure 4-2b. By the combination of constructive and destructive interference of the wave at the waveguide boundaries, the guided wave is formed. Illustrated in Figure 4-3 is the formation of the guided wave. Once the wave excitation energy has propagated a short distance beyond the near field of the excitation transducer, a wave packet is formed and it contains multiple modes of propagation.

The three main advantages of ultrasonic guided waves for non-destructive evaluation and structural health monitoring are: 1) in comparison to global vibrations, ultrasonic guided waves have an increased sensitivity to small defects due to the smaller frequencies, 2) the energy of the ultrasonic guided waves has complete coverage of the

waveguide cross-section, and 3) in waveguide type elements the ultrasonic wave travels long distances for a long range inspection.

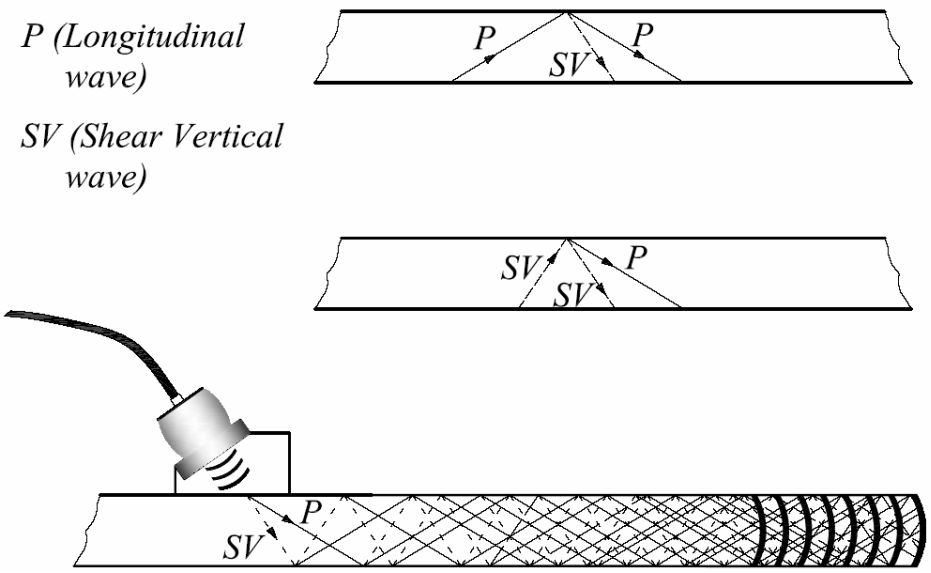

Figure 4-3: Guided Plate Wave in an Isotropic Homogeneous Plate

However, in order to properly use ultrasonic guided waves, the complexities of the wave propagation, in terms of dispersion and multimode behavior, need to be understood.

An accurate knowledge of the dispersive properties of the guided wave propagation phenomena is critical to avoid errors in the interpretation of wave measurements. For mode identification, a knowledgeable determination of phase and group/energy velocities is necessary. Furthermore, in order to maximize inspection ranges, knowledge of the mode attenuation is needed to exploit the guided wave propagation. Lastly, in

order achieve the highest sensitivity of the guided wave application, an accurate prediction of the mode shapes is indispensable.

At the end of the 19th century the foundation to the study of guided wave in cylindrical and flat waveguides was laid. The solution of the mechanical wave equation for cylindrical symmetry were developed by Pochhammer in 1876 and followed by Chree in 1889 [47, 48]. Nevertheless, detailed calculations of the roots did not appear until the 20th century due to the complexity of the solution. During the same time period, the propagation phenomena for hollow single layer elastic cylinders in a vacuum were explored by Gazis in 1959 [49]. This subject is covered by several papers from the middle of 20th century on. Experimental, numerical and theoretical studies of cylindrical elastic waveguides were conducted. As an example, Zemanek was one of the first to present a complete analytical and experimental study [50].

In 1887 Rayleigh, followed by Lamb in 1917, laied the basis for the comprehension of guided waves in flat layered waveguides [51, 52]. The equation for waves travelling on the free surface of semi-infinite half spaces were derived by Lord Rayleigh. The derivation resulted in a third order expression with roots that determine the velocity of the propagating surface wave like that shown in Figure 4-4. In 1924 Stoneley produced a generalization the Rayleigh waves for a single interface [53]. Stoneley studied the interface of waves propagating without leakage that exist at the boundary between two solid half spaces. Extending the study of Stoneley, Scholte explored the range of free wave solutions in which the wave propagates indefinitely without loss [54]. The leaky

wave solutions, that represent waves that attenuate as they travel, was studied by Pilant in an extension of Stoneley's work [55].

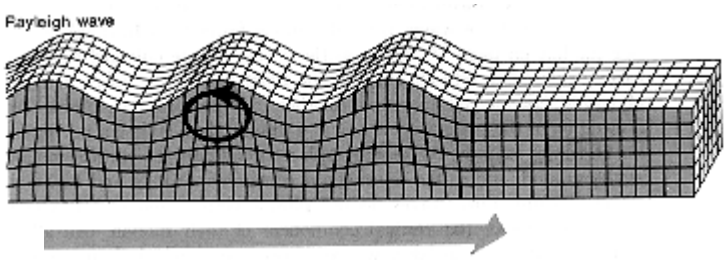

Figure 4-4: Rayleigh Surface Wave

The notion of a flat layer of finite thickness was introduced by Love and Lamb by adding another interface to the problem explored by Rayleigh [51, 56]. The Rayleigh-Lamb equations derived by Lamb consist of two distinct expresses representing the roots of symmetric and antisymmetric plate modes that are shown in section 4.5. Plotting the roots in the frequency domain results in the well know Lamb wave dispersion curves.

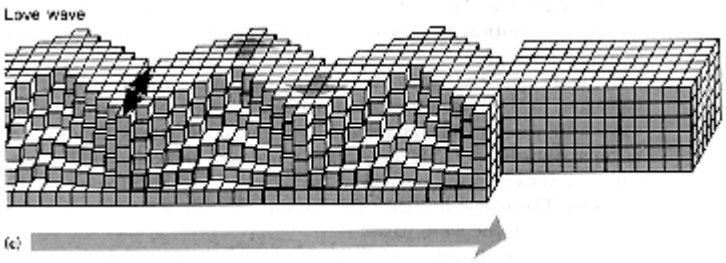

Figure 4-5: Love Wave

4.2 Waves in Unbounded Medium

The possibility of transverse modes in a half-space covered by a layer of finite thickness and different elastic properties was shown to occur by Love [56]. The modes

involved shearing motion in the plane of the layer as shown in Figure 4-5.Details of the calculation and theory of guided waves in isotropic mediums can be found in several classic textbooks such as those by Auld, Achenbach, Graff and Rose [57-60]

An understanding of wave propagation in an unbounded medium is important in the comprehension of wave propagating in bounded medium such as a plate. Consider a medium with density ρ with displacements u_x, u_y, and u_z along the *x*, *y*, and *z* in the Cartesian coordinate system. Neglecting body forces Newton's second law leads to the equations of motion for a three-dimensional body is shown in eq. 4.1[57].

$$\begin{aligned}
\frac{\partial \sigma_x}{\partial x} + \frac{\partial \tau_{xy}}{\partial y} + \frac{\partial \tau_{xz}}{\partial z} &= \rho \frac{\partial^2 u_x}{\partial t^2} \\
\frac{\partial \sigma_y}{\partial y} + \frac{\partial \tau_{xy}}{\partial x} + \frac{\partial \tau_{yz}}{\partial z} &= \rho \frac{\partial^2 u_y}{\partial t^2} \\
\frac{\partial \sigma_z}{\partial z} + \frac{\partial \tau_{yz}}{\partial y} + \frac{\partial \tau_{xz}}{\partial x} &= \rho \frac{\partial^2 u_z}{\partial t^2}
\end{aligned} \qquad \textbf{(4.1)}$$

Irrespective of the stress-strain behavior of the medium, these equation will hold. The stress and strain in the elastic material are related by Hooke's law expressed in its general form in equation 4.2:

$$\begin{Bmatrix} \sigma_{xx} \\ \sigma_{yy} \\ \sigma_{zz} \\ \sigma_{yz} \\ \sigma_{zx} \\ \sigma_{xy} \end{Bmatrix} = \begin{bmatrix} C_{11} & C_{12} & C_{13} & C_{14} & C_{15} & C_{16} \\ C_{12} & C_{22} & C_{23} & C_{24} & C_{25} & C_{26} \\ C_{13} & C_{23} & C_{33} & C_{34} & C_{35} & C_{36} \\ C_{14} & C_{24} & C_{34} & C_{44} & C_{45} & C_{46} \\ C_{15} & C_{25} & C_{35} & C_{45} & C_{55} & C_{56} \\ C_{13} & C_{26} & C_{36} & C_{46} & C_{56} & C_{66} \end{bmatrix} \begin{Bmatrix} \varepsilon_{xx} \\ \varepsilon_{yy} \\ \varepsilon_{zz} \\ \varepsilon_{yz} \\ \varepsilon_{zx} \\ \varepsilon_{xy} \end{Bmatrix} \qquad \textbf{(4.2)}$$

with C_{ij} containing the elastic constants of the material. In anisotropic materials, 21 independent constants occur. The total number of elastic constants is reduced to two for

isotropic materials denoted by the Lamé constants λ and μ.The Lamé constants are defined by the Young's modulus, *E*, Poisson' ratio, ν, of the material. In tensor form the stress-strain relationship is represented in the form:

$$\boldsymbol{\sigma_{ij}} = \boldsymbol{\lambda \delta_{ij} \varepsilon_{kk}} + 2\boldsymbol{\mu \varepsilon_{ij}} \qquad \textbf{(4.3)}$$

such that $\varepsilon_{kk} = \varepsilon_{xx} + \varepsilon_{yy} + \varepsilon_{zz}$ is the dilatation and δ_{ij} is the Kronecker delta. Navier's equation of motion for an isotropic elastic medium is achieved when the stress-strain relation is substituted into equation 4.1:

$$\left(\boldsymbol{\lambda} + \boldsymbol{\mu}\right)\vec{\nabla}\left(\vec{\nabla} \bullet \vec{\boldsymbol{u}}\right) + \boldsymbol{\mu}\nabla^2\vec{\boldsymbol{u}} = \boldsymbol{\rho}\frac{\partial^2 \vec{\boldsymbol{u}}}{\partial \boldsymbol{t}^2} \qquad \textbf{(4.4)}$$

Here $\vec{u}$ is the displacement vector, $\vec{\nabla}$ is the divergence vector, and $\nabla^2 = \frac{\partial^2}{\partial x^2} + \frac{\partial^2}{\partial y^2} + \frac{\partial^2}{\partial z^2}$ is Laplance differential operator. The displacement vector , $\vec{u}$, can be decomposed into dilatation and rotation by the scalar and vector potentials ϕ and $\vec{\psi}$ by Clebsch's theorem, such that:

$$\vec{\boldsymbol{u}} = \vec{\nabla}\phi + \vec{\nabla} \times \vec{\boldsymbol{\psi}} \qquad \text{with} \qquad \vec{\nabla} \cdot \vec{\boldsymbol{\psi}} = 0 \qquad \textbf{(4.5)}$$

The result of substituting the displacement vector into Navier's equation yields the following:

$$\vec{\nabla}\left[\left(\boldsymbol{\lambda} + 2\boldsymbol{\mu}\right)\nabla^2\phi - \boldsymbol{\rho}\frac{\partial^2 \phi}{\partial \boldsymbol{t}^2}\right] + \vec{\nabla} \times \left[\boldsymbol{\mu}\nabla^2\vec{\boldsymbol{\psi}} - \boldsymbol{\rho}\frac{\partial^2 \vec{\boldsymbol{\psi}}}{\partial \boldsymbol{t}^2}\right] = 0 \qquad \textbf{(4.6)}$$

Equation 4.6 is satisfied if both the scalar and vector potential vanish, which results in two decoupled wave equations:

$$c_1^2 \nabla^2 \phi = \frac{\partial^2 \phi}{\partial t^2} \qquad \textbf{and} \qquad c_2^2 \nabla^2 \psi = \frac{\partial^2 \psi}{\partial t^2} \tag{4.7}$$

where:

$$c_1 = \sqrt{\frac{\lambda + 2\mu}{\rho}} \qquad \textbf{and} \qquad c_2 = \sqrt{\frac{\mu}{\rho}} \tag{4.8}$$

The result show that two types of bulk waves exist: the dilatation (longitudinal) wave with a constant velocity c_1 , and the rotational (shear) wave with a constant velocity c_2.

4.3 Bounded Medium

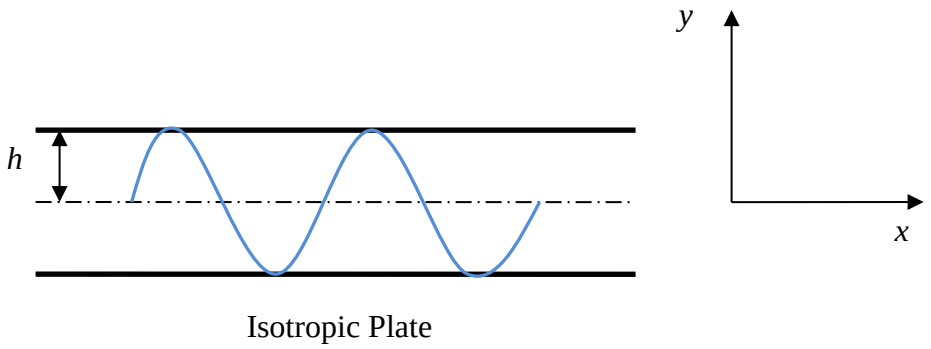

Figure 4-6: Guided wave in a thin isotropic plate

Consider an isotropic plate of thickness *2h* to investigate the wave propagation in a bounded geometry. The wave propagation direction is along the *x* axis corresponding to the displacement u_x and displacement u_y that corresponds to the through thickness direction along the *y* axis as shown in Figure 4-6. The mid-plane of the plate defines the coordinate y=0. Plain stain conditions are assumed thus the displacement and strains in the *z* plane are $u_z = 0$ and $\frac{\partial u_z}{\partial z} = 0$. From eq. 4.5 the displacements are expressed as [58]:

$$\boldsymbol{u_x = \frac{\partial \phi}{\partial x} + \frac{\partial \psi}{\partial y}}$$
$$\boldsymbol{u_u = \frac{\partial \phi}{\partial y} + \frac{\partial \psi}{\partial x}} \qquad \textbf{(4.9)}$$

The subscript *z* is omitted from ψ for simplicity in eq. (4.9). Two partial differential wave equations are obtained for plain strain that are two-dimensional after the expressions for u_x and u_y *are* substituted into Navier's equation:

$$\boldsymbol{\frac{\partial^2 \phi}{\partial x^2} + \frac{\partial^2 \phi}{\partial y^2} = \frac{1}{c_L^2}\frac{\partial^2 \phi}{\partial t^2}}$$
$$\boldsymbol{\frac{\partial^2 \psi}{\partial x^2} + \frac{\partial^2 \psi}{\partial y^2} = \frac{1}{c_T^2}\frac{\partial^2 \psi}{\partial t^2}} \qquad \textbf{(4.10)}$$

Expressions for the general solution for ϕ and ψ are:

$$\boldsymbol{\phi = \Phi(y) e^{i(\xi x - \omega t)}}$$
$$\boldsymbol{\psi = \Psi(y) e^{i(\xi x - \omega t)}} \qquad \textbf{(4.11)}$$

Such that Φ(*y*) and Ψ(*y*) are the expressions that characterize the standing wave in the y direction and the term $e^{i(\xi x - \omega t)}$ represents the propagating wave in the *x* direction. The terms ξ and ω are the wavenumber and angular frequency, also known as the spatial distribution and temporal frequency of the wave respectively. The two partial differential equations in (4.10) are reduced into two ordinary differential equations by substituting in equation (4.11). In the solution *p* and *q* are imaginary and the two complex expressions Φ(*y*) and Ψ(*y*) are simplified to:

$$\boldsymbol{\Phi(y) = A_1 \sin(py) + A_2 \cos(py)}$$
$$\boldsymbol{\Psi(y) = B_1 \sin(qy) + B_2 \cos(qy)} \qquad \textbf{(4.12)}$$

where $A_1, A_2, B_1, \text{and } B_2$ are the wave amplitudes and the terms *p* and *q* are represented as:

$$p = \sqrt{\frac{\omega^2}{c_L^2} - \xi^2}$$
$$q = \sqrt{\frac{\omega^2}{c_T^2} - \xi^2} \qquad \textbf{(4.13)}$$

From the wave equations solutions in eq. (4.11), the displacements and stresses can be expresses from eq. (4.3) and (4.9) respectively as:

$$u_x = \left[ik\Phi + \frac{d\Psi}{dy} \right] e^{i(\xi x - \omega t)}$$
$$u_x = \left[\frac{d\Phi}{dy} + ik\Psi \right] e^{i(\xi x - \omega t)}$$
$$\sigma_{xy} = \left[\mu \left(2i\xi \frac{d\Phi}{dy} + \xi^2 \Psi + \frac{d^2\Psi}{dy^2} \right) \right] e^{i(\xi x - \omega t)} \qquad \textbf{(4.14)}$$
$$\sigma_{yy} = \left[\lambda \left(-\xi^2 \Phi + \frac{d^2\Phi}{dy^2} \right) + 2\mu \left(\frac{d^2\Phi}{dy^2} - i\xi \frac{d\Psi}{dy} \right) \right] e^{i(\xi x - \omega t)}$$

such that $\Phi(y)$ and $\Psi(y)$ are defined in eq. (4.12). It can be seen in eq. (4.14) that the displacement components can be written in terms of elementary functions. Displacement in the x direction are symmetric (antisymmetric) with respect to the mid-plane if u_x contains cosines (sines). Also displacement in the y are symmetric (antisymmetric) if u_y contains cosines (sines). Wave propagation modes are thus split into symmetric and antisymmetric solutions [58]. Thus for symmetric and antisymmetric modes are:

$$\Phi(h) = A_2 \cos(py)$$
$$\Psi(h) = B_1 \sin(qy) \qquad \textbf{Symmetric} \qquad \textbf{(4.15)}$$

$$\Phi(h) = A_1 \sin(py)$$
$$\Psi(h) = B_2 \cos(qy) \qquad \textbf{Antisymmetric} \qquad \textbf{(4.16)}$$

Expressions for the frequency ω and the wave number ξ are obtained by applying the boundary conditions. If the boundary is free then at $y = \pm h$, the stresses $\sigma_{xy} = \sigma_{yy} = 0$ are imposed. Application of these boundary conditions yields a system of two homogeneous equations for the constants A_2 and B_1 for the symmetric modes. For antisymmetric modes, two homogeneous equations for the constants A_1 and B_2 are obtained. For the homogeneous systems the simplified expressions for ω and ξ are obtained by taking the determinate of each system. The resulting simplified expressions are in the following form:

$$\frac{\tan(qh)}{\tan(ph)} = -\frac{4\xi^2 pq}{\left(q^2 - \xi^2\right)^2} \qquad \textbf{Symmetric} \qquad \textbf{(4.17)}$$

$$\frac{\tan(qh)}{\tan(ph)} = -\frac{\left(q^2 - \xi^2\right)^2}{4\xi^2 pq} \qquad \textbf{Antisymmetric} \qquad \textbf{(4.18)}$$

These expressions are those commonly determined for the Rayleigh-Lamb frequency equations.

From eqs. (4.14) and (4.15), there is an infinite number of eigensolutions, and thus an infinite number of guided waves. A particular angular frequency and mode of propagation corresponding to the symmetric and antisymmetric are present for each eigenvalue. For low frequencies, only two fundamental modes exist, the symmetric S_0 mode and the antisymmetric A_0 mode. A corresponding set of eigencoefficients, A_2 and B_1 for the symmetric modes and A_1 and B_2 for the antisymmetric modes,can be found. Applying these coefficients to eq. (4.14) allows for the evaluation of the Lamb mode shapes across the plate thickness. Velocities of the Lamb waves are a function of

frequency (dispersion), such that the phase velocity c_P is given as $c_P = \frac{\omega}{\xi}$ for each particular mode. The velocity at which the wave packet, or envelope, propagates is known as the group velocity and is evaluated as $c_g = \frac{d\omega}{d\xi}$. In order to represent the dispersive solution to the guided wave for a particular system, phase velocity vs. frequency and group velocity vs. frequency plots are commonly called dispersion curves.

4.4 Semi Analytical Element Method for Prestressed Arbitrary Cross Section

In order to solve the equations of motion for a prestressed waveguide in the Lagrarangian framework an incremental approach is employed. The configuration of an arbitrary cross section is shown in Figure 4-7 where C^0 is the stress-free alignment, C is the prestressed alignment, and C' is the current configuration in which the wave motion has deformed the waveguide. Assuming equilibrium of the externally applied surface $\mathbf{t}^0$ and body forces $\mathbf{f}^0$, the general particle at $\mathbf{x}$ is subjected to a stress field donoted by the Cauchy stress tensor $\mathbf{T}^0$ in the prestressed state. In this section, the derivation follows the work of Mazzotti *et al* [61].

Using the Updated Lagrangian formulation, the C alignment is a reference and is determined from C^0 considering the initial static displacement $\mathbf{u}_0$. The current position of the particle $\mathbf{x}'(\mathbf{u})=\mathbf{x}+\mathbf{u}$ at time t is the superimposition of a small incremental time-dependent displacement field $\mathbf{u}=[u_x, u_y, u_z]^T$ resulting from the wave displacement on the prestressed state $\mathbf{x}$.

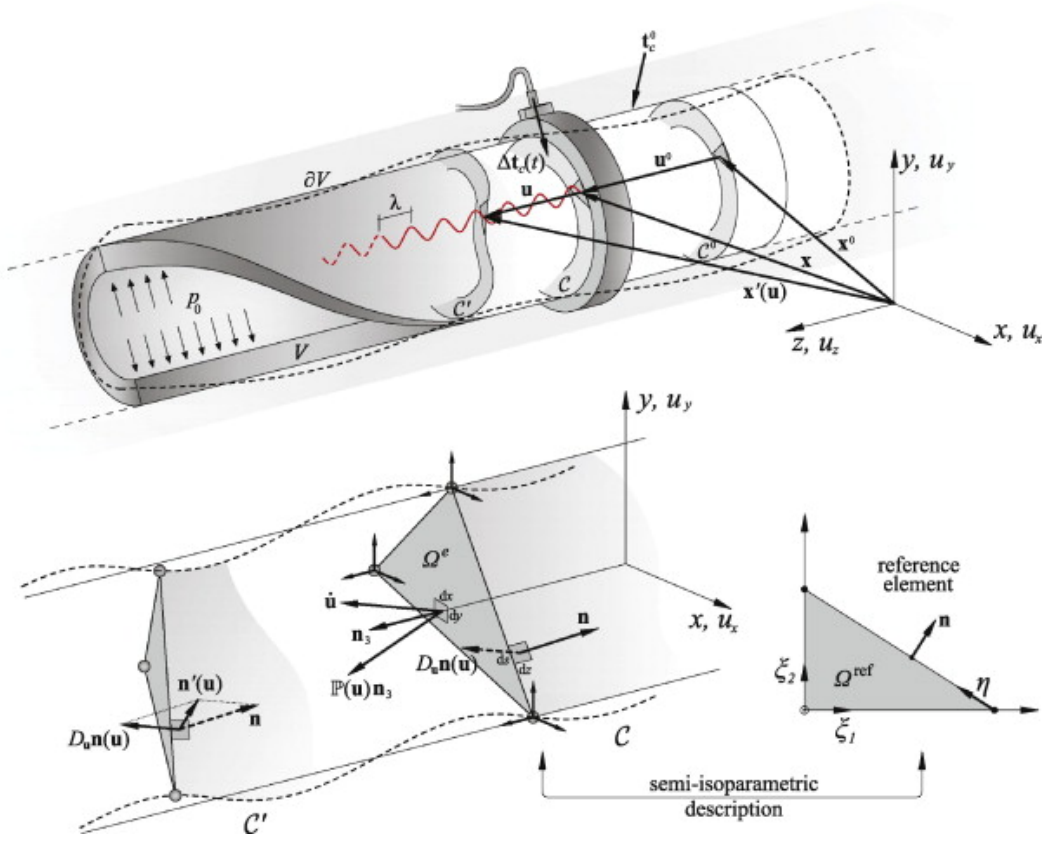

Figure 4-7: Fundamental configurations for the wave propagation problem in prestressed waveguides.[61]

The symmetric components of the Green-Lagrange strain tensor $\mathbf{E}(\mathbf{u}) = \frac{1}{2}\left[\nabla\mathbf{u} + (\nabla\mathbf{u})^{\mathrm{T}} + (\nabla\mathbf{u})^{\mathrm{T}}\nabla\mathbf{u}\right]$ collected into a 6x1 vector $\varepsilon(\mathbf{u}) = \varepsilon_{\mathrm{L}}(\mathbf{u}) + \varepsilon_{\mathrm{NL}}(\mathbf{u})$ make for the appropriate representation of the strain measure. The strain vector contains a linear $\varepsilon_{\mathrm{L}}(\mathbf{u})$ and a nonlinear component $\varepsilon_{\mathrm{NL}}(\mathbf{u})$ defined as:

$$\varepsilon(\mathbf{u}) = \left[L_x\frac{\partial}{\partial x} + L_y\frac{\partial}{\partial y} + L_z\frac{\partial}{\partial z}\right]\mathbf{u} \qquad \textbf{4.19}$$

and

$$\varepsilon_{NL}(\mathbf{u}) = \frac{1}{2}\left[\frac{\partial\mathbf{u}^T}{\partial x}\frac{\partial\mathbf{u}}{\partial x}, \frac{\partial\mathbf{u}^T}{\partial y}\frac{\partial\mathbf{u}}{\partial y}, \frac{\partial\mathbf{u}^T}{\partial z}\frac{\partial\mathbf{u}}{\partial z}, 2\frac{\partial\mathbf{u}^T}{\partial y}\frac{\partial\mathbf{u}}{\partial z}, 2\frac{\partial\mathbf{u}^T}{\partial x}\frac{\partial\mathbf{u}}{\partial z}, 2\frac{\partial\mathbf{u}^T}{\partial x}\frac{\partial\mathbf{u}}{\partial y}\right]^{\mathrm{T}} \qquad \textbf{4.20}$$

In equation 4.19 the L_i operator is defines as:

$$L_x = \begin{bmatrix} 1 & 0 & 0 \\ 0 & 0 & 0 \\ 0 & 0 & 0 \\ 0 & 0 & 0 \\ 0 & 0 & 1 \\ 0 & 1 & 0 \end{bmatrix} \quad L_y = \begin{bmatrix} 0 & 0 & 0 \\ 0 & 1 & 0 \\ 0 & 0 & 0 \\ 0 & 0 & 1 \\ 0 & 0 & 0 \\ 1 & 0 & 0 \end{bmatrix} \quad L_z = \begin{bmatrix} 0 & 0 & 0 \\ 0 & 0 & 0 \\ 0 & 0 & 1 \\ 0 & 1 & 0 \\ 1 & 0 & 0 \\ 0 & 0 & 0 \end{bmatrix} \qquad \textbf{4.21}$$

The difference in motion between C' and C is assumed to be incremental and the linear strain-displacement relationship is obtained for the small increments of $\mathbf{u}(\mathbf{x},t)$ by a first order Taylor series expansion $f(\mathbf{x}+\varepsilon\mathbf{u}) - f(\mathbf{x}) = D_u f(\mathbf{x})$ in the near field of the prestressed configuration. $D_{\mathrm{u}} f(\mathbf{x}) = \left.\frac{d}{dt}\right|_{\varepsilon=0} f(\mathbf{x}+\varepsilon\mathbf{u})$ is the directional derivative at $\mathbf{x}$ in the direction of the incremental displacement $\mathbf{u}$. The linearization of the Green-Lagrange strain tension and the virtual Green-Lagrange strain tensor take the form $D_{\mathbf{u}}\varepsilon(\mathbf{u}) = \varepsilon_{\mathrm{L}}(\mathbf{u})$ for the linear component and $D_{\mathbf{u}}\delta\varepsilon(\mathbf{u}) = \delta\varepsilon_{\mathrm{NL}}(\mathbf{u})$ for the nonlinear component, such that δ is the first variation with respect to **u.**

The assumption of small wave displacements results in an incremental stress from the incremental strain $\varepsilon(\mathbf{u})$. As a work-conjugate of the Green-Lagrange strain tensor, the 2nd order Piola-Kirchhoff stress tensor $\mathbf{S}(\mathbf{u})$ is required to satisfy the energy requirements. Since only small amplitude waves are imposed on the prestressed state, the current state will differ slightly from the prestresses configuration. The slight difference allows for the symmetric part of the 2nd order Piola-Kirchhoff stress tensor $\mathbf{s}(\mathbf{u}) = \left[S_{xx}, S_{yy}, S_{zz}, S_{yz}, S_{xz}, S_{xy}\right]^{\mathrm{T}}$ can be linearized as follows:

$$D_{\mathbf{u}}\mathbf{s}(\mathbf{u}) = \left.\frac{\partial \mathbf{s}(\mathbf{u})}{\partial \varepsilon(\mathbf{u})}\right|_{\mathbf{u}=0} \quad D_{\mathbf{u}}\varepsilon(\mathbf{u}) = \mathbf{D}^0(\mathbf{x})\varepsilon_{\mathrm{L}}(\mathbf{u}) \qquad \textbf{4.22}$$

Such that $\mathbf{D}_{ij}^0(\mathbf{x}) = \partial \mathbf{s}_i(\mathbf{u}) / \partial \varepsilon_j(\mathbf{u})\big|_{\mathrm{x}'=\mathrm{x}}$ is the 6 x 6 fourth order symmetric tensor of the tangential moduli referring to the prestressed configuration.

The Boltzmann superposition principle can be used to express the incremental stress in force of small amplitude wave and the linearized incremental 2^{nd} Piola-Kirchhoff stress tensor for a linear viscoelastic material can be rewritten in terms of convolution integral as [62, 63]:

$$D_{\mathbf{u}}\mathbf{s}(\mathbf{u}) = \int_{-\infty}^{t} \mathbf{D}^0(\mathbf{x}, t-\tau)\frac{\partial \varepsilon_{\mathrm{L}}(\mathbf{u}(\mathbf{x},\tau))}{\partial \tau} d\tau \qquad \textbf{4.23}$$

The result is that now $\mathbf{D}^0(\mathbf{x}, t-\tau)$ is a symmetric tensor of the fourth order that is function of the relaxation and *t* is the current time instant.

Equilibrium is obtained incrementally from the linearized equilibrium equations by subtracting the equations of the *C*' from the *C* configurations. For both states the equilibrium equations are the result of applying the Hamilton variation principle:

$$\delta H(\mathbf{u}, \delta\mathbf{u}) = \int_{t_1}^{t_2} \delta\left(K - W + V_C + V_{NC}\right) dt = 0 \qquad \textbf{4.24}$$

with the kinetic energy beginning $K = \frac{1}{2}\int_V \rho(\mathbf{x})\dot{\mathbf{u}}^{\mathrm{T}}\mathbf{u} d\upsilon$, the stored plus the dissipated energies are $W = \int_V \boldsymbol{\varepsilon}^{\mathrm{T}}(\mathbf{u})\mathbf{s}(\mathbf{u}) d\upsilon$, external conservative work done on the volume and surface loads $\mathbf{f}_{\mathrm{c}}(\mathbf{x},t)$ and $\mathbf{t}_{\mathrm{c}}(\mathbf{x},t)$ is $V_C = \int_V \mathbf{u}^{\mathrm{T}}\mathbf{f}_c(\mathbf{x},t) d\upsilon + \int_{\partial V} \mathbf{u}^{\mathrm{T}}\mathbf{t}_c(\mathbf{x},t) da$ and the external deformation dependent loads $\mathbf{t}_{\mathrm{nc}}(\mathbf{u})$ give the non-conservative work

$\delta W_{nc} = \int_{\partial V} \delta \mathbf{u}^{\mathrm{T}} \mathbf{t}_{\mathrm{nc}}(\mathbf{u})\, da$. In the definitions of integration limits in the functions in the Hamliton variation V is the volume of the solid and ∂V is the boundary of the surface. Any non-conservative external work must be evaluated at the current state **x**'(**u**) that is unknown, and thus the spatial description should be used rigorously instead of the material description. Nevertheless, if the magnitude of the incremental load is sufficiently small, the integration of the current load can be performed over the surface of the prestressed state ∂V with sufficient accuracy [63].

The variations of the internal and non-conservative external works are linearized as follows:

$$\mathbf{D}_{\mathbf{u}} \delta W(\mathbf{u}, \delta \mathbf{u}) = \int_V \delta \boldsymbol{\varepsilon}_{\mathrm{NL}}^{\mathrm{T}}(\mathbf{u}) \boldsymbol{\sigma}^0(\mathbf{x})\, d\upsilon + \int_V \int_{-\infty}^{t} \delta \boldsymbol{\varepsilon}_{\mathrm{L}}^{\mathrm{T}} \mathbf{D}^0\left((\mathbf{x}), t-\tau\right) \frac{\partial \boldsymbol{\varepsilon}_{\mathrm{L}}\left(\mathbf{u}(\mathbf{x}, \tau)\right)}{\partial \tau} d\tau d\upsilon \quad \textbf{4.25}$$

$$\mathbf{D}_{\mathbf{u}} \delta W_{nc}(\mathbf{u}, \delta \mathbf{u}) = \int_{\partial V} \delta \mathbf{u}^{\mathrm{T}} \frac{\partial \mathbf{t}_{\mathrm{nc}}^0(\mathbf{u})}{\partial \mathbf{u}} \mathbf{u} da + \int_{\partial V} \delta \mathbf{u}^{\mathrm{T}} \frac{\partial \Delta \mathbf{t}_{\mathrm{nc}}(\mathbf{u})}{\partial \mathbf{u}} \mathbf{u} da \quad \textbf{4.26}$$

here the vector $\boldsymbol{\sigma}^0(\mathbf{x}) = \left[\sigma_{xx}^0, \sigma_{yy}^0, \sigma_{zz}^0, \sigma_{yz}^0, \sigma_{xz}^0, \sigma_{xy}^0\right]^{\mathrm{T}}$ are the terms collected from the symmetric components of the Cauchy stress tensor $\mathbf{T}^0(\mathbf{x})$ of the prestressed state, $\mathbf{t}_{\mathrm{nc}}^0(\mathbf{u})$ is the vector of non-conservative loads in the prestressed state with $\Delta \mathbf{t}_{\mathrm{nc}}(\mathbf{u})$ being the corresponding increment. Applying equations 4.25 and 4.26 to the Hamilton's variation of equation 4.24 results in the following after some algebra:

$$\begin{aligned}\delta H\left(\mathbf{u},\delta\mathbf{u}\right)=&\int_{t_1}^{t_2}\int_V\left(-\delta\mathbf{u}^{\mathrm{T}}\rho\left(\mathbf{x}\right)\ddot{\mathbf{u}}-\left(\delta\boldsymbol{\varepsilon}_{\mathrm{NL}}\left(\mathbf{u}\right)\right)^{\mathrm{T}}\boldsymbol{\sigma}^0\left(\mathbf{x}\right)+\delta\mathbf{u}^{\mathrm{T}}\Delta\mathbf{f}_{\mathrm{C}}\left(\mathbf{x},t\right)\right)d\upsilon dt\\&-\int_{t_1}^{t_2}\int_V\int_{-\infty}^{t}\left(\delta\boldsymbol{\varepsilon}_{\mathrm{L}}\left(\mathbf{u}\right)\right)^{\mathrm{T}}\mathbf{D}^0\left(\mathbf{x},t-\tau\right)\frac{\partial\boldsymbol{\varepsilon}_{\mathrm{L}}\left(\mathbf{u}\left(\mathbf{x},\tau\right)\right)}{\partial\tau}d\tau d\upsilon dt\\&+\int_{t_1}^{t_2}\int_{\partial V}\delta\mathbf{u}^{\mathrm{T}}\Delta\mathbf{t}_{\mathrm{C}}\left(\mathbf{x},t\right)dadt+\int_{t_1}^{t_2}\int_{\partial V}\delta\mathbf{u}^{\mathrm{T}}\Delta\mathbf{t}_{\mathrm{nc}}\left(\mathbf{u}\right)dadt\\&+\int_{t_1}^{t_2}\int_{\partial V}\delta\mathbf{u}^{\mathrm{T}}\left(\frac{\partial\mathbf{t}_{\mathrm{nc}}^0\left(\mathbf{u}\right)}{\partial\mathbf{u}}\mathbf{u}+\frac{\partial\Delta\mathbf{t}_{\mathrm{nc}}\left(\mathbf{u}\right)}{\partial\mathbf{u}}\mathbf{u}\right)dadt=0\end{aligned}\qquad\textbf{4.27}$$

Therefore equation 4.27 represents the basic system governing the dynamics of small oscillations of a three dimensional viscoelastic material subjected to a generic stress field.

The starting point of the SAFE formulation consists in assuming the displacement field dependence in the *z*-direction represented by a through thickness finite element mesh. By using mono-dimensional quadratic elements with 3 degrees of freedom per node associated to the displacements u_i., for the cross section a planar mesh of n_{el} finite elements with an area Ω^e is assumed. Mapping of in-plane and linear based a reference element identified by the area Ω^{ref} and boundary $\partial\Omega^{ref}$ with a corresponding area Ω^e and boundary $\partial\Omega^e$ of the generic e^{th} element. The result of the discretization is a semi-isoparametric representation of the out-of-plane and in-plane motion that are uncoupled.

At a point $\mathbf{x}^e=\left(x^e,y^e,0\right)$ the displacement vector can be approximated by:

$$\mathbf{u}^e\left(\xi,z,t\right)=\mathbf{N}\left(\xi\right)\mathbf{q}^e\left(z,t\right)\quad\mathbf{x}^e\in\Omega^e\qquad\textbf{4.28}$$

$$\mathbf{u}^e\left(\eta,z,t\right)=\mathbf{H}\left(\eta\right)\mathbf{q}^e\left(z,t\right)\quad\mathbf{x}^e\in\partial\Omega^e\qquad\textbf{4.29}$$

such that $\mathbf{N}(\xi)$ and $\mathbf{H}(\xi)$ are matrices that contain the shape function with natural coordinates $\boldsymbol{\xi}=(\xi_1,\xi_2)$ and η on Ω^{ref} and $\partial\Omega^{\text{ref}}$ respectively and $\mathbf{q}^{\text{e}}(z,t)$ is the vector of

nodal displacements. The displacement field is considered harmonic with an angular frequency ω, thus the wave equation can be transformed from a time component *t* to an angular frequency ω and the longitudinal coordinate *z* to the wavenumber κ_z by using the Fourier transforms in time and space.

$$\overline{f}(z,\omega) = \Im\left[f(z,t)\right](\omega) = \int_{-\infty}^{\infty} f(z,t) e^{-i\omega t} dt \qquad \textbf{4.30}$$

$$\overline{f}(\kappa_z,\omega) = \Im\left[f(z,t)\right](\kappa_z) = \int_{-\infty}^{\infty} f(z,t) e^{-i\kappa_z z} dz \qquad \textbf{4.31}$$

with *i* beginning the imaginary number. Acting only on the *t* and *z* dependent fields the Fourier transforms, every wavenumber κ_z, and each angular frequency ω is projected on the *x*-*y* plane with the propagation of the corresponding waveform in the *z*-direction is acquired by the in-plane mesh of waveguide cross section.

The fundamental property $\Im\left[d^n f(z,t) / \ dt^n \right](\omega) = (i\omega)^n \overline{f}(z,\omega)$ in conjunction with the transforms of equations 4.30 and 4.31 the displacement and acceleration vectors are determined as $\overline{\overline{\mathbf{u}}}^e(\xi,\kappa_z,\omega) = \mathbf{N}(\xi)\overline{\overline{\mathbf{q}}}^e(\kappa_e,\omega)$ and $\overline{\overline{\ddot{\mathbf{u}}}}^e(\eta,\kappa_z,\omega) = -\omega^2\mathbf{N}(\xi)\overline{\overline{\mathbf{q}}}^e(\kappa_z,\omega)$ respectively on Ω^e. On the element boundary $\partial\Omega^e$ the results is $\overline{\overline{\mathbf{u}}}^e(\eta,\kappa_z,\omega) = \mathbf{H}(\eta)\overline{\overline{\mathbf{q}}}^e(\kappa_z,\omega)$. External volume and surface loads for the generic e^{th} element in the wavenumber-frequency domain, $\overline{\overline{\mathbf{f}}}^e(\xi,\kappa_z,\omega)$ and $\overline{\overline{\mathbf{t}}}^e(\eta,\kappa_z,\omega)$ are also determined by the same temporal and spatial transforms.

For equation 4.19 the kinematic relation is transformed to be:

$$\underline{\underline{\boldsymbol{\varepsilon}}}_{\mathrm{L}}^{e}\left(\xi,\kappa_z,\omega\right)=\left[\mathbf{B}_{xy}\left(\xi\right)+i\kappa_z\mathbf{B}_z\left(\xi\right)\right]\underline{\underline{\mathbf{q}}}^{e}\left(\kappa_z,\omega\right) \qquad \textbf{4.32}$$

Such that

$$\mathbf{B}_{xy}\left(\boldsymbol{\xi}\right)=\left[L_x\frac{\partial\mathbf{N}\left(\boldsymbol{\xi}\right)}{\partial x}+L_y\frac{\partial\mathbf{N}\left(\boldsymbol{\xi}\right)}{\partial y}\right] \quad \text{and} \quad \mathbf{B}_z\left(\boldsymbol{\xi}\right)=L_z\mathbf{N}\left(\boldsymbol{\xi}\right) \qquad \textbf{4.33}$$

Transformation of the non-linear strain vector in equation 4.20 result in:

$$\underline{\underline{\boldsymbol{\varepsilon}}}_{\mathrm{NL}}^{e}=\frac{1}{2}\begin{bmatrix}\left(\underline{\underline{\mathbf{q}}}^{e}\right)^{\mathrm{T}}\dfrac{\partial\mathbf{N}^{\mathrm{T}}}{\partial x}\dfrac{\partial\mathbf{N}}{\partial x}\left(\underline{\underline{\mathbf{q}}}^{e}\right)\\ \left(\underline{\underline{\mathbf{q}}}^{e}\right)^{\mathrm{T}}\dfrac{\partial\mathbf{N}^{\mathrm{T}}}{\partial y}\dfrac{\partial\mathbf{N}}{\partial y}\left(\underline{\underline{\mathbf{q}}}^{e}\right)\\ -\kappa_z^2\left(\underline{\underline{\mathbf{q}}}^{e}\right)^{\mathrm{T}}\mathbf{N}^{\mathrm{T}}\mathbf{N}\underline{\underline{\mathbf{q}}}^{e}\\ 2i\kappa_z\left(\underline{\underline{\mathbf{q}}}^{e}\right)^{\mathrm{T}}\dfrac{\partial\mathbf{N}^{\mathrm{T}}}{\partial y}\mathbf{N}\underline{\underline{\mathbf{q}}}^{e}\\ 2i\kappa_z\left(\underline{\underline{\mathbf{q}}}^{e}\right)^{\mathrm{T}}\dfrac{\partial\mathbf{N}^{\mathrm{T}}}{\partial x}\mathbf{N}\underline{\underline{\mathbf{q}}}^{e}\\ 2\left(\underline{\underline{\mathbf{q}}}^{e}\right)^{\mathrm{T}}\dfrac{\partial\mathbf{N}^{\mathrm{T}}}{\partial x}\dfrac{\partial\mathbf{N}}{\partial x}\left(\underline{\underline{\mathbf{q}}}^{e}\right)\end{bmatrix} \qquad \textbf{4.34}$$

Assuming constant material properties in the *z*-direstion and across the element domain Ω^e the Fourier transformation of equation 4.23 yields:

$$D_{\mathbf{u}}\underline{\underline{\mathbf{s}}}^{e}\left(\xi,\kappa_z,\omega\right)=\int_{-\infty}^{\infty}\int_{-\infty}^{t}\mathbf{D}^{0}\left(\mathbf{x},t-\tau\right)\frac{\partial\varepsilon_{\mathrm{L}}\left(\mathbf{u}\left(\mathbf{x},\tau\right)\right)}{\partial\tau}e^{i\omega t}d\tau dt=\overline{\mathbf{D}^{0}}\left(i\omega\right)\underline{\underline{\boldsymbol{\varepsilon}}}_{\mathrm{L}}^{e}\left(\xi,\kappa_z,\omega\right) \qquad \textbf{4.35}$$

Therefore the incremental stress relative to small deformation is obtained in the wavenumber-frequency domain as in linear elastic study. The analysis is executed by providing the substitution of the real tensor of the elastic moduli along with the relaxation functions $\overline{\mathbf{D}_e^0}\left(i\omega\right)=\boldsymbol{Re}\left(\overline{\mathbf{D}_e^0}\left(\omega\right)\right)+i\,\boldsymbol{Im}\left(\overline{\mathbf{D}_e^0}\left(\omega\right)\right)$ with the real part

$\boldsymbol{Re}\left(\overline{\mathbf{D}_e^0(\omega)}\right)$ beginning the storage moduli and the imaginary part is the loss moduli. The elastic moduli constants tensor $\mathbf{D}_e^0$ becomes independent of time if the material is assumed to by elastic and will then not be affected by the time-frequency contraction.

For an infinite long waveguide the equation of motion is discretized by the relationship between an infinitesimal volume $d\upsilon = dxdydz$ with the resultant volume in the reference system $d\xi_1 d\xi_2 dz$ which is given by $dxdysz = \int_\upsilon^e d\xi_1 d\xi_2 dz$ with $\int_\upsilon^e \det\left[\frac{\partial(x,y)}{\partial(\xi_1,\xi_2)}\right]$ that is the Jacobian of the mapping from the $\xi_1 - \xi_2$ to the *x*-*y* plane. With these relationships, each volume integral in equation 4.27 is computed as $\int_{V^e} d\upsilon = \int_{-\infty}^{\infty} dz \int_{\Omega^e} \int_\upsilon^e d\xi_1 d\xi_2$ such that the integral over the *z*-coordinate remains unchanged.

As with the volume the infinitesimal area of the waveguide in the prestressed and reference state are written as $da = dsdz = \int_a^e d\eta dz$ such that the Jacobian of the in-plane transformation is $\int_a^e = \left\| \frac{\partial \mathbf{x}^e}{\partial \eta} \times \mathbf{n}_3 \right\|$, with $\mathbf{n}_3$ denoting the unit vector along the *z*-direction. Thus each surface integral of equation 4.27 is written as $\int_{\partial V^e} da = \int_{-\infty}^{\infty} dz \int_{\partial\Omega^e} \int_a^e d\eta$ and the integration along *z*-direction is unaltered giving:

$$\int_V d\upsilon = \int_{-\infty}^{+\infty} dz \int_{\Omega^{ref}} f(\xi_1,\xi_2) J(\xi_1,\xi_2) d\xi_1 d\xi_2, \quad J(\xi_1,\xi_2) = \boldsymbol{det}\left[\frac{\partial(x,y)}{\partial(\xi_1,\xi_2)}\right] \qquad \textbf{4.36}$$

$$\int_{\partial V} da = \int_{-\infty}^{+\infty} dz \int_{\partial \Omega^{ref}} f(\eta) J(\eta) d\eta, \quad J(\eta) = \boldsymbol{det}\left[\frac{\partial x}{\partial \eta} \times M_3 \right] \qquad \textbf{4.37}$$

A linear system of *M* equations in the (κ_z, ω) domain is achieved by substituting equations 4.32, 4.34 and 4.35 into equation 4.27 with some algebra resulting in the following:

$$\left[\kappa_z^2 \mathbf{K}_3 - i\kappa_z \mathbf{K}_2 + \mathbf{K}_1 - \omega^2 \mathbf{M} \right] \overline{\overline{\mathbf{Q}}}(\kappa_z, \omega) = 0 \qquad \textbf{4.38}$$

With the global vector of nodal displacements is $\overline{\overline{\mathbf{Q}}}(\kappa_z, \omega) = \bigcup_{e=1}^{n_{el}} \overline{\overline{\mathbf{q}}}^{e}(\kappa_z, \omega)$ and $\mathbf{M} = \bigcup_{e=1}^{n_{el}} \mathbf{m}^e$ is the global mass matrix. The global quantity is obtained with the operator $\bigcup_{e=1}^{n_{el}}$ with the application of a finite element assembling procedure for all the elements, n_{el}, of the mesh. The $\mathbf{K}_i$ stiffness operators are defined as:

$$\begin{aligned}
\mathbf{K}_3 &= \bigcup_{e=1}^{n_{el}} \left[\mathbf{k}_3^e + \mathbf{k}_{\sigma_{zz}^0}^e \right] \\
\mathbf{K}_2 &= \bigcup_{e=1}^{n_{el}} \left[\mathbf{k}_2^e - \left(\mathbf{k}_2^e \right)^{\mathrm{T}} + \mathbf{k}_{\sigma_{yz}^0}^e - \left(\mathbf{k}_{\sigma_{yz}^0}^e \right)^{\mathrm{T}} + \mathbf{k}_{\sigma_{xz}^0}^e - \left(\mathbf{k}_{\sigma_{xz}^0}^e \right)^{\mathrm{T}} \right] \\
\mathbf{K}_3 &= \bigcup_{e=1}^{n_{el}} \left[\mathbf{k}_1^e + \mathbf{k}_{\sigma_{xx}^0}^e + \mathbf{k}_{\sigma_{yy}^0}^e + \mathbf{k}_{\sigma_{xy}^0}^e + \left(\mathbf{k}_{\sigma_{xy}^0}^e \right)^{\mathrm{T}} \right] - \bigcup_{r=1}^{n_r} \mathbf{k}_{nc}^r
\end{aligned} \qquad \textbf{4.39}$$

At the element level the affiliated stiffness quantities for assembly are:

$$
\begin{aligned}
\mathbf{k}_1^e &= \int_{\Omega^{ref}} \mathbf{B}_\xi^{\mathrm{T}} \overline{\mathrm{D}}(i\omega) \mathbf{B}_\xi \int_\upsilon^e d\xi_1 d\xi_2 \\
\mathbf{k}_2^e &= \int_{\Omega^{ref}} \mathbf{B}_\xi^{\mathrm{T}} \overline{\mathrm{D}}(i\omega) \mathbf{B}_\xi \int_\upsilon^e d\xi_1 d\xi_2 \\
\mathbf{k}_3^e &= \int_{\Omega^{ref}} \mathbf{B}_z^{\mathrm{T}} \overline{\mathrm{D}}(i\omega) \mathbf{B}_z \int_\upsilon^e d\xi_1 d\xi_2 \\
\mathbf{k}_{\sigma_{xx}^0}^e &= \int_{\Omega^{ref}} \sigma_{xx}^0(\xi) \frac{\partial \mathbf{N}^{\mathrm{T}}}{\partial x} \frac{\partial \mathbf{N}}{\partial x} \int_\upsilon^e d\xi_1 d\xi_2 \\
\mathbf{k}_{\sigma_{yy}^0}^e &= \int_{\Omega^{ref}} \sigma_{yy}^0(\xi) \frac{\partial \mathbf{N}^{\mathrm{T}}}{\partial y} \frac{\partial \mathbf{N}}{\partial y} \int_\upsilon^e d\xi_1 d\xi_2 \\
\mathbf{k}_{\sigma_{zz}^0}^e &= \int_{\Omega^{ref}} \sigma_{zz}^0(\xi) \mathbf{N}^{\mathrm{T}} \mathbf{N} \int_\upsilon^e d\xi_1 d\xi_2 \\
\mathbf{k}_{\sigma_{yz}^0}^e &= \int_{\Omega^{ref}} \sigma_{yz}^0(\xi) \frac{\mathbf{N}^{\mathrm{T}}}{\partial y} \mathbf{N} \int_\upsilon^e d\xi_1 d\xi_2 \\
\mathbf{k}_{\sigma_{xz}^0}^e &= \int_{\Omega^{ref}} \sigma_{xz}^0(\xi) \frac{\mathbf{N}^{\mathrm{T}}}{\partial x} \mathbf{N} \int_\upsilon^e d\xi_1 d\xi_2 \\
\mathbf{k}_{\sigma_{xy}^0}^e &= \int_{\Omega^{ref}} \sigma_{xy}^0(\xi) \frac{\partial \mathbf{N}^{\mathrm{T}}}{\partial x} \frac{\partial \mathbf{N}}{\partial y} \int_\upsilon^e d\xi_1 d\xi_2 \\
\mathbf{m}^e &= \int_{\Omega^{ref}} \rho_e \mathbf{N}^{\mathrm{T}} \mathbf{N} \int_\upsilon^e d\xi_1 d\xi_2
\end{aligned}
\qquad \textbf{4.40}
$$

Gauss quadrature rules allow for the integrations to be performed in a straight forward manner [64]. At this point equation 4.36 represents only the homogeneous part with the omission of the external force contributions for the rationale that dispersion curve extraction can be performed. With the assumption the load along the *z*-direction is invariant and the system present thus far is not represent the complete general form for all the possible loadings. As this system is not representative of the actual stress distributions in the waveguide, however the operators defined in equations 4.36 and 4.38 will remain unchanged and only their positions in the final system may vary.

For the consideration of a non-conservative force applied to the waveguide a pressure type force with a friction interface with the fluid-solid interface. Such a force is

concerned to the system as $\mathbf{t}_{nc} = -p\mathbf{n}$ such that p is the pressure applied and $\mathbf{n}$ is the normal to the surface that the external force is applied. Neglecting the fluid solid interface force eliminates the second term from the right hand side of equation 4.26. Due to the fact that the magnitude of the pressure is not dependent on the deformation of the body and is only dependent on the load direction $p\mathbf{n}(\mathbf{n})$. Therefore the linearized external force can now be expressed as:

$$\mathbf{D}_{\mathbf{u}}\delta V_p\left(\mathbf{u},\delta\mathbf{u}\right) = \int_{\partial\Omega} -p_0\delta\mathbf{u}^{\mathrm{T}}\left(\mathbf{D}_{\mathbf{u}}\mathbf{n}\left(\mathbf{n}\right)\right)da \qquad \textbf{4.41}$$

with p_0 as the hydrostatic pressure in the prestressed state and $\mathbf{D_n n(n)}$ is the linearized change of the surface normal orientation due to the displacement at the same point. By introducing linearization, the surface integral in equation 4.41 is reduced to a line integral over the boundary of the reference element $\partial\Omega^{ref}$ [64, 65].

$$\mathbf{D}_{\mathbf{u}}\mathbf{n}\left(\mathbf{n}\right) = \frac{\dfrac{\partial\mathbf{u}}{\partial\eta}\times\mathbf{n}_3}{\left\|\dfrac{\partial\mathbf{u}}{\partial\eta}\times\mathbf{n}_3\right\|} \qquad \textbf{4.42}$$

The linearization in equation 4.42 requires a counterclockwise numeration of the element nodes of the mesh to preserve the positiveness of the sign of the outward normal $\mathbf{n}(\mathbf{u})$. The incremental non-conservative virtual work is rewritten for the finite element mesh by substituting equation 4.41 into 4.42 resulting in:

$$\mathbf{D}_{\mathbf{u}}\delta V_p\left(\mathbf{u},\delta\mathbf{u}\right)=\bigcup_{r=1}^{n_r}\int_{\partial\Omega^{ref}}-p_0\delta\mathbf{u}^{\mathrm{T}}\left(\frac{\dfrac{\partial\mathbf{u}}{\partial\eta}\times\mathbf{n}_3}{\left\|\dfrac{\partial\mathbf{u}}{\partial\eta}\times\mathbf{n}_3\right\|}\right)\int_a^e d\eta$$
$$=\bigcup_{r=1}^{n_r}\int_{\partial\Omega^{ref}}-p_0\mathbf{H}^{\mathrm{T}}\left(\frac{\partial\mathbf{H}}{\partial\eta}\times\mathbf{n}_3\right)d\eta=\delta\mathbf{Q}^{\mathrm{T}}\mathbf{K}_p\mathbf{Q} \qquad \textbf{4.43}$$

The total number of elements with edges lying on the cross section boundary are represented by n_r. $\mathbf{K}_p$ is the global pressure stiffness matrix that is determined by assembling each element's stiffness contribution $\mathbf{k}_p^r$ with:

$$\mathbf{k}_p^r=\int_{\partial\Omega^{ref}}-p_0\mathbf{H}^{\mathrm{T}}\begin{bmatrix}0&1&0\\-1&0&0\\0&0&0\end{bmatrix}\frac{\partial\mathbf{H}}{\partial\eta}d\eta \qquad \textbf{4.44}$$

In general $\mathbf{K}_p$ is nonsymmetric, but in the particular case of a closed and constant pressure symmetry is preserved thus, an incremental pseudo pressure potential is assumed such that $\mathbf{D}_{\mathbf{u}}V_p=\frac{1}{2}\mathbf{Q}^{\mathrm{T}}\mathbf{K}_p\mathbf{Q}$. The operator in equation 4.44 is not affected by time and space contractions since it is real and independent of z.

With the incremental form of the wave equation and the SAFE formulation define the dispersion of the waveguide can analysis. Considering homogeneous system in equation 4.38 is a polynomial eigenvalue problem that can be converted into the state space and solved in wavenumbers $\kappa_z^m\left(\omega\right)=\mathbf{Re}\left(\kappa_z^m\right)+i\mathbf{Im}\left(\kappa_z^m\right),\left(m=1,\ldots,2M\right)$ for any real positive value of the angular frequency ω. The m^{th} mode shape of the waveguide is defined by $\overline{\square}^m=\mathbf{Re}\left(\overline{\square}^m\right)+i\mathbf{Im}\left(\overline{\square}^m\right)$ and the dispersive quantities such

as phase velocity $\left(c_p^m(\omega)=\omega/\mathbf{Re}\left(\kappa_z^m\right)\right)$, group velocity $\left(c_{gr}^m(\omega)=\partial\omega/\partial\kappa_z^m\right)$ and attenuation $\left(\alpha^m(\omega)=\mathbf{Im}\left(\kappa_z^m\right)\right)$ that are related to the wavenumber $\kappa_z^m(\omega)$.

The computation of the group velocity in a lossless medium for an axial load has been determined in close form [66-68] as:

$$c_{gr}^m(\omega)=\frac{\partial\omega}{\partial\kappa}=\frac{\overline{\overline{\mathbf{Q}}}^{\mathrm{T}}\left[\mathbf{T}^{\mathrm{H}}\mathbf{K}_2\mathbf{T}+2\kappa_z^m(\omega)\mathbf{K}_3\right]\overline{\overline{\mathbf{Q}}}}{2\omega\overline{\overline{\mathbf{Q}}}^{\mathrm{T}}\mathbf{M}\overline{\overline{\mathbf{Q}}}} \qquad \textbf{4.45}$$

For a general initial stress the formula is valid with the expectation in the fact that the $\mathbf{K}_i$ operator has the geometric stiffness terms associated with the nonzero initial stress components σ_{yz}^0 and σ_{xz}^0. The parameter **T** is an *M x M* identity matrix with the imaginary unit inserted for each degree of freedom in the *z* direction and H is the complex conjugate.

Group velocity in unique to a lossless material. In the case of a non-conservative the dissipation mechanism results in complex wavenumbers, thus the group velocity loses sequence and energy velocity is then the meaningful parameter. Determination of the energy velocity begins by determining the transfer of the energy. The transfer of energy is the ratio between the energy flux density per unit time and the total energy density of the system following the energy conservation law such that [69, 70]

$$\frac{D\mathrm{K}}{Dt}+P_{\boldsymbol{int}}+P_D=P_{ext}^{\upsilon}+P_{ext}^{s} \qquad \textbf{4.46}$$

Where P_{int} is the stress power, P_D the viscous power loss, external volume forces from the power supplied on the system P_{ext}^{υ}, the external surface forces power P_{ext}^{s}, that are defined as followed:

$$P_{int} + P_D = \int_V \mathbf{P}(\mathbf{u}) : \dot{\mathbf{F}}(\mathbf{u})\, d\upsilon \qquad \textbf{4.47}$$

$$P_{ext}^{\upsilon} = \int_{\upsilon} \dot{\mathbf{u}}\mathbf{f}_C\, d\upsilon \qquad \textbf{4.48}$$

$$P_{ext}^{s} = \int_{\partial V} \dot{\mathbf{u}}\left(\mathbf{t}_c - p\mathbf{n}\right) da \qquad \textbf{4.49}$$

With **P(u)** is the first Piola-Kirchhoff stress tensor and $\mathbf{F}(\mathbf{u}) = \dfrac{\partial \mathbf{x}'(\mathbf{u})}{\partial \mathbf{x}}$ is the deformation gradient. Introducing the positions of equations 4.47-4.49 and applying the linearization concept equation 4.46 is recast in the linear incremental form. Considering a constant pressure p_0 on the closed boundary conditions during motion and using the power equivalence $\int_V \mathbf{P}(\mathbf{u}) : \dot{\mathbf{F}}(\mathbf{u})\, d\upsilon = \int_V \mathbf{S}(\mathbf{u}) : \dot{\mathbf{E}}(\mathbf{u})\, d\upsilon$ results in :

$$\frac{\partial}{\partial t}\left(\Delta \mathrm{K} + \mathbf{D}_{\mathbf{u}} W + \mathbf{D}_{\mathbf{u}} V_p\right) = \int_V \dot{\mathbf{u}}^{\mathrm{T}} \Delta \mathbf{f}_c(t)\, d\upsilon + \int_{\partial V} \dot{\mathbf{u}}^{\mathrm{T}} \Delta \mathbf{t}(t)\, da \qquad 4.50$$

thus the incremental form of the balance of energy in the material description is denoted in equation 4.48. Recognizing that $\mathbf{D}_{\mathbf{u}}\mathbf{P}(\mathbf{u})\mathbf{n} = \Delta \mathbf{t}_c(t)$, the second integral of the right hand side of equation 4.48 is in terms of the incremental equilibrium and the force relations:

$$
\begin{aligned}
&\mathbf{P}(\mathbf{u}) = \mathbf{F}(\mathbf{u})\mathbf{S}(\mathbf{u}),\\
&\mathbf{D}_{\mathbf{u}}\mathbf{F}(\mathbf{u}) = \nabla\mathbf{u},\\
&\mathbf{S}(\mathbf{u})\big|_{\mathbf{u}=\mathbf{0}} = \mathbf{T}^0(\mathbf{x}),\\
&\mathbf{F}(\mathbf{u})\big|_{\mathbf{u}=\mathbf{0}} = \mathbf{I},\\
&\mathbf{E}_L = sym(\nabla\mathbf{u}),\\
&\mathbf{D}_{\mathbf{u}}\mathbf{S}(\mathbf{u}) = \mathbf{D}^0(t-\tau):\mathbf{E}_L(\mathbf{u})
\end{aligned}
\qquad \textbf{4.51}
$$

with the these definitions the linearized 1st Piola-Kirchhoff stress tensors take the form:

$$\mathbf{D}_{\mathbf{u}}\mathbf{P}(\mathbf{u}) = \nabla\mathbf{u}\mathbf{T}^0(\mathbf{x}) + \int_{-\infty}^{t}\mathbf{D}^0(t-\tau):\frac{\partial\mathbf{E}_L(\mathbf{u}(\mathbf{x},\tau))}{\partial\tau}d\tau \qquad \textbf{4.52}$$

A material description of the Poynting theorem is achieved by multiplying equation 4.52 by **n** and substituting inside the boundary integral on the right hand side of equation 4.50 given the resultant:

$$\frac{\partial}{\partial t}\left(\Delta\mathrm{K} + \mathbf{D}_{\mathbf{u}}W + \mathbf{D}_{\mathbf{u}}V_p\right) + \int_{\partial V} -\left(\mathbf{D}_{\mathbf{u}}\mathbf{P}(\mathbf{u})\right)^{\mathrm{T}}\dot{\mathbf{u}}\cdot\mathbf{n}da = \Delta P_{ext}^{\upsilon} \qquad \textbf{4.53}$$

With the incremental form of the Poynting vector defined as $\left(\mathbf{D}_{\mathbf{u}}\mathbf{P}(\mathbf{u})\right)^{\mathrm{T}}\dot{\mathbf{u}}$. The time derivative can be replaced with the average time over a time period [t, t + 2π/ω] due to the harmonic behavior of the wave motion thus

$$\left\langle \Delta\mathrm{K} + \mathbf{D}_{\hat{\mathbf{u}}}W - \mathbf{D}_{\hat{\mathbf{u}}}V \right\rangle + \int_{\partial V}\left\langle \mathbf{D}_{\hat{\mathbf{u}}}\hat{\mathbf{J}}(\hat{\mathbf{u}})\cdot\mathbf{n}\right\rangle da = \left\langle \Delta P_{ext}^{\upsilon}\right\rangle \qquad \textbf{4.54}$$

with $\langle\ \rangle = \frac{\omega}{2\pi}\int_t^{t+\frac{2\pi}{\omega}}dt$ denoting the time average operation. In the frequency-wavenumber domain the Poynting vector $\mathbf{D}_{\hat{\mathbf{u}}}\hat{\mathbf{J}}(\hat{\mathbf{u}}) = -\left(\mathbf{D}_{\hat{\mathbf{u}}}\hat{\mathbf{P}}(\hat{\mathbf{u}})\right)^{\mathrm{T}}\hat{\dot{\mathbf{u}}}$ becomes:

$$\mathbf{D}_{\hat{\mathbf{u}}}\hat{\hat{\mathbf{J}}}\left(\hat{\hat{\mathbf{u}}}\right)=-i\omega\left[\mathbf{T}^{0}\left(\mathbf{x}\right)\otimes y\left(\nabla\hat{\hat{\mathbf{u}}}\right)^{\mathrm{T}}+\overline{\mathbf{D}}^{0}\left(\omega\right)\cdot\overline{\hat{\hat{\mathbf{E}}}}_{L}\left(\hat{\hat{\mathbf{u}}}\right)\right]\hat{\hat{\mathbf{u}}} \qquad \textbf{4.55}$$

From the eigenvalue problem in equation 4.36 the wave solution is known in terms of κ_z^m and $\overline{\hat{\hat{\mathbf{Q}}}}^m$ for the m^{th} propagating mode, previously the resulting parameters were strictly functions of the angular frequency ω. Determined from the ratio of average energy flux component in the *z* direction and the total energy density of the waveguide at a given angular frequency ω the energy velocity of the m^{th} propagating mode base on the Umov's definition [71].

$$c_e^m\left(\omega\right)=\frac{\int_{\Omega}\left\langle\mathbf{D}_{\hat{\mathbf{u}}}\hat{\hat{\mathbf{J}}}^m\left(\omega\right)\cdot\mathbf{M}_3\right\rangle d\Omega}{\left\langle\Delta\overline{\hat{\hat{\mathbf{K}}}}^m\left(\omega\right)+\mathbf{D}_{\hat{\mathbf{u}}}\overline{\hat{\hat{\mathbf{W}}}}^m\left(\omega\right)\right\rangle\Big|_{\Omega}-\left\langle\mathbf{D}_{\hat{\mathbf{u}}}\overline{\hat{\hat{\mathbf{V}}}}_p^m\left(\omega\right)\right\rangle\Big|_{\partial\Omega}} \qquad \textbf{4.56}$$

Making use of the matrix operators defined previously equation 4.56 can be rewritten as shown in other studies [72]. Applying the compatibility operator L_z to equation 4.55 the incremental energy flux in the *z*-direction is obtained:

$$\left\langle\mathbf{D}_{\hat{\mathbf{u}}}\hat{\hat{\mathbf{J}}}^m\left(\omega\right)\cdot\mathbf{n}_3=\frac{\omega}{2}\mathbf{Im}\left[\left(\hat{\hat{\mathbf{u}}}^m\right)^{\mathrm{H}}\left(\sigma_{13}^0\frac{\partial\hat{\hat{\mathbf{u}}}^m}{\partial x}+\sigma_{23}^0\frac{\partial\hat{\hat{\mathbf{u}}}^m}{\partial y}+i\kappa_z^m\left(\omega\right)\sigma_{33}^0\hat{\hat{\mathbf{u}}}^m+L_z^{\mathrm{T}}\overline{\mathbf{D}}^0\hat{\hat{\boldsymbol{\varepsilon}}}_L^m\right)\right]\right\rangle \qquad \textbf{4.57}$$

The integral of the energy flux intensity over the waveguide is now achievable by substituting equation 4.28 and using the operators of equation 4.38 resulting in:

$$\int_{\Omega}\left\langle\mathbf{D}_{\hat{\mathbf{u}}}\hat{\hat{\mathbf{J}}}^m\left(\omega\right)\cdot\mathbf{n}_3\right\rangle d\Omega=\frac{\omega}{2}\mathbf{Im}\left\{\left(\overline{\hat{\hat{\mathbf{Q}}}}^m\right)^{\mathrm{H}}\left[\begin{array}{l}\mathbf{K}_{\sigma_{xz}^0}^{\mathrm{T}}+\mathbf{K}_{\sigma_{yz}^0}^{\mathrm{T}}+\mathbf{K}_2^{\mathrm{T}}\\+i\kappa_z^m\left(\omega\right)\left(\mathbf{K}_3+\mathbf{K}_{\sigma_{zz}^0}\right)\end{array}\right]\overline{\hat{\hat{\mathbf{Q}}}}^m\right\} \qquad \textbf{4.58}$$

Lastly the stored and dissipated energy of the time average incremental kinetic energy and the non-conservative work are defined as:

$$\left\langle \Delta\overline{\overline{\mathrm{K}}}^{m}(\omega) \right\rangle\Big|_{\Omega} = \frac{\omega^2}{4}\mathbf{Re}\left[\left(\overline{\overline{\mathbf{Q}}}^{m} \right)^{\mathrm{H}} \mathbf{M}\overline{\overline{\mathbf{Q}}}^{m} \right] \qquad \textbf{4.59}$$

$$\left\langle \mathbf{D}_{\mathbf{u}}\overline{\overline{\mathbf{W}}}^{m} \right\rangle\Big|_{\Omega} = \frac{1}{4}\mathbf{Re}\left\{ \left(\overline{\overline{\mathbf{Q}}}^{m} \right)^{\mathrm{H}} \begin{bmatrix} \left(\kappa_z^m(\omega)\right)^2 \left(\mathbf{K}_3 + \mathbf{K}_{\sigma_{zz}^0}\right) \\ +i\kappa_z^m(\omega)\left(\mathbf{K}_2 - \mathbf{K}_2^{\mathrm{T}} + 2\mathbf{K}_{\sigma_{yz}^0} + 2\mathbf{K}_{\sigma_{xz}^0}\right) \\ +\mathbf{K}_1 + \mathbf{K}_{\sigma_{xx}^0} + \mathbf{K}_{\sigma_{yy}^0}\ 2\mathbf{K}_{\sigma_{xy}^0} \end{bmatrix} \overline{\overline{\mathbf{Q}}}^{m} \right\} \qquad \textbf{4.60}$$

$$\left\langle \mathbf{D}_{\mathbf{u}}\overline{\overline{\mathbf{V}}}_{p}^{m}(\omega) \right\rangle\Big|_{\Omega} = \frac{1}{4}\mathbf{Re}\left[\left(\overline{\overline{\mathbf{Q}}}^{m} \right)^{\mathrm{H}} \mathbf{K}_p\overline{\overline{\mathbf{Q}}}^{m} \right] \qquad \textbf{4.61}$$

With the substitution of equations 4.58-4.61 into equation 4.56 the energy velocity for the assumed m^{th} wave at the given frequency ω. The relationships defined will hold a generic 3D prestressed field for linear elastic and viscoelastic materials.

4.5 Numerical Analysis for Rail Cross Section

The SAFE method was applied to the rail geometry for a 136 rail section. The mesh of the cross section is shown in Figure 4-8. Dispersion curves for the phase velocity and group velocity for the frequency rannge of 1kHz to 1MHz that were generated for the 136 rail cross section. Made up of 242 elements the shortest element dimesion of 6.19 x 10^{-5} m is more than 10 times smaller than the shortest wave legnth of 0.0058 m expected at 1 MHz. This element size insures that mapping of the mode propagation will not be truncated.

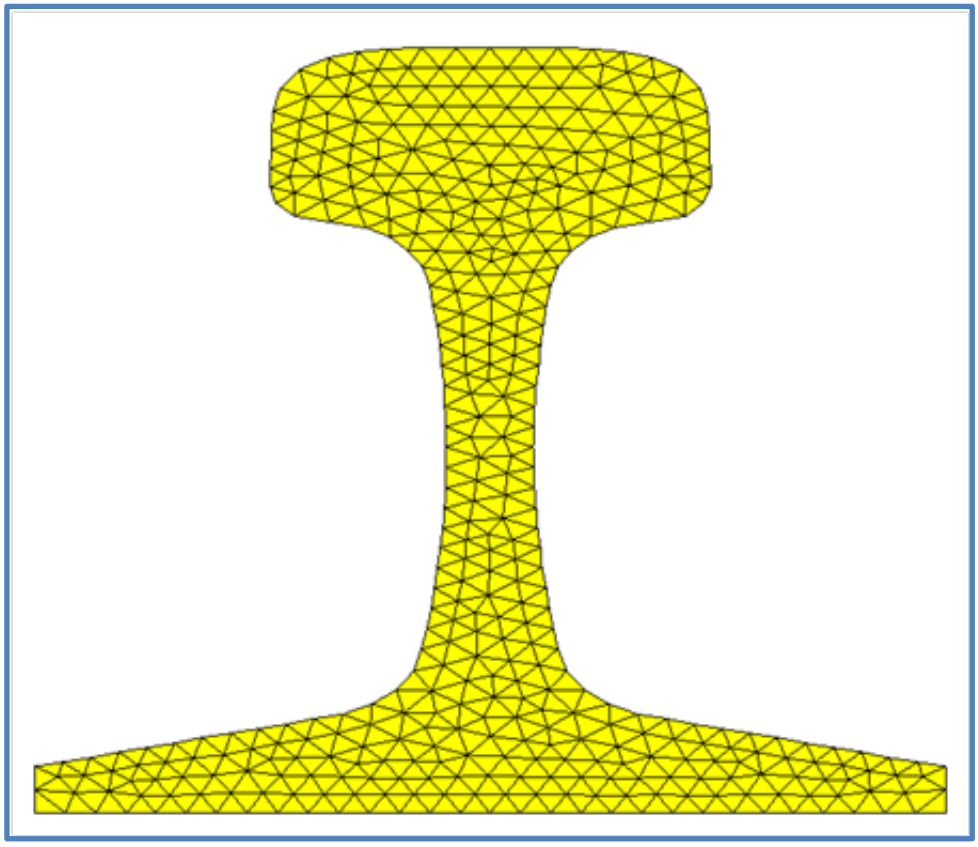

Figure 4-8: 136 Rail Meshed Cross Section

The SAFE results of the phase and group velocity dispersion curves are shown in Figure 4-9. In the dispersion curves it is clear that the 136 rail geometery makes for very complex wave propagration. At 200kHz over 100 diferent modes are proagating. While there are many modes they all tend to converge to the bulk wave velocitites as seen in the dispersion curves. As frequencies increase the number of modes increases as the propagating wave lengths become smaller and smaller. In practice these are the velocities are measurable and the multiple modes in small frequency ranges actually are what make guided waves attractive

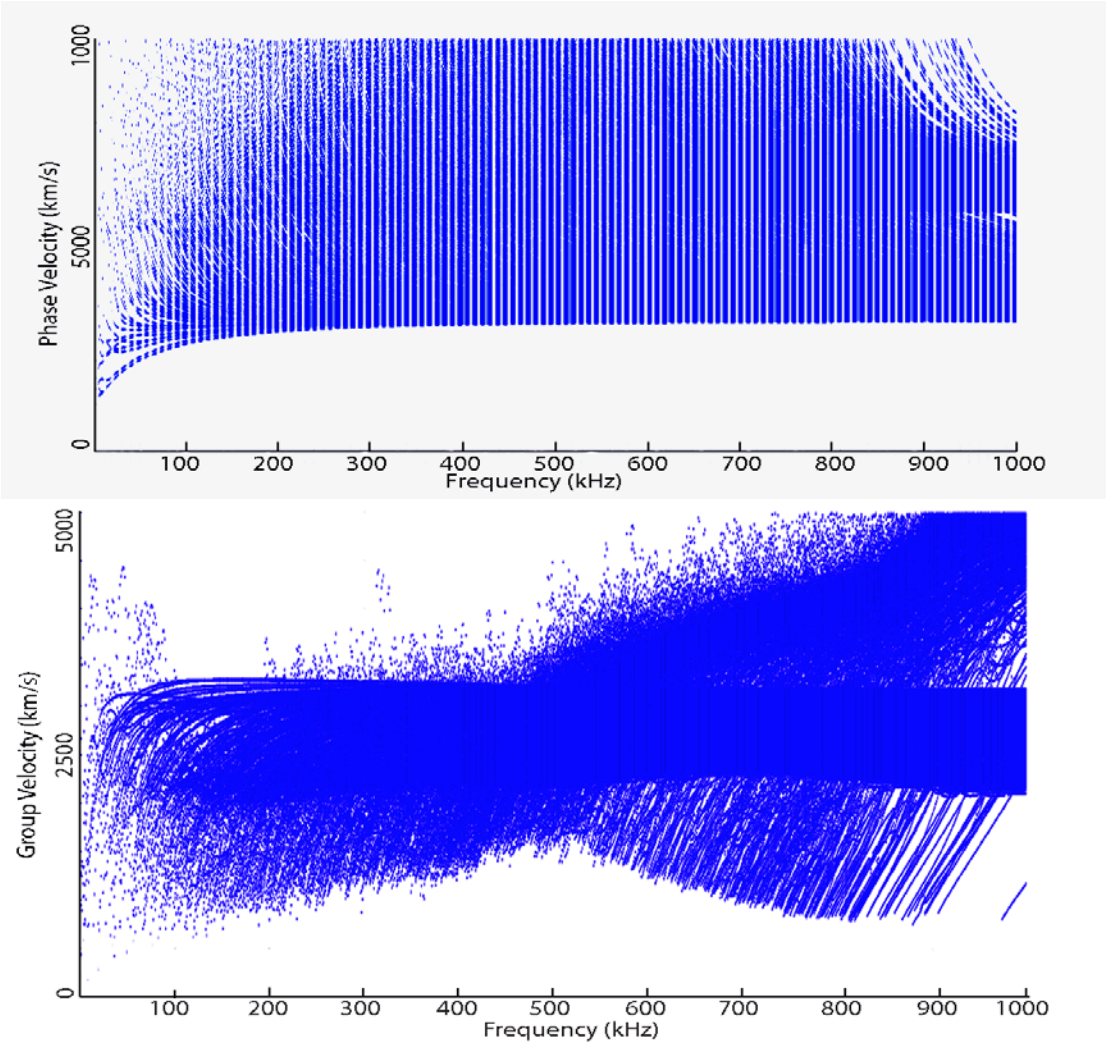

Figure 4-9: Phase and Group Velocity Dispersion Cure for 136 Rails

4.6 Mode Shapes for Defect Detection

In defect detection of the rail, the multiple modes make coverage of the entire railhead cross section possible. Modes travelling in a small velocity range at a specific frequency will have constructive and destructive interference as they interact. The

signal that is measured in a time window will be the result of this interference. By filtering to isolate certain frequency ranges there will still be several modes.

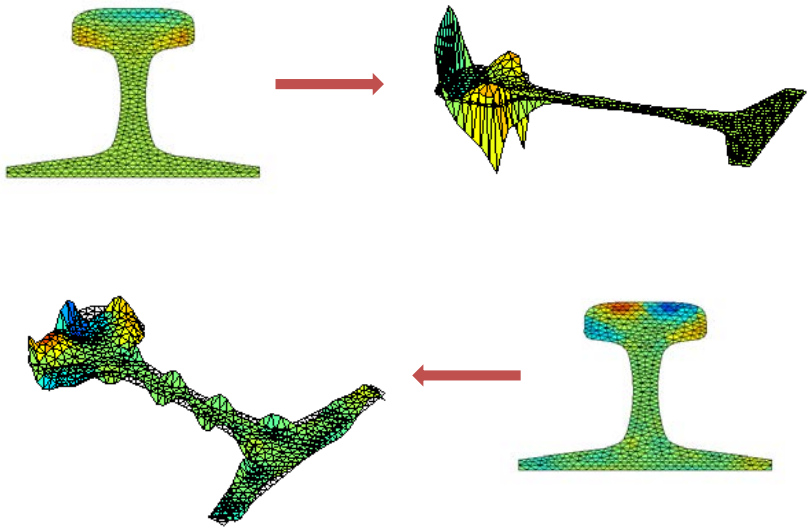

Figure 4-10: Beneficial Modes for Defect Detection in Railhead (200kHz)

For the detection of defects in the railhead, the modes that propagate with the most energy in the head cross section. Figure 4-10 is an example of two modes that propagate with the in head and give coverall to critical areas. One mode is concentrated in the bottom gauge corner where detail fractures originate. Carrying its energy in the top of the railhead the other mode would be good for the detection of Tache ovals associated with defects from manufacturing defects.

Figure 4-11 shows a pair of modes that would be inefficient in the detection of railhead defects. In both of the modes the wave energy is distributed to the web. One of the modes indicates the wave will focus the energy to the base of the head. The second mode spread the energy throughout the entire cross section covering the web and foot of

the rail. Little energy is in the head of rail which is not beneficial to evaluating the railhead.

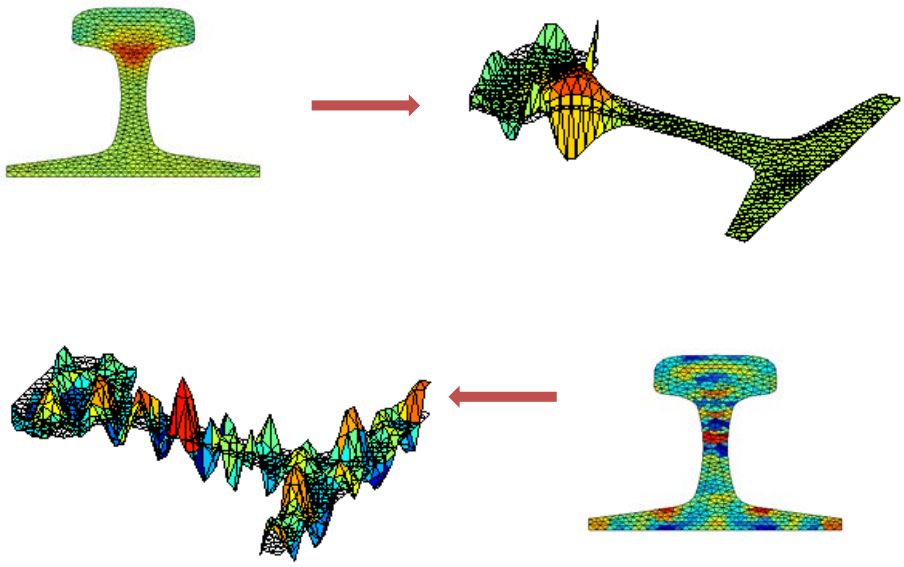

Figure 4-11: Ineffective Modes For Defect Detection for Railhead (200kHz)

While several mode are available at high frequency wave propagation not all are beneficial. The modes presented here are all found at 200 kHz and they are only four of many. Multiple wave mode propagation in the railhead make guided waves ideal for defect detection. The focus of the dissertation is concentrated on railhead defects with different acquisition set-ups other areas of the rail can be inspected.

4.7 Velocity Change for Guided Wave

In the study of asouto-elasticity the measure of stress has been widely investigated for ultrasonic bulk waves by the variations in velocity. Since the middle of the 20th century studies have been published on the asouto-elatic measure of stresses [73-76]. Egle first reported on the application of acousto-elasticity on rails[77] and more recently

by Gokhale [78].However the previous research is performed on specimens at constant temperature and has mention by Loveday [67] in guided waves temperature will have a larger effect on velocity than axail loads. In this section the effects of temperature and strains of the rail cross section to see if velocities changes are a feasible meassure for the rail neutral temperature.

In the section a simple parameter syudy is performed on the effect of strain and temperature on the velocity on the guided waves in rails. The load scenerios are use for the mechanical loads are 1000 μstrain in tension, zero strain and 1000 μstrain. Three temperatures were chosen for thethermal loading 20 ^{o}C, 65 ^{o}C and 80 ^{o}C which reflect ambient, the hieght of a hot day and an extreme that would produce a thermal load of ~900 μstrain.

In the SAFE analysis the solution is based on the longitudinal and transverse bulk wave speeds. To calculate the velocities the common 3-D wave speed equations were solved with the Young's modulus and the Shear modulus determined by the material properties found at the Engineering Toolbox website [79]. In the temperature range analyized the muduli change is essentially linear and the following equations were used to determine the bulk velocities.

$$E(T) = -68.9\frac{MPa}{^{\circ}C}T + 206GPa \qquad \textbf{4.62}$$

$$G(T) = \frac{E(T)}{2(1+\upsilon)} \qquad \textbf{4.63}$$

With Poisson's ratio (ν) taken to be 0.28 and the density (ρ) is 7932 $^{kg}/_{m^3}$. The 3-D velocity equations for the longitudinal and transverse velocities respectively are:

$$c_l = \sqrt{\frac{E(T)}{\rho}\frac{1-\upsilon}{(1+\upsilon)(1-2\upsilon)}} \qquad \textbf{4.64}$$

$$c_t = \sqrt{\frac{G(T)}{\rho}}$$

Figure 4-12 show the plots of the velocity change over temperature for (a) the longitudinal and (b) the transverse velocities.

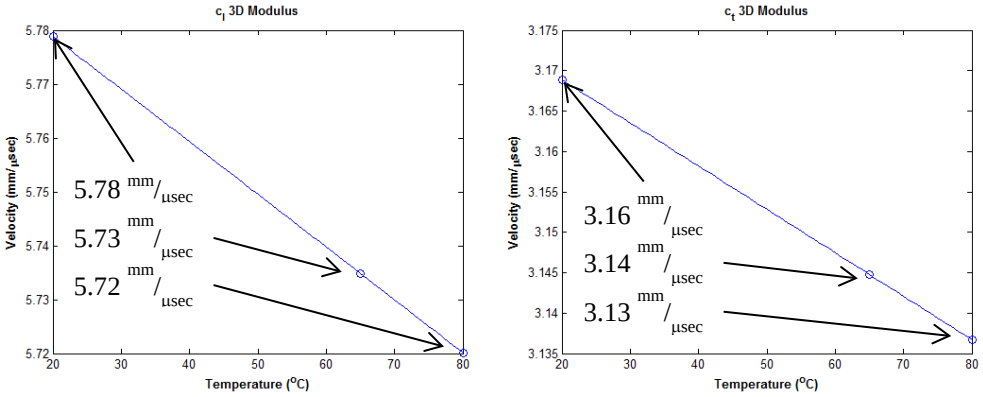

(a) Longitudinal Bulk Velocity (b) Transverse Bulk Velocity

Figure 4-12: Velocity Change with Temperature (a) Longitudinal Bulk Velocity (b) Transverse Velocity

The resulting phase velocity dispersion curves for the frequency range of 0-25kHz are shown in Figure 4-13. It is clear in the zoomed window of the velocity range 2000 $^{km}/_{sec}$ and 3000 $^{km}/_{sec}$ that the temperature loading produces a greater change in the velocity speeds. While it difficult to see in the strain loading there is a change albeit very small. The small results are seen in Figure 4-14 of the group velocity dispersion

curves over the same frequency range. In testing, it would be the group velocity that is measurable with relative ease. Measuring phase velocities require specialized and highly accurate data acquisition tools. For the temperature loading the average change

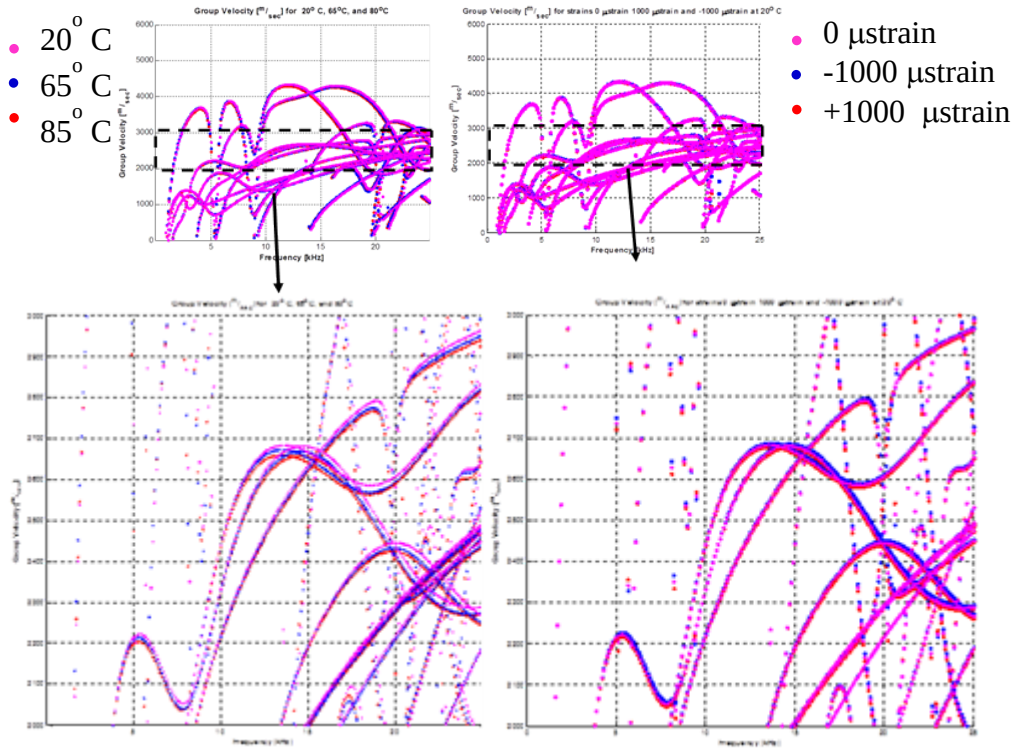

(a) Phase Velocity Temperature (b)Phase Velocity Strain Loading

Figure 4-13: Phase Velocity Dispersion Curves (a) Temperature Loading (b) Strain Loading

in velocity is ~1% while the strains produce average changes of ~0.1%. The fact that the magnitude of the temperature effect is an order of magnitude greater than the desired measure, the measure of velocity change for the determination of the rail neutral temperature is not desirable. Through this parameter study it was determined that the method would not be pursued experimentally.

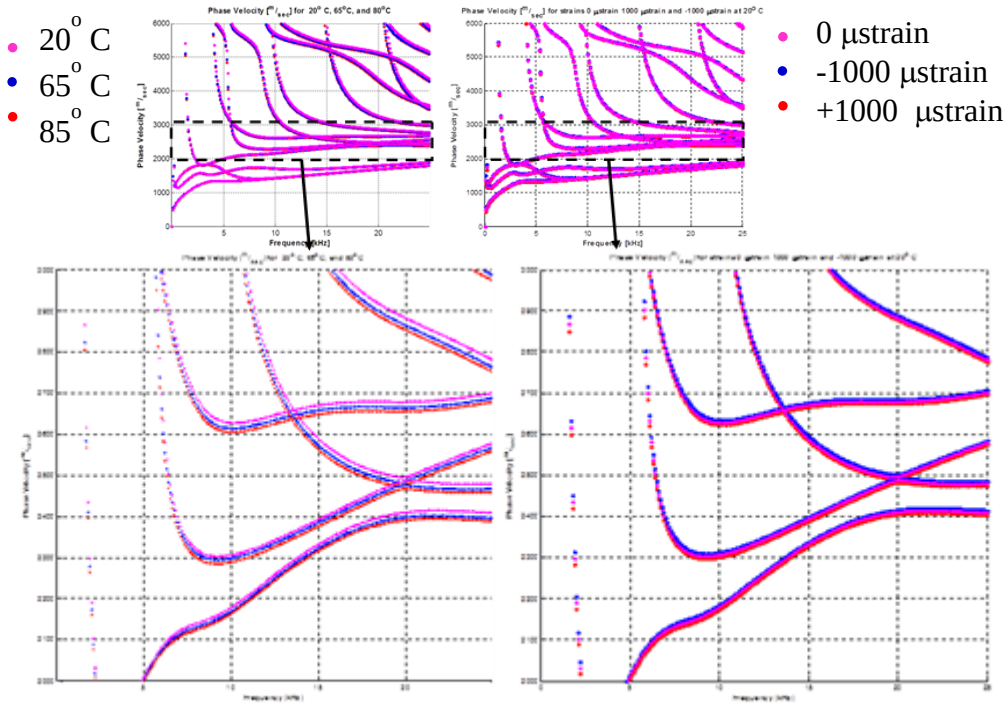

(a) Group Velocity Temperature Loading (b) Group Velocity Strain Loading

Figure 4-14: Group Velocity Dispersion Curves (a) Temperature Loading (b) Strain Loading

5. Modeling Electro Mechanical Impedance in Loaded Solids

5.1 Electro Mechanical Impedance

For several decades, piezoelectric transducers have been widely used in the field of structural health monitoring (SHM) and nondestructive evaluation (NDE) as both actuators and receivers. Lead Zirconate Titanate (PZT) is the most commonly available type of piezoceramic, which is formed into small sized patches. The PZT patches have the characteristic properties of a ceramic with a high elastic modulus, low tensile strength, and are highly durable with negligible aging. Extremely light and non-invasive PZT transducers will not have a significant influence on the dynamic function of the host structure to which it is bonded [80]. When bonded to a structure, the PZT transducer through its piezoelectric properties and electro-mechanical coupling will act as both actuator and receiver and respond to small variations of the frequency response of the host structure. Measuring the electrical impedance of the PZT gives the structure's frequency response to the PZT excitation in the method known as Electro-Mechanical Impedance (EMI).

The study of mechanical impedance for nondestructive testing dates back to 1978 with the work of Lange in the Soviet Union [81] and then the work of Lange was extended to bonded plate by Cawley in 1984 [82]. These pervious works have been extended to the use of piezoelectric materials to measure the mechanical impedance via the electrical signature of the transducer response. The Electro-Mechanical Impedance method has been widely investigated for the identification of damage in a host structure.

Giurgiutiu and Rogers [83] reported the ability of Electro-Mechanical Impedance to be implemented as a SHM method for detection of the onset of delimitations, cracks, and disbonds in composite plates. Xu et al [84] performed damage detection experiments on a plate and beam in the low frequency range. Yang et al [85] measured the propagation of damage in a plate with the Electro-Mechanical Impedance technique. Park and Inman [86] used Electro-Mechanical Impedance at high frequencies, greater than 30 kHz, to detect damage in the complex structures of a cinder block wall and frame specimen. Through these studies, the EMI method has shown potential to identify the onset and monitor the propagation of damage via changes in the resonance frequencies of the structure in a variety of structural configurations.

Annamdas and Soh [87] discussed the wide range of applications for the Electro-Mechanical Impedance techniques for structural health monitoring. The potential for stress measurements as an application for the Electro-Mechanical Impedance method has only recently been explored. In 2002, Ong et al [88] applied the EMI technique to an experiment to measure in-situ stress of a laboratory sized beam specimen. In the following decade, Annamdas et al, Annamdas and Rizzo, Yang et al, and Lim and Soh [89-92] all reported the results of their experiments to measure the loading of test specimens. In these studies, the capability of the Electro-Mechanical Impedance measurement was limited to observations and trends found in the conductance signature, which only reflects the response in the real domain of the PZT admittance.

5.2 1-D Model of Constrained Piezoelectric Wafer

The modeling of the piezoelectric system used in the Electro-Mechanical Impedance method begins with the piezoelectric transducer's interaction with the structure. When bonded to a structural element, the piezoelectric transducer is constrained by the structure and the dynamic behavior of the transducer is modified. Several studies have exploited the modification of the transducer dynamic response due structural damage and employed several modeling methods [93-98]. The common tie to all the aforementioned studies comes from the work of Giurgiutiu [99] which is followed here in the following section. In this approach the dynamic stiffness, k_{str}, constraining the piezoelectric is frequency dependent, and thus any change to the structural dynamic stiffness will affect the response of the constrained piezoelectric element.

Consider a piezoelectric wafer transducer of length l_a, width b_a, and thickness t_a constrained by a structural stiffness k_{str} as shown Figure 5-1. When the piezoelectric wafer is induced by an electric field E_3 polarized through the thickness, it will undergo a longitudinal expansion. The application of a harmonic voltage $V(t) = \hat{V}e^{i\omega t}$ between the top and bottom surface electrodes produces the electrical field. It is assumed that the electric field $E = V/t$ is uniform with respect to x_1 such that $\partial E_1/\partial x_1 = 0$.

For a piezoelectric material the constitutive equations are:

$$S_1 = s_{11}^E T_1 + d_{31} E_3 \qquad \textbf{5.1}$$

$$D_3 = d_{31} T_1 + \varepsilon_{33}^T E_3 \qquad \textbf{5.2}$$

In which S_1 is the strain, T_1 is the stress, the electrical displacement in charge per unit area is E_3, in a zero field the mechanical compliance is s_{11}^E, at a zero stress the dielectric constant is ε_{33}^T , and the mechanical strain per unit electric field or the induced strain coefficient is d_{31}.

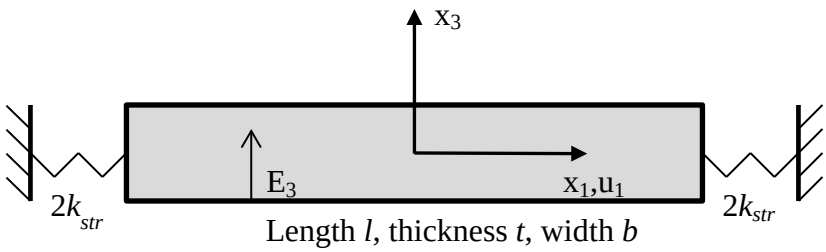

Figure 5-1: PZT wafer constrained by structural stiffness k_{str}

By bonding the piezoelectric wafer to the structural element, the wafer's motion will be constrained by the structural stiffness, k_{str}. As shown in Figure 5-1, the overall structural stiffness constrains the elastic response of the piezoelectric wafer. In the presented model, the structural stiffness that is applied is split into two equal components. The total stiffness of the two components applied to the piezoelectric wafer has a value of k_{str} such that:

$$k_{total} = \left[\left(2k_{str}\right)^{-1} + \left(2k_{str}\right)^{-1} \right]^{-1} = k_{str} \qquad \textbf{5.3}$$

The stress resultant, $T_1 b_a t_a$, and spring reaction force, $2k_{str}u_1$, define the boundary conditions of the piezoelectric wafer response in which:

$$T_1\left(\frac{1}{2}l_a\right)b_a t_a = -2k_{str}u_1\left(\frac{1}{2}l_a\right)$$
$$T_1\left(-\frac{1}{2}l_a\right)b_a t_a = 2k_{str}u_1\left(-\frac{1}{2}l_a\right) \quad \textbf{5.4}$$

Consistency of the sign convention is held with the choice of where + and – are place in equation 5.4. Now recall the stress-displacement relationship:

$$S_1 = u' = \frac{\partial u_1}{\partial x_1} \quad \textbf{5.5}$$

The boundary conditions are redefined in terms of displacements and the imposed electric field by substituting equations 5.1 and 5.5 into equation 5.4 giving:

$$u_1'\left(+\frac{1}{2}l_a\right)b_a t_a + \frac{s_{11}^E}{bt}u_1\left(\frac{1}{2}l_a\right) = d_{31}E_3$$
$$u_1'\left(-\frac{1}{2}l_a\right)b_a t_a + \frac{s_{11}^E}{bt}u_1\left(\frac{1}{2}l_a\right) = d_{31}E_3 \quad \textbf{5.6}$$

The quasi-static stiffness of the piezoelectric wafer (PWAS) can be represented as

$$k_{\text{PWAS}} = \frac{A_a}{s_{11}^E l_a} \quad \textbf{5.7}$$

A stiffness ratio of the piezoelectric to the structure is defined as:

$$r = \frac{k_{str}}{k_{\text{PWAS}}} \quad \textbf{5.8}$$

Thus equation 5.6 can be rewritten as:

$$u_1'\left(+\frac{1}{2}l_a\right)b_a t_a + \frac{r}{\frac{1}{2}l_a}u_1\left(\frac{1}{2}l_a\right) = d_{31}E_3$$
$$u_1'\left(-\frac{1}{2}l_a\right)b_a t_a + \frac{r}{\frac{1}{2}l_a}u_1\left(\frac{1}{2}l_a\right) = d_{31}E_3 \qquad \textbf{5.9}$$

5.2.1 Mechanical Response

The axial wave equation is obtained by applying Newton's law of motion, $T_1' = \rho\ddot{u}$, and the strain-displacement relation $S_1 = u'$ to equation 5.1:

$$\ddot{u}_1 = c_a^2 u_1'' \qquad \textbf{5.10}$$

such that $\dot{u} = \partial u/\partial t$, $u' = \partial u/\partial x$ and the piezoelectric material wave speed is $c_a^2 = 1/\rho s_{11}^E$. A general solution to equation 5.10 is

$$u_1(x,t) = \hat{u}_1(x)e^{i\omega t} \qquad \textbf{5.11}$$

where

$$\hat{u}_1(x) = C_1 \textbf{sin}\,\kappa x + C_2 \textbf{cos}\,\kappa x \qquad \textbf{5.12}$$

The constants C_1 and C_2 are determined by the boundary conditions with the parameter $\kappa = \omega/c_a$ being the wavenumber. A linear system in C_1 and C_2 is the result of substituting the general solution of equation 5.8 into the boundary conditions of equation 5.6 as follows:

$$\frac{1}{2}\kappa l\left(\textbf{cos}\frac{1}{2}\kappa l + r\,\textbf{sin}\frac{1}{2}\kappa l\right)C_1 + \left(-\frac{1}{2}\kappa l\,\textbf{sin}\frac{1}{2}\kappa l + r\,\textbf{cos}\frac{1}{2}\kappa l\right)C_2 = \frac{1}{2}l\cdot d_{31}E_3$$
$$\frac{1}{2}\kappa l\left(\textbf{cos}\frac{1}{2}\kappa l + r\,\textbf{sin}\frac{1}{2}\kappa l\right)C_1 + \left(+\frac{1}{2}\kappa l\,\textbf{sin}\frac{1}{2}\kappa l - r\,\textbf{cos}\frac{1}{2}\kappa l\right)C_2 = \frac{1}{2}l\cdot d_{31}E_3 \qquad \textbf{5.13}$$

By substitution of the notation $u_{\mathrm{ISA}} = d_{31}\bar{E}_3 l$ and $\phi = \frac{1}{2}\kappa l$, the linear system in C_1 and C_2 is simplified to:

$$\begin{aligned}(\phi\cos\phi + r\sin\phi)C_1 - (\phi\sin\phi - r\cos\phi)C_2 &= \frac{1}{2}u_{\mathrm{ISA}} \\ (\phi\cos\phi + r\sin\phi)C_1 + (\phi\sin\phi - r\cos\phi)C_2 &= \frac{1}{2}u_{\mathrm{ISA}}\end{aligned} \qquad \textbf{5.14}$$

The solution is obtained by first subtracting the first equation from the second and assuming that the determinant of the system is nonzero, $\Delta \neq 0$, resulting in:

$$2(\phi\sin\phi - r\cos\phi)C_1 = 0 \qquad \textbf{5.15}$$

Therefore C_2=0 and, by the addition of the two equation:

$$(\phi\cos\phi + r\sin\phi)C_1 = \frac{1}{2}u_{\mathrm{ISA}} \qquad \textbf{5.16}$$

Thus the solution for the constants results in

$$C_1 = \frac{1}{2}u_{ISA}\frac{1}{\phi\cos\phi + r\sin\phi}, C_2 = 0 \qquad \textbf{5.17}$$

Then, substituting C_1 and C_2 into equation 5.12 yields the displacement solution

$$\hat{u}_1(x) = \frac{1}{2}u_{\mathrm{ISA}}\frac{\sin\kappa x}{\phi\cos\phi + r\sin\phi} \qquad \textbf{5.18}$$

Rewriting equation 5.18 by substituting $\phi = \frac{1}{2}\kappa l$,

$$\hat{u}_1(x) = \frac{1}{2}u_{\mathrm{ISA}}\frac{\sin\kappa x}{\frac{1}{2}\kappa l\cos\frac{1}{2}\kappa l + r\sin\frac{1}{2}\kappa l} \qquad \textbf{5.19}$$

5.2.2 Electrical Response

The electrical response of the constrained piezoelectric wafer shown in Figure 5-2 is considered next.

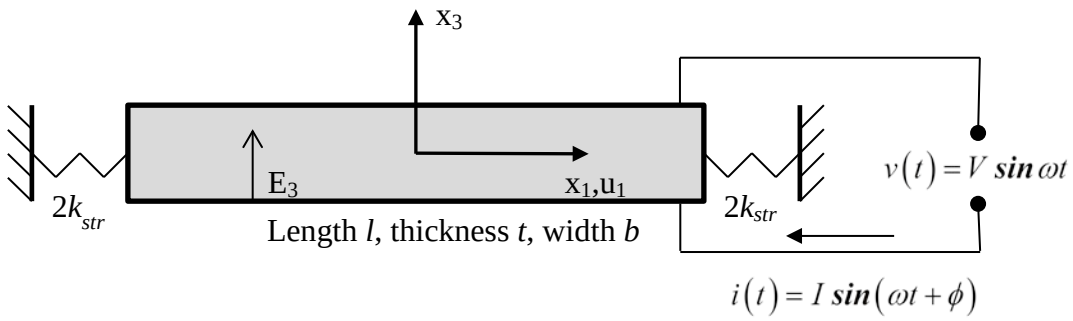

Figure 5-2: Schematic of electrical response of constrained piezoelectric wafer

Recall the electrical displacement expressed in equation 5.2:

$$D_3 = d_{31}T_1 + \varepsilon_{33}^{T}E_3 \qquad \textbf{5.20}$$

The stress as a function of strain and electric field is determined from equation 5.1.

$$T_1 = \frac{1}{s_{11}^{E}}\left(S_1 - d_{31}E_3\right) \qquad \textbf{5.21}$$

Therefore the electrical displacement is conveyed as

$$D_3 = \frac{d_{31}}{s_{11}^{E}}\left(S_1 - d_{31}E_3\right) + \varepsilon_{33}^{\mathrm{T}}E_3 \qquad \textbf{5.22}$$

By substituting the result of equation 5.22 into equation 5.1, the strain-displacement relation becomes

$$D_3 = \varepsilon_{33}^{\mathrm{T}} E_3 \left[1 - k_{31}^2 \left(1 - \frac{u'}{d_{31} E_3} \right) \right] \qquad \textbf{5.23}$$

where the electromechanical coupling coefficient is $k_{31}^2 = d_{31}^2 \big/ \left(s_{11}^E \varepsilon_{33}^{\mathrm{T}} \right)$. By integrating over the electrode areas $A=bl$, equation 5.23 yields the total charge. Now equation 5.2 can be re-expressed as:

$$D_3 = \frac{d_{31}}{s_{11}^E} \left(u_1' - d_{31} E_3 \right) + \varepsilon_{33}^{\mathrm{T}} E_3 = \varepsilon_{33}^{\mathrm{T}} E_3 \left[1 + k_{31}^2 \left(\frac{u_1'}{d_{31} E_3} - 1 \right) \right] \qquad \textbf{5.24}$$

The total charge can be determined by integrating equation 5.24 over the area of the piezoelectric wafer, giving the result:

$$Q = \int_{-\frac{l_a}{2}}^{+\frac{l_a}{2}} \int_{-\frac{l_a}{2}}^{+\frac{l_a}{2}} D_3 dx dy = \varepsilon_{33}^{\mathrm{T}} \frac{b_a l_a}{t_a} V \left[1 + k_{31}^2 \left(\frac{1}{l_a} \frac{1}{d_{31} E_3} u_1 \Big|_{-\frac{1}{2}l}^{\frac{1}{2}l} - 1 \right) \right] \qquad \textbf{5.25}$$

With the assumption that there is a harmonic time dependence $\left(\bar{Q} = Q e^{i\omega t}, \text{etc.} \right)$, the total charge is written:

$$\bar{Q} = C \bar{E}_3 \left\{ 1 + k_{31}^2 \left(\frac{1}{l_a} \frac{1}{d_{31} \bar{E}_3} \left[\hat{u}_1 \left(\frac{1}{2} l \right) - \hat{u}_1 \left(-\frac{1}{2} l \right) \right] - 1 \right) \right\} \qquad \textbf{5.26}$$

with the conventional stress-free capacitance of the piezoelectric wafer C is

$$C = \varepsilon_{33}^{\mathrm{T}} \frac{b_a l_a}{t_a} \qquad \textbf{5.27}$$

Applying to equation 5.26 the definitions $u_{\mathrm{ISA}} = d_{31} \bar{E}_3 l$ and $\bar{V} = \bar{E}_3 \big/ t_a$ gives:

$$\hat{Q} = C\hat{V}\left[1 - k_{31}^2 + k_{31}^2\left(\frac{\hat{u}_1\left(\frac{1}{2}l\right) - \hat{u}_1\left(-\frac{1}{2}l\right)}{u_{\mathrm{ISA}}}\right)\right] \qquad \textbf{5.28}$$

By taking the time derivative of the electric charge the electric current is obtained:

$$I = \dot{Q} = i\omega Q \qquad \textbf{5.29}$$

Then,

$$\hat{I} = i\omega C\hat{V}\left[1 - k_{31}^2 + k_{31}^2\left(\frac{\hat{u}_1\left(\frac{1}{2}l\right) - \hat{u}_1\left(-\frac{1}{2}l\right)}{u_{\mathrm{ISA}}}\right)\right] \qquad \textbf{5.30}$$

Now the admittance, *Y*, which is defined as the ratio of the current to the voltage, is

$$Y = \frac{\hat{I}}{\hat{V}} = i\omega C\left[1 - k_{31}^2 + k_{31}^2\left(\frac{\hat{u}_1\left(\frac{1}{2}l\right) - \hat{u}_1\left(-\frac{1}{2}l\right)}{u_{\mathrm{ISA}}}\right)\right] \qquad \textbf{5.31}$$

Remembering the displacement solution in equation 5.18

$$\hat{u}_1(x) = \frac{1}{2}u_{\mathrm{ISA}}\frac{\boldsymbol{\sin}\,\kappa x}{\phi\,\boldsymbol{\cos}\,\phi + r\,\boldsymbol{\sin}\,\phi} \qquad \textbf{5.32}$$

The $\hat{u}_1$ term in equation 5.31 becomes

$$\hat{u}_1\left(\frac{1}{2}l\right) - \hat{u}_1\left(-\frac{1}{2}\right) = \frac{1}{2}\frac{\boldsymbol{\sin}\frac{1}{2}\kappa l - \left(-\boldsymbol{\sin}\frac{1}{2}\kappa l\right)}{\phi\,\boldsymbol{\cos}\,\phi + r\,\boldsymbol{\sin}\,\phi} = \frac{1}{2}2\frac{\boldsymbol{\sin}\,\phi}{\phi\,\boldsymbol{\cos}\,\phi + r\,\boldsymbol{\sin}\,\phi} = \frac{1}{r + \phi\,\boldsymbol{\cot}\,\phi} \qquad \textbf{5.33}$$

In which the notation $\phi = \frac{1}{2}\gamma l$ was used. Substituting 5.33 in to 5.31 results in

$$Y = \frac{\hat{I}}{\hat{V}} = i\omega C\left(1 - k_{31}^2 + k_{31}^2 \frac{1}{r + \phi \cot \phi}\right) \qquad \textbf{5.34}$$

Conversely, the impedance, *Z*, defined as the ratio of voltage to current is:

$$Z = \frac{\hat{V}}{\hat{I}} = \frac{1}{i\omega C}\left(1 - k_{31}^2 + k_{31}^2 \frac{1}{r + \phi \cot \phi}\right)^{-1} \qquad \textbf{5.35}$$

5.2.3 Electro Mechanical Impedance Behavior

The effect of the piezoelectric coupling between mechanical and electrical variable modifies the pure imaginary response that consists of a capacitive admittance $i\omega C$. The structural stiffness ratio, *r*, in equations 5.34 and 5.35 is additive to the piezoelectric wafer response resonance term $\phi \cot \phi$. Since the structural stiffness k_{str} is frequency dependent, the apparent structural stiffness will pass through zero at structural resonances and extreme values at anti-resonances as the piezoelectric wafer is used in a frequency sweep. In both the admittance and impedance equations it is implied that structural and piezoelectric wafer resonances will be reflected across the frequency spectra.

The expected structural response is either known from previous investigation or easily calculated from simple analysis of the asymptotic behavior of the electro-mechanical impedance measures. When the structural stiffness k_{str} =0 such that r=0, the impedance response will reflect the response of a unconstrained piezoelectric wafer. Applying this to equations 5.34 and 5.35, it is noted that the stiffness ratio *r* in the denominator will disappear and the following is obtain:

$$Y_{free} = i\omega C\left[1-k_{31}^2\left(1-\frac{1}{\phi\,\boldsymbol{cot}\,\phi}\right)\right]$$
$$Z_{free} = \frac{1}{i\omega C}\left[1-k_{31}^2\left(1-\frac{1}{\phi\,\boldsymbol{cot}\,\phi}\right)\right]^{-1} \qquad \textbf{5.36}$$

The resulting equations of the admittance and impedance are the expressions for a free piezoelectric wafer. Conversely, when the structural stiffness $k_{str} \to \infty$ such that $r \to \infty$, the response is that of a fully constrained piezoelectric wafer. In this case the stiffness ratio, r, in the denominator of the admittance and impedance expressions vanishes, giving the result:

$$Y_{fixed} = i\omega C\left(1-k_{31}^2\right)$$
$$Z_{fixed} = \frac{1}{i\omega C}\left(1-k_{31}^2\right)^{-1} \qquad \textbf{5.37}$$

These are the expressions for a fully constrained or blocked piezoelectric wafer.

Consider a piezoelectric wafer bonded to a 1-D structural, such as a beam or railroad rail. The wafer has a length l_a bounded by the points x_a and x_a+$l_a$as shown in Figure 5-3a. When excited by an electric field, the piezoelectric will expand by the strain ε_a. The strain will impose a force F_a on the beam and an equal and opposing reaction force from the beam will be acted upon the piezoelectric wafer as shown in Figure 5-3b. Along the neutral axis, the excitation is felt as an axial excitation N_a and a bending moment excitation M_a. Elastic waves are induced in the beam structure from a

5.3.1 Analysis of Piezoelectric Wafer Bonded on 1D Beam

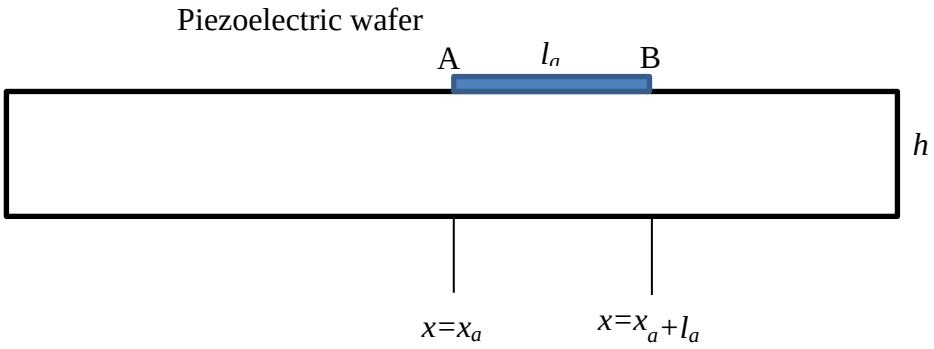

(a) Beam/Piezoelectric Geometry

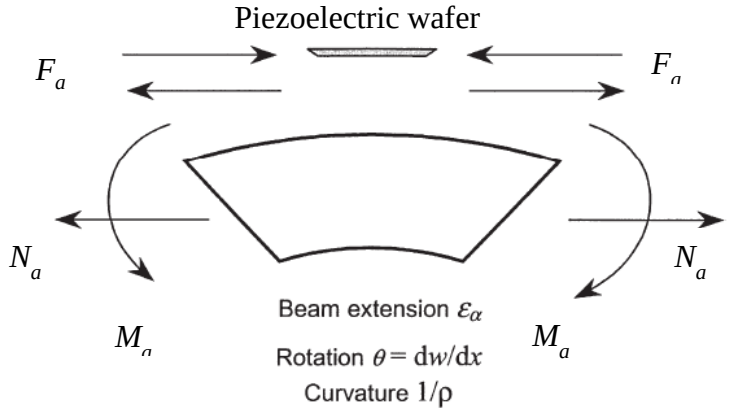

(b) Resultant Forces and Moments

Figure 5-3: Beam and Bonded Piezoelectric Wafer Interaction (a)Beam/Piezoelectric Geometry (b) Resultant Forces and Moments

high-frequency harmonic electric excitation induced on the piezoelectric wafer. The structure oscillates at the piezoelectric wafer excitation frequency in a steady-state regime. The internal state of the structure, excitation frequency, and boundary conditions all effect the force per unit displacement (dynamic stiffness) presented by the structure to the piezoelectric wafer.

$$k_{str}(\omega) = \frac{\hat{F}_a(\omega)}{\hat{u}_a(\omega)} \quad \textbf{5.38}$$

such that $\hat{u}_a(\omega)$ is the displacement amplitude at frequency ω, $\hat{F}_a(\omega)$ is the reaction force , and $k_{str}(\omega)$ is the structural dynamic stiffness. The complex amplitude of a time-varying function is represented by the ˆ symbol. Considering that the piezoelectric wafer is very small in size with respect to the structure, k_{str} is the point-wise dynamic stiffness.

5.3.1 Excitation Forces and Moments

From the piezoelectric wafer force, $F_a = \hat{F}_a e^{i\omega t}$, the excitation forces and moments are determined using the beam cross-section geometry:

$$M_a = F_a \frac{h}{2}, \quad N_a = F_a \quad \textbf{5.39}$$

Using the Heavyside function, $H(x - x_a) = 0$, defined as $H(x - x_a) = 0$ for $x < x_a$, and $H(x - x_a) = 1$ for $x_a \le x$, to express the space-wise distribution of the excitation bending moment and axial force:

$$N_e(x,t) = N_a\left[-H(x - x_a) + H(x - x_a - l_a)\right]e^{i\omega t} \quad \textbf{5.40}$$

$$M_e(x,t) = -M_a\left[-H(x - x_a) + H(x - x_a - l_a)\right]e^{i\omega t} \quad \textbf{5.41}$$

Equation 5.40 corresponds to the axial vibrations and equation 5.41 to the flexural vibrations.

5.3.2 PZT Axial Vibrations

The equation of motion for axial vibrations is:

$$\rho A\ddot{u}(x,t) - EAu''(x,t) = N_e'(x,t) \quad \textbf{5.42}$$

Substituting equation 5.40 into equation 5.42 results in

$$\rho A\ddot{u}(x,t) - EAu''(x,t) = \hat{N}_a\left[-\delta(x-x_a) + \delta(x-x_a-l_a)\right]e^{i\omega t} \quad \textbf{5.43}$$

such that δ is the Dirac function. A modal expansion is assumed as:

$$u(x,t) = \sum_{n=0}^{\infty} C_n X_n(x) e^{i\omega t} \quad \textbf{5.44}$$

where $X_n(x)$ are the orthonormal mode shapes and C_n are the modal amplitudes.

The free-vibration differential equation to satisfy the mode shapes is:

$$EAX_n'' + \omega^2 \rho A X_n = 0 \quad \textbf{5.45}$$

Integration over the length of the beam after multiplication by $X_n(x)$ gives:

$$C_n = \frac{1}{\omega_n^2 - \omega^2} \cdot \frac{\hat{N}_a}{\rho A}\left[-X(x_a) + X(x_a + l_a)\right] \quad \textbf{5.46}$$

The axial vibration response is then

$$u(x,t) = \frac{\hat{N}_a}{\rho A}\sum_{n=0}^{\infty} \frac{-X_n(x_a) + X_n(x_a + l_a)}{\omega_n^2 - \omega^2} X_n(x) e^{i\omega t} \quad \textbf{5.47}$$

5.3.3 PZT Flexural Vibrations

The equation of motion under a moment excitation for a Euler-Bernoulli beam is

$$\rho A\ddot{w}(x,t) + EIw''''(x,t) = -M_e''(x,t) \quad \textbf{5.48}$$

Substituting equation 5.41 into equation 5.48 results in:

$$\rho A\ddot{w}(x,t)+EIw''''(x,t)=\bar{M}_a\left[-\delta'(x-x_a)+\delta'(x-x_a-l_a)\right]e^{i\omega t} \qquad \textbf{5.49}$$

Here δ' is the first derivative of the Dirac function $(\delta'=H'')$. A modal expansion is assumed as:

$$w(x,t)=\sum_{n=N_1}^{N_2} C_n X_n(x)e^{i\omega t} \qquad \textbf{5.50}$$

where $X_n(x)$ are the orthonormal bending mode shapes that satisfy the free-vibration differential equation:

$$EIX_n''''=\omega_n^2\rho A X_n \qquad \textbf{5.51}$$

Integration over the length of the beam after multiplication by $X_n(x)$ gives:

$$C_n=\frac{1}{\omega_n^2-\omega^2}\frac{\bar{M}_a}{\rho A}\int_0^l X_n(x)\left[\delta'(x-x_a)-\delta'(x-x_a-l_a)\right]dx \qquad \textbf{5.52}$$

Substituting the integration by parts of equation 5.52 into the modal expansion in equation 5.50 results in

$$C_n=-\frac{1}{\omega_n^2-\omega^2}\frac{\bar{M}_a}{\rho A}\left[-X_n'(x_a)+X_n'(x_a+l_a)\right] \qquad \textbf{5.53}$$

Therefore the flexural vibration response is

$$w(x,t)=-\frac{\bar{M}_a}{\rho A}\sum_{n=1}^{\infty}\frac{-X_n'(x_a)+X_n'(x_a+l_a)}{\omega_n^2-\omega^2}\cdot e^{i\omega t} \qquad \textbf{5.54}$$

5.2.4 Frequency Response Function And Dynamic Structural Stiffness Of PZT

By calculating the elongation between the two points A and B connected to the piezoelectric wafer ends, one obtains the dynamic structural stiffness $k_{str}(\omega)$ imposed on the piezoelectric wafer by the structural element. The horizontal displacement of a generic point P on the surface of a beam is determined by the kinematic analysis of the displacement in terms of the axial and flexural displacements as:

$$u_{\mathrm{P}} = u(x) - \frac{h}{2} w'(x) \qquad \textbf{5.55}$$

(a)

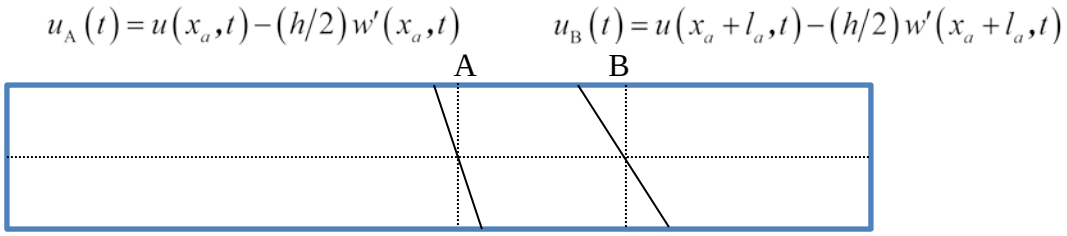

(b)

Figure 5-4: Total Horizontal Displacement u_p by Superposition of Axial and Flexural Displacements (a) Displacement components at the Neutral Axis (b) Horizontal Displacements of Points A and B

such that *u* and *w* are the axial and flexural displacement at the neutral axis, see Figure 5-4.

Considering P as the points A and B, the taking the difference yields:

$$u_{PZT} = u_{\mathrm{B}}(t) - u_{\mathrm{A}}(t) = u(x_a, t) - u(x_a + l_a, t) - \frac{h}{2}\left[w'(x_a, t) - w'(x_a + l_a, t)\right] \qquad \textbf{5.56}$$

The total vibration response is given by substituting equations 5.47 and 5.54 into equation 5.56, resulting in:

$$\hat{u}_{PZT} = \frac{\hat{F}_{PZT}}{\rho A}\left\{\sum_{n_a}\frac{\left[U_{n_a}(x_a + l_a) - U_{n_a}(x_z)\right]^2}{\omega_{n_a}^2 - \omega^2} + \left(\frac{h}{2}\right)^2 \sum_{n_a}\frac{\left[W'_{n_w}(x_a + l_a) - W'_{n_w}(x_z)\right]^2}{\omega_{n_w}^2 - \omega^2}\right\} \qquad \textbf{5.57}$$

using $n_a, \omega_{n_a}, U_{n_a}(x)$ and $n_w, \omega_{n_w}, U_{n_w}(x)$ to distinguish the axial, flexural vibration frequencies and modes shapes, respectively. The structural frequency response function to a single-input single-output excitation applied to the piezoelectric wafer is obtained by dividing equation 5.57 by $\hat{F}_{PZT}$. The total frequency response function is then expressed as:

$$\hat{u}_{PZT} = \frac{1}{\rho A}\left\{\sum_{n_a}\frac{\left[U_{n_a}(x_a + l_a) - U_{n_a}(x_z)\right]^2}{\omega_{n_a}^2 - \omega^2} + \left(\frac{h}{2}\right)^2 \sum_{n_a}\frac{\left[W'_{n_w}(x_a + l_a) - W'_{n_w}(x_z)\right]^2}{\omega_{n_w}^2 - \omega^2}\right\} \qquad \textbf{5.58}$$

The structural dynamic compliance of the piezoelectric wafer modal sensor bonded on the structural element is the same as the single-input single-output frequency response function. The inverse of the structural compliance if the structural dynamic stiffness and then:

$$k_{PZT}(\omega)=\frac{\hat{F}_{PZT}}{\hat{u}_{PZT}}=\rho A\left\{\begin{array}{l}\displaystyle\sum_{n_a}\frac{\left[U_{n_a}(x_a+l_a)-U_{n_a}(x_z)\right]^2}{\omega_{n_a}^2-\omega^2}\\ \displaystyle+\left(\frac{h}{2}\right)^2\sum_{n_a}\frac{\left[W'_{n_w}(x_a+l_a)-W'_{n_w}(x_z)\right]^2}{\omega_{n_w}^2-\omega^2}\end{array}\right\}^{-1} \quad \textbf{5.59}$$

The axial and flexural mode shapes of the structural element are then determined by the dynamic analysis of the element based on the boundary conditions.

5.2.5 Mechanical Impedance and Dynamic Structural Stiffness of Structure

Through the mechanical impedance of the element the ratio of the piezoelectric wafer and the structural element dynamic stiffness is determined Considering frequency-dependent displacement amplitude

$$\hat{u}(\omega)=\frac{\hat{F}}{-\omega^2+i2\zeta\omega_n\omega+\omega_n^2} \quad \textbf{5.60}$$

such that $\omega_n^2=\frac{k}{m}$ are the natural frequency and $\hat{f}=\frac{\hat{F}}{m}$ is the dynamic force amplitude.

The dynamic frequency-dependent stiffness of the structure is defined as:

$$k_{dyn}=-\omega^2 m+ic\omega+k \quad \textbf{5.61}$$

Then equation 5.60 can be viewed as the force and the frequency-dependent dynamic stiffness of a single of degree system:

$$\hat{u}(\omega)=\frac{\hat{F}}{k_{dyn}} \quad \textbf{5.62}$$

Defined as the ratio between the excitation force and the velocity response, the mechanical impedance can be developed in a similar manner. The velocity response is:

$$\dot{u}(t) = i\omega u(t) \quad \textbf{5.63}$$

Equation 5.60 can be rearranged considering that amplitude of equation 5.63 as $\hat{\dot{u}} = i\omega\hat{u}$ then:

$$\hat{\dot{u}} = i\omega\frac{\hat{F}}{-\omega^2 m + ic\omega + k} = \frac{\hat{F}}{i\omega m + c + \frac{k}{i\omega}} \quad \textbf{5.64}$$

Considering the mechanical impedance of a signal of degree system $Z(\omega)$ defined as:

$$Z(\omega) = i\omega m + c + \frac{k}{i\omega} \quad \textbf{5.65}$$

the dynamic stiffness of the structural element is:

$$k_{str} = Z(\omega) = \frac{\hat{F}}{\hat{\dot{u}}} \quad \textbf{5.66}$$

6. Experimental Testing of Flaw Detection

6.1 Prototype Current Deployment

This chapter describes the current configuration of a rail inspection prototype that has been designed at the Non Destructive Evaluation & Structural Health Monitoring lab of the University of California, San Diego. Details of the development have been presented in multiple technical reports submitted to the Federal Railroad Administration and papers [100-106]. The majority of the last section of this chapter was presented in the most recent technical report to the Federal Railroad Administration in 2010 [107]. The prototype design has grown from rudimentary laboratory tests to a field deployable system. Blind testing of the current system has shown the good potential of the prototype in finding internal rail defects. The basic layout of the six major hardware components of the prototype is displayed in Figure 6-1. At the heart of the system is a National Instruments© PXI chassis and CPU running the National Instruments© Real Time LabView© operating system. The Real Time chassis is employed as the server in a client Ethernet-linked platform. Operator interface is through a laptop running LabView©. The laptop is an interface to the Real Time system that executes all the computation, data acquisition, timing, hardware control tasks. Data storage of all the acquired signals is store in an additional National Instruments© PXI chassis running a Windows© operating system. The on board positioning system of the support vehicle interfaces with the Real Time chassis via a counter/counter module. Laser control and diagnostics communicate via the Real Time chassis' serial (RS 232) port. The Real

Time chassis with multiple analog input/output modules digitizes the received signals from the air-coupled transducer. More details of the system are discussed in the following sections of this chapter.

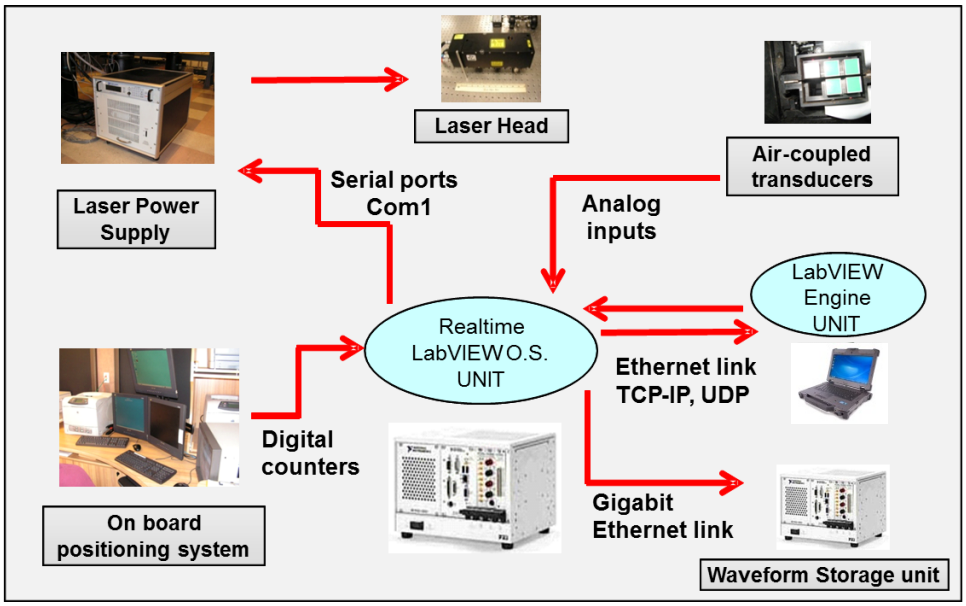

Figure 6-1: Hardware Layout of the Hybrid Laser/Aircouple System

6.1.1 Hardware Layout

In order to handle the environmental conditions expected in the field, a rugged laser was need for installation on the Federal Railroad Administration R-4 research Hy-Railer vehicle. The Quantel DRL laser chosen, for its capabilities to fulfill the following requirements:

- Rugged power supply that is rack mountable
- Rugged laser head for vertical and horizontal mounting
- Flash with repetition rate greater than 100 Hz

- Adjustability of the emission power
- Serial port external triggering

Figure 6-2: Quantel DRL Laser Head Unit

Table 6.1: Quantel DRL Specifications

Source Power	208/240 VAC 3-phase
Repetition Rate (Hz)	120
Energy (mJ)	200
Pulsewidth (nsec)	8.5
Divergence (mrads)	6.5
Rod Diameter (mm)	4.3
Beam Point Stability (±%)	100
Jitter (±ns)	0.5
Energy stability (±%)	2.5
Laser Head Mounting	Horizontal-Vertical
Laser Head Dimensions (W x H x D)	9.3” x 4” x 15.7”

Table 6.1 contains the specifications for the Quantel DRL laser.

The acting/sensing hardware components are arranged in a mounting shoe that attaches to a cart towed by the R-4 Hy-Railer in the layout shown in Figure 6-3. Within the costume shoe frame, the following elements are mounted (1) the laser head, (2) the

laser optics, and (3) the air coupled transducers. Figure 6-4 shows the actual shoe mounted to the cart out in the field.

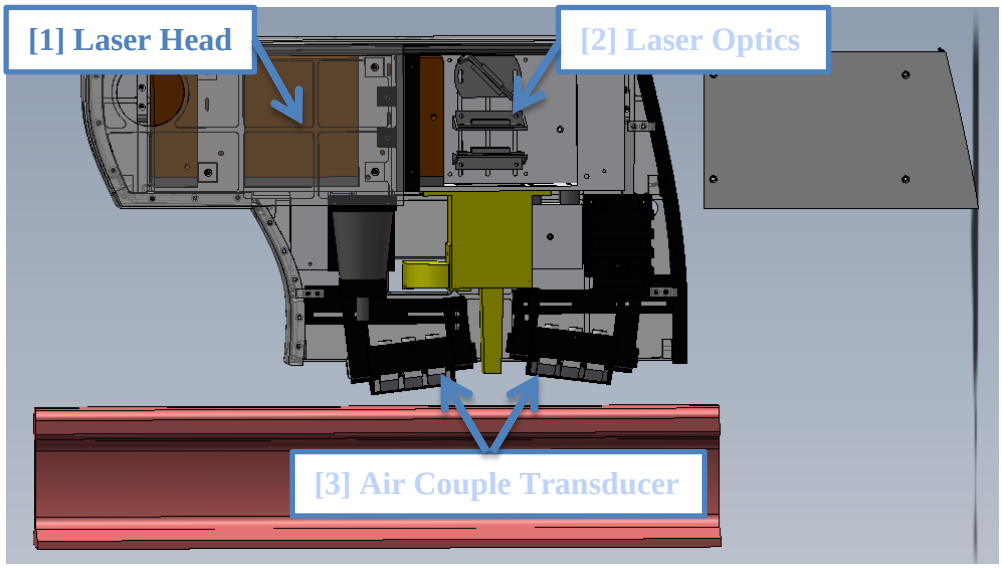

Figure 6-3: Rail Inspection Prototype Shoe Components

Figure 6-4: Rail Inspection Prototype Shoe and Cart

To interfaces between the electronic hardware in the shoe and the controls and data acquisition systems are done in different manners based on the component and purpose. A multi-conductor cable provided by the manufacturer does linking the laser

head to the laser controller. The laser head requires cooling, which is done by a cold water line from the output of a water to water chiller and the heated water from the laser head is returned to the chiller

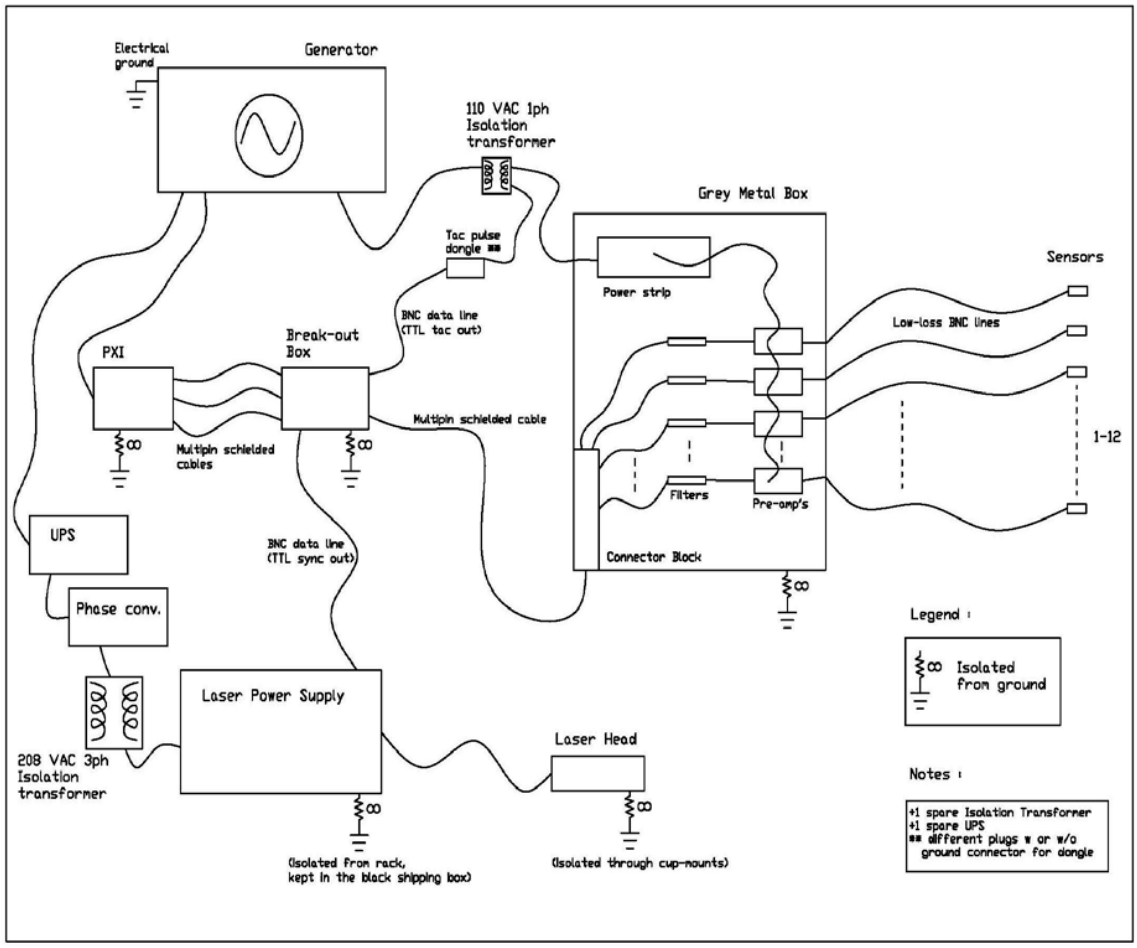

Figure 6-5: Electrical Wiring Scheme of Prototype

Figure 6-5 shows the schematic of the electrical wiring of the prototype. The support contactor ENSCO Inc. took responsibility for the electrical power source on the Federal Railroad Administration's R-4 Hy-Railer. A single phase generator was installed on the R-4 and a phase converter was used to meet the requirement of three

phase power for the laser power supply. In addition to the phase converter, an uninterrupted power supply was provided to protect the laser power supply against hot fire ups and voltage drains if the generator were fail. Isolation transformers were provided to all the components to limit electrical noise in the grounding circuit. While the electrical power source was the responsibility of ENSCO Inc., the NDE/SHM Laboratory group took the responsibility in the design of components to interface the positioning and ultrasonic signal to the prototype's CPU's.

Figure 6-6: Weatherproof NEMA Box for Outboard Analog Electronics

In order to connect the ultrasonic transducers to the PXI Real-Time chassis, cabling must be connected to each individual transducer and then the individual cabling is reduced to multiple multi-conductor cable and connector. For each transducer, a 50Ω BNC cable that attaches to the transducer with a UHF connection is routed to a NEMA weatherproof box, see Figure 6-6. Within the NEMA box are the analog filters and pre-

amps that are configured for the expected response of each transducer. The outputs of the analog components are routed to a connector block, see Figure 6-7 a, that outputs to a multi-pin connector. This reduces the wiring to a single multi-conductor cable that is sent into the operations cabin of the R-4 vehicle. Once in the cabin, to single cable has to split into three connectors to interface module in the PXI Real-Time chassis. This is done by doing the reverse of the operation it took to place all the sensor lines into a single cable. Figure 6-7 b shows how this down with four connector blocks, one to open the circuits from the sensor and three to send the signal into sets of four to each of the PXI modules.

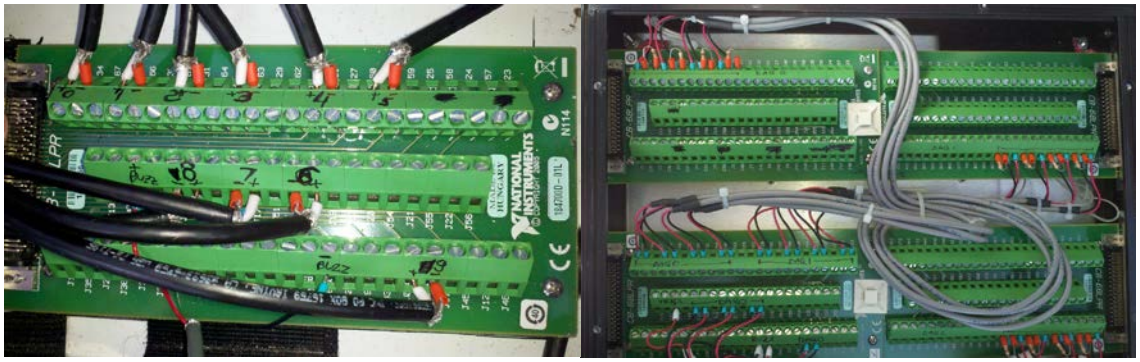

(a) Wiring to Multi-Conductor Cable (b) Break Out of Multi-Conductor Cable

Figure 6-7: Connector Block and Break Out for Multi-Conductor Cabling (a) Connector to Reduce to Multi-Pin Connector (b) Break Out of Multi-Pin Connector to Multiple Connectors.

Acquiring and digitizing of the transducer signals are performed by a PXI-6115 multifunction data acquisition module, Figure 6-8. The PXI 6115 is capable of meeting the required signal acquisition requirements with the follow specifications:

- Four analog signals
- Sampling rate of 10 MS/s

- Voltage range of ±0.2 V to ±42V
- Input resolution is 12-bit

(a) PXI-6115 **(b) PXI-6624**

Figure 6-8: National Instruments™ Multifunction Data Acquisition Modules (a) PXI 6115 and (b) PXI 6624

For the positioning system, the interface has much different requirements. Positioning is tracked in the R-4 Hy-Railer by a quadrature encoder mounted to the axle hub. The positioning signal is shared with many components in the R-4 Hy-Railer that are proprietary to ENSCO Inc. The signal is fed to the prototype system via an Ethernet link that contains the quadrature encoder signal requires counter/timer module for acquisition. The requirements are achieved with a PXI-6624 module, see Figure 6-8 b. The specification for the PXI-6624 that met these requirements are:

- 8 Counter channels
- Buffered Operations
- Voltage range 0-48 V
- Minimum input pulse 1 μsec
- 32-bit voltage resolution

- TTL logic
- Channel to channel isolation

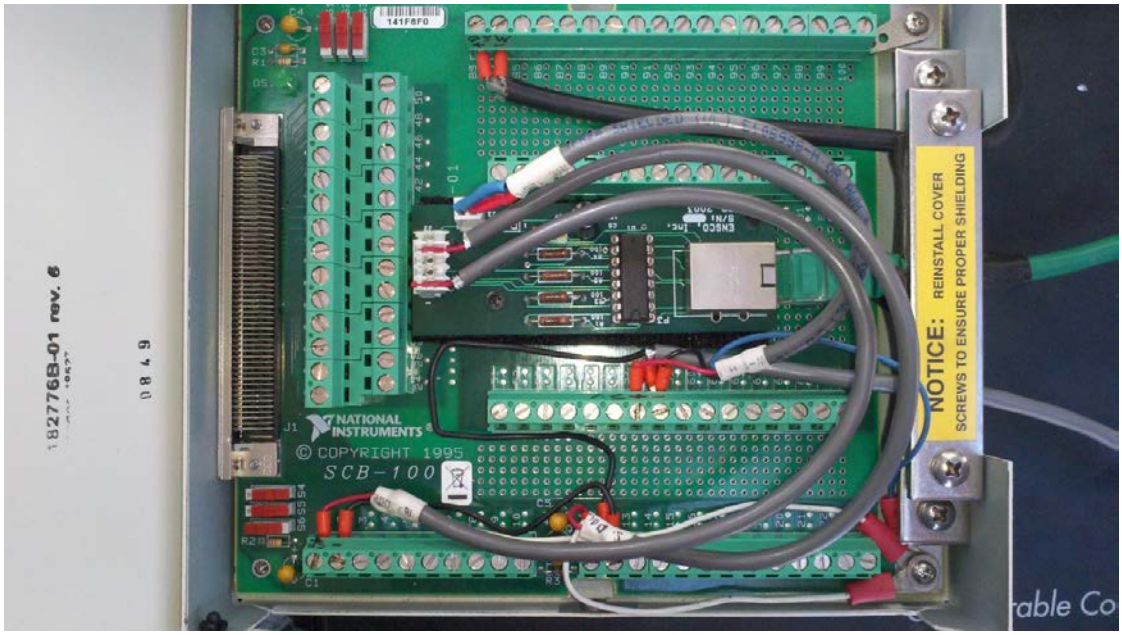

Figure 6-9: Connector Block for PXI-6624

In order to interface with the module, a special powered connector block is needed as shown in Figure 6-9. ENSCO Inc. provided the IC circuit need to extract the encoder signal from the Ethernet link and a 5V DC power source is provided by an external power supply. Two signals are received from the ENSCO Inc. system, one at every one foot mark and the second one based on a user defined resolution in hundredths of feet. With all the interfaces discussed above connected, the work of the prototype software takes over. The software will be discussed in the section that follows

6.1.2 Software Execution

The prototype software was developed with National Instruments™ LabView© software using the Real Time module by implementing Producer/Consumer design patterns. As the producer the Real Time PXI chassis, Figure 6-10, is the center of the software operations with all the other system components being consumers of the producer actions. A Real Time operating system and the Producer/Consumer design patterns was a necessity to meet the maximum capabilities of the system, see Figure 6-11. At the maximum repetition rate of the laser the data acquisition receives 5.7 MB/sec with computations occurring at 8 *m*sec intervals.. Running on a Windows© operating system timing synchronization is not guaranteed at intervals less than 10 *m*sec, and memory access is very constricted compared to a Real Time operating system.

Figure 6-10: PXI Real Time Operating System Chassis and Client Laptop

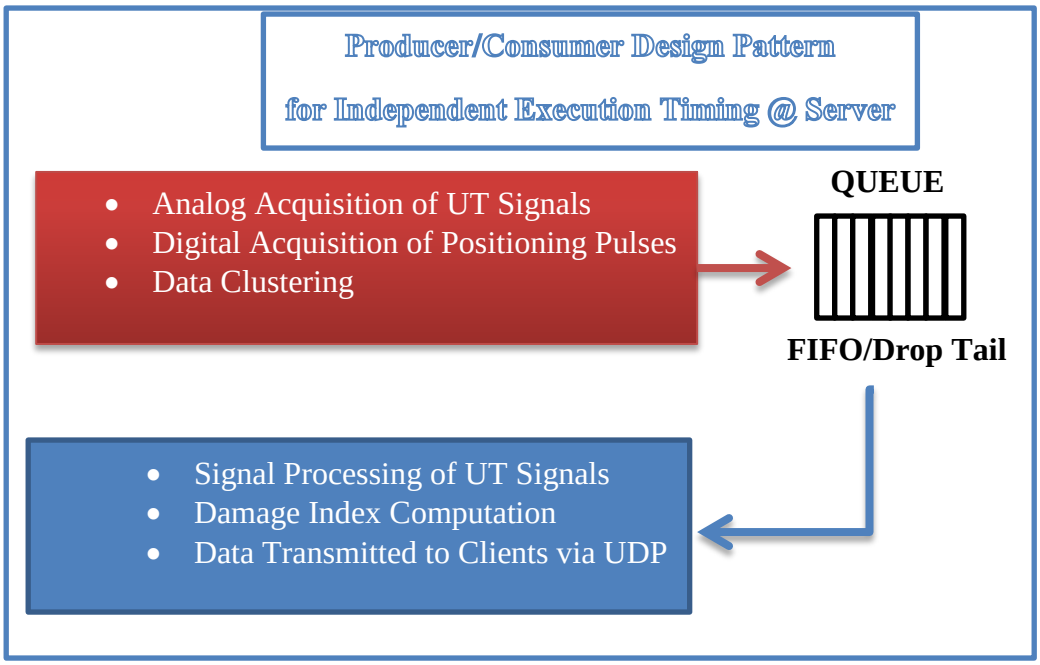

Figure 6-11: Producer/Consumer Design Pattern for Independent Execution Timing of the Prototype Software

In the operation of the system, the laser repetition rate is set at its maximum of 120 Hz, and the ultrasonic signals are acquired continuously and stored as a dynamic variable. Upon the triggering pulse from the positioning system, the values are read and processed. Analog signal acquisition of signals, digital acquisition of the positioning trigger, and the operation of the data clustering, all require deterministic execution which are then executed by the Producer loop at the fastest speed the CPU will allow. Once the deterministic action is executed, the acquired data is put in a First In First Out Drop Tail (FIFO-DT) queue. The queue allows other programs to retrieve the queue elements and execute the processes that have less execution timing restrictions. By using the Producer/Consumer design pattern, the Producer loop has greater and more frequent access to the CPU while the Consumer loop is limited which gives the

Producer loop priority and allows for independent timing of the access and reduced added processing delays and errors of the data. All actions that require the Producer/Consumer design pattern are executed in the Real Time operating system since display needs and disk drive accessing do not slow the operating system.

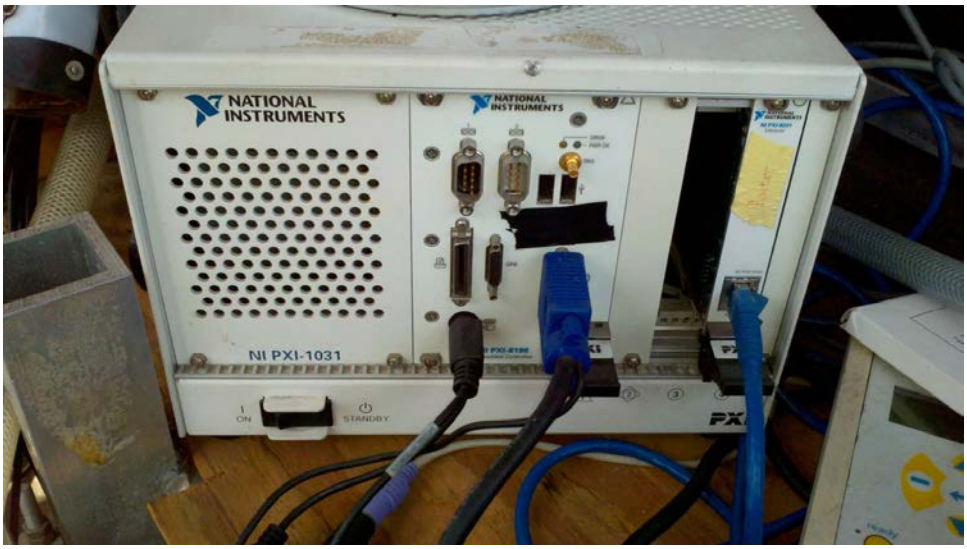

Figure 6-12: Data Storage PXI Chassis

6.1.3 User Interface

All display and disk access data storage are done on the two client CPUs of the system. The laptop client the operator has the ability to start and stop the data acquisition, adjust the laser repetition rate, change the laser power, change damage index features, monitor the results in real-time, and open a report window. The second client CPU is a PXI chassis , Figure 6-12, that has a large hard drive that strictly stores the acquired waveform and positioning data. Figure 6-13 shows the architecture for the prototype client server link. All messages that used to control the server such as, laser control and starting/stopping the acquisition are sent using the TCP-IP linking. TCP-IP

protocols insure delivery of these type of commands, due to the reliability of connection. UPD messages are used to deliver the data to be stored to the data storage PXI client and the processed data to the laptop client. While the message delivery is not as reliable as the TCP-IP protocol, the UDP is good for streaming large amounts of data at a high rate of speed

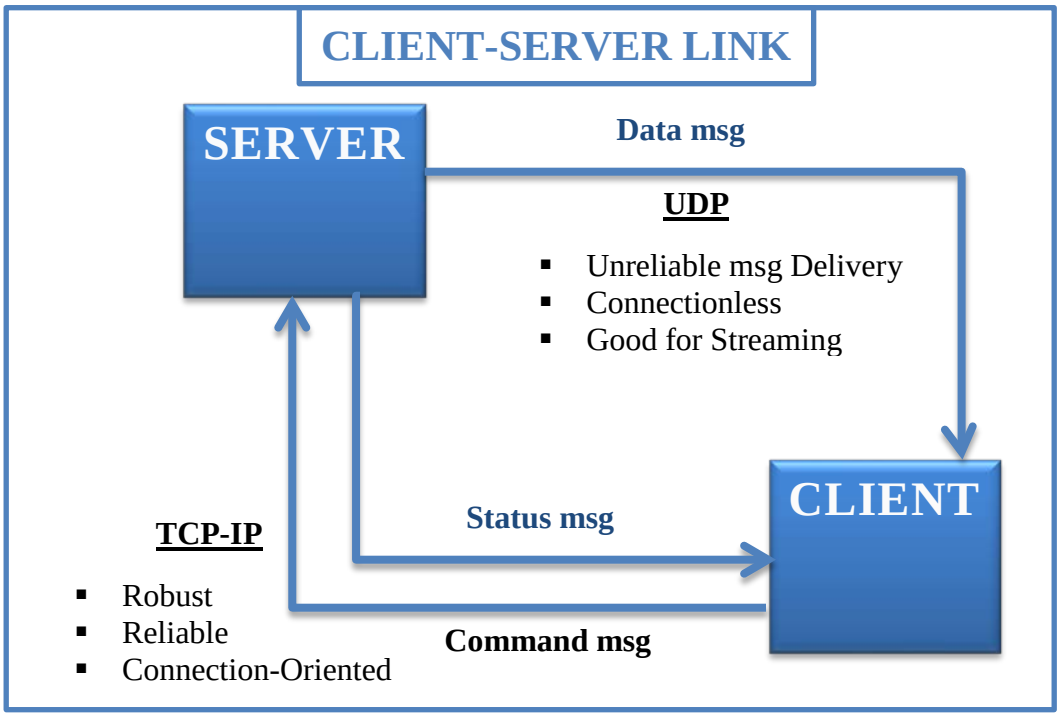

Figure 6-13: Prototype Client-Server Architecture

The user interface, see Figure 6-14, is designed to be easy to understand and operation can take place after relatively little training. Subdivided into three boxes, each with categorized tasks, the user interface is simple to comprehend. Box A holds the action controls, variable inputs, and communication link status for the server, laser, and data storage client. The action controls in box A include launching the calibration program, start a testing session and opening test session reports. Box B holds all the laser control

functions and display laser diagnostic information. The diagnostic information informs the user of what type of fault has occurred and needs attention. Laser controls include firing frequency, output power, and the activation of the laser output. Real-time results, calibration waveforms and report results are displayed in box C.

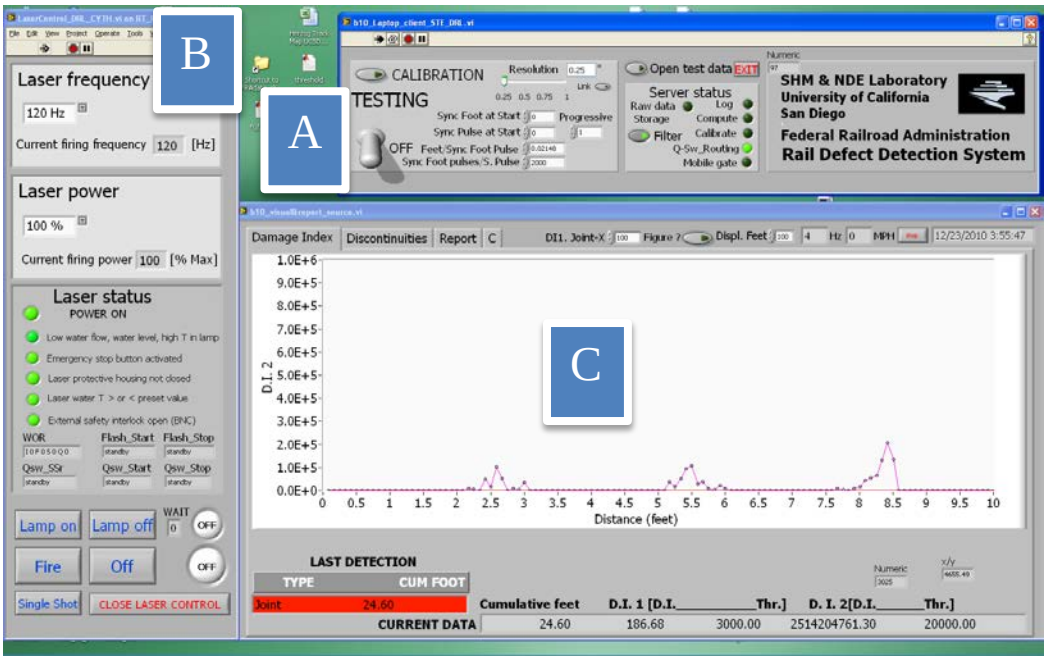

Figure 6-14: Prototype User Interface

The first task of the prototype operator is to check the sensor alignment. This done by activating the calibration program by pressing the calibration button in box A. Launching the program changes the display in box C as seen in Figure 6-15. It is a tabulated display with tab changing the display and input prompt for the appropriate calibration task. In Figure 6-15 the filtered and unfiltered waveform for a symmetric pairs of transducers. When aligning the sensors, the laser is operating a low frequency and

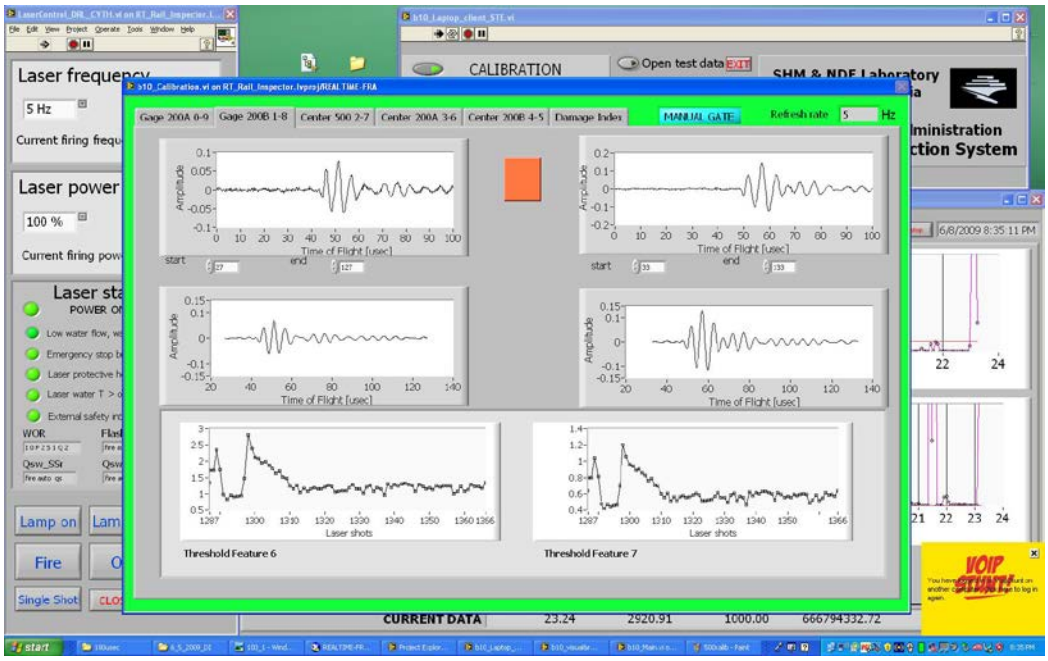

Figure 6-15: Calibration Display

the user can see the changes in the waveforms as the sensor alignment is changed until the desired signals are achieve. In addition to the tabs for each sensor pair, there is a tab that changes the display and input prompts needed to make adjustments the features to be used in the damage index computation. The prototype software currently calculates two damage indexes and the features for each computation selected in this display. Also a threshold for each damage index is chosen, and this threshold is used for the identification of defects for the final report that is generated. A large indicator light changes to red if any changes are made in the screen and will return to green after the damage index and threshold have been updated by pressing the update button. It is noted that the adjustments available in the display are for research purposes and will most likely be included in a final commercial package. After calibrating the system, the prototype is ready for testing session

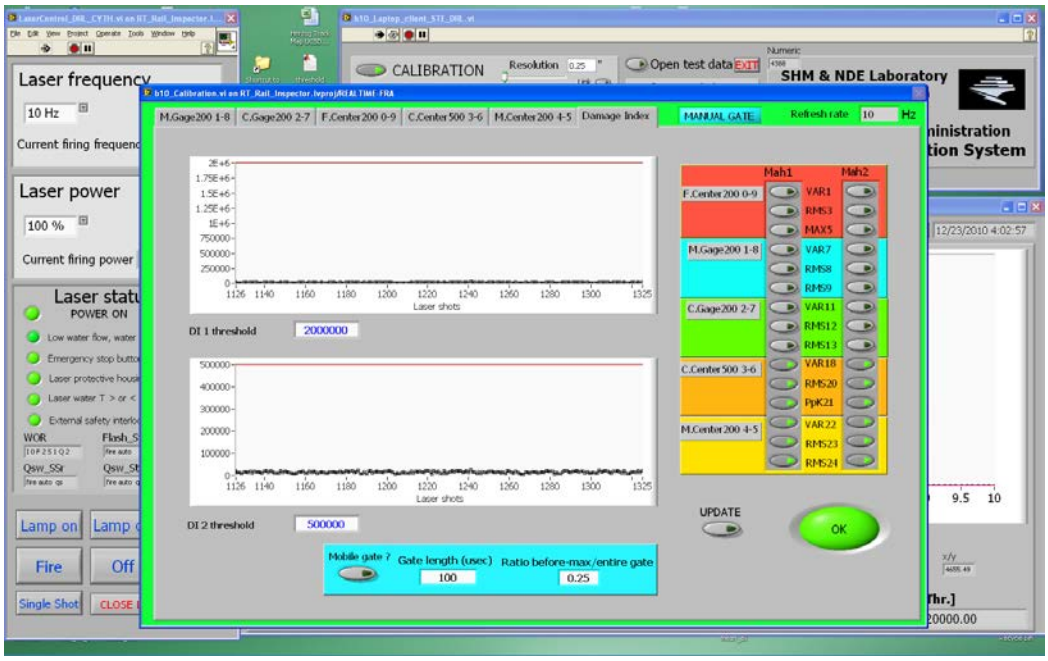

Figure 6-16: Damage Index and Threshold Adjustment Screen

The common screen the operator is going to be viewing is shown in Figure 6-17. In this screen the operator views the damage index in real-time as the prototype is running a test session. Large values, or large peaks, in the values will indicate discontinuity location. Damage indexes with a variety of discontinuity are discussed in section 6.6 with more detail. Another option is to choose the “Discontinuities” and only the locations of damage index value passing the threshold will be displayed as markers on a linear plot, see Figure 6-18. Also a texted based report is viewable in the “Report” tab. The report functions are available after the test session has been completed. A

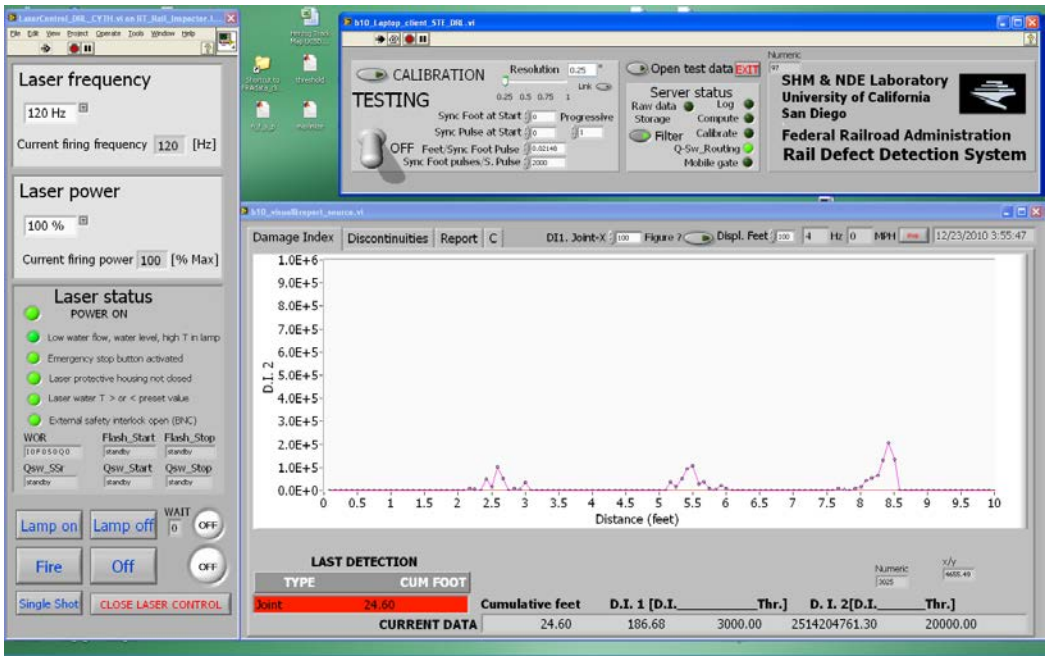

Figure 6-17: Damage Index Screen

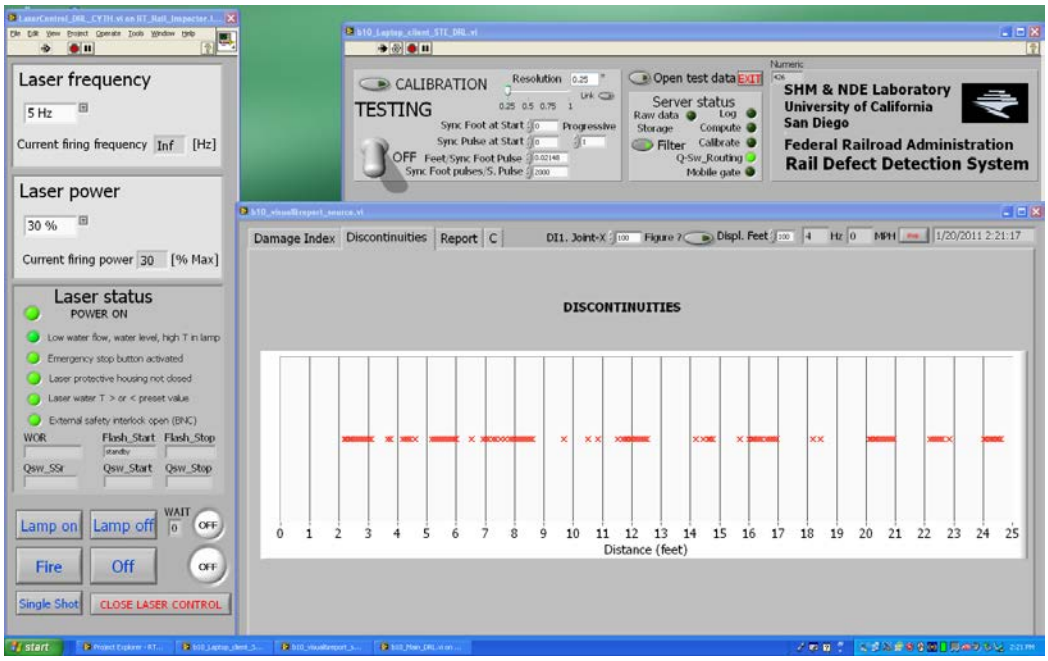

Figure 6-18: Discontinuities Screen

review of the test data in report form is available by pressing the “Open test data” button and choosing the test data by date and time the file was created.

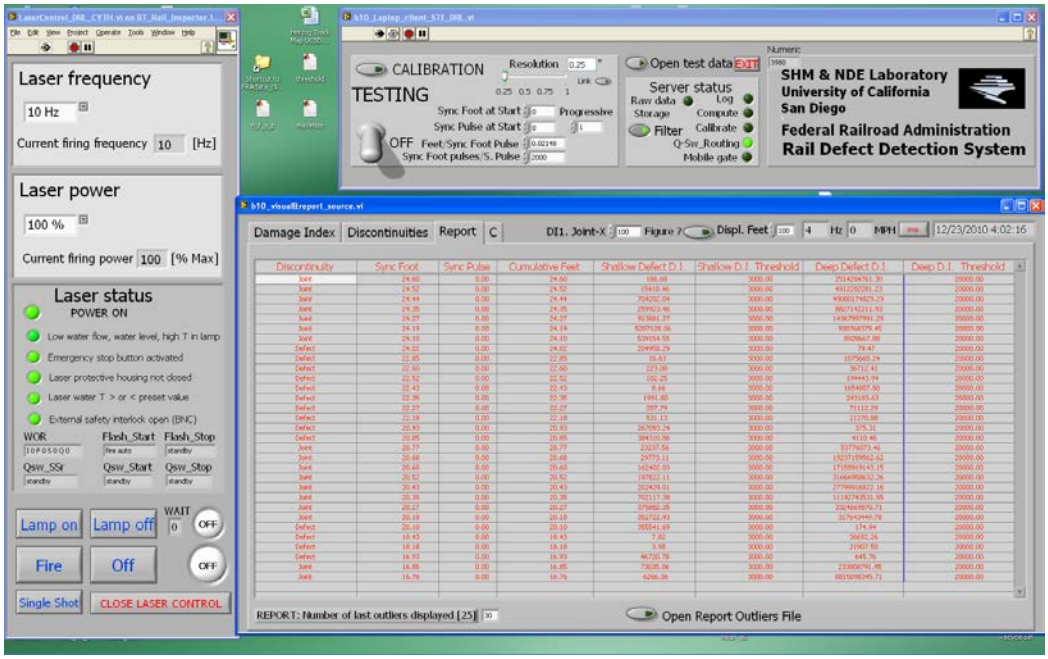

Figure 6-19: Report Screen

6.1.4 Improved Sensor Arrangement

The transducer arrangement shown in Figure 6-20 is configured to exploit the bi-direction wave propagation generated by the laser excitation. Two air-coupled sensor arrays are installed symmetrically centers on the laser excitation point. In this configuration the wave received by the transducer will have travelled an equal distance from the ultrasonic source. Defect detection is achieved by the computation of the damage index. The damage index is based a deviation from a baseline of several feature values. The feature are based on differences in the signals of symmetric sensor pairs, If a defect is present in the between the laser excitation point the either of the sensors. The

sensor holders are design for a wide range of sensors in order to explore additional configurations for additional experimental studies.

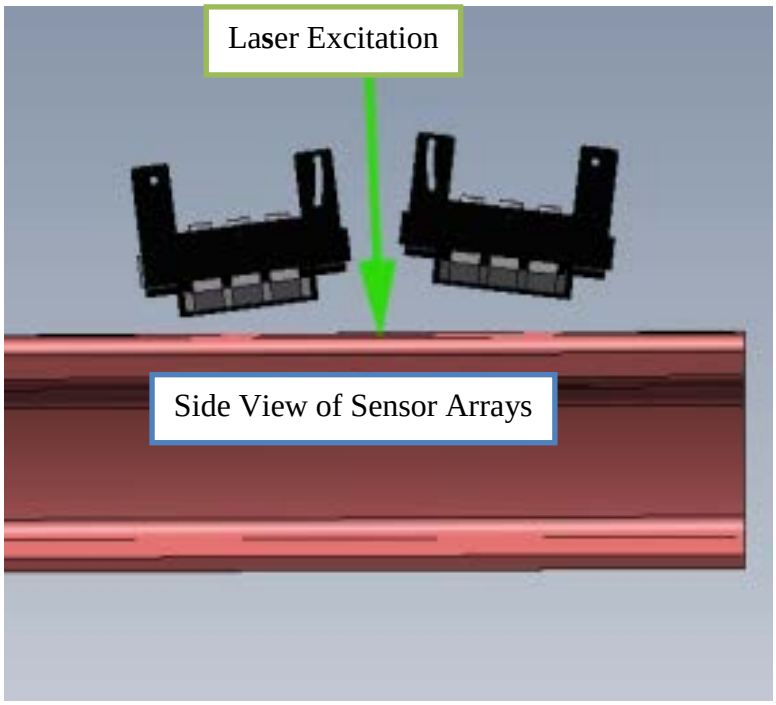

Figure 6-20: Sensor Arrays Placed for Detection of Bi-Directional Laser Induced Ultrasonic Guided Wave

6.1.5 Damage Index Computation

The damage index is a datum that is inconsistent with a baseline data set. Baseline data is based on a normal condition of the rail. Due to normal changes in operating conditions, such as temperature, humidity, or rail wear, there be some statistical variation to the features used in the baseline data set [108, 109].

Detection is a straightforward process for univariate data as the determination of a discordancy between a single observed datum and the baseline statistic. A common discordancy test that is based on deviation statistics is defined as:

$$z_i = \frac{\left| x_i - \bar{x} \right|}{s} \qquad \textbf{6.1}$$

where x_i is the potential outlier, $\bar{x}$ is the mean and s is the standard deviation of the baseline, and z_i quantifies the extent of the discordance. By using a defined threshold that is compared to the value of z_i the determination of whether x_i is an outlier (above the threshold) or not is made.

In the rail inspection prototype a multivariate data set is used. A set of multivariate data that is q-dimensional contains n observations in q variables. The discordancy test used is expressed by a non-negative scalar know by the Mahalanobis Squared Distance as follows:

$$DI = \left(\mathbf{x} - \bar{\mathbf{x}}\right)^{\mathrm{T}} \mathbf{S}^{-1} \left(\mathbf{x} - \bar{\mathbf{x}}\right) \qquad \textbf{6.2}$$

here $\mathbf{x}$ is the potential vector, $\bar{\mathbf{x}}$ is a mean vector for the baseline and $\mathbf{S}$ is the covariance matrix of the baseline data. The resulting scalar value is used to determine defect location when they are outlier (above the threshold).

A good way of understanding the effects of the multivariate outlier analysis is to visualize the waveforms. A damage index example using six features is shown in Figure 6-21. In order to visualize how small the differences are in the waveforms of a sensor pair, four positions are chosen and the waveforms for two sensor pairs a displyed. Of the four position, the locations are of a defect, near the defect, no defect, and a joint. For each position, the same sensor pairs are shown to better understand the differences are the positons.

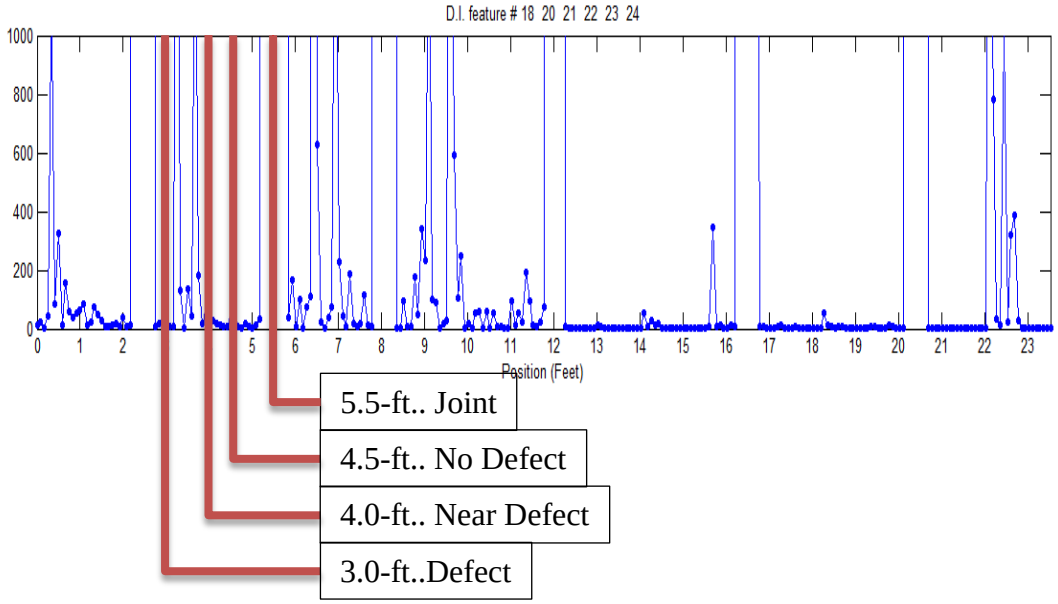

Figure 6-21: Six Feature Damage Index

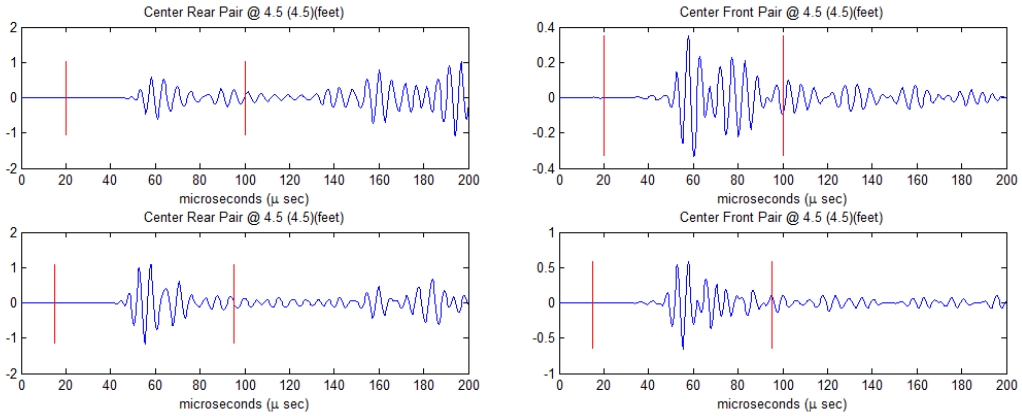

Figure 6-22: Waveforms at No Defect Location (4.5 Feet)

Waveforms for the location with no defect are seen inFigure 6-22: Waveforms at No Defect Location (4.5 Feet). While there are similarities to the wave forms they are not a perfect match. However, in order to accommodate the variations of the singles in the sensor pair for a clean rail, the feature baselines are taken for several waveforms. At

a minimum, in order to get a good representation of the ditribution baseline, 1000 waveforms collected on clean rail can be used.

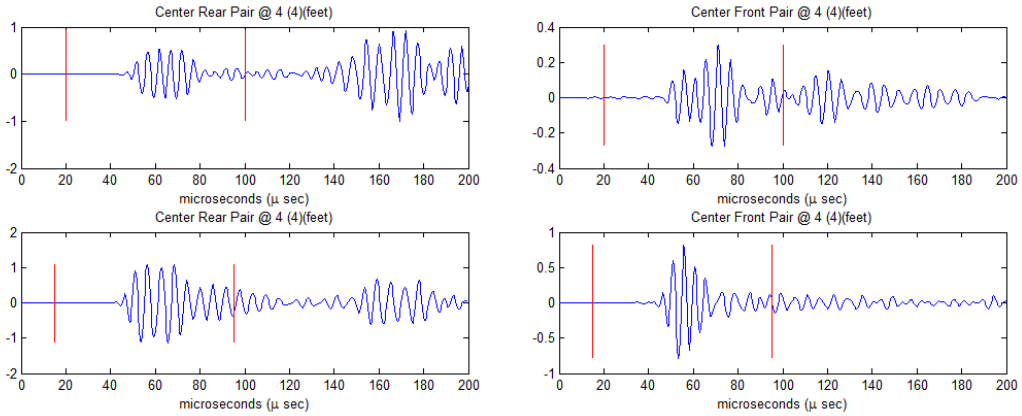

Figure 6-23: Waveforms at Near Defect Location (4 Feet)

The waveforms of Figure 6-23 are not from a position with a defect, yet they are different than those seen in a defect free position. In this particular case, the position is very close to the defect , thus the waveforms are rather different. The amplitude has increased, possibly from reflections off the defect. Also there are some modes in the wave packet that are removed and others that are increased. Because of the nature of the wave propagation, the presence of a defect can have several effect on the measured signal. This helps to illustrate the need to monitor multiple waveform features to identify defects accurately.

The waveforms collected over the defect location are shown in Figure 6-22. Here the waveforms have some significant differences to those seen in the defect free waveforms. Amplitudes are changed some have increased others have decrease. Frequency content has change with a small variation in the cycle period of the waveforms. Also, multiple modes have been added and removed from the waveform.

The fact the changes in the waveforms can be both additive and subtractive the features used to calculate the damage index need to be immune to such changes.

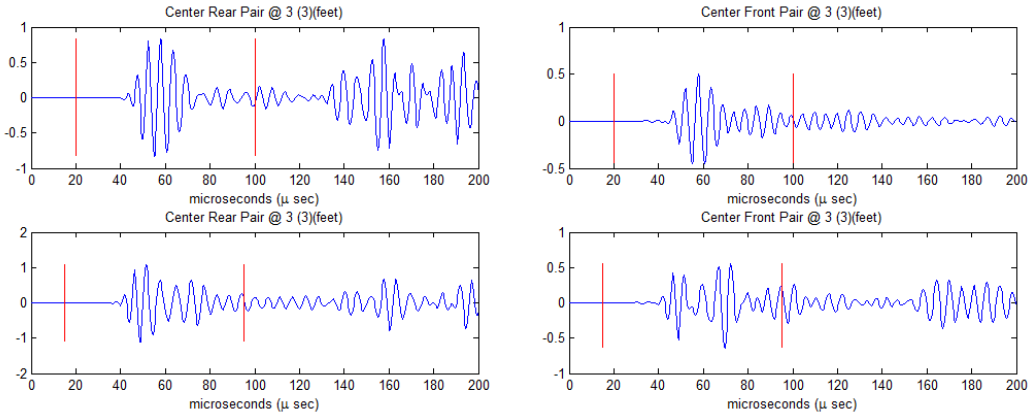

Figure 6-24: Waveforms at Defect Location (3 Feet)

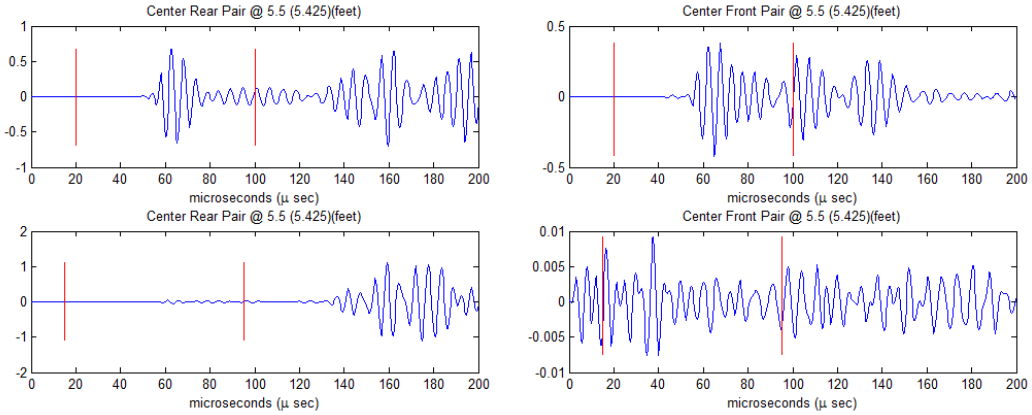

Figure 6-25: Waveforms at Joint Location (5.5 Feet)

In an ideal world, the change due to a defect would completely remove the acquisition of one more of the waveforms. Figure 6-25 the waveform at a joint represents this ideal situation. In one sensor pair, one of the waveform is completely absent while the other is still received. The other sensor pair has one sensor that appears to have received noise and the other still acquired a waveform with good energy. This

ideal case is not possible for the location of small discontinuities that are transverse defects.

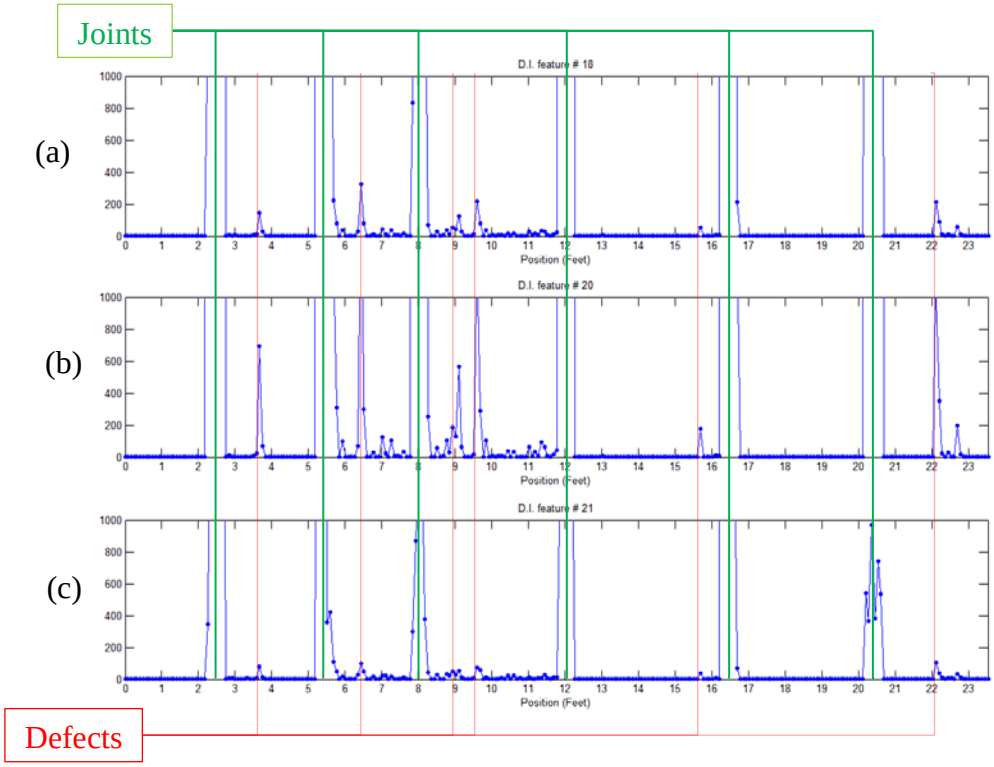

Figure 6-26: Univariate Damage Indexes (a) Feature 18, (b) Feature 20, (c) Feature 21

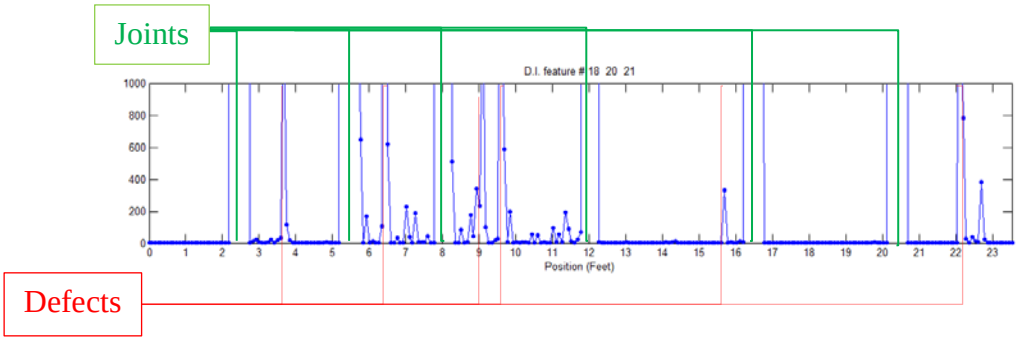

Figure 6-27: Multivariate Damage Index Combining Features 18, 20, and 21

Examples of the damage index with single features are shown in Figure 6-26 with three separate features. The feature used in the damage index in Figure 6-26a is a measure of how well the waveforms fit in a statistical distribution. For Figure 6-26b the energy level of the waveform is measured. Lastly, in Figure 6-26c the feature represents the strength of the received signal. Each feature has some ability to locate the defect as seen in the individual damage indexes. Yet, as an outlier, the singular features are poor indicators relative to the noise floor.

Figure 6-27 shows the damage index when the three previously presented features are combined in the multivariate analysis. It is seen that when the features are combined, the defects discontinuities stand out better the in the univariate damage indexes. All the plots have the same scale and, in the univariate analysis, only the joints are out the scale and the defect stand out, but within the scale. In the multivariate damage index, several of the defects are now off the scale and identified more easily.

In order to confirm quantitatively the benefits of the multivariate damage index, the Receiver Operating Characteristic (ROC) metric is used. The ROC curve plots the True Positive Rate versus the False Positive Rate of the detector. The ROC is a tool from the signal processing discipline, in particular for radar systems, to determine the optimal model for a binary classification system in which outcomes are labeled as either positive or negative. As a plot, the ROC illustrates the performance of the binary classifier system as the detection threshold is varied. By plotting the fraction of true positive indications versus the fraction of false positive

indications, the sensitivity of the system to detect a true positive is indicated. The resultant curve allows for an analysis of the relative trade-offs of the costs (false positive) and benefits (true positives) of the system.

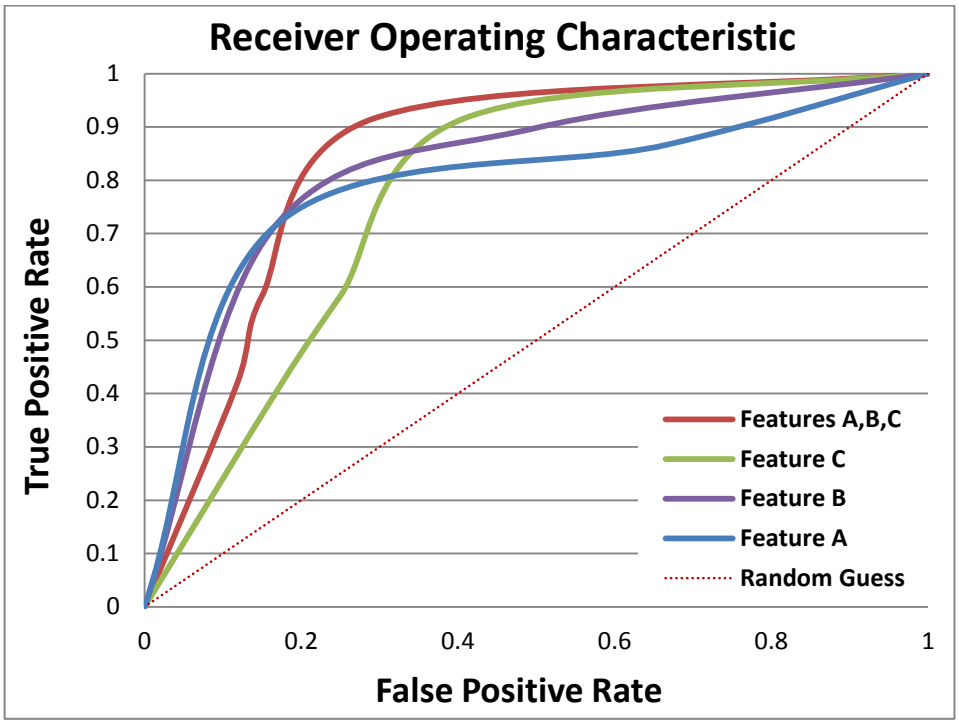

Figure 6-28: Receiver Operating Characteristic Curve for Damage Index Features

Figure 6-28 is the resulting ROC plot for the damage index features presented previously in Figure 6-26 and Figure 6-27 obtained from the UCSD defect farm located at Camp Elliott. The diagonal line that divides equally the ROC space represents a completely random guess such as a coin flip. Results lying above the random guess line represent a good classification result, while values below the diagonal would be considered a poor classification. An ideal operator would give a point a (0, 1) such that all resulting observations are true positives and no false positives are detected.

Evaluation of the receiver operating characteristic as shown in Figure 6-28 shows that the combination of the features A, B, and C in a multivariate outlier analysis produce the best results. Both features A and B have the lowest false positive rate up to a 70 % detection rate, yet beyond that the detection rate falls off appreciably. In contrast feature C only achieves a high true positive rate with a hgh false positive rate making it a poor detector on its own. When the three features are combined with the Mahalanobis Squared Distance, the detector has the best performance. The use of the collective features creates a detector with a 90% detection rate with a false positive rate of 20%.

6.2 Background for Field Test at Herzog Inc.

The rail inspection system developed at UCSD uses a laser and air-coupled sensors to excite and detect ultrasonic guided waves in the rail head. Guided waves interact with transverse defects in a manner that is more effective than traditional bulk waves employed by common wheel-based rail inspections. The envisaged advantages of the proposed system over conventional rail inspection are:

(a) increased reliability of defect detection, including transverse defects under surface shelling as well as horizontal split head defects (both of which are notoriously hard to detect with conventional methods);

(b) increased inspection speed compared to conventional rail inspections due to the non-contact nature of the probes and the use of guided waves, rather than bulk waves (i.e. simultaneous inspection of a finite length of rail as opposed to inspection of one cross-section at a time).

Six field tests were previously conducted, respectively in March 2006, April 2007, March 2008, December 2008, May 2009, and June 2009. A comprehensive report summarizing the results of the first two tests was submitted to the FRA in June 2007 (Coccia, Bartoli, Lanza di Scalea and Rizzo, *Non-contact rail defect detection: first and second field tests*, UCSD Report SSRP-07/15, June

2007). A report summarizing the results of the third field test was submitted to FRA in April 2008 (Coccia, Phillips, Bartoli, Salamone, Lanza di Scalea, *Non-contact rail defect detection: third field test*, UCSD Report SSRP-08/02). A report summarizing the results of the fourth field test was submitted to FRA in February 2009 (Coccia, Bartoli, Phillips, Salamone, Lanza di Scalea, *Non- contact rail defect detection: fourth field test*, UCSD Report SSRP-09/04). Letter reports with the results of the fifth and sixth field tests were submitted to FRA respectively in May 2009 (Coccia, Bartoli, Lanza di Scalea, *Non-contact Rail Defect Detection, results of fifth field test*) and in June2009 (Coccia, Bartoli, Phillips, Salamone, Lanza di Scalea, *Non-contact Rail Defect Detection, results of sixth field test (System Evaluation at TTC)*).

The chapter contains the results of the seventh field test/technology development test conducted in June 2010 at Herzog Services, Inc. in St. Joseph, MO

6.3 Seventh field test timeline

The seventh field test occurred at Herzog Services, Inc., for 6 days between June 13th and June 18th 2010. UCSD and ENSCO teams were actively involved in testing the prototype, while Herzog Services provided access to their facility, including the rail

defect farm, to accommodate the tests. In addition, several visitors from BNSF, UP and FRA participated to the tests.

Day #1 and part of day #2 were spent by UCSD and ENSCO teams setting up the prototype on R-4 in Herzog Services main building. R-4 was equipped with a new system of nozzles spraying water at the four R-4 wheel locations, aiming at reducing the noise occurring at the wheel-rail interface. The water reservoir was installed in the front of R-4. (Figure 6-29)

Figure 6-29:Water reservoir for the supply of the water spray system installed to reduce the noise created at the wheel-rail interface

On day #2 ENSCO personnel installed reflective targets on the track to mark 20' blocks, welds and joints.

The new positioning system installed by ENSCO on R-4 was tested and it performed satisfactorily at a resolution of 0.25”. At the end of Day #2, two blind tests were conducted as previously agreed with Herzog. The results of the blind tests were submitted to Volpe (J. Choros), FRA (L. Al-Nazer) and to Herzog (T. Elbert).

In the morning of Day #3 several tests were run with the purpose of testing multiple system configurations, varying from different sensor sets and new settings for the ultrasonic signal time gating.

During Day #3, after Mr. Elbert released a list with the known defect locations, ENSCO installed and tested reflective targets near the flaws (Figure 6-30).

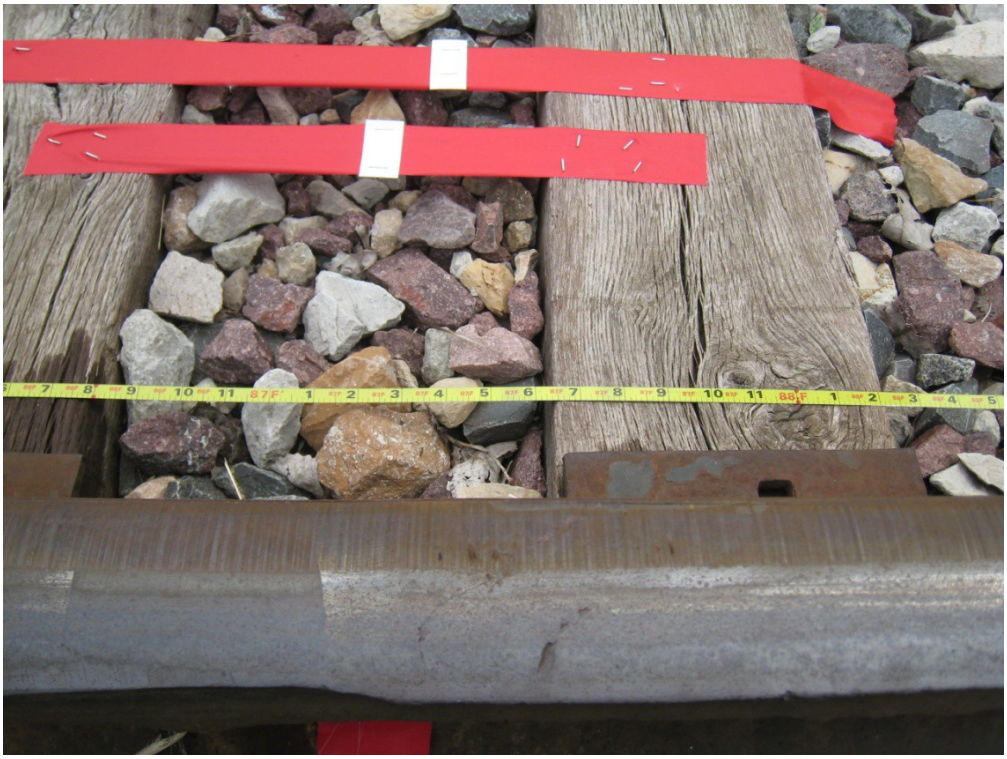

Figure 6-30: Reflective targets placed in correspondence of joints, weld and defects.

The rest of Day #3 was spent comparing UCSD results to Herzog's list of known defects.

In the morning of Day #4, a different set of sensors responding at higher frequency was installed, and several tests were run to assess the new configuration. During the day, the prototype performance was demonstrated to representatives of BNSF, UP as well as to several Herzog employees. At the end of the day, the initial sensor setting was re-installed on the prototype

The beginning of Day #5 was spent running several tests showing the prototype performance to representatives of BNSF and Union Pacific. In the afternoon a new configuration with the sensors slightly moved towards the field side of the rail head was also tested.

In the morning of Day #6 the prototype was tested at higher speed (~8/9 MPH) and later the sensors were moved back towards the gage side of the rail head. More runs at higher speed were conducted before concluding the field test. Some problems with the flanging of the cart occurred during the latest higher speed tests. These were solved by adjusting the pressure of the actuators installed on the cart. Teardown activities begun in the late morning and at 3 pm all the equipment was packed, ready to be shipped back to UCSD. Soon after, UCSD and ENSCO left Herzog facility.

Figure 6-31 shows pictures of the UCSD prototype as well as a group picture of participants to the tests.

Figure 6-31: The UCSD prototype at Herzog and picture of some of the test participants from UCSD, ENSCO, FRA, Volpe, Herzog, BNSF, and UP

Figure 6-32: Aerial view of Herzog railroad track testing facility (rail defect farm).

Figure 6-32 shows an aerial view of Herzog railroad track testing facility. Areas 1 (Tangent) and 2 (Spiral) were composed of 136 RE rails, while the track in areas 3 and 4 had smaller rail sections (115 RE and 90 RE, respectively).

Table 6.2: Mapping of the test zone

Tie Number/Event Catalog at Hezog Test Facility			
Date: June 14, 2010			
NOTE:	Tie Numbering starts at "0"		
	DM = Distance Marker		
	LE = Leading Edge of Tie (in Direction of Increasing Tie Count)		
	TE = Trailing Edge of Tie (in Direction of Increasing Tie Count)		

Tie	Event Description	Tie	Event Description
0	UCSD Laser Position at Start of Test	88	160' DM 1" after TE of Tie 88
1	0 DM at TE of Tie 1	90	**End of Guard Rail**
7	**UCSD DEFECT FROM BLIND TEST (9' 2")**	92	**Joint** 14" after TE of Tie 92
12	20' DM at TE of Tie 12	94	**Weld** 14" after TE of Tie 94
14	**UCSD DEFECT FROM BLIND TEST (24' BETWEEN TIE 14 & 15)**	**95**	**UCSD DEFECT FROM BLIND TEST (174' ON TIE 95)**
18	**UCSD DEFECT FROM BLIND TEST (29' 6" ON TIE 18)**	98	180' DM 3" after LE of Tie 98 on Tie
20	**Joint** at LE of Tie 20	101	**UCSD DEFECT FROM BLIND TEST (186' 6" BETWEEN TIE 101 & 102)**
22	**UCSD DEFECT FROM BLIND TEST (37' ON TIE 22)**	103	**Joint** 5" after LE of Tie 103 on Tie
23	**UCSD DEFECT FROM BLIND TEST (39' ON TIE 23)**	106	**Weld** 7" after LE of Tie 106 on Tie
23	40' DM 10" after TE of Tie 23		**UCSD DEFECT FROM BLIND TEST (194' BETWEEN TIE 106 & 107)**
25	**UCSD DEFECT FROM BLIND TEST (43' ON TIE 25)**		**UCSD DEFECT FROM BLIND TEST (195' 3" BETWEEN TIE 106 & 107)**
27	**UCSD DEFECT FROM BLIND TEST (46' ON TIE 27)**	110	200' DM 5" after TE of Tie 110
32	**UCSD DEFECT FROM BLIND TEST (55' 2" ON TIE 32)**	113	**Joint** 0.5" after LE of Tie 113 on Tie
34	**Weld** 2.5" after TE of Tie 34	116	**Weld** 8" after LE of Tie 116 on Tie
	UCSD DEFECT FROM BLIND TEST (59' 2" BETWEEN TIE 34 & 35)	123	220' DM 2" after TE of Tie
	60' DM 12" after TE of Tie 34	**127**	**UCSD DEFECT FROM BLIND TEST (230' 6" BETWEEN TIE 127 & 128)**
42	**Joint** on Tie 42	130	**Joint** 3" after LE of Tie 130 on Tie
46	80' DM 5" after TE of Tie 46	135	240' DM 5.5" after LE of Tie 135 on Tie
50	**Weld** 6" after TE of Tie	138	**Weld** 0.5" after TE of Tie 138
	UCSD DEFECT FROM BLIND TEST (87' 4" BETWEEN TIE 50 & 51)	139	**Joint** 1.5" after TE of Tie 139
55	**Weld** at LE of Tie 55 on Tie	147	280' DM 3" after LE of Tie 147 on Tie
56	**Joint** at TE of Tie 56 on Tie	151	**Joint** 2" after TE of Tie 151
57	100' DM 6" after TE of Tie 57	159	280' DM 0.5" after LE of Tie 159 on Tie
58	**Weld** 5" after LE of Tie 58 on Tie	160	**Joint** 7.5" after TE of Tie 160
62	**Weld** 11" after TE of Tie 62	169	300' DM 9" after TE of Tie 169
68	120' DM 2.5" after LE of Tie 68 on Tie	180	320' DM 1.5" after LE of Tie 180 on Tie
72	**Joint** 13.5" after TE of Tie 72		**Joint** 6" after TE of Tie 160
73	**Start of Frog**	190	340' DM on LE of Tie 190 on Tie
78	140' DM 8" after TE of Tie 78	199	**Joint** 1.5" after LE of Tie 199 on Tie
81	**Joint** 3" after LE of Tie 81 on Tie		360' DM 17" after TE of Te 199
	End of Frog	209	380' DM 13" after TE of Tie 209
85	**Start of Guard Rail**	217	**Joint** 2.5" after TE of Tie 217
		219	400' DM 14" after TE of Tie 219

Table 6.2 contains the mapping of the test zone. Joints, welds, 20-feet distance marks and defects detected by the blind tests performed on Day #2 are included in the table.

Table 6.3: Schedule of the runs performed during the tests at Herzog Services.

Test #	Day #	Date	Speed [MPH]	End of test area	Distance resolution [in]	Test type
1	2	Monday June 14th	2	spiral	0.25	Baseline
2	2	Monday June 14th	2	spiral	0.25	Baseline
3	2	Monday June 14th	2	spiral	0.25	Baseline
4	2	Monday June 14th	2	spiral	0.25	tack pulse check
5	2	Monday June 14th	2	spiral	0.25	tack pulse check
6	2	Monday June 14th	2	curve	0.25	noise check
7	2	Monday June 14th	2	spiral	0.25	noise check
8	2	Monday June 14th	2	spiral	0.25	overall check
9	2	Monday June 14th	2	spiral	0.25	Blind test #1
10	2	Monday June 14th	2	spiral	0.25	Blind test #2
11	3	Tuesday June 15th	2	spiral	0.25	Damage Index
12	3	Tuesday June 15th	2	spiral	0.25	Damage Index
13	3	Tuesday June 15th	1	spiral	0.25	Damage Index
14	3	Tuesday June 15th	2	spiral	0.25	Damage Index
15	3	Tuesday June 15th	2	spiral	0.25	Damage Index
16	3	Tuesday June 15th	2	spiral	0.25	Damage Index
17	3	Tuesday June 15th	2	spiral	0.25	Damage Index
18	3	Tuesday June 15th	2	spiral	0.25	Damage Index
19	4	Wednesday June 16th	2	spiral	0.25	Baseline
20	4	Wednesday June 16th	2	spiral	0.25	Damage Index
21	4	Wednesday June 16th	2	spiral	0.25	Damage Index
22	4	Wednesday June 16th	2	spiral	0.25	Damage Index
23	4	Wednesday June 16th	2	spiral	0.25	Damage Index
24	4	Wednesday June 16th	2	spiral	0.25	Baseline
25	4	Wednesday June 16th	5	spiral	0.25	Damage Index
26	4	Wednesday June 16th	5	spiral	0.25	Damage Index
27	4	Wednesday June 16th	2	spiral	0.25	Damage Index
28	4	Wednesday June 16th	2	spiral	0.25	Damage Index
29	5	Thursday June 17th	2	spiral	0.25	Damage Index
30	5	Thursday June 17th	2	spiral	0.25	Damage Index
31	5	Thursday June 17th	2	spiral	0.25	Damage Index
32	5	Thursday June 17th	2	spiral	0.25	Damage Index
33	5	Thursday June 17th	2	frog	0.25	Damage Index
34	5	Thursday June 17th	2	frog	0.25	Damage Index
35	5	Thursday June 17th	2	frog	0.25	Damage Index
36	5	Thursday June 17th	2	frog	0.25	Damage Index
37	5	Thursday June 17th	2	frog	0.25	Damage Index
38	5	Thursday June 17th	2	frog	0.25	Damage Index
39	5	Thursday June 17th	2	frog	0.25	Damage Index
40	5	Thursday June 17th	5	frog	0.25	Damage Index

Table 6.3 (continued) Schedule of the runs performed during the tests at Herzog Services.

Test #	Day #	Date	Speed [MPH]	End of test area	Distance resolution [in]	Test type
41	5	Thursday June 17th	2	curve	0.25	Damage Index
43	5	Thursday June 17th	2	spiral	0.25	Baseline
44	5	Thursday June 17th	2	spiral	0.25	Damage Index
45	5	Thursday June 17th	2	spiral	0.25	Damage Index
46	5	Thursday June 17th	5	spiral	0.25	Damage Index
47	6	Friday June 18th	9	spiral	0.25	Damage Index
48	6	Friday June 18th	9	spiral	0.25	Damage Index
49	6	Friday June 18th	9	spiral	0.25	Damage Index
50	6	Friday June 18th	2	frog	0.25	Damage Index
51	6	Friday June 18th	9	spiral	0.25	Damage Index
52	6	Friday June 18th	5	spiral	0.25	Damage Index
53	6	Friday June 18th	5	curve	0.25	Damage Index
54	6	Friday June 18th	5	spiral	0.25	Damage Index

Table 6.3 contains the schedule of the runs performed during the entire period at Herzog. A total of fifty-four tests were performed, running the prototype in the different areas of the track. Most of the tests were run up to the track spiral (Area 2), while a few were extended to the curve (Areas 3 and 4). Some runs were limited to the area with the frog (within Area 1). Most of the tests were run at walking speed. A few tests at 5 and 9 MPH were run to assess the dependence of the prototype performance on speed. The distance positioning resolution was maintained at 0.25” for all the runs.

6.4 Blind test results

The results of the blind tests performed on Day #2 are reported in Table 6.4.

The inspected area included twelve railhead defects, such as Detail Fractures, Transverse Defects Under shelling, Defective Field and Plane Welds, Side Drilled Holes (simulating TDs), Horizontal and Vertical Split Heads.

Two different signal processing approaches were used for the two tests. One configuration was less sensitive to small railhead discontinuities (blind test 1, run #9) than the other one (blind test 2, run #10).

Table 6.4: Results of the two blind tests performed on Day #2.

Herzog defect farm June 15, 2010			
Transverse defects on gage and center of rail head			
feet	inches	tie #	Defect
9	4	7	90% DF (3 field holes, 2 up to gage)
23	11	14	SDH (1/4" dia, 3/4" deep on gage)
29	9	18	SDH (1/4" dia, 1/2" deep on gage)
33	4	22	2" HSH
38	11	23	1' VSH
42	8	25	gage TD (10% H.A. very deep)
46	1	27	10% DPW (TD in weld center head, width of web)
55	0	32	small TD (10% H.A. center head) (newly found)
59	2	34	50% DFW (center head width of web)
87	2	50	DFW under shelling (10% H.A. center head/field)
193	8	106	TD under shelling (10% H.A.)
245	1	136	80% DFW (starts at gage)

	UCSD List 1		UCSD list 2	
	1	7	1	7
	1	14	1	14
	1	18	1	18
	1	22	1	22
	1	23	1	23
	1	25	1	25
	1	27	1	27
	1	32	1	32
	1	34	1	34
	0		1	50
	1	106	1	106
	0		0	
Detected	**10**		**11**	
All	**12**		**12**	
%	**83.33**		**91.67**	
F.P.	**0**		**4***	

*(3 of 4 mapped to shallow defects under shelling at ties # 101, 107 & 127)

feet	inches	tie#
174		95
186	**6**	**101**
195	**4**	**107**
230	**8**	**127**

As shown in Table 6.4, ten out of twelve (10/12) defects were correctly detected by blind test #1 (“less sensitive configuration”), while eleven out of twelve (11/12) defects were correctly detected by blind test #2 (“more sensitive configuration”). Blind test #1 therefore had an 83.34 % Detection Rate with zero False Positives (0 F. P.). Blind test #2 had a 91.67% Detection Rate at the cost of four False Positives (4 F. P.).

However, following hand-mapping of the test area, three out of the four (3 out of 4) False Positives mapped to shallow defects under shelling, as noted in Table 6.4. Hence the true False Positive detection for blind test #2 was as low as 1 F.P.

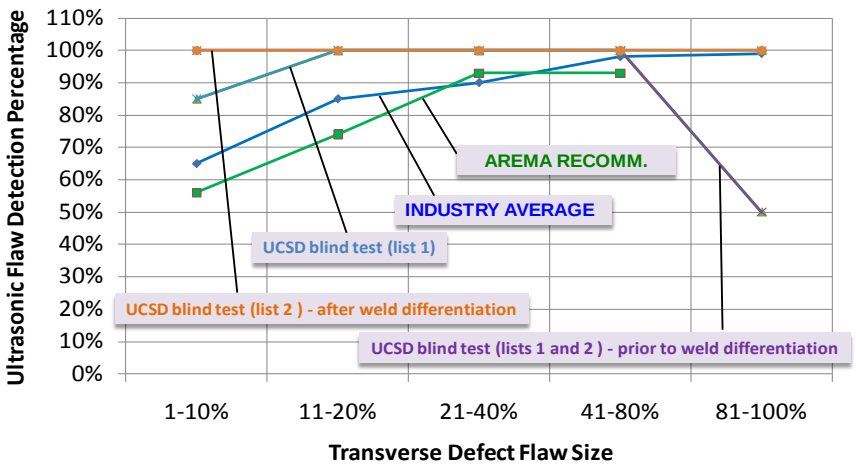

Figure 6-33: Results of UCSD blind tests at Herzog rail defect farm on June 15, 2010 (comparison with Industry Average and AREMA Standards).

As shown in the Table 6.4, the UCSD list provided for both blind test #1 and #2 did not include the 80% Defective Plane Weld (DFW) at tie #136. However, this defect was correctly detected by the system, but not included in the original list because considered a weld. Later in the tests a method was identified to distinguish “good welds” from “defective weld” based on their different ultrasonic signature. When this differentiation was applied, the last defect at tie #136 was consistently detected as a defect by the system. Figure 6-33 plots the results of the blind tests along with Industry Average and AREMA Recommendation for reliability of defect detection (particularly TDs). The detection percentage was computed as the number of detected defects divided by the total number of defects of a given size class. The 21-40% size class was not tested since

no defect of such size was present on the track. The plot shows that the UCSD system outperformed both Industry Average and AREMA Recommendations in all defect size classes, including the largest size class of 81-100% once the weld differentiation method was implemented.

6.5 Damage Index plots

This section includes the Damage Index plots of some sample tests. For display purposes, the plots are here reported as partial zooms of different areas of the track. In addition to the Damage Index plots, all raw data were collected during the tests. These raw data are being currently analyzed at UCSD to explore other signal processing strategies for potential further enhancement of the system performance.

6.5.1 Level of shelling

Different scales of visualization of the Damage Index plots were used for different areas of the rail. This is to adapt the response of the system to different levels of shelling of the rail. In the different conditions of shelling encountered during the test, the defect-free level of the Damage Index was varying, but the defect indications were always easily distinguishable from the noise level. An Automatic Gain Control feature should be implemented in the final configuration of the system to solve the visualization issue related to rescaling the data in presence of moderate and heavy shelling. Such Automatic Gain Control is also used in conventional ultrasonic rail inspection systems.

The system sensitivity to shelling could also be an interesting feature of the system, potentially used to estimate the severity of shelling, hence the thickness of the layer that

needs to be grinded during rail maintenance. This potential for rail surface characterization was highlighted by Carlo Patrick from the FRA Office of Safety who attended the tests.

Figure 6-38 shows an example of a rail with moderate level of shelling. The Damage Index increases but the Defective Field Weld at 87'2" is still well recognizable.

Figure 6-34-12 show Damage Index plots related to run #20, conducted at 2 MPH. Figure 6-41 includes the Damage Index plot of the full run #20 (feet 0-255).

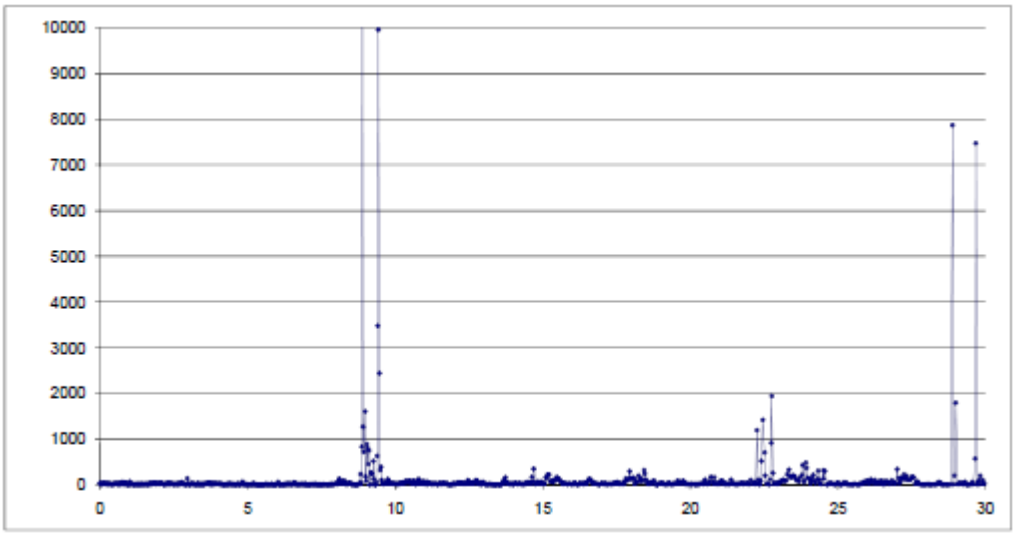

Figure 6-34: Damage Index plot (0-30 feet), run #20 conducted at 2 MPH

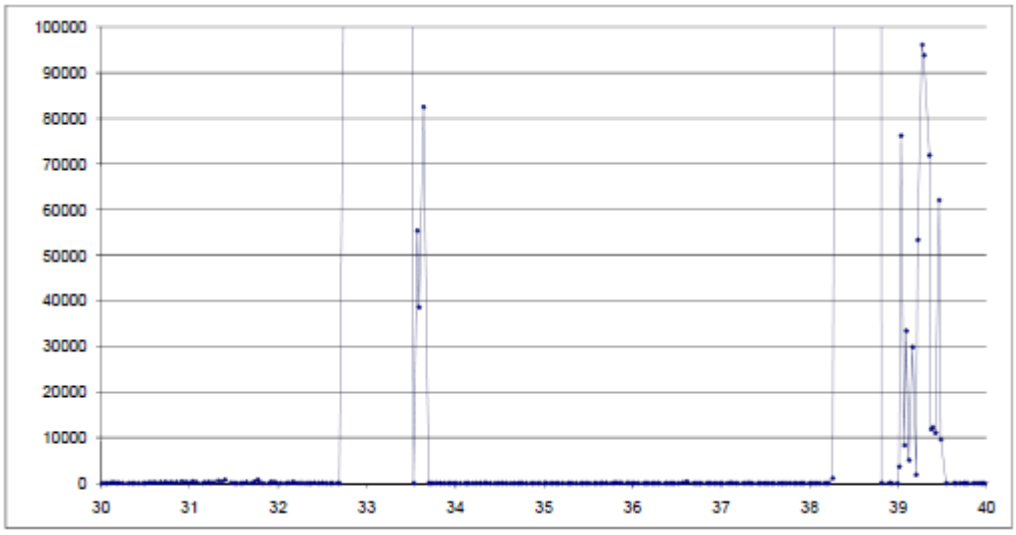

Figure 6-35: Damage Index plot (30-40 feet), run #20 conducted at 2 MPH

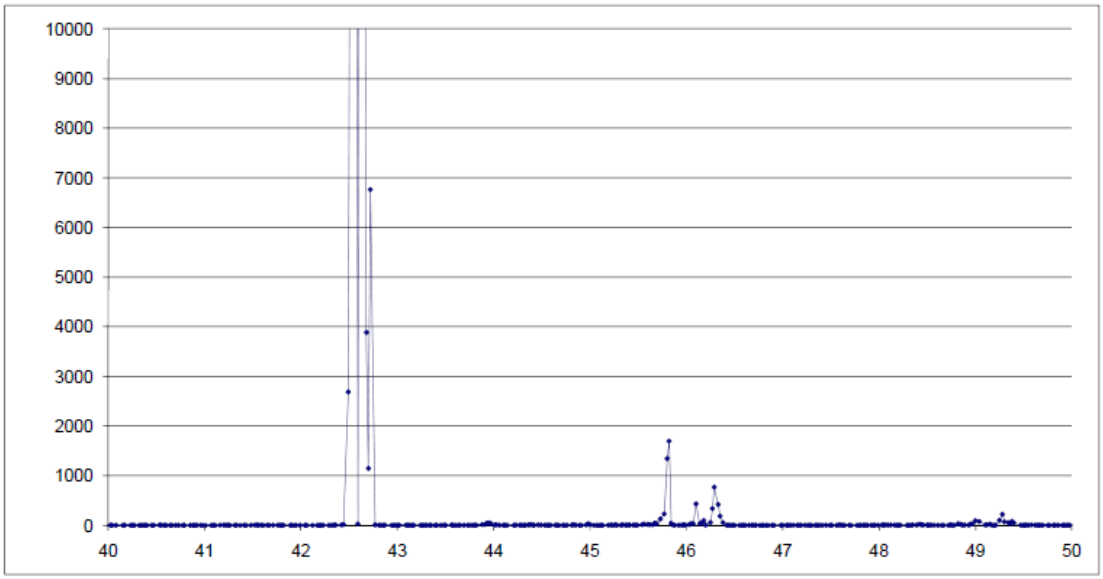

Figure 6-36: Damage Index plot (40-50 feet), run #20 conducted at 2 MPH

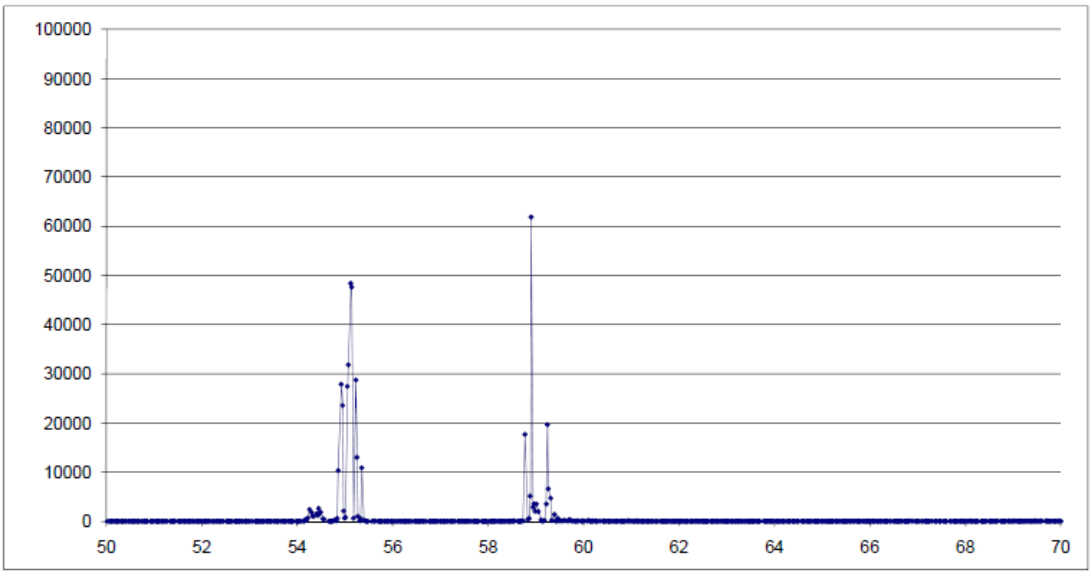

Figure 6-37: Damage Index plot (50-70 feet), run #20 conducted at 2 MPH

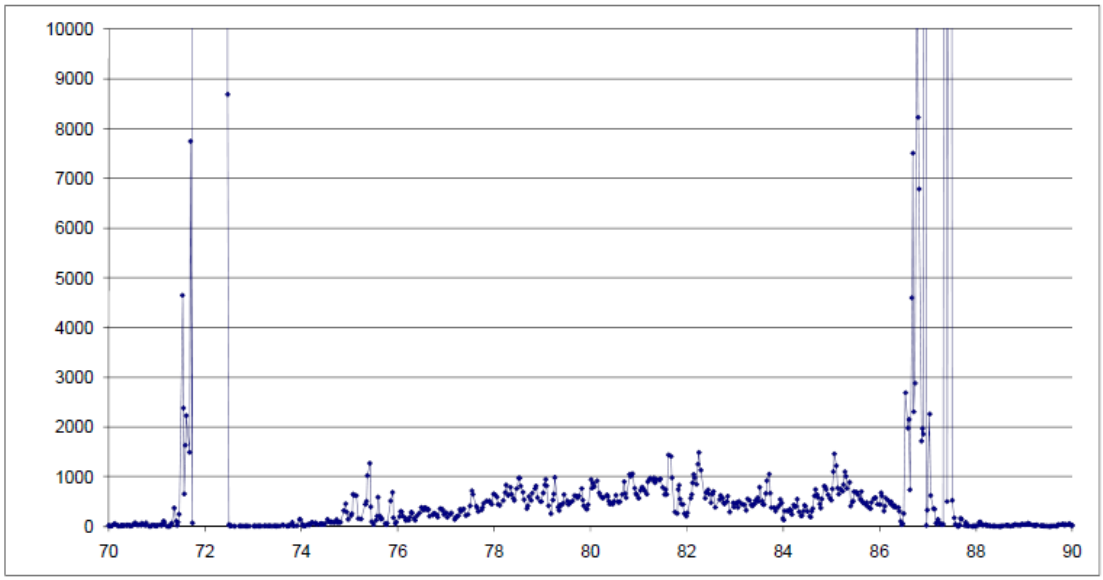

Figure 6-38: Damage Index plot (70-90 feet), run #20 conducted at 2 MPH

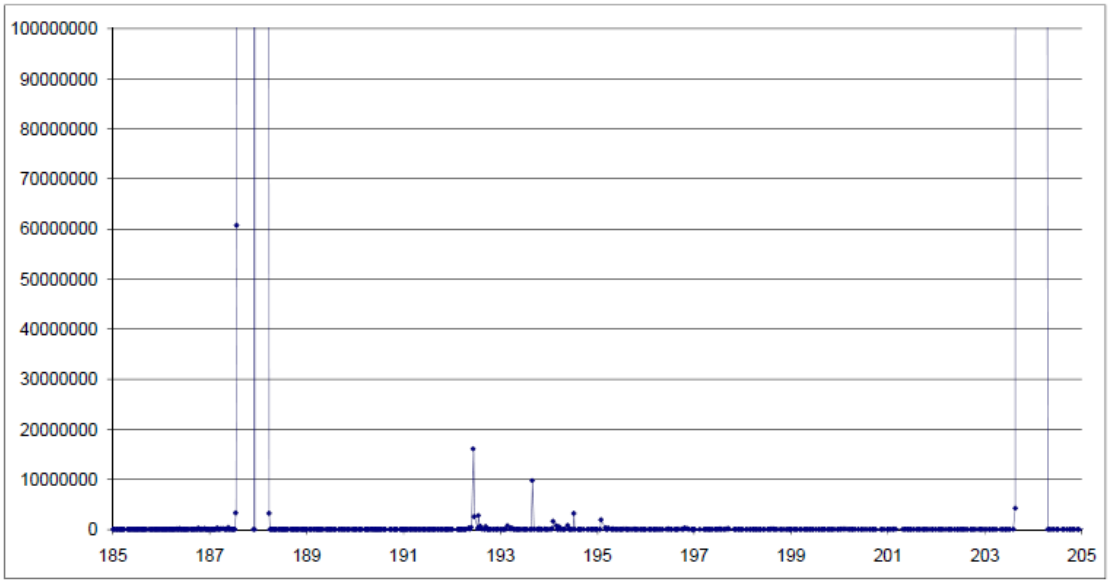

Figure 6-39: Damage Index plot (185-205 feet), run #20 conducted at 2 MPH

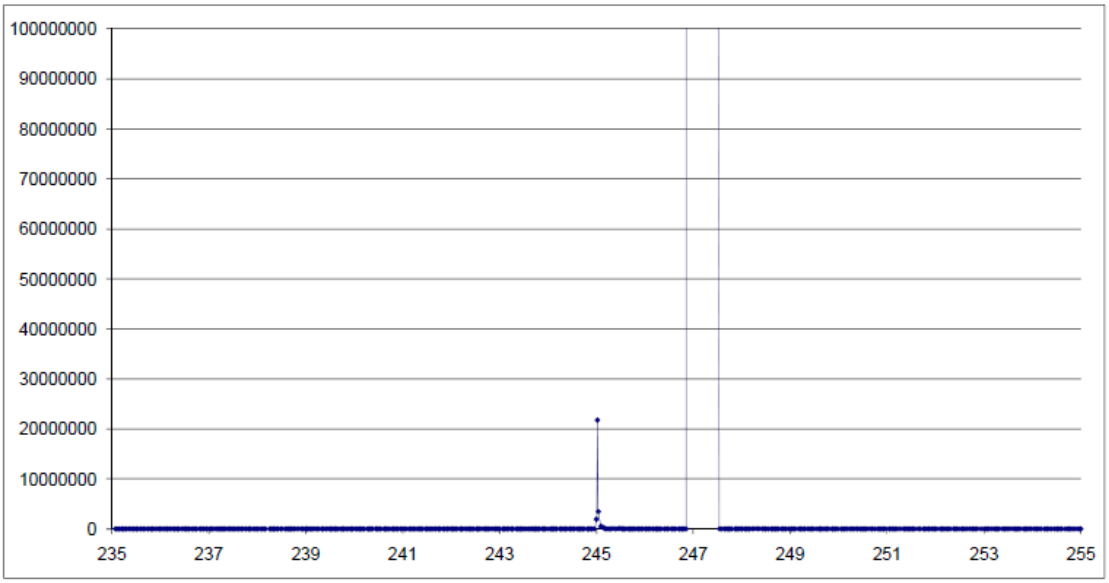

Figure 6-40: Damage Index plot (235-255 feet), run #20 conducted at 2 MPH

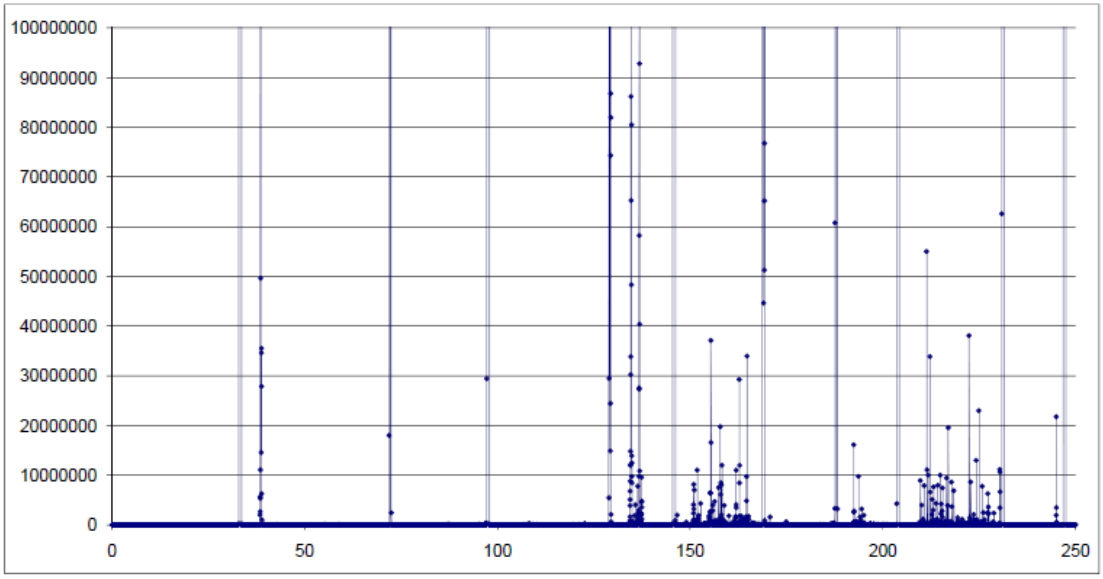

Figure 6-41: Damage Index plot (0-255 feet), run #20 conducted at 2 MPH

Figure 6-42-20 report Damage Index plots related to run #47, conducted at 9 MPH, the maximum speed obtainable on the track. Figure 6-49 includes the Damage Index plot of the full run #47 (feet 0-255).

The runs at 9 MPH showed that the system is mechanically reliable. Defect detection repeatability at this speed is somewhat reduced due to the degraded position resolution (severely reducing overlapping). Maintaining position resolution at higher speed could be achieved by a higher repetition-rate laser, a second laser, and/or a larger inspection gage (distance between sensor pairs).

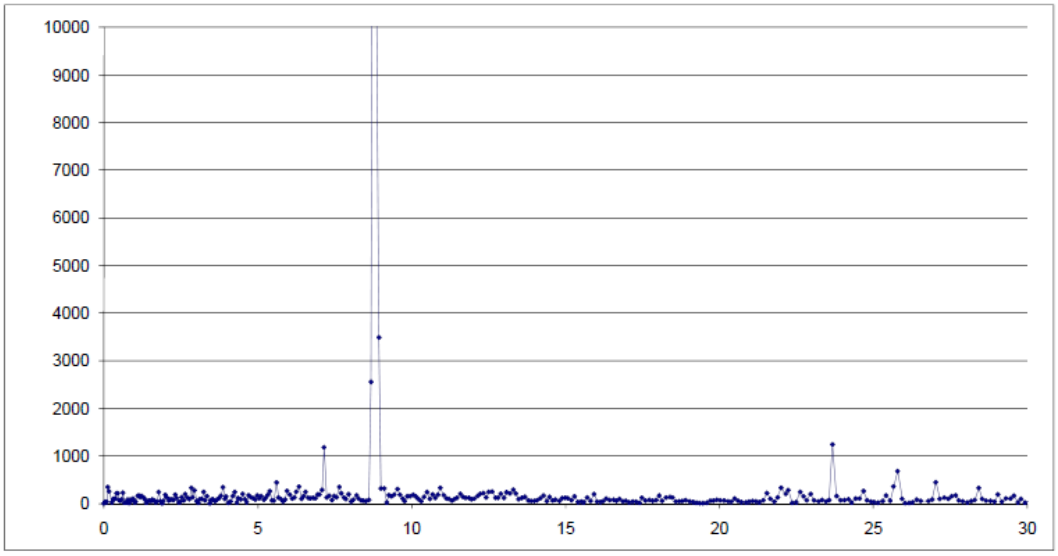

Figure 6-42: Damage Index plot (0-30 feet), run #47 conducted at 9 MPH

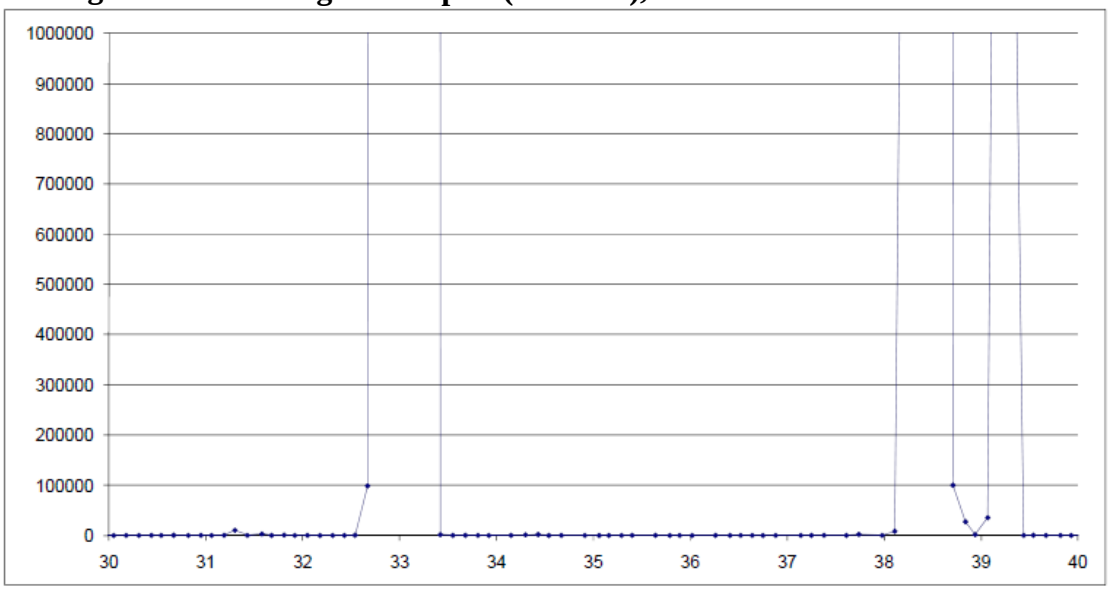

Figure 6-43: Damage Index plot (30-40 feet), run #47 conducted at 9 MPH

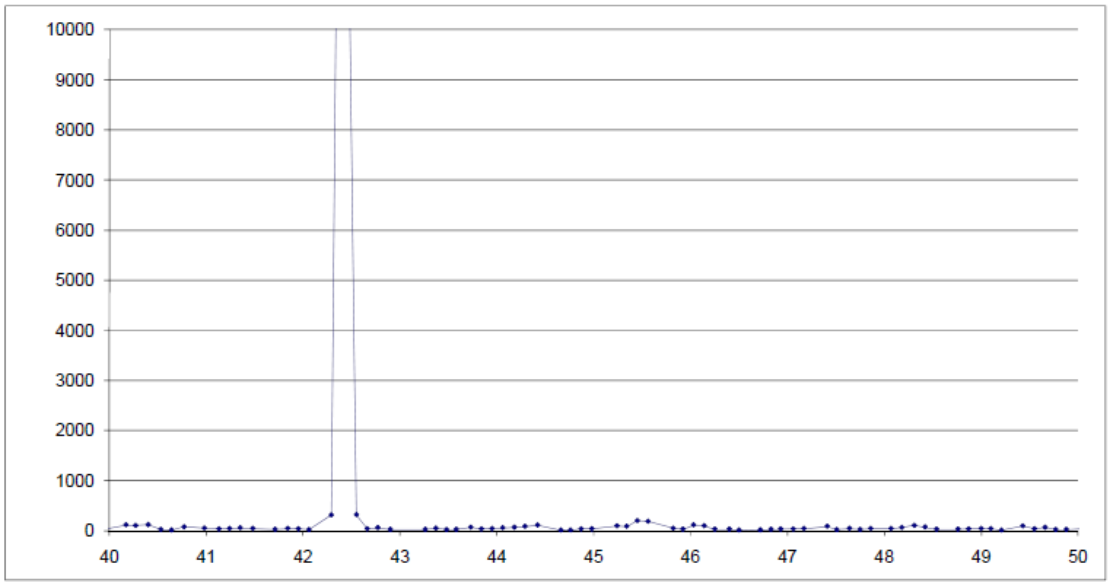

Figure 6-44: Damage Index plot (40-50 feet), run #47 conducted at 9 MPH

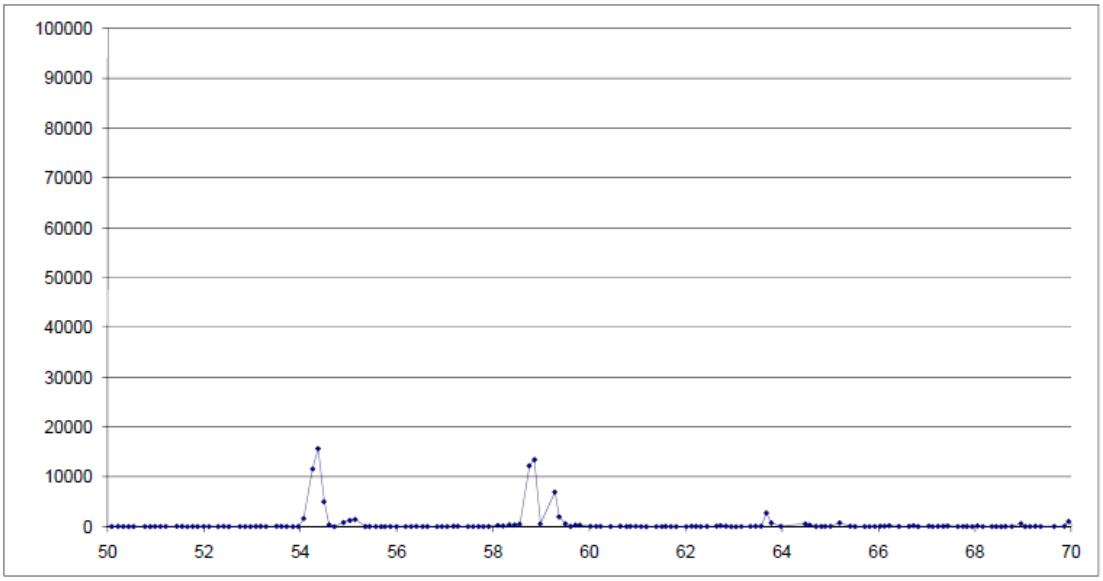

Figure 6-45: Damage Index plot (50-70 feet), run #47 conducted at 9 MPH

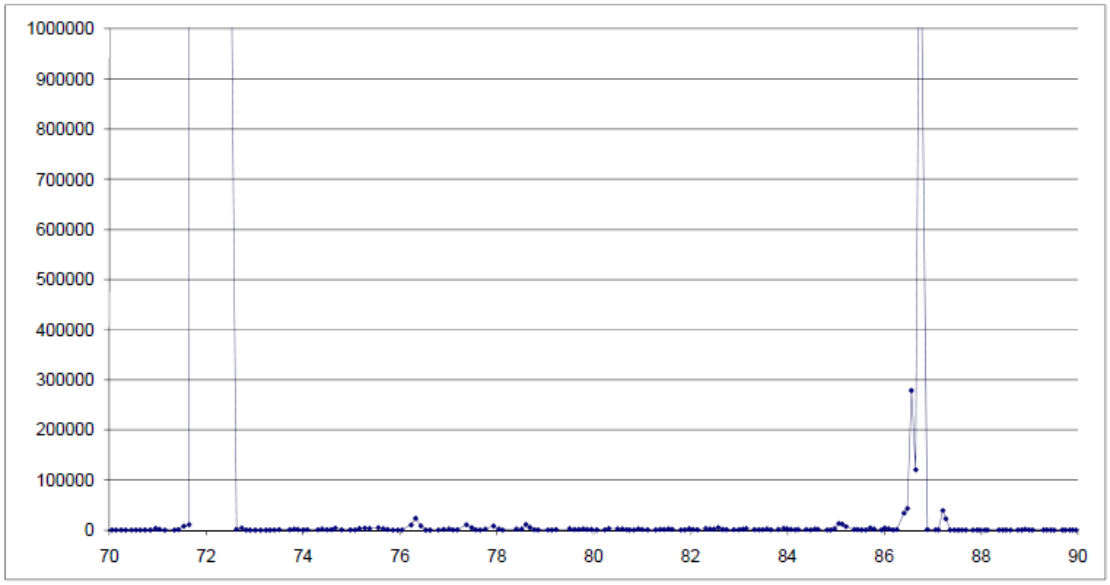

Figure 6-46: Damage Index plot (70-90 feet), run #47 conducted at 9 MPH

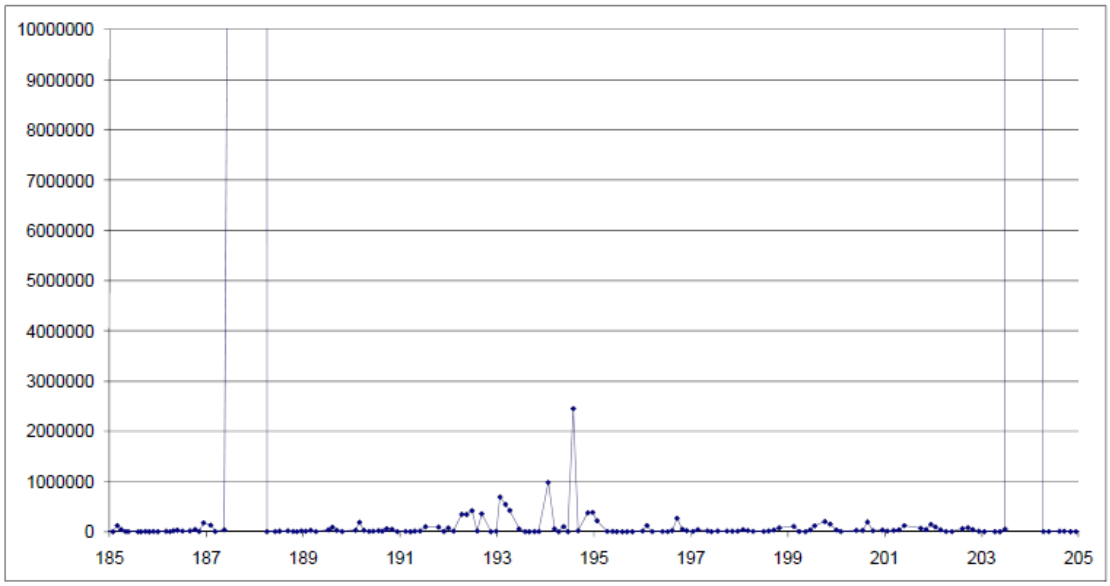

Figure 6-47: Damage Index plot (185-205 feet), run #47 conducted at 9 MPH

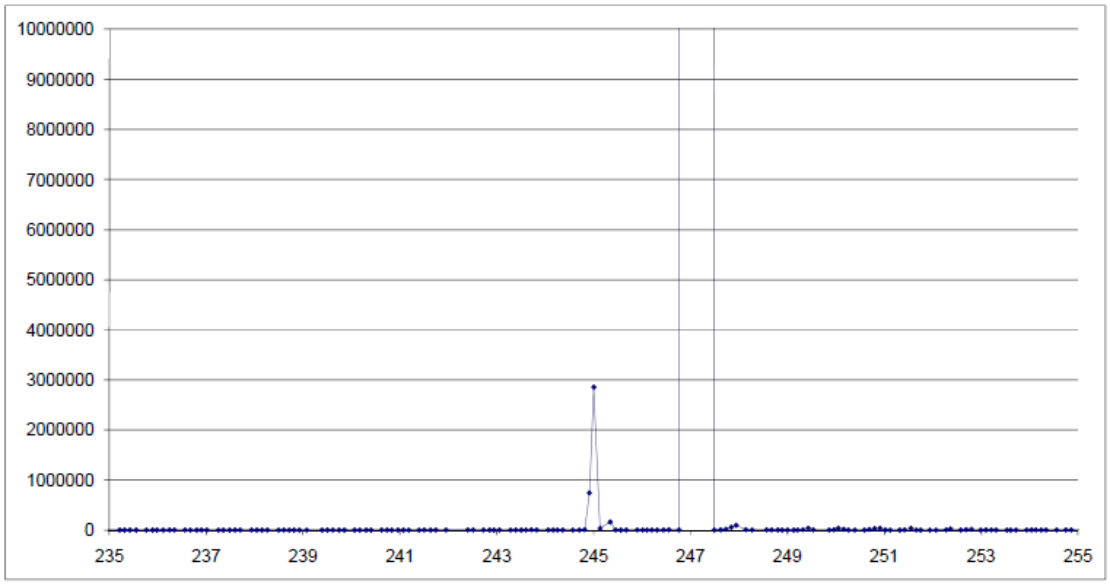

Figure 6-48: Damage Index plot (235-255 feet), run #47 conducted at 9 MPH

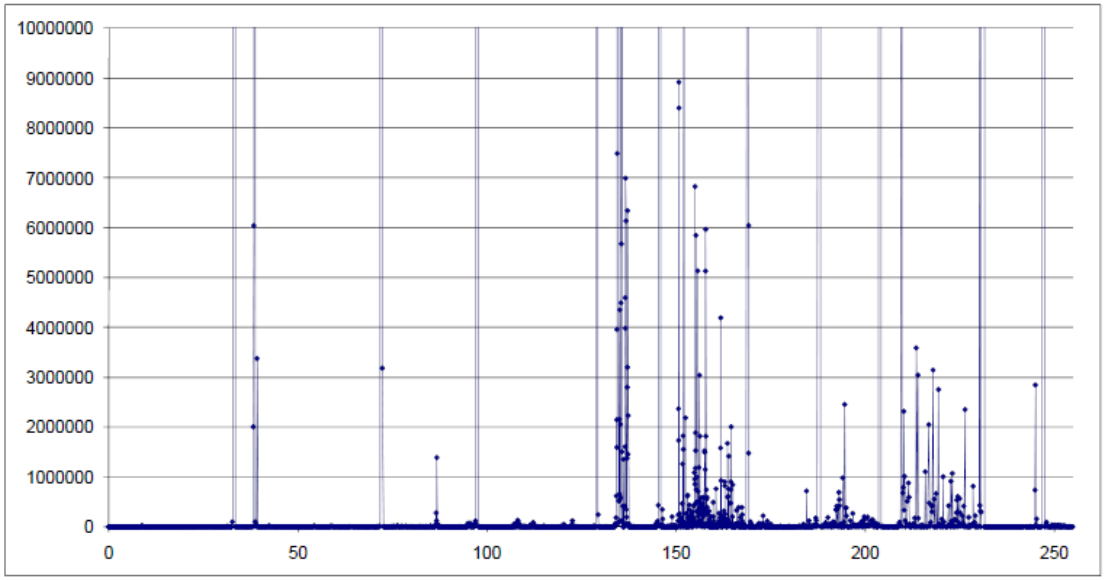

Figure 6-49: Damage Index plot (0-255 feet), run #47 conducted at 9 MPH

6.5.2 Weld signatures

One achievement of the tests was the realization that the system showed a different response between “good welds” and “defective welds,” hence allowing for the detection

of weld defects. This differentiation is rarely achievable by current ultrasonic rail inspection systems. As shown in the example of Figure 6-50, the prototype detected a good weld at feet 54'6", a 10% TD at feet 55'0" and a 50% Defective Field Weld at feet 59'2". It can be seen in this plot that the response to a "good weld" is a high-level stable plateau with no local minima points, while defects and "defective welds" produce a more "jumpy" Damage Index with several local minima points. This behavior could be used to train an automatic defect classification algorithm or used under operator's judgment to detect defects within welds.

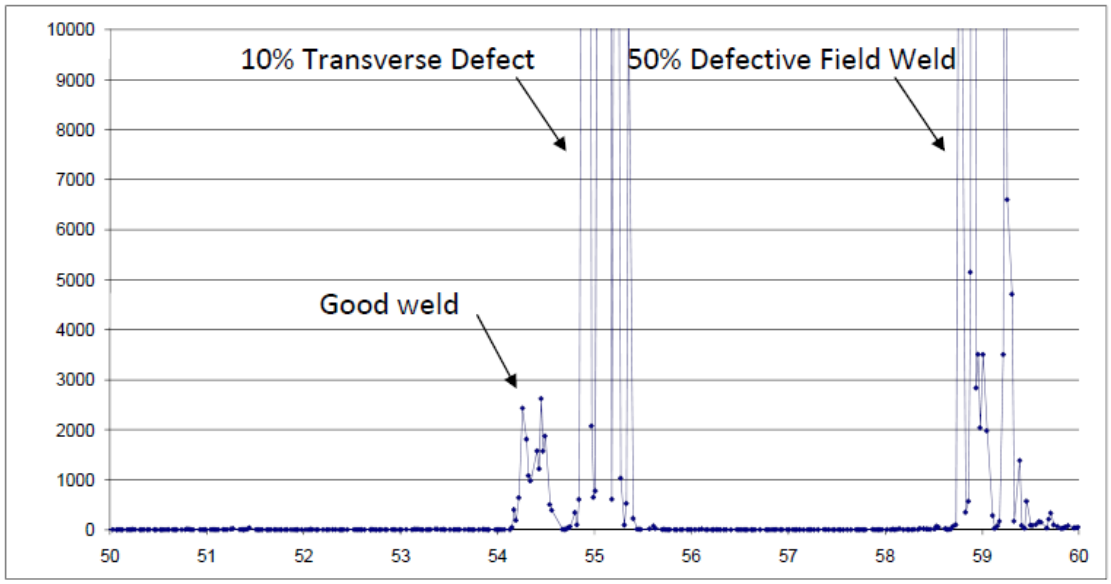

Figure 6-50: Example of different signatures of "good weld", "transverse defect" and "defective weld"

6.5.3 Detection of Horizontal and Vertical Split Head defects

The prototype overall goal was targeting Transverse Defects as these are historically the number one cause of concern for train accidents. However, the number two cause of concern is Vertical Split Head (VSH) defects. An excellent outcome of the tests was the

realization that the system showed an excellent reliability of detection of the VSH defect. This is an important achievement, since VSH are often missed by conventional ultrasonic rail inspections because their orientation may not render a reflection of the ultrasonic beam from ultrasonic wheel search units. Figure 6-51 shows an example of detection of the 1’ long VSH defect present at Herzog’s rail defect farm (tie #23 from Table 6.4).

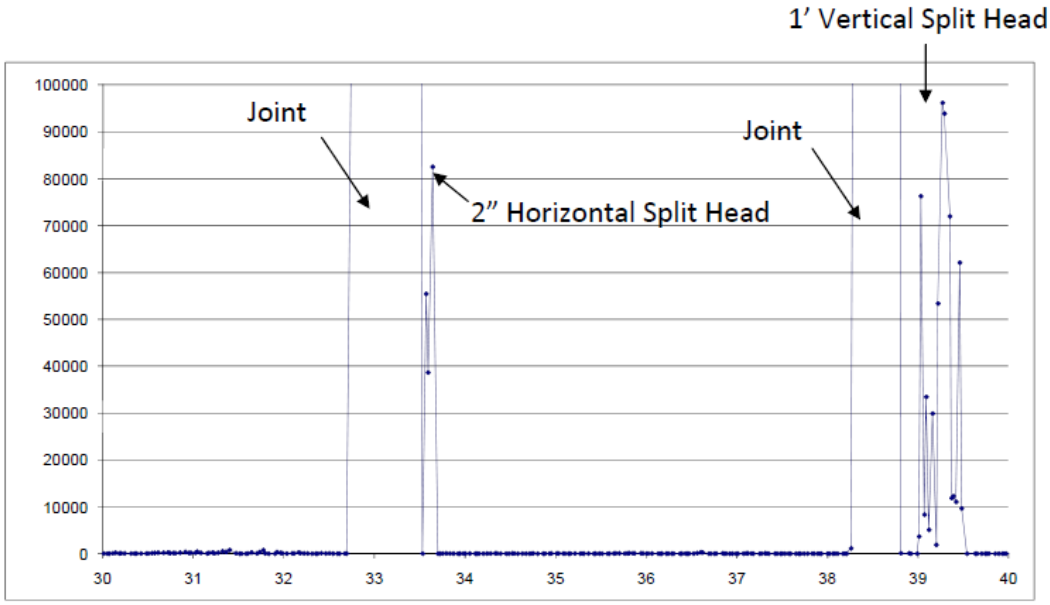

Figure 6-51: Example of clear detection of 1’ long Vertical Split Head (VSH) defect (two Joints and a Horizontal Split Head defect also shown).

7. Rail Thermal Stress Measurements in Rails by EMI: Experimental Results

7.1 Electromechanical Impedance at UCSD Powell Labs

A series of tests were conducted to test the ability of the EMI technique to measure thermal stresses in rails at UCSD's Powell laboratories of the Structural Engineering Department . The Powell laboratories are a unique testing environment for structural engineering testing. In this chapter three experiments are discussed. The first test is a proof of concept test with a beam that was machined from a section 136RE rail. The beam is not large in scale, making it easy to handling and testing. The second and third experiments are much larger in scale, and could have only been executed in the Powell laboratory or would have been done in the field at even greater expense. These test were performed on full-scale sections of rail in both a fixed-fixed boundaries and free-free boundaries.

7.2 EMI Measurement Parameters

As discussed in chapter five, traditionally the Electromechanical Impedance method has been used for damage detection by tracking a variety of measurement parameters. Considering the expected response due to a stress in the structural element, the same parameters have the potential to track the changes in the resonance frequencies due to the stress. Several studies have applied this hypothesis to small laboratory size test specimens that have low stiffness, where the resonance frequencies are easily changed by applied stresses. In order to apply this method to the determination of the rail neutral

temperature, it has to be tested on an element that has the high stiffness that is expected. Hence any change in the resonance frequencies will be small and difficult to measure in the impedance response.

The most common measure for damage detection is a shift in the frequencies of the resonance in the admittance measurement. Ong *et. al.* [88] investigated this measure in an analytic study on a loaded simply supported beam. In this study, it was shown that a compressive force will shift the resonance to a lower frequency and that tension had the inverse affect, shifting the resonance to a higher frequency. Following the same hypothesis, Lim *et. al.* [92] performed an experimental study on small laboratory specimens. Their results showed that, in the application of the method to a real structure, not only does the frequency peak shifts, but also it changes in amplitude. In the study by Lim, both the frequency shift and the amplitude of the same frequencies were measured.

Two other measures requiring a baseline measurement are also very common in the EMI method. The Root Mean-Squared Deviation (RMSD) has been widely used. Yang *et. al.* and Annamdas *et. al.* [89, 91] both used the RMSD to measure the in-situ stress in laboratory test specimens. The RMSD is a measure of differences between a predicted, or baseline, value and the current measured value. It is defined as:

$$RMSD(\%) = \sqrt{\frac{\sum_{i=1}^{N}(y_i - x_i)^2}{x_i}} \times 100 \qquad \textbf{7.1}$$

such that x_i and y_i are the signatures obtained from the piezoelectric wafer before (baseline) and after loading, respectively. The second measure is variation of the RMAS that focuses on specific frequency ranges to isolate the changes to those ranges and not the entire frequency range covered by the RMSD. Introduced by Annamdas and Soh [110, 111], the Piezoelectric Efficiency Factor (PEF) is defined as:

$$PEF\left(\%\right)=\frac{\frac{C_1+C_2+\cdots+C_k+\cdots+C_N}{N}\sqrt{R_1^2+R_2^2+\cdots+R_k^2+\cdots+R_N^2}}{R_1C_1+R_2C_2+\cdots+R_kC_k+\cdots+R_NC_N}\times 100 \qquad \textbf{7.2}$$

where the subscripts 1, 2, *k*, and *N* are the number of the frequencies considered, $C_1, C_2, \ldots, C_k, \ldots, C_N$ are the means of the frequency ranges, and $R_1, R_2, \ldots, R_k, \ldots, R_N$ are the RMSD values of the same frequency ranges.

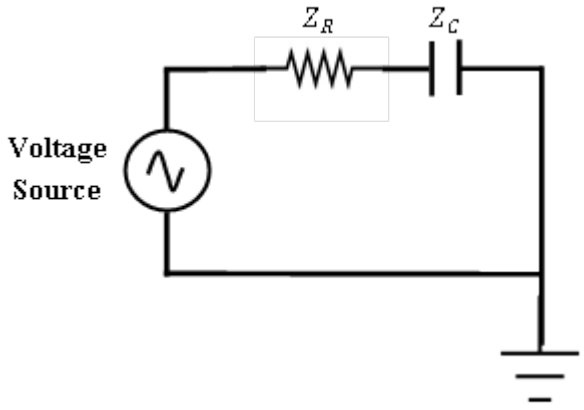

Figure 7-1 Resistor/Capacitor Circuit for Impedance Analysis

In previous studies, the focus has been on changes in the real part admittance signature, the conductance. However, as mentioned in the study by Annamdas *et.al.* [89], load could have a larger influence on the imaginary part, the susceptance. In this dissertation's study there is agreement with this hypothesis. Both the admittance and

susceptance signatures were investigated. Additionally, the slope of the signatures will reinforce that susceptance is a better measure in the change in frequency response based on the following logic. Impedance analysis is based on the response of a regular resistor capacitor circuit as that shown in Figure 7-1. The impedance analysis of the circuit is:

$$Z = Z_{\mathrm{R}} + Z_{\mathrm{C}} = R + \frac{1}{i\omega C} \qquad \textbf{7.3}$$

Then the admittance will be:

$$Y = \frac{1}{Z} = \frac{1}{R + \dfrac{1}{i\omega C}} = \frac{\omega^2 C^2 R}{1 + \left(\omega RC\right)^2} + i\frac{\omega C}{1 + \left(\omega RC\right)^2} \qquad \textbf{7.4}$$

The susceptance is then:

$$B = \frac{\omega C}{1 + \left(\omega RC\right)^2} \qquad \textbf{7.5}$$

Since, for piezoelectric transducer, the resistance is comparably small, the susceptance can be written as:

$$B = \omega C \qquad \textbf{7.6}$$

Thus the susceptance will be a function of the frequency response, whereas the conductance is considered to be a constant to the frequency response.

For this dissertation's study, none of the above parameters are dismissed for the conductance or susceptance. Instead, all the parameters responses are investigated for both the conductance and the susceptance. It will be shown that the susceptance is indeed the better measure to monitor load/stress levels in the structure.

7.3 Proof of Concept Experiment

The first experiment performed to investigate the EMI method was performed on a rectangular section of rail steel. In order to accommodate the dimension of the MTS 110 tension compress test apparatus, it was necessary to fabricate a test sample. Considering the geometry of the rail steel that is in question, it was chosen to use that rectangular beam that best replicated the web section of the rail geometry and fit in the test apparatus flat grips. The beam was machined from a section of 136RE rail in order to insure that the material properties were consistent for all the experimental investigations. Rail steel is a unique high carbon steel that has a high modulus (~205 GPa) and tensile strength (~730 MPa) and matching the properties was cost prohibitive with the available stock material of material suppliers. The final dimensions of the beam were 15.4mm x 150.7mm x 915mm (see Figure 7-2).

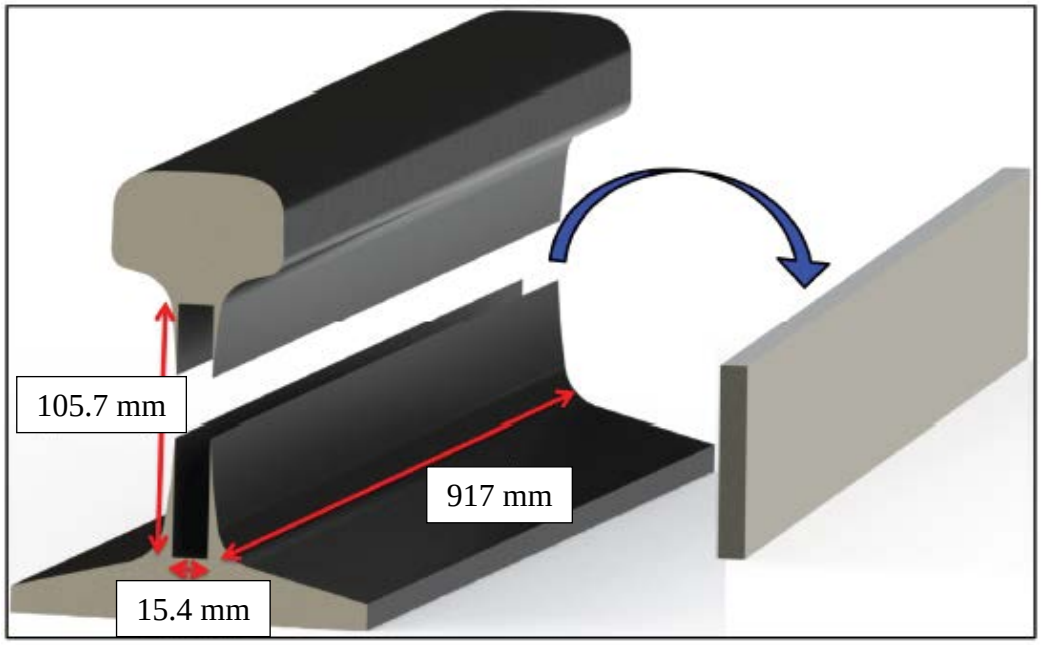

Figure 7-2: Origin of Rectangular Beam for Proof of Concept Experiment.

A piezoelectric transducer was bonded to the neutral axis of the beam for the impedance measurements. Figure 7-3 shows the wafer bonded to the test specimen. The wafer was an APC 850 WFB with the dimensions of 12.7mm x 12.7mm x 0.635mm manufactured by APC International. The wafer used has commonly available properties and are affordable. Clearly, from Figure 7-3 the mass and size of the piezoelectric will have no effect on the dynamic behavior of the steel beam. It is important to note that the transducer must be compliant to the structure in order the measure variations of structure without any influence of the transducers mass and stiffness.

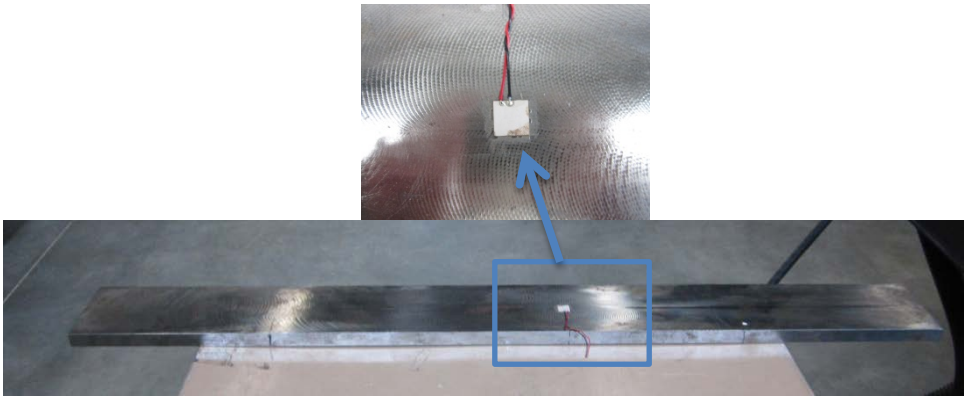

Figure 7-3: Piezoelectric Wafer Bonded to Test Specimen

Figure 7-4 displays the proof of concept experimental set up. The test specimen was mounted in the MTS 110 machine vertically. In order to take advantage of the testing time several sensors were placed on the beam, here only the results from the piezoelectric wafer are presented. The test performed with the other sensors were not pertinent to this investigation. Displayed in Figure 7-5, the location of the piezoelectric wafer and a strain gauge are shown. Impedance measurements were taken with a HP 4194A impedance analyzer and the data was acquired via a GPIB interface on a

National Instruments™ PXI chassis and a LabView™ virtual instrument software program. Measurements were taken over a frequency range of 100 kHz to 600 kHz in order to capture the changes of the resonant frequencies of the beam.

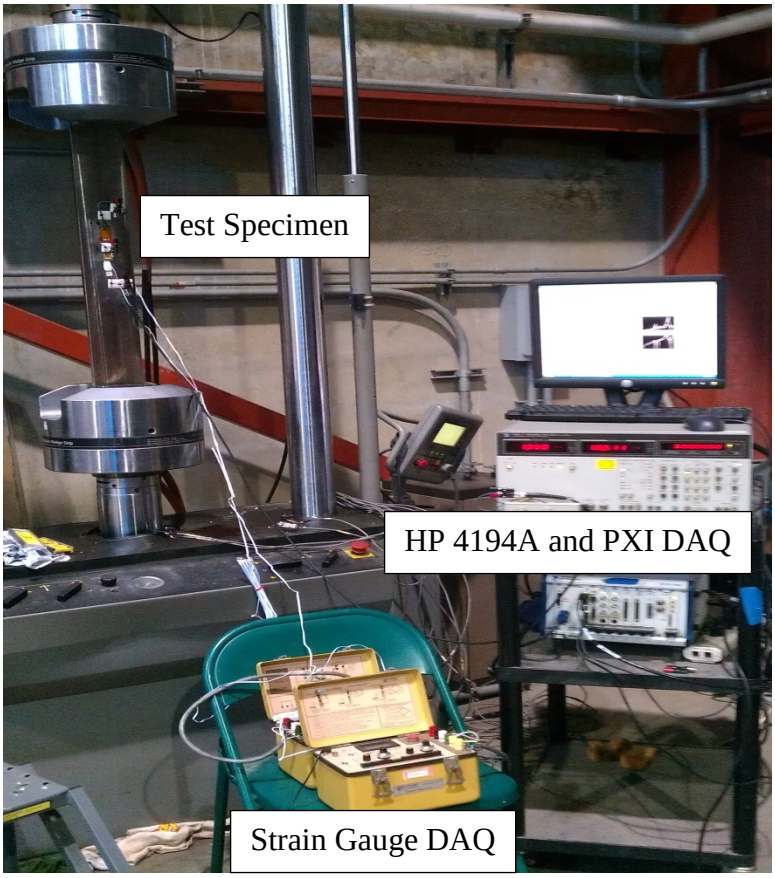

Figure 7-4: Proof of Concept Experimental Test Set Up

Both tension and compression loads were applied to the beam in order to test the method for both stress states. The stresses applied to the specimen ranged from 54.5 MPa (266 μstrain) in tension to -81.8 MPa (-400 μstrain) in compression in 20 steps of 6.8 MPa (33 μstrain) each. In this range, the test sample was loaded in the purely elastic range such that only 20% of the critical buckling load was reached and less of 10% of the tensile yield. Within this loading range, the only change in the structural stiffness

was due to the stress in the beam as no damage occurred. Therefore, the only influence on the changes to the EMI signatures was expected to result from changes in the dynamic stiffness of the test specimen.

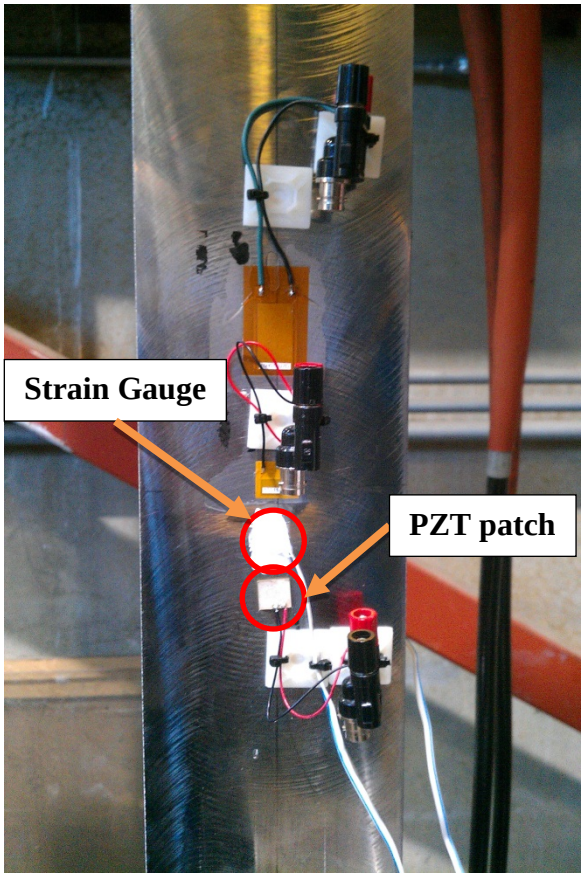

Figure 7-5: Location of Piezoelectric Wafer and Strain Gauge

7.4.1 Proof of Concept Experimental Results

The test specimen was a very stiff structure and variations in the frequency response do to the imposed loads were small, even at the extremes of the loading relative to the zero stress state. The conductance and susceptance signatures measured in the test are given in Figure 7-6a and 7b for the extreme loadings. It is clearly shown that the changes in the signatures are small. The three parameters discussed in the previous

section (RMSD, PEF and slopes of conductance and susceptance) were considered as possible stress measurements.

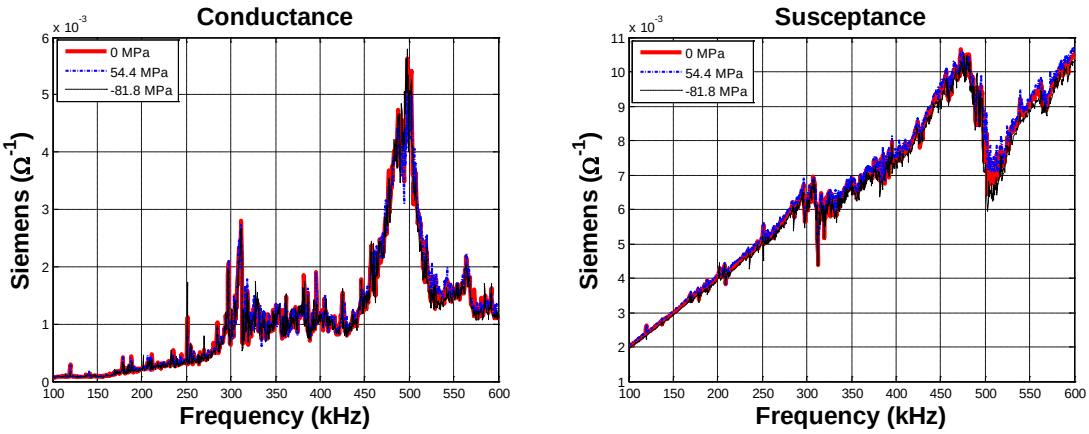

Figure 7-6: (a) Conductance and (b) Susceptance at -81 MPa, 0 MPa, and 54.4 MPa

In the RMSD measurement, shown in Figure 7-7a and 7.7b, both the conductance and the susceptance have good monotonic trends. It is clear that the susceptance has a better linear trend through the loading than the conductance. The tendency is linear, with the rate of change between each loading step relatively constant. Moreover, the symmetry of the curve shows that the measurement is consistent through both the tensile and compressive load phases. In addition, the location of the minimum of both parameters at the -6.8 kN is interesting, as the minima should occur at the baseline measurement that was taken at zero load. The location of the minima in the RMSD of conductance and susceptance is only off by 33μstrain from the true zero stress point. This is an acceptable level of error for rail Neutral Temperature

measurement as it translates into an accuracy of about ±4.5 °F considering a thermal expansion coefficient of steel of about 7 ppm/°F.

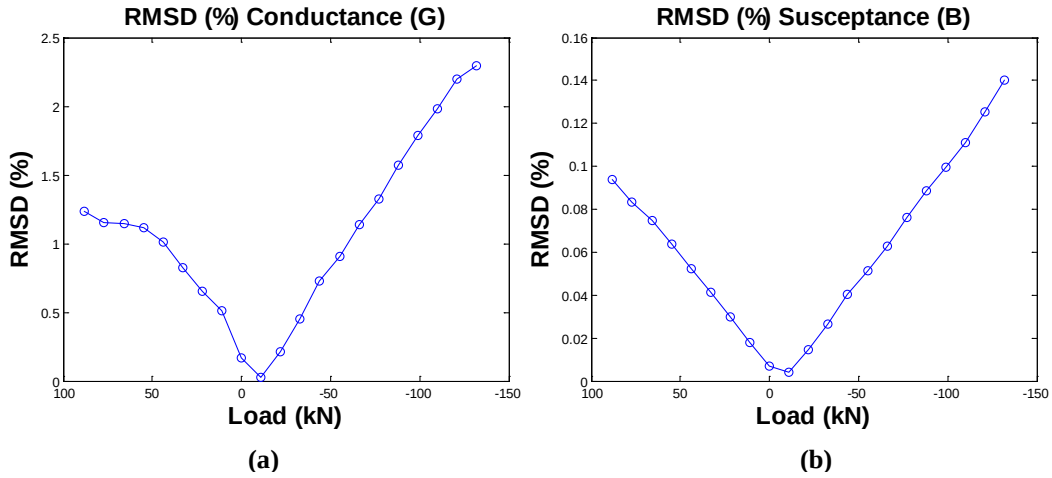

(a) (b)

Figure 7-7: RMSD for (a) Conductance and (b) Susceptance

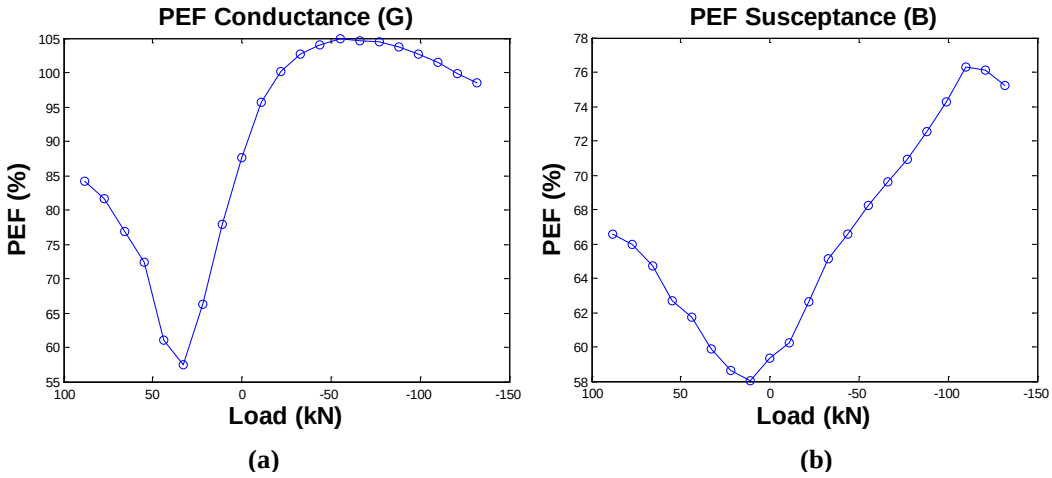

(a) (b)

Figure 7-8: PEF for (a) Conductance and (b) Susceptance

The PEF factor, seen in Figure 7-8a and b, is not as stable as the RMSD. The trend is not as clear for either the conductance or the susceptance indicators. The PEF is only a measure of a limited frequency range, and it thus has difficulty capturing the small variations in the structural response that are expected for such a stiff specimen. In this

study, three frequencies were chosen from the dominant resonant structural frequencies found in the zero stress load measurement. Previously it had been shown that the PEF becomes more stable and sensitive when the number of frequency ranges is increased [90].

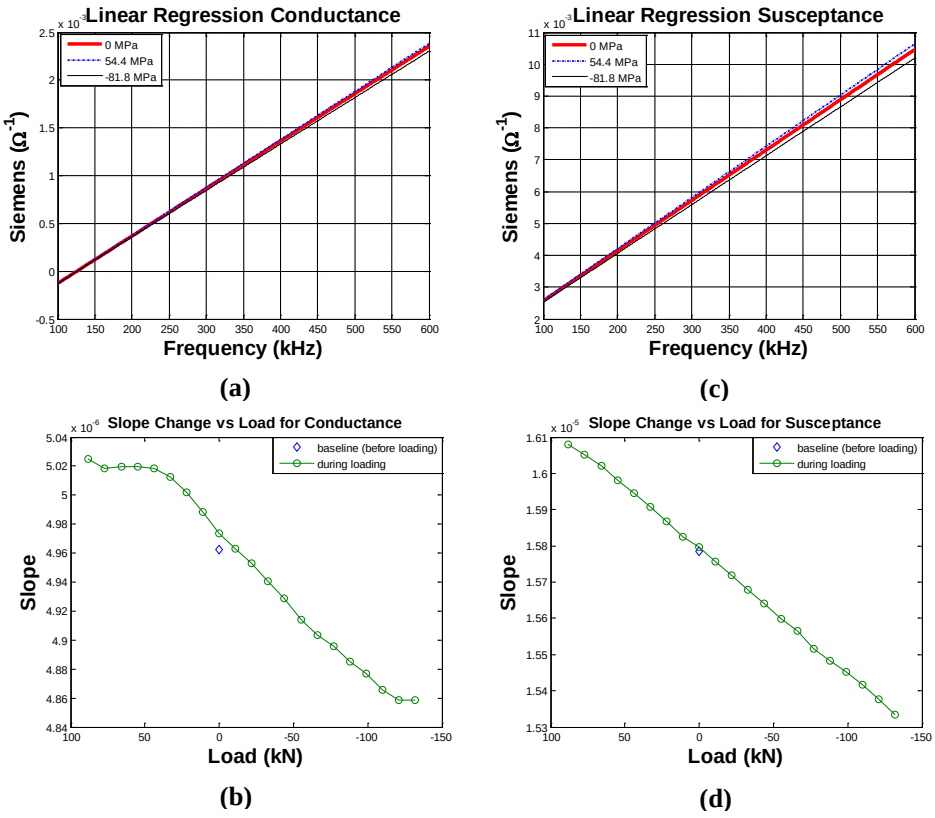

Figure 7-9: (a) Linear Regression of Conductance, (b) Slope Change of Conductance, (c) Linear Regression of Susceptance, (d) Slope Change of Susceptance

In Figure 7-9a and c, the slope change of the conductance and susceptance signatures are shown for the extreme loads to the zero load. Both signatures have a rotation that is counter-clockwise in tension and clockwise in compression. It is clear that there is a greater rotation in the susceptance. Plots of the slope vs. load are shown

in Figure 7-9b and d. Comparing the conductance to the susceptance, it is seen that the susceptance has an appealing linear trend with very good correlation to the baseline value taken at the zero load. While the conductance also has a linear trend, it is inconsistent in tension and at the higher compressive loads. Additionally, the change per load step in the susceptance is very stable through the loading cycle. With a constant change is each load step the resonant frequencies of the structure will also have a constant change as was determined in the study by Shaker[112]. The linear trend with a constant change in the susceptance slopes over the loading shows that the measure reflects the change in the structural frequencies. Having a good correlation with the baseline zero stress slope measurement shows the consistency of the measurement.

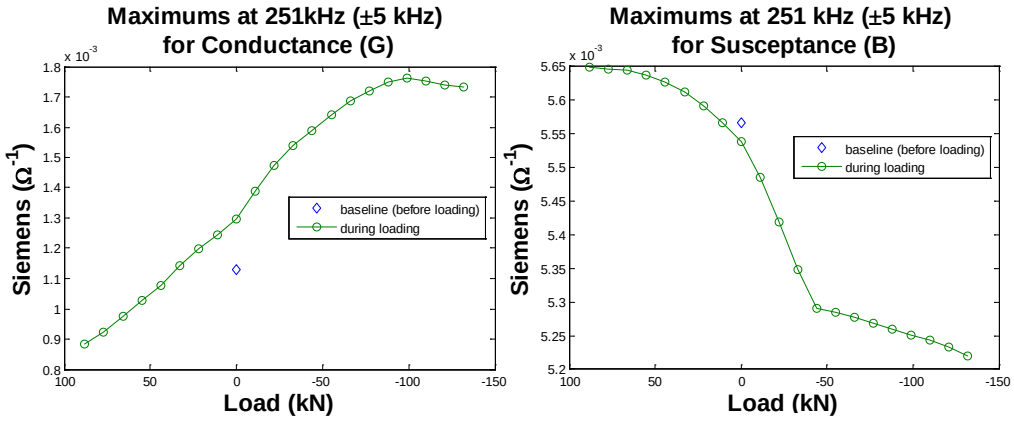

(a) (b)

Figure 7-10: Amplitude Change for 251 kHz ± 5kHz (a) Conductance (b) Susceptance

The amplitude changes were measured by taking the maximum within a defined frequency range. Here three ranges were investigated 251 kHz ± 5kHz, 310 kHz ± 5kHz, and 351 kHz ± 5kHz. The results are shown in Figure 7-10-12 and upon

inspection, it is seen that there is no discernible trend in either the conductance or the susceptance.

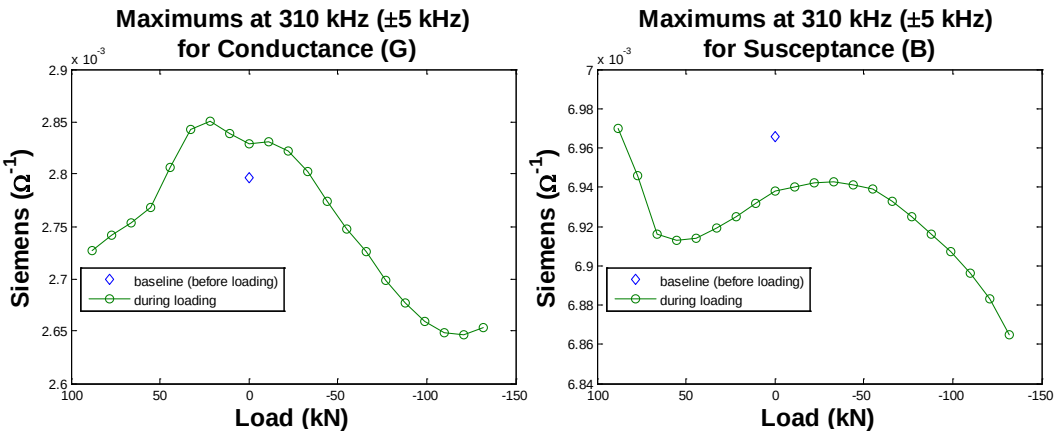

(a) (b)

Figure 7-11: Amplitude Change for 310 kHz ± 5kHz (a) Conductance (b) Susceptance

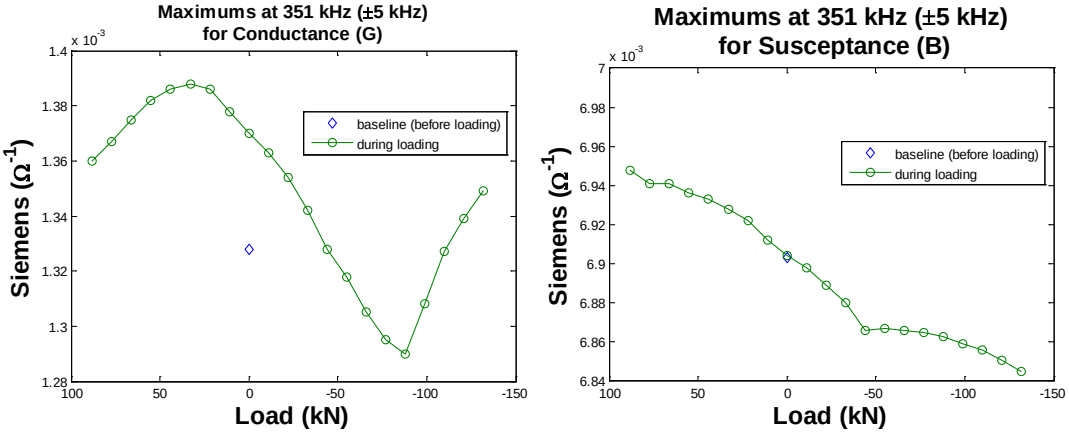

(a) (b)

Figure 7-12: Amplitude Change for 351 kHz ± 5kHz (a) Conductance (b) Susceptance

The frequency shift was also inspected over the same frequency ranges as the amplitude change. It is seen in Figure 7-13-15 that there is no frequency shift in these frequency ranges.

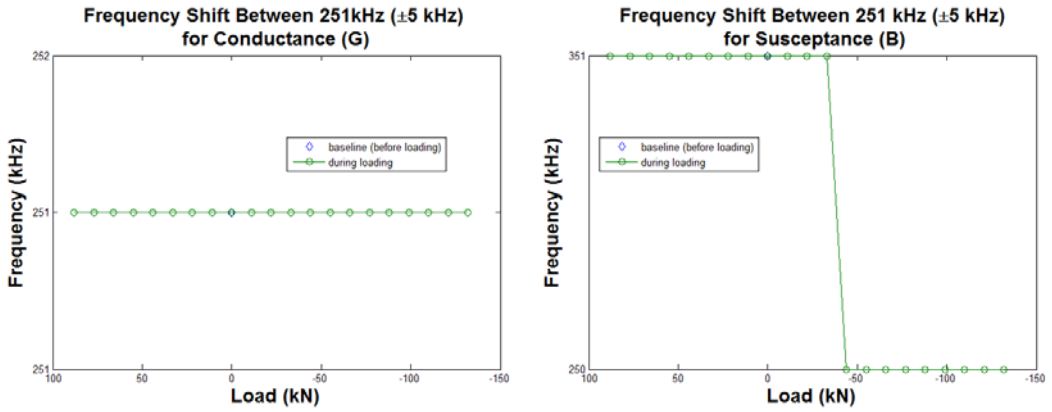

(a) (b)

Figure 7-13: Frequency Shift for 251 kHz ± 5kHz (a) Conductance (b) Susceptance

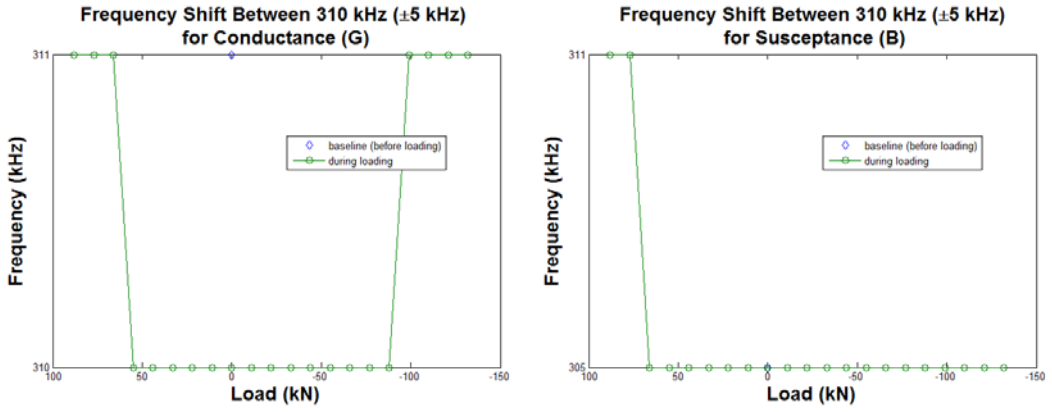

(a) (b)

Figure 7-14: Frequency Shift for 310 kHz ± 5kHz (a) Conductance (b) Susceptance

Conclusions:

The EMI method was tested next for a proof of concept to track changes in stress in a full section of rail steel. Several parameters were explored and it was found the RMSD, PEF, and slope change are valid for further investigation. Additionally there is a better trend in the susceptance parameters than in the conductance as was expected since the susceptance is a function of the frequency response. In the next section the scale of the specimen will be increased to a full size rail track.

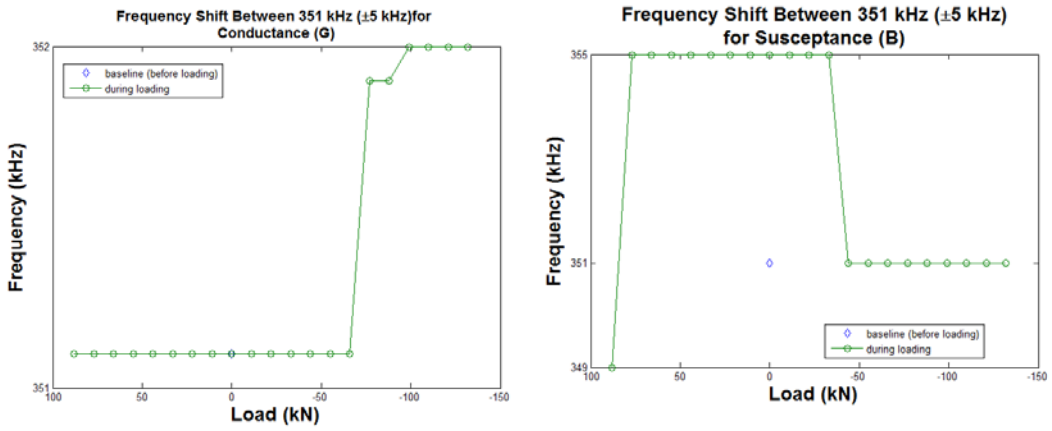

(a) (b)

Figure 7-15: Frequency Shift for 351 kHz ± 5kHz (a) Conductance (b) Susceptance

7.4 Large Scale Experiment (Fixed Rail)

Since the ultimate purpose of the EMI method is to measure the rail neutral temperature, testing the method needs to be executed on a test platform that is representative of what is to be expected in the field. To achieve this, a full scale test bed was constructed at the Powell labs.

In Figure 7-17 the layout for the test bed is shown in a conceptual drawing. In order to simulate field conditions, the rail that was installed at a prestress, with a constrained end condition. This was achieved by embedding the rail in two concrete blocks, one

held in a fixed position and the other one initially free to slide in order to apply the prestress. Once the blocks had cured to an acceptable strength, the sliding block was placed on rollers and the preload was applied. Consideration of a variety of loading steps had to be considered in the design process. Particular attention was given to the loading for the application of the prestress and the ability to constrain the rain in the thermal loading cycles. An electrical heating element (rail switch heater)was then attached to the rail to simulate environmental heating to build up thermal stresses in a controlled manner.

Figure 7-16: The Powell Lab's North Building (in foreground) and UCSD's landmark Geisel Library (in distance) at dusk. The lab building features an outdoor neon sculpture, 'Vices & Virtues', by Bruce Naumann; the Stuart Art Collection

The experimental study of buckling in continuous welded rail in a large scale dates back to the 1930's. An extensive review of the history of large scale laboratory

testing is given by Kerr [113]. In the past studies the focus is on the mechanics of the

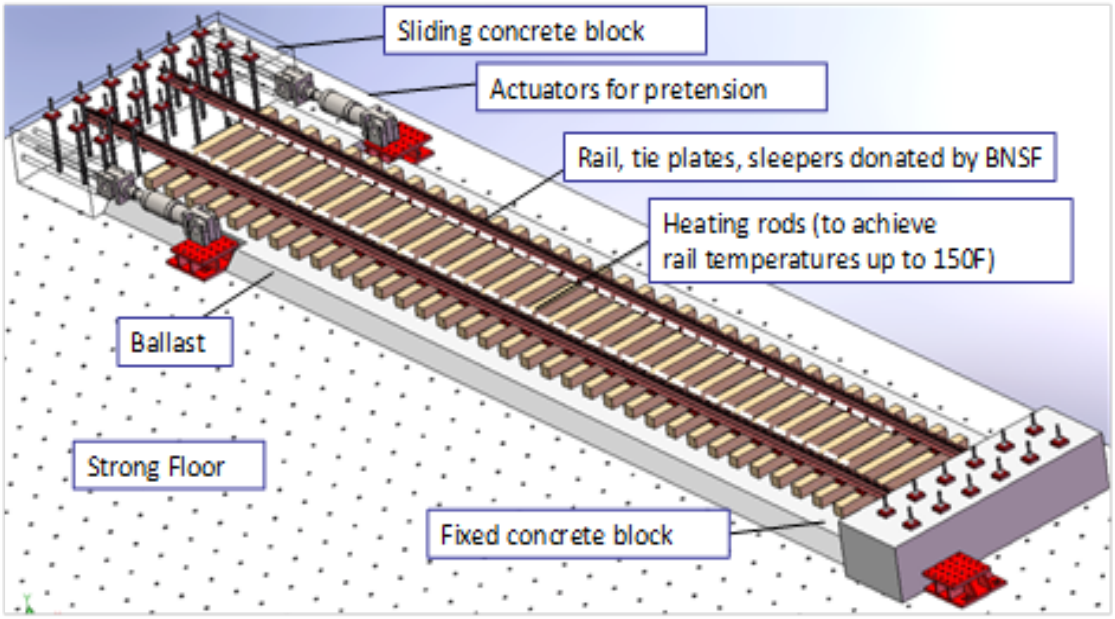

Figure 7-17: Layout for Large Scale Rail Neutral Temperature Test Bed

buckling mechanism. In this experimental exercise the rail is constrained to have a fixed-fixed boundary and the loading is well below the critical buckling load. Materials for the test specimen were donated in part from Burlington Northern and Santa Fe Railway (BNSF). Technical design support has given by John Choros of the Volpe National Transportation Systems Center. In this set up, a full-scale ballast bed was used as the foundation of the system. BNSF provided four sections of AREMA 136 rail and used wood ties with tie plates giving enough material to build the 70-ft set up. Additional funding came from a research grant from the Federal Railroad Administration.

7.4.1 Large-scale Rail Test-bed: Construction and Instrumentation

A general overview of the construction will be given here. Figure 7-18 displays the detail and a picture of the fixed concrete block. Similarly, Figure 7-19 is the rebar cage and detail for the sliding block.

In order to insure proper shear transfer from the rail to the concrete blocks, a series of C-channels and a flat backing plate were welded on to the ends of each rail section. Figure 7-20 displays the conceptual drawing and the finished product of two of the four rail sections needed to complete the system.

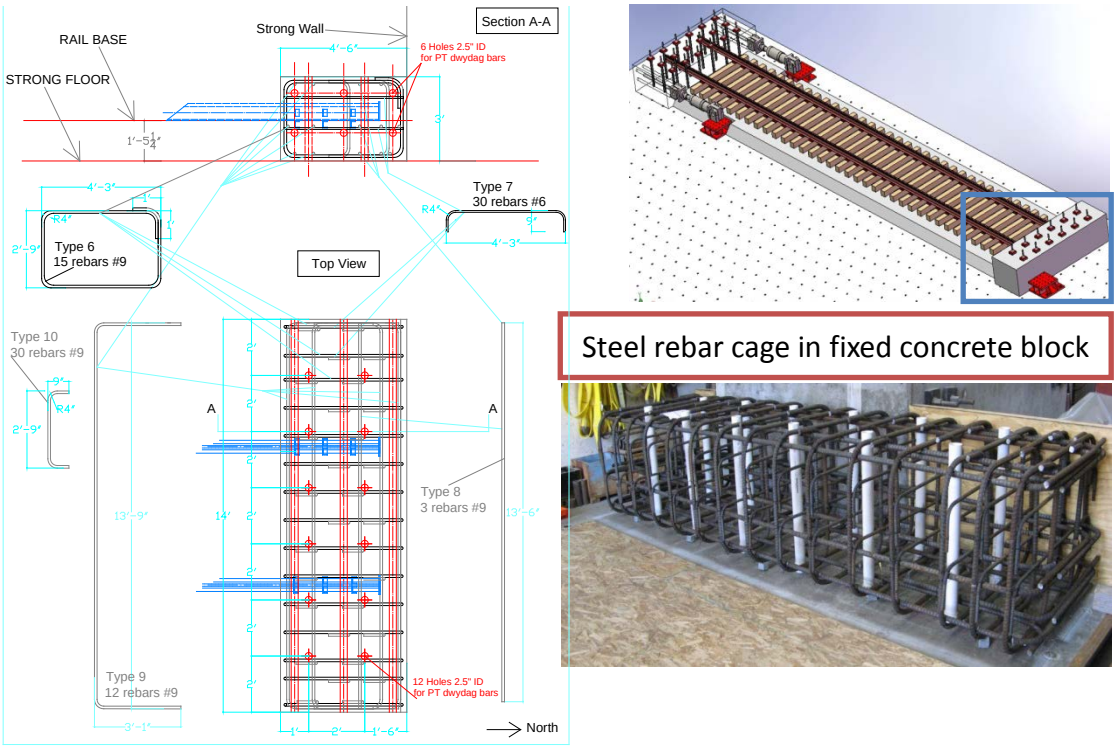

Figure 7-18: Fixed Reaction Block Rebar Cage and Detail

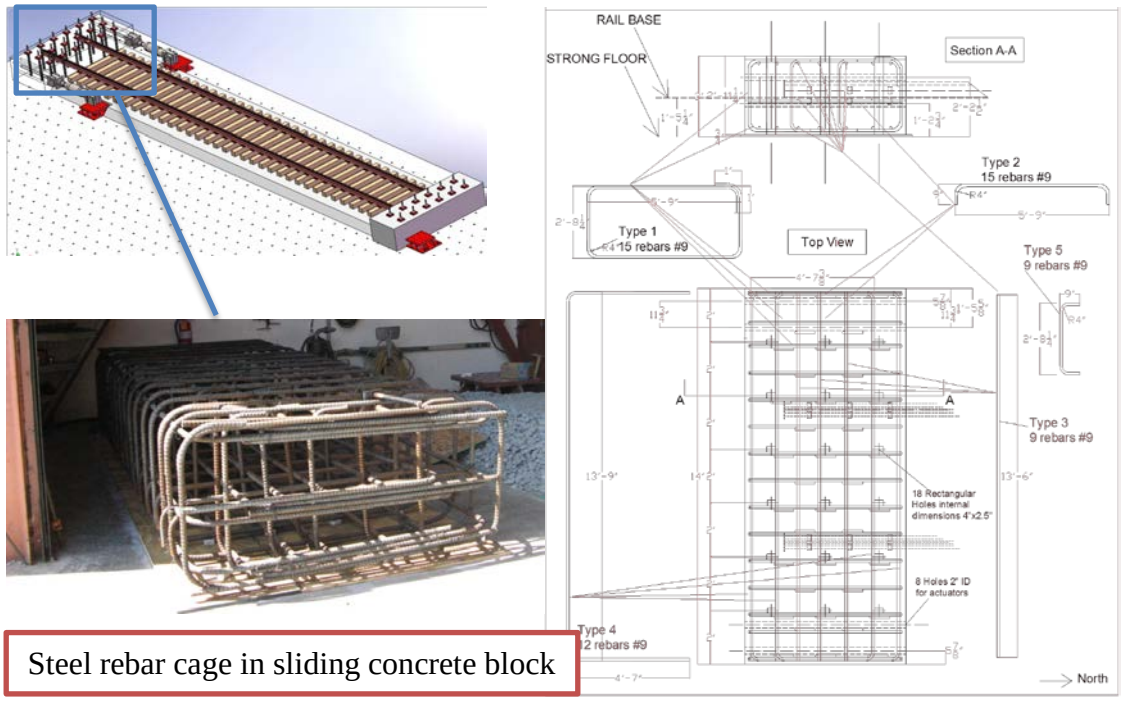

Figure 7-19: Sliding Reaction Block Rebar Cage and Detail

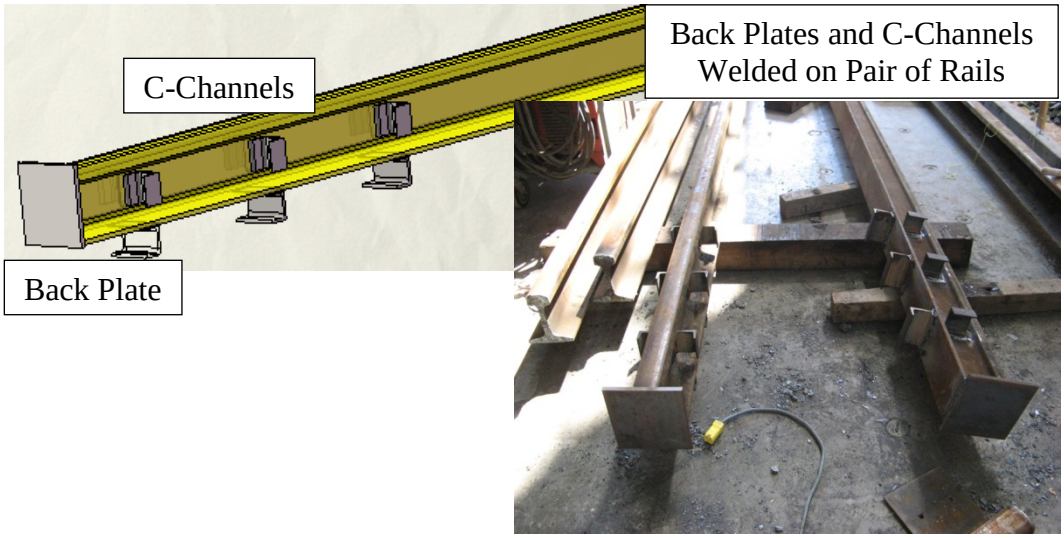

Figure 7-20: Back Plate and C-Channels for Shear Transfer

Because of the rough nature of the crushed rock ballast, the strong floor was protected with a layer of plywood. With the plywood in place, the rebar cages were placed and the formwork was constructed. Then the ballast was placed on the plywood in 6” lifts that were compacted with vibration tamper in between lifts until the 18”

based was achieved. Once the base was in place, the wood ties were installed at a spacing of 18” on center and in filled with ballast. Four rail sections were then placed on the ballast and tie foundation with the ends that have the shear transfer C-channels and back plate inserted into the concrete block form work. The steps are outlined in Figure 7-21.

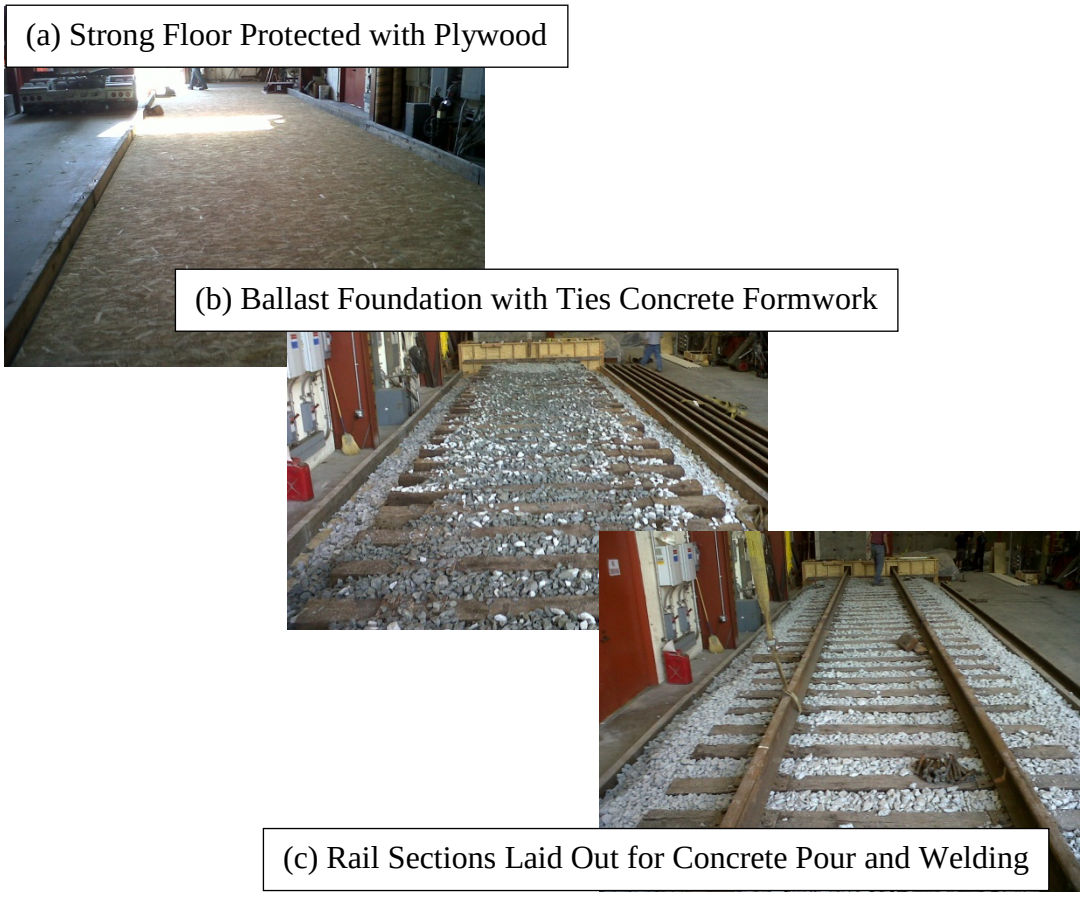

Figure 7-21: Construction step of Ballast Foundation and Reaction Blocks (a) Open Floor with Plywood Protection (b) Ballast with Ties and Reaction Block Formwork (c) Rail Sections Laid Out for Concrete Pour and Welding

Figure 7-22 shows the nest steps in the process of installing the rail. First, the four rails had to be cut length to fit into the ballast foundation. Next, each pair of rails was welded together using the Thermite welding method. Thermite welding is and exothermal chemical process between Iron (II, III) Oxide and Al. in one of the two most common reactions:

$$Fe_2O_3 + 2Al \rightarrow 2Fe + Al_2O_3 + 181.5kcal \quad \textbf{7.7}$$

$$3Fe_3O_4 + 8Al \rightarrow 9Fe + 4Al_2O_3 + 719.3kcal \quad \textbf{7.8}$$

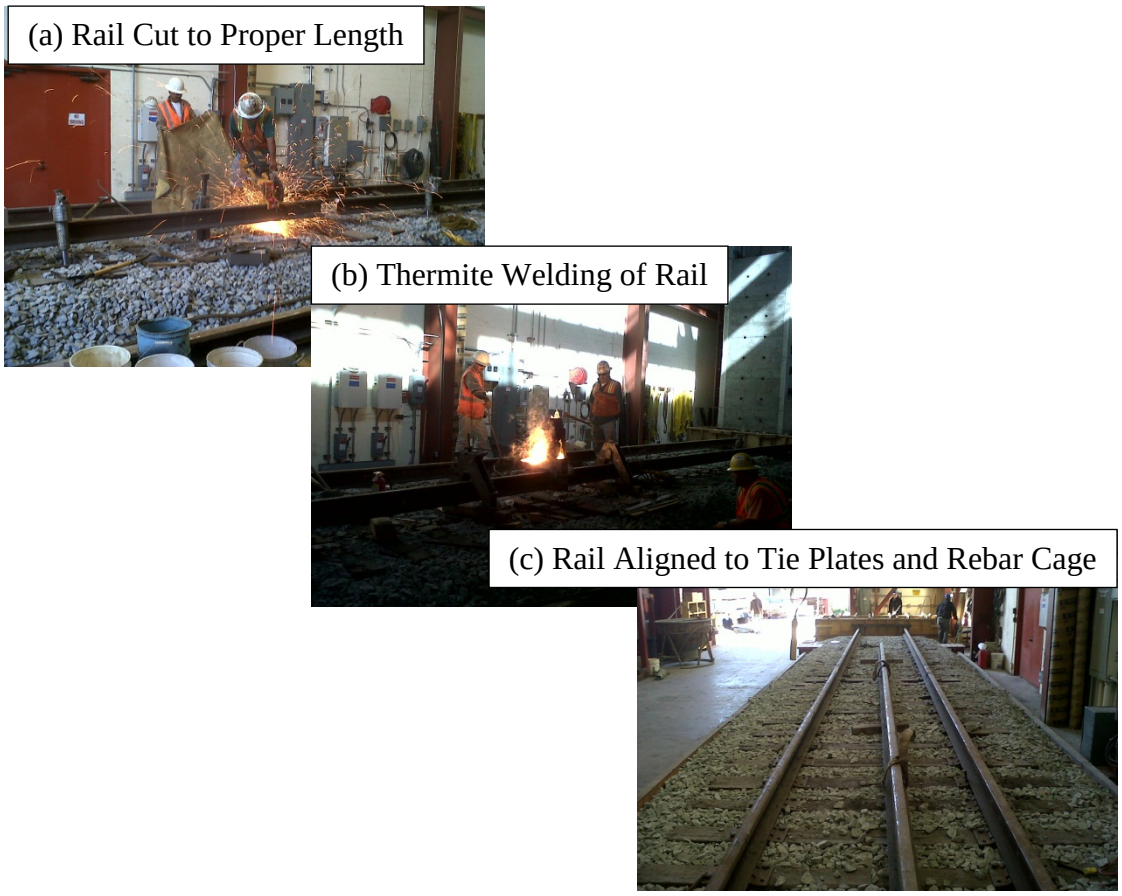

Figure 7-22: Rail Connection (a) Rail Cut to Proper Length, (b) Thermite Welding of Rail, (c) Rail Aligned to Tie Plates and Rebar Cage

The byproduct of the reaction is molten Iron used to fill the gap between the two rails to be joined and Aluminum Oxide plus the excess heat from the reaction. After the welding, the rails were aligned to the tie plates and in the rebar cage to be ready for the nest step of pouring the concrete block. Figure 7-23 displays the rails in the rebar cages and the completed concrete blocks. In order to speed up the construction process a high strength concrete was used to insure that in seven days of cure the strength of 6 ksi was achieved. The high strength gave a 30 day cure strength of 12 ksi. The cost difference between the high strength concrete and the additional three weeks of cure time justified the use of the 12 ksi concrete in order to expedite testing.

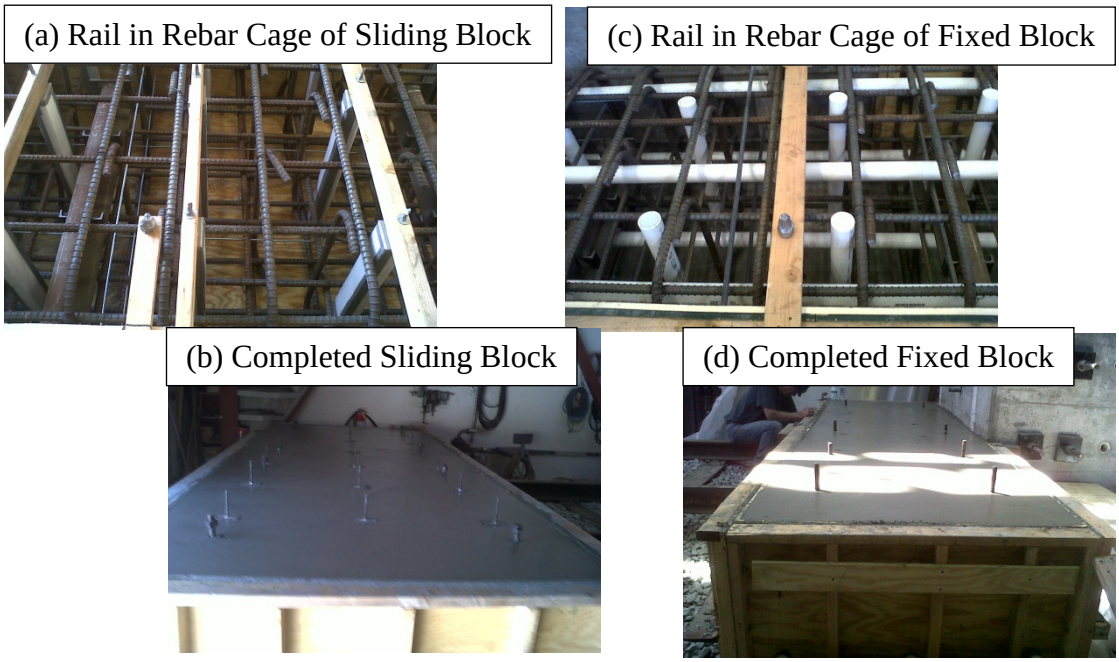

Figure 7-23: Reaction Block Completion (a) Rail in Rebar Cage of Sliding Block, (b) Completed Sliding Block, (c) Rail in Rebar Cage of Fixed Block, (d) Completed Fixed Block

After an acceptable curing, strength had been reached the rail tensioning procedure was executed and the steps are outlined in Figure 7-24. First, the fixed block was anchored to the strong floor by post tension rod inserted thru the block and into the strong floor. With on block anchored the sliding block was lifted with a hydraulic jack and high strength steel rollers were inserted in preparation of the rail tensioning process. The rail tensioning was done with two 150 kip actuators pushing the block until a stress of 3.8 ksi (26.2 MPa) was achieved in the rail. This stress corresponds to a rail neutral temperature of 90^{o}F (32.2^{o}C). The final step in the prestressing procedure the fixed rail was post tensioned to the strong floor and the void created by the rollers was filled with hydro-stone grout to insure the proper coefficient of friction was achieved.

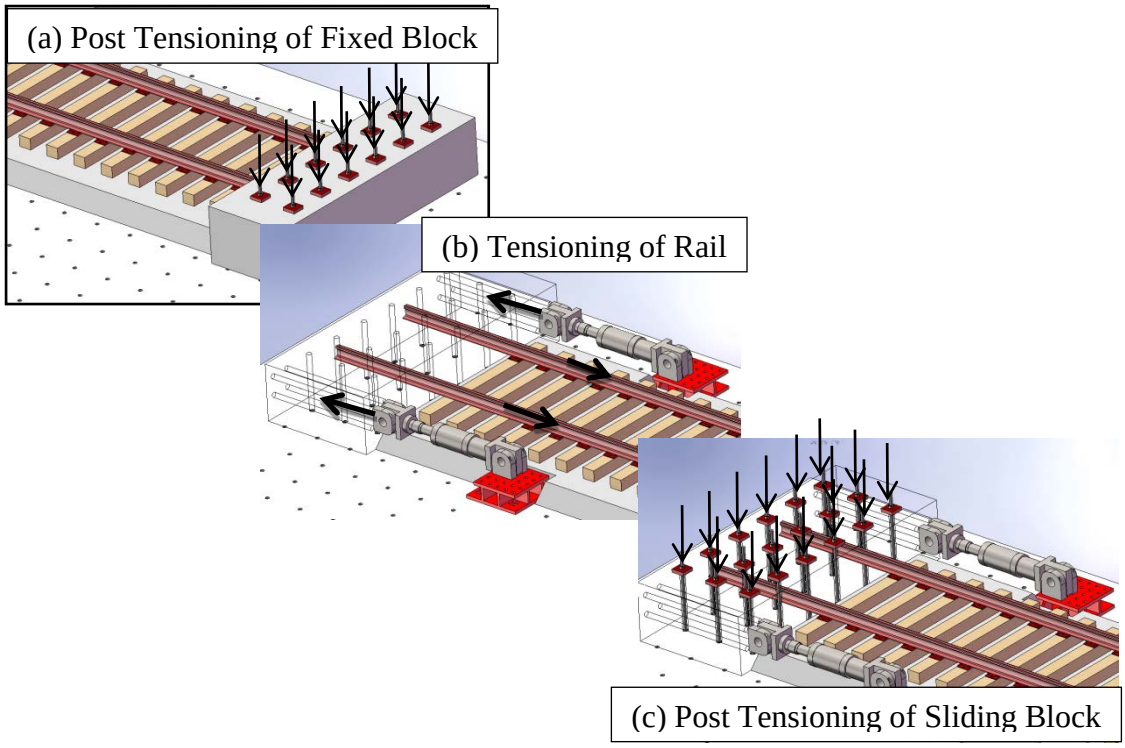

Figure 7-24: Rail Tensioning Procedure (a) Post Tensioning of Fixed Block, (b) Tensioning of Rail, (c) Post Tensioning of Sliding Block

In order to impose thermal loads a heating system was specially designed. The system consists an electrical heating element with a controller. Figure 7-26 shows the components of the rail heating system. The heating element is a rail custom rail switch heating purchased from Thermal-Flex Systems, Inc. The heating element provides 1200 Watts/foot to the rail. Protected by an aluminum shield the heating element is attached to the rail neutral axis by a spring steel rail clip. Achievable temperatures with the heating element are in the excess of 90^{o} C (194^{o} F), which is highest temperature attempted in testing to date. It is possible to reach temperatures that impose large enough to buckle the rail. The standard thermal protocol was in the heating test cycles is shown in Figure 7-25

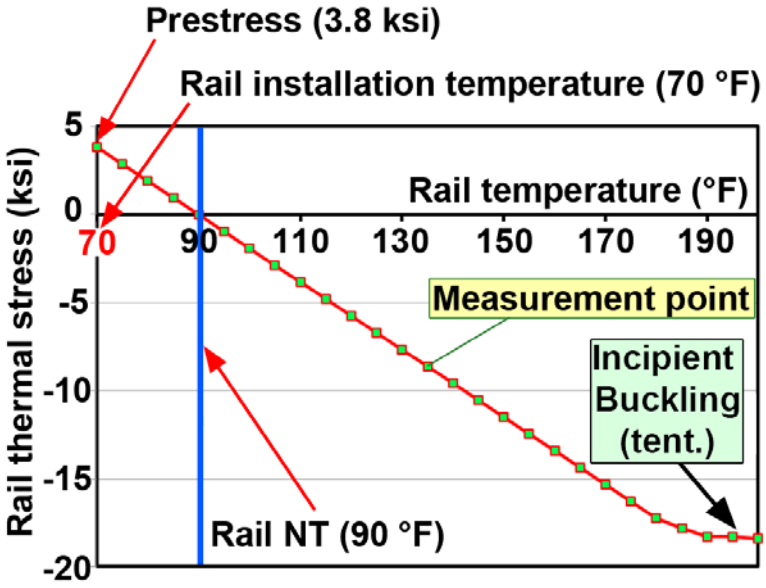

Figure 7-25: Standard Thermal Loading Protocol

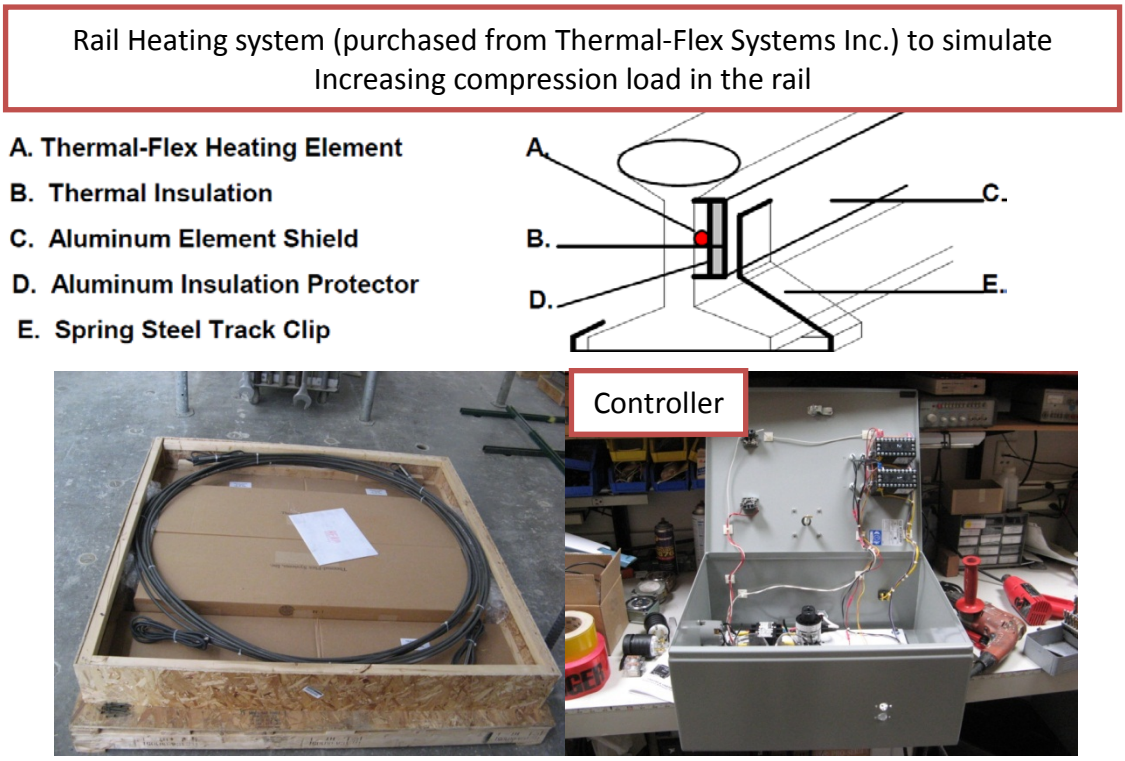

Figure 7-26: Rail Heating System

Extensive instrumentation was applied to the rail in order to monitor the rail behavior (Figure 7-27). To track the temperature in the rail three thermal couples per rail are installed on the neutral axis. Rail strains are monitored by 48 strain gauges, 24 per rail, at six locations on each rail. Strain gauge placement was at the neutral axis at each location the monitor axial strains. Additionally, at several locations multiple gauges were installed to monitor horizontal and vertical bending in the railhead and foot.

The completed system is shown in Figure 7-28 along with a thermal camera image of the rail as it is heated.

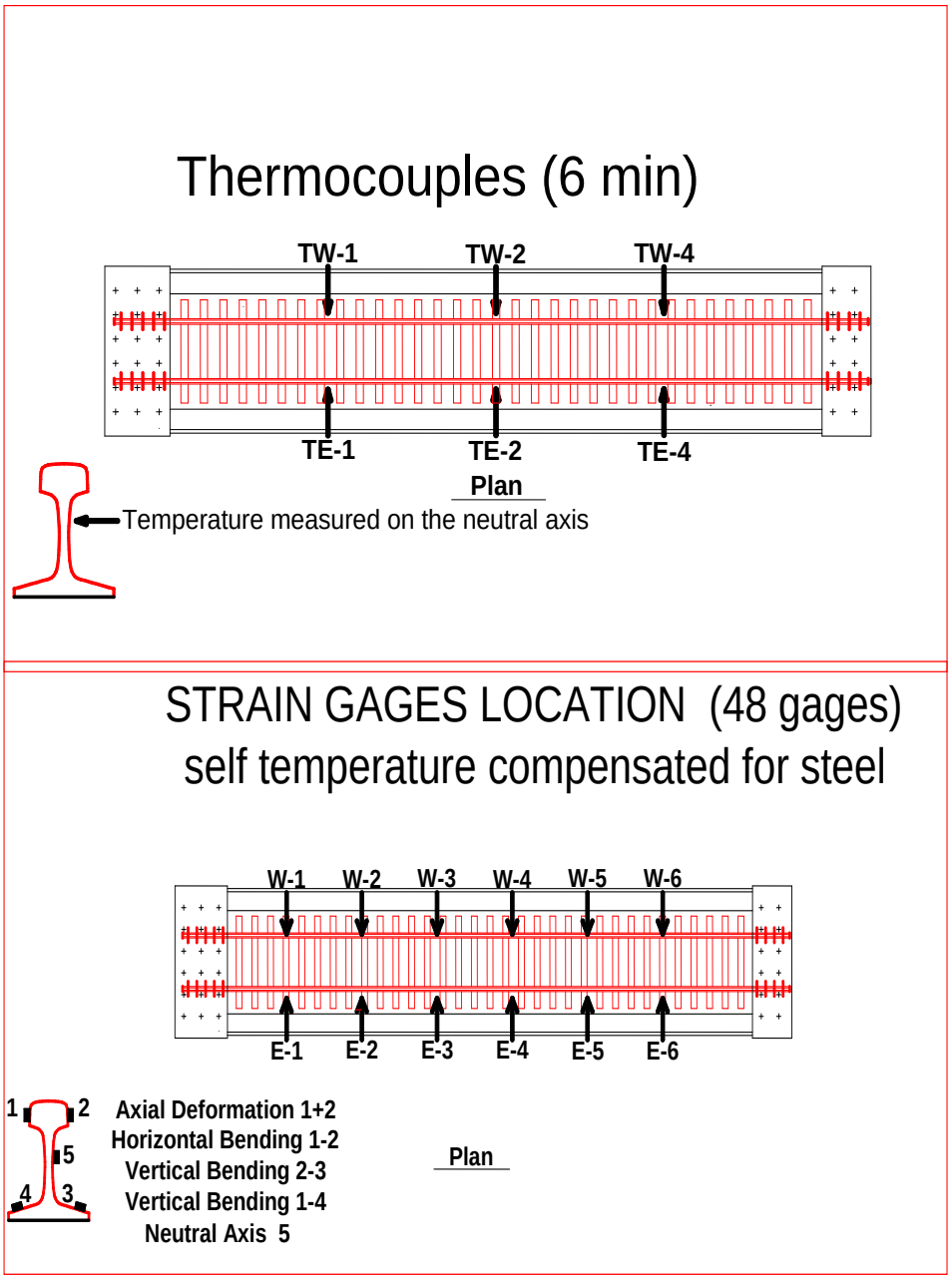

Figure 7-27: Rail Instrumentation

Figure 7-28: Completed Rail Neutral Temperature Test Platform

7.4.2 Electromechanical Impedance Large Scale Testing on Fixed Rail

The investigation of the EMI method was expanded to the full-scale test platform. Testing was testing in the small format as that which was undertaken in the proof of concept test on the beam section of rail steel. In the large- scale test the capability of the method to handle changes in stress imposed by a thermal source is tested. The large-scale testing was intended to simulate the thermal loads imposed on the continuous welded rail found in the field generated by the radiant heat of the sun. Testing was performed on both available rails for a comparison to examine the robustness of the measurements.

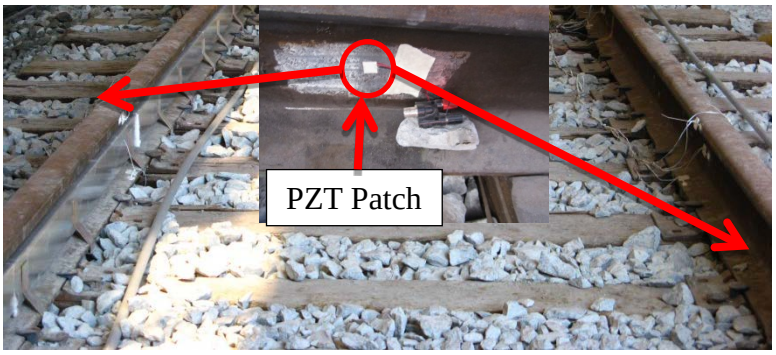

Figure 7-29: PZT Patch as Attached to West and East Rail

For this experiment, the piezoelectric wafer attached was the same material and dimension and from the same manufacturing batch as that used in the proof of concept beam test. The wafer was an APC 850 WFB with the dimensions of 12.7mm x 12.7mm x 0.635mm manufactured by APC International. A patch was attached to both the West and East at the neutral axis. As in the previous testing, the frequency range that is examined is 100 kHz to 600 kHz.

For this test, the measurements were taken on the fixed rail through a heating and cooling cycle. Starting at 25.8^{o} C the rail was heated to 74.3^{o} C and then allowed to cool to 25^{o} C. In this testing cycles both the East and West rails loads will pass the zero stress state at 35^{o} C twice, once in the heating and one in the cooling cycle. In Figure 7-30, the conductance and susceptance signatures for all the temperatures are shown for both the East and West rail. It is seen that the signature a consistent for both rails. While the amplitudes have some variation in magnitude, the trends measured are not solely dependent on amplitude. The trends of the parameters used are the important measure used to determine the rail neutral temperature.

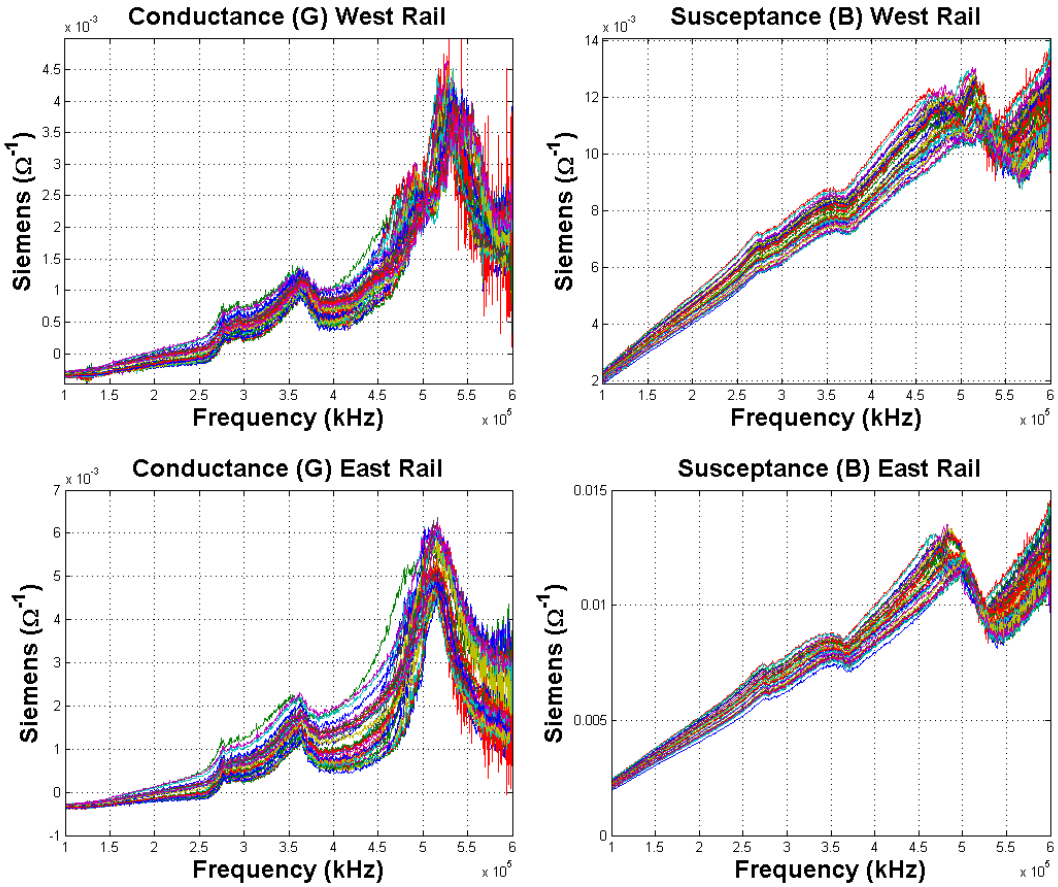

Figure 7-30: Conductance and Susceptance Signals for West and East Rails

In the results of this test, the tracking of the amplitude over the loading cycle was examined. Three frequency ranges are tracked for the amplitude change. The ranges 280-290 kHz, 605-315 kHz and 500-540 kHz represent the discontinuity peaks that are seen the conductance and susceptance signature. In the chosen frequency ranges the amplitude changes are small due to the stiffness of the structure and are very difficult to track. The parameters used in the previous test, with the exception of the frequency shift, are monitored for both the conductance and the susceptance. There are stable parameters in the susceptance that are reflected in the results.

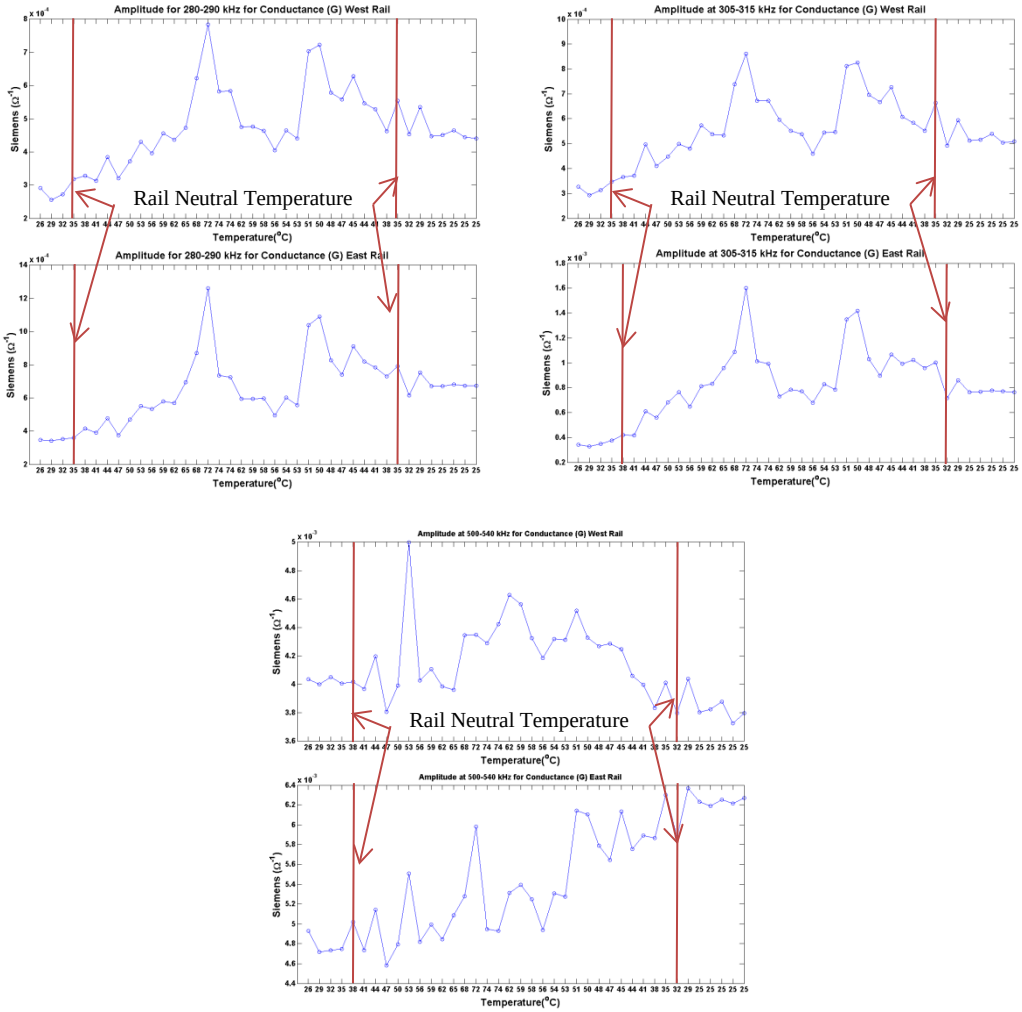

Figure 7-31: Amplitude Change of Conductance for West and East Rail

As seen in the prior proof of concept test, the susceptance shows better trends with loads than the cunductance. In two of the frequency ranges examined, there is a good montontic trend as the rail is heated. However, in both frequenct ranges there is no clear indication of the rail neutral temperture. The amplitude change for the 280-290 kHz is shown in Figure 7-32. In this range, the trend is similar for both the West and East rail. Figure 7-33 shows that in the range of 305-315 kHz the trend is similar to the pervious range. As with the lower range, the trend is stable for both the West and East rail. For

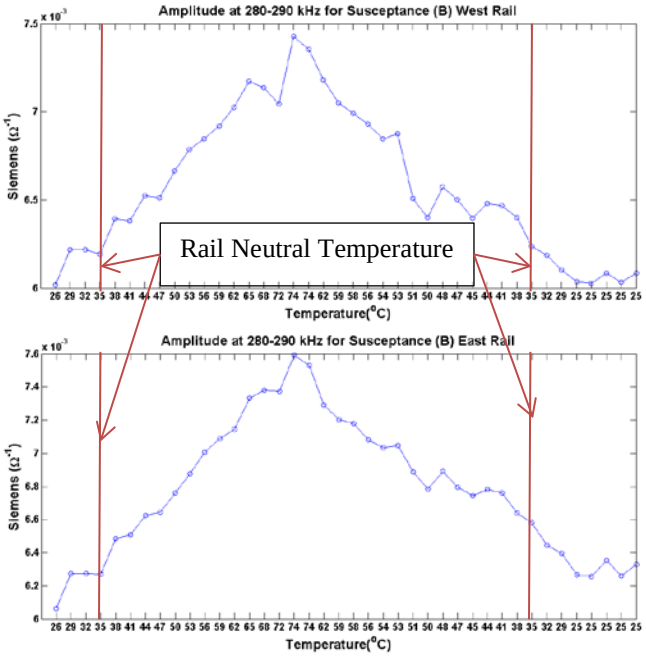

Figure 7-32: Amplitude Change for 280-290 kHz of Susceptance for West and East Rail

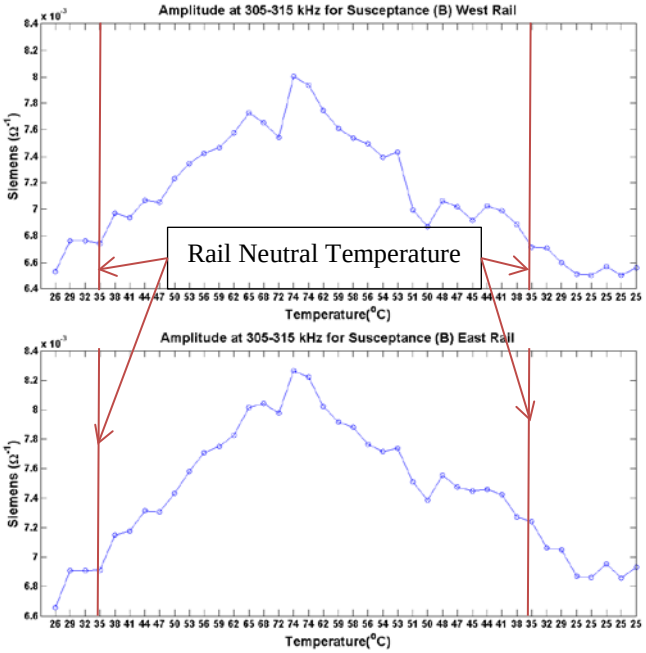

Figure 7-33: Amplitude Change for 305-315 kHz of Susceptance for West and East Rail

the range of 500-540 kHz there is not a difinative trend that can be said to be acceptable. Also, the measurements of the West and East rail have a lagre variation.

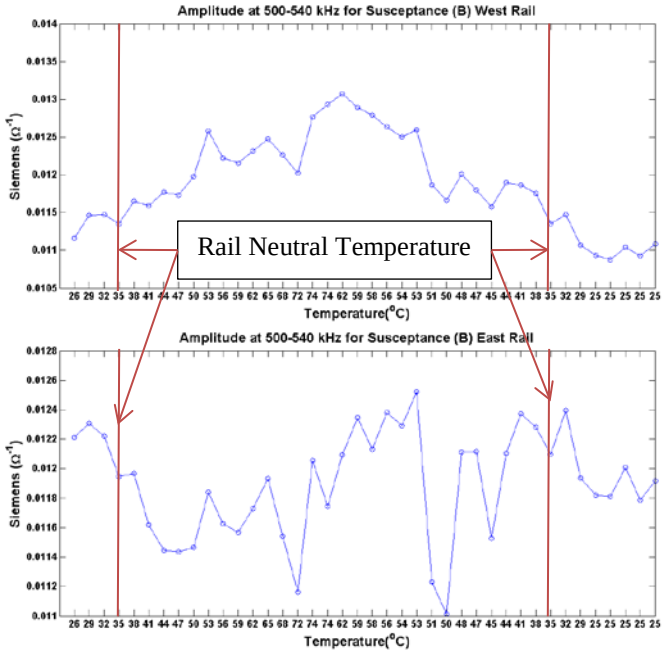

Figure 7-34: Amplitude Change for 500-540 kHz of Susceptance for West and East Rail

Once again, the slope of the signatures is determined and plotted against the loading, or temperature in this case. As before, the slope is calculated by a simple first order linear regression such that the change in slope represents the change of the admittance signatures over the entire frequency range. In the previous experiment with the beam section a good monotonic linear trend.

The results of the susceptance slope change showed to have a better trend, as expected, since the susceptance is a function of the frequency and capacitance. In Figure 7-35, the slope change of the conductance has no trend. In fact the values are relatively constant for both the West and East rail. This is also an expected result, as conductance is a measure of structural resistance that is a constant in this case. Aside from a few outliers near the maximum temperature, the slope change in the susceptance

has a good monotonic trend rising to the maximum and decreasing back to the starting value as seen in Figure 7-36.

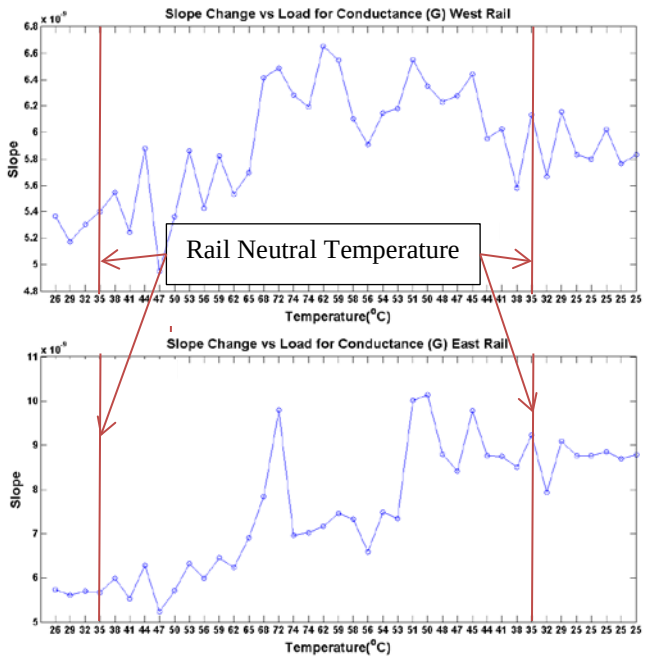

Figure 7-35: Conductance Slope Change for West and East Rails

The Piezoelectric Efficiency Factor did not show any perceptible trend in either the susceptance or the conductance (Figure 7-37). The baseline required for the computation of Piezoelectric Efficiency factor was taken from a 40-ft section of 136RE that was tress free and at ambient temperature. The frequency ranges used were the same as those used in the computation of the amplitude change. The purpose of the selection of those particular ranges is to isolate the largest peaks that are likely to have the greatest change in the temperature loading cycle. However as discussed in section 7.4.1 the limited frequency range gives poor results of the structures overall changes.

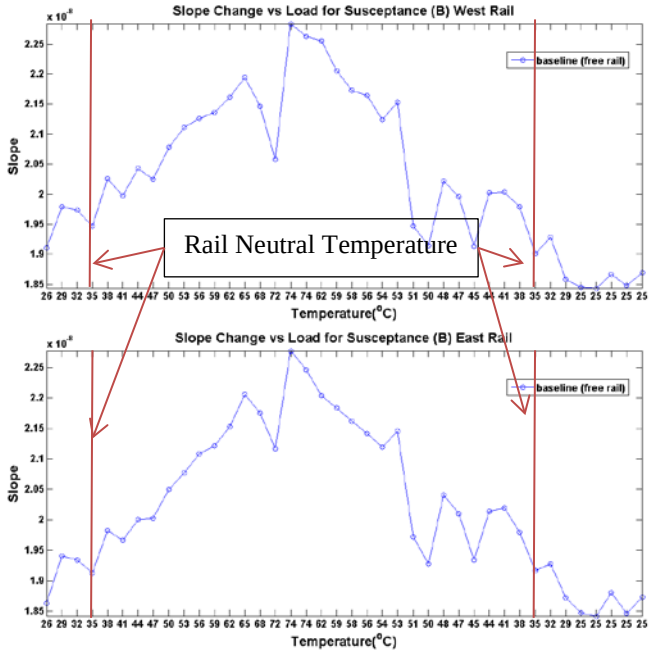

Figure 7-36: Susceptance Slope Change for West and East Rails

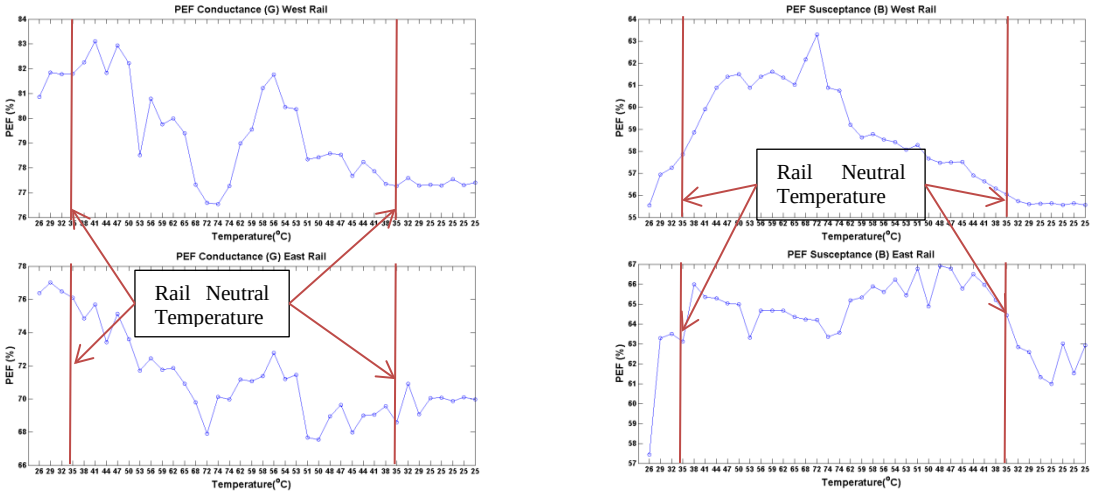

Figure 7-37: Piezoelectric Efficiency Factor for Conductance and Susceptance of West and East Rails

The final parameter, and the one that gave the best results in locating the zero stress value in the beam proof of concept test for the susceptance signature, was the

Root Means Squared Deviation. In this test, the susceptance once again had a better trend than the conductance. The RMSD had no real trend, and difference in the values showed it as relatively constant in the conductance (Figure 7-38). Recalling the RMSD parameter trend in the beam section experiment that was a linear symmetric trend with a minimum at the zero state it is not replicated in this test. In this test, it is clear that the temperature has an effect on the measurement of the mechanical impedance of the structure. The result in Figure 7-39 is a good monotonic trend, that is symmetric about the maximum compressive load. However, there is no minimum seen at the rail neutral temperature as it was seen in beam test at the zero stress state. It is noted that value of the change is higher, but is very close to, that seen in the beam test where the loading was purely mechanical.

In the purely mechanical test of the beam section, the slope change and Root Means Squared Deviation parameter both had good trends. The same observation can be made in the large-scale experiment where the loading was thermally induced. The difference is that Root Means Squared Deviation did not locate the rail neutral temperature. Clearly, in this experiment the temperature shows to have an effect on the EMI of the structure. With these results in mind, the next experiment was conducted on an unconstrained rail with a thermal change. The test of the unconstrained rail will show the effect of temperature only, without any axial stress on the rail. This test is covered in the next section.

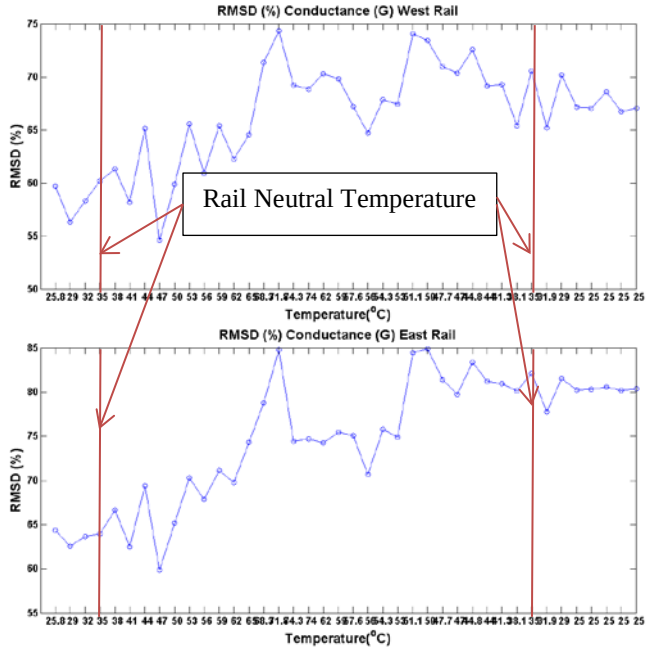

Figure 7-38: Root Means Squared Deviation for Conductance of West and East Rail

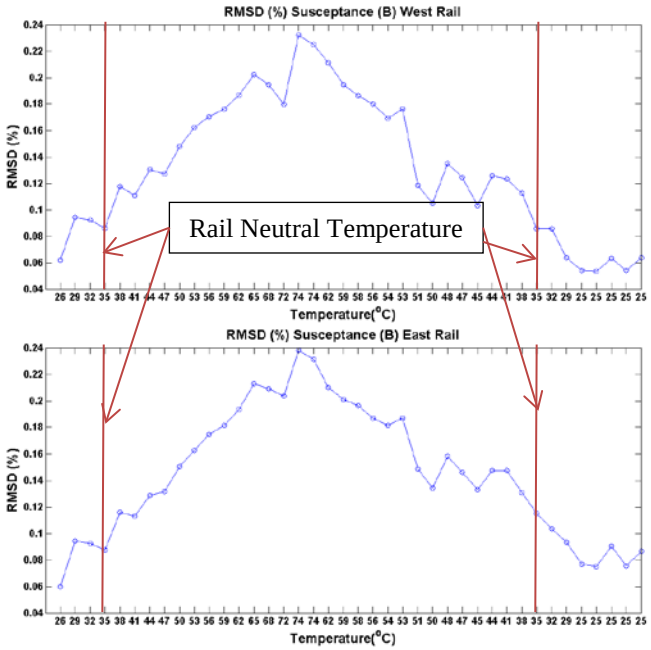

Figure 7-39: Root Means Squared Deviation for Susceptance of West and East Rail

7.5 Large Scale Experiment (Free Rail)

In order to isolate the temperature effect on the EMI method, a 40-fot long free rail was laid next to the large-scale test-bed at the Powell Labs. Figure 7-40 is a depiction of how the test is set up. To reduce any the friction between the rail and the ties, the rail was placed on hardened steel rollers. The rail is free to expand and the heating element used in the previous test was moved over to the free rail in order to heat it. The test set up is shown in Figure 7-41.

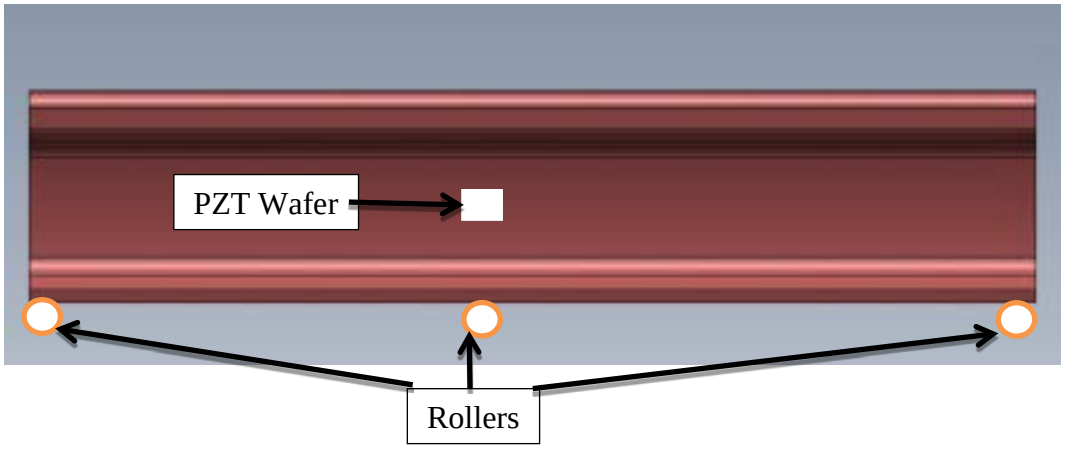

Figure 7-40: Depiction of Free Rail Set Up (not to scale)

This test was performed in the same manner as the two previous tests. Coming from the same manufacturing batch, the wafer was an APC 850 WFB with the dimensions of 12.7mm x 12.7mm x 0.635mm manufactured by APC International. The piezoelectric wafer was bonded to the rail's neutral axis near the midpoint of the 40-ft. length. Admittance measurements were taken over the range of 100-600 kHz and then temperature ranged from an ambient of 23.6^{o} C to 74^{o} C in heating only. Measurement frequencies and thermal loading matched those used in the fixed-fixed experiment.

Additionally, the baseline values used for the parameters that require them are the same used in the fixed-fixed test.

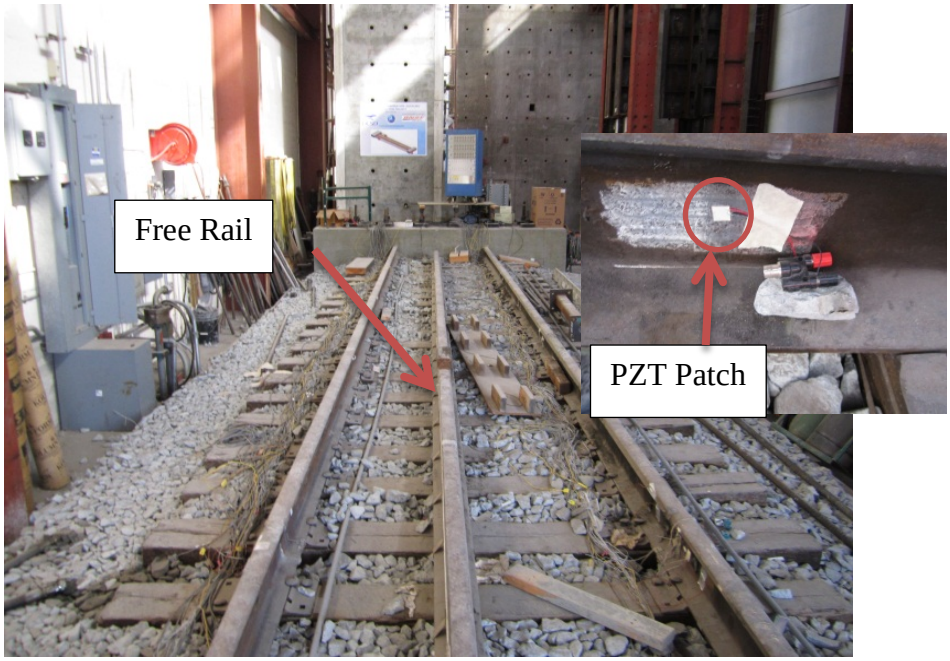

Figure 7-41: Free Rail Test Set Up in Powell Laboratory

Signatures of the conductance and susceptance for the experiment on the free rail are shown in Figure 7-42. There is no apparent difference in the signatures than those seen in the two previous tests. Peaks in the signatures are occurring in the same frequency ranges as seen in the fixed-fixed rail.

Throughout the experiments, it should be noted that the measurements were rather stable considering the activity in the laboratory. Happenings in the laboratory included large machinery and active testing that can induce low vibrations and electromagnetic fields. Considering the signatures collected the analysis of the

parameters will the same as in the previous assessments and the environmental conditions in the laboratory had little to no effect.

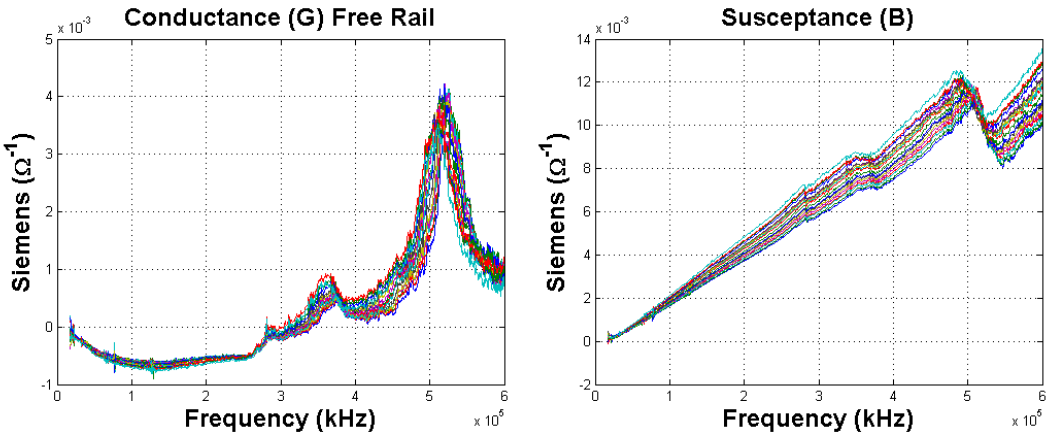

Figure 7-42: Conductance and Susceptance Signatures for Free Rail

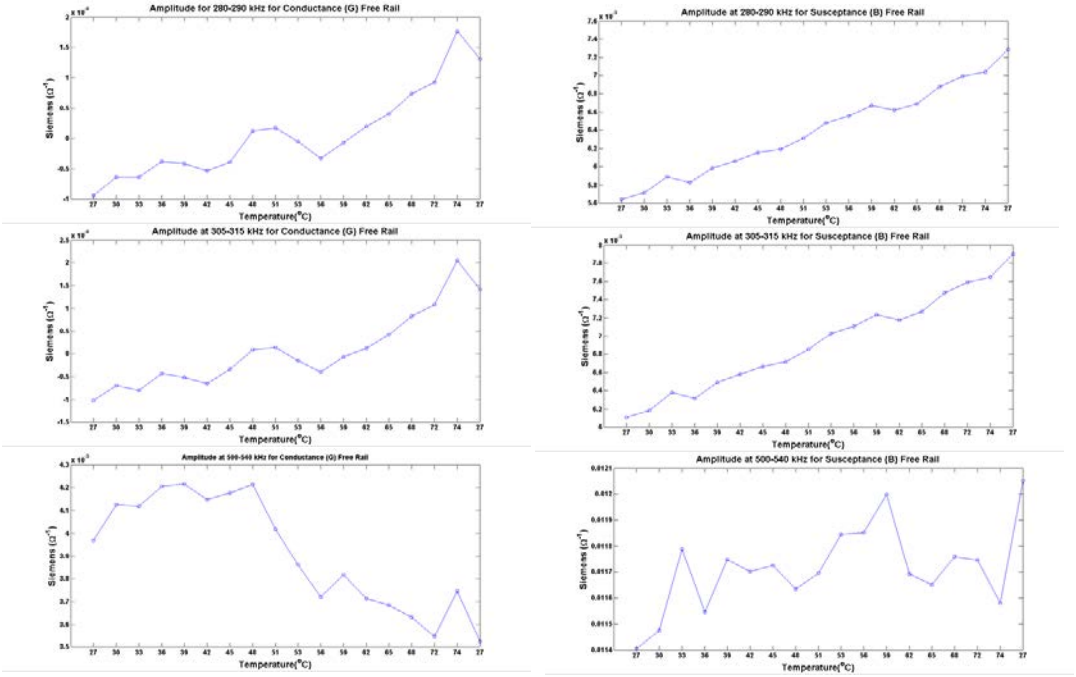

(a) Conductance (b) Susceptance

Figure 7-43: Amplitude Change for Free Rail Test (a) Conductance (b) Susceptance

Amplitude changes were tracked across the temperature increase and are plotted in Figure 7-43 for both the conductance and the susceptance. For the frequency ranges 280-290 kHz and 305-315 kHz, there is a reasonable trend for both parameters. In the frequency range of 500-540 kHz, neither the conductance nor the susceptance show

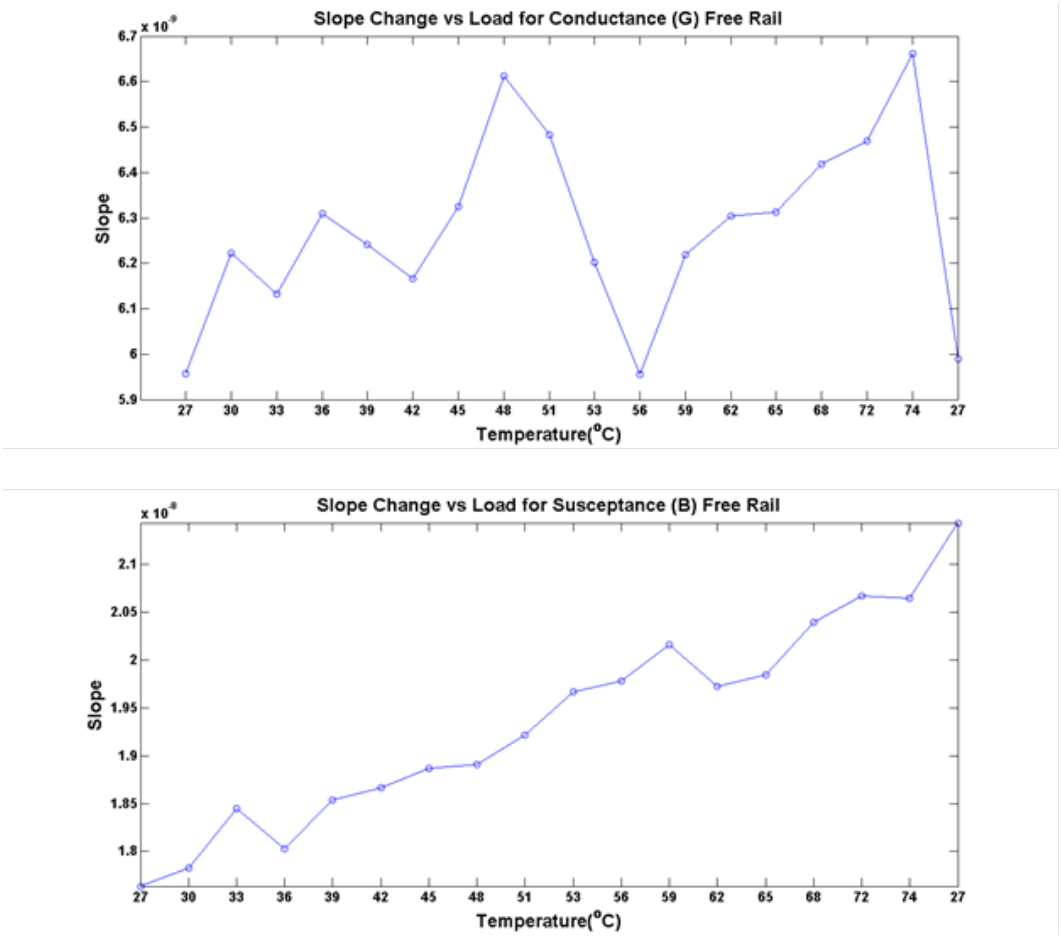

Figure 7-44: Slope Change of Conductance and Susceptance for Free Rail

good results with trends matching those in the previous measurements. Upon inspection of the susceptance amplitude change, the total change over the temperature for the frequency ranges 280-290 kHz and 305-315 kHz is similar but lower than that seen in the fixed-fixed rail test.

In the slope change parameter, the trends are, again, very similar to those seen in the fixed-fixed- rail. Figure 7-44 displays the plots of the slope change for the conductance and the susceptance. In the plots, it is seen that the trend in the susceptance is, again, a linear trend, while the conductance is a scattered data set. For the susceptance trend, the change over the temperature range is essentially the same as that seen in the fixed-fixed rail. As with the amplitude change, thermal loading is dominating the effect on the slope change.

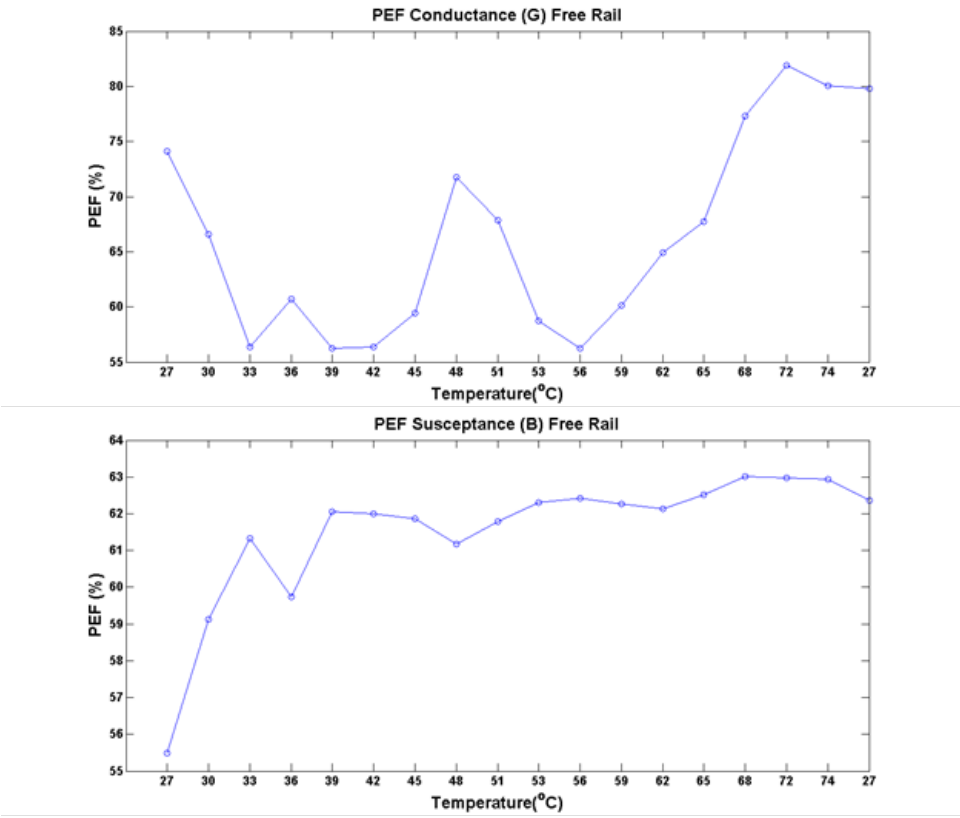

Figure 7-45: Free Rail Piezoelectric Efficiency Factor for Conductance and Susceptance

The Piezoelectric Efficiency Factor has proven in the three tests to be an ineffective measurement parameter for both the conductance and the susceptance.

Presented in Figure 7-45, the plots of the tendencies in the parameter appear mostly constant.

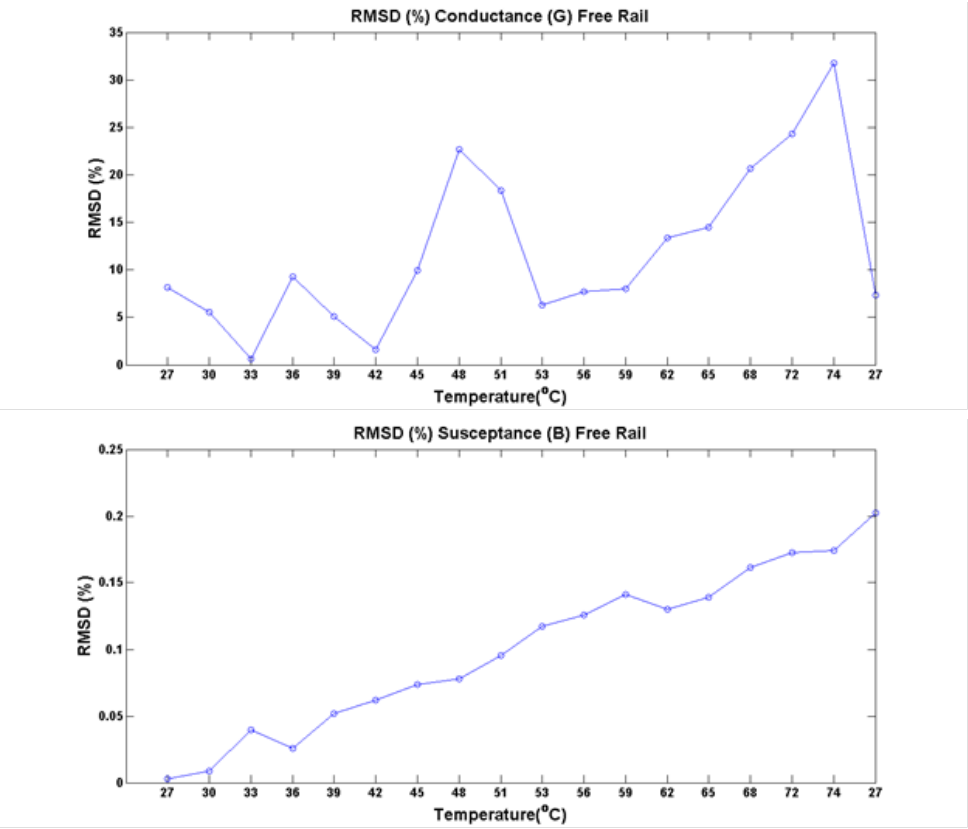

Figure 7-46: Root Means Squared Deviation for Conductance and Susceptance of Free Rail

Similar to the amplitude change parameter, the Root Means Squared results for the free rail correspond to the trend seen in the fixed-fixed rail. In Figure 7-46 the Root Means Squared Deviation plots of values versus the temperature range of the conductance and susceptance. The conductance shows again a scatter of values. In the susceptance measure of the Root Means Squared Deviation, a good monotonic linear trend is seen. The change over the temperature is similar to that in the fixed rail. For the

free rail there was a 0.20% change and the fixed rail had a 0.14% change of the slope. This indicates that the temperature effect is dominating the change in the slope.

8. Conclusions

8.1 Conclusions of Rail Defect Detection

The dissertation has discussed the use of ultrasonic guided waves as a better option compared to traditional bulk waves for detection of internal defects in rails. A prototype has been constructed based on ultrasonic guided waves, non-contact rail probing (laser / air-coupled hybrid setup), and real-time statistical pattern analysis to enhance defect detectability and minimize false positive rates. The prototype was filed tested at Herzog Services, Inc.

The system performance at Herzog Services rail defect farm was very promising.

The system was able to detect, reliably, Transverse Defect including some under shelling, Side Drilled Holes, artificial Horizontal and Vertical Split Heads and Defective Field and Plane welds. The defect detection reliability shown during the blind tests exceeded industry average and AREMA recommendations.

The UCSD rail inspection prototype was also sensitive to the presence of good welds, but with a different signature than the one related to the flaws. Specifically, the Damage Index plotted in real-time indicated a good weld as a high-level stable plateau without local minima, whereas it indicated defects (including defective welds) as peaks with several local maxima with interposed one or more local minima.

Testing at higher speed (up to the allowed 9 MPH) did not show any mechanical/ultrasonic related problem to the prototype. The only problem noticed at higher speeds was the degradation in signal positioning resolution from the desired 0.25” intervals. This loss in resolution could be avoided with the use of a faster-repetition laser, the use of a second laser firing off-phase from the existing laser, and/or a larger inspection gage (distance between sensor pairs).

8.2 Future Work of Rail Defect Detection

Possible improvements to the technique considered so far for internal defect detection in rails include:

- Implementation of an Automatic Gain Control for Damage Index visualization, to respond adequately to the different rail surface conditions.
- Increase in the number of air-coupled sensors for full coverage of the rail head including gage side, center and field side (current coverage is for gage side and center head with limited field side).
- Upgrade for testing at higher speeds without loss in position resolution, achievable with a faster laser, multiple lasers with sequential firing, and/or increased inspection gage (distance between sensors).
- Design and implementation of an Automatic Pattern Recognition algorithm, for distinguishing good welds from defective welds and defects automatically.

- Possible replacement of the ultrasound generation laser with an air-coupled ultrasound transmitter. This option would greatly simplify the system and increase its speed (the repetition rate of an air-coupled transmitter is typically much higher than that of a Q-switched laser). However, efficient filtering algorithms must be devised to obtain an acceptable signal-to-noise ratio of the air-coupled measurements. Current research of the UCSD group is aimed at exploring the air-coupled ultrasound generation option.

8.3 Conclusions of Rail Thermal Stress Measurement

Two possible methods were investigated for the measurement of thermal stresses in rail, or detection of the rail neutral temperature. First, a parametric study on the velocity change of ultrasonic guided waves due to stresses in the waveguide was performed numerically with the SAFE method. Secondly, the Electro-Mechanical Impedance (EMI) method was explored theoretically and experimentally as a practical approach to rail stress measurements. The application of the EMI method for load measurements is still relatively new to the field. In this study, the scale of the test specimens (rails) was brought to the full length, well beyond the small-coupon scale of the studies found in current literature on the subject. Both methods showed sensitivity to the presence of stress. However, they also indicated a comparable sensitivity to temperature alone. Therefore, the need for temperature compensation must be addressed before any of these approaches can be successfully used in the field for thermal stress measurements. This dissertation has

laid the foundations for this possibility, by producing numerical and experimental results shining light on the relative sensitivity of the techniques to both temperature plus stress (thermal stress), and temperature alone.

Specifically, the parametric study of the guided wave velocity change indicated two important findings:

- in purely mechanical loading of the waveguide, only certain vibrating modes have an appreciable change in velocity.
- Temperature changes alone affects the material elastic constants in a manner that the guided wave velocity is highly affected for a wide range of vibrating modes.

Specific findings from the EMI method included:

- EMI can be an effective method to determine the zero-stress point of a structural element under purely mechanical load.
- When a thermal loading is imposed on the structural element, the temperature effect is comparable or larger than the stress effect.

8.4 Future Work of Rail Thermal Stress Measurement

Possible future steps for the measurement of guided-wave velocity change due to thermal loads include:

- Isolate modes most sensitive to stress while of practical use (for example, modes with high group velocity that are easily recognizable in a measurement as early arrivals).

- Develop methods to decouple temperature effect from stress effects in the wave velocity measurements.
- Track the polarization of the wave propagation to better isolate the modes more sensitive to stress than temperature.
- Study the thermal effect in CWR by using higher-order elastic constants in the SAFE modeling to determine if wave nonlinearities can provide better indication of stress with smaller temperature effects.

Future work on the EMI method for thermal stress measurement may include:

- Develop a robust temperature compensation algorithm for the admittance measurement.
- Undertake a Finite Element Method to model the piezoelectric transducer/structure interaction in the presence of both stress and temperature fluctuations.

Investigate practical measurement devices, such as simple circuits, to measure the individual electrical components of the voltage and current of the admittance measure. By using individual electrical components, it may be possible to isolate the temperature effect on the piezoelectric transducer. In addition, use of a simple circuit will allow for the acquisition of waveform data which is not achievable with a standard impedance analyzer that only gives the impedance components. The acquisitions of the waveforms will allow for a greater evaluation of the structural response.

REFERENCES

[1] Federal Railroad Administration Office of Safety Analysis.

[2] Derailment of Norfolk Southern Railway Company Train 68QB119 with Release of Hazardous Materials and Fire.

[3] Cannon DF, Edel KO, Grassie SL, Sawley K. Rail defects: an overview. Fatigue & Fracture of Engineering Materials & Structures. 2003;26:865-86.

[4] Pantano A, Cerniglia D. Simulation of laser-generated ultrasonic wave propagation in solid media and air with application to NDE. Applied Physics A. 2009;98:327-36.

[5] Lee CM, Rose JL, Cho Y. A guided wave approach to defect detection under shelling in rail. NDT & E International. 2009;42:174-80.

[6] Coccia S, Phillips R, Nucera C, Bartoli I, Salamone S, di Scalea FL, et al. UCSD/FRA non-contact ultrasonic guided-wave system for rail inspection: an update. In: Tomizuka M, editor. 1 ed. San Diego, California, USA: SPIE; 2011. p. 798113-8.

[7] Zhang W. RailScan: Effective and Nondestructive Measurement System of Neutral Temperature of Continuous Welded Rails. 2009.

[8] Hayes AP. MAPS-SFT, a new tool in the infrastructure manager's toolbox. IET; 2008. p. 1-6.

[9] Read D, Shust B. Investigation of Prototype Rail Neutral Temperature Measurement System. Railway Track and Structures. 2007;103.

[10] Phillips R, Zhu X, Lanza di Scalea, F. The Influence of Stress on Electro-meachnical Impedance Measurements in Rail Steel. Materials Evaluation. 2012;in press.

[11] Track Inspector Rail Defect Reference Manual. In: Administration FR, editor. 392132011.

[12] Title 49 Code of Federal Regulations (CFR) Part 212.

[13] Wickens A. A History of Railway Vehicle Dynamics. Handbook of Railway Vehicle Dynamics: CRC Press; 2006. p. 5-38.

[14] Esveld C. Modern railway track: MRT-Productions Zaltbommel, The Netherlands; 2001.

[15] Hugues C, Jean-Bernard A. Wheel - Rail Contact. Handbook of Railway Vehicle Dynamics: CRC Press; 2006. p. 85-120.

[16] Tyfour WR. Predicting the Effect of Grinding Corrugated Rail Surface on the Wear Behavior of Pearlitic Rail Steel. Tribology Letters. 2008;29:229-34.

[17] Stuart L G. Rail corrugation: advances in measurement, understanding and treatment. Wear. 2005;258:1224-34.

[18] Grassie SL, Kalousek J. Rail corrugation: characteristics, causes and treatments. ARCHIVE: Proceedings of the Institution of Mechanical Engineers, Part F: Journal of Rail and Rapid Transit 1989-1996 (vols 203-210). 1993;207:57-68.

[19] Stuart L G. Rolling contact fatigue on the British railway system: treatment. Wear. 2005;258:1310-8.

[20] Ulf O, Roger L. Tribology of the Wheel -Rail Contact. Handbook of Railway Vehicle Dynamics: CRC Press; 2006. p. 121-41.

[21] R. Care SC, M. Dembosky, A. Doherty. Why rails crack: Gauge corner cracking on the British network – Analysis. Aruo Journal. 2006;41:16-9.

[22] Canadian National Engineering Asset M, Management CNEA. Rail defect reference manual. Montreal, Quebec: CN; 1998.

[23] Fan Y, Dixon S, Edwards RS, Jian X. Ultrasonic surface wave propagation and interaction with surface defects on rail track head. NDT & E International. 2007;40:471-7.

[24] Clarke R. “Rail Testing – Where we go from here,” Sperry Rail Service,. Bulletin of the National Railway Historical Society; 1968.

[25] Murav'ev VV, Boyarkin EV. Nondestructive Testing of the Structural-Mechanical State of Currently Produced Rails on the Basis of the Ultrasonic Wave Velocity. Russian Journal of Nondestructive Testing. 2003;39:189-97.

[26] Lanza di Scalea F. Ultrasonic Testing in the Railroad Industry, Part 2. In: Testing ASfN, editor. Nondestructive Testing Handbook. 3 ed: American Society for Nondestructive Testing; 2007.

[27] Robin C. Rail flaw detection: overview and needs for future developments. NDT & E International. 2004;37:111-8.

[28] Marais JJ, Mistry KC. Rail integrity management by means of ultrasonic testing. Traffic. 2003;600:700-.

[29] Oukhellou L, Aknin P, Perrin J-P. Dedicated sensor and classifier of rail head defects. Control Engineering Practice. 1999;7:57-61.

[30] Rizzo P, Coccia S, Bartoli I, di Scalea FL. Noncontact Rail Monitoring by Ultrasonic Guided Waves. Encyclopedia of Structural Health Monitoring: John Wiley & Sons, Ltd; 2009.

[31] Kenderian S, Djordjevic BB, Green JRE. Point and Line Source Laser Generation of Ultrasound for Inspection of Internal and Surface Flaws in Rail and Structural Materials. Research in Nondestructive Evaluation. 2001;13:189-200.

[32] Robert E G, Jr. Non-contact ultrasonic techniques. Ultrasonics. 2004;42:9-16.

[33] Rizzo P, Cammarata M, Bartoli I, di Scalea FL, Salamone S, Coccia S, et al. Ultrasonic Guided Waves-Based Monitoring of Rail Head: Laboratory and Field Tests. Advances in Civil Engineering. 2010;2010.

[34] Coccia S, Bartoli I, Marzani A, Lanza di Scalea F, Salamone S, Fateh M. Numerical and experimental study of guided waves for detection of defects in the rail head. NDT & E International. 2011;44:93-100.

[35] Hayes AP. MAPS-SFT, a new tool in the infrastructure manager's toolbox. Railway Condition Monitoring, 2008 4th IET International Conference on2008. p. 1-6.

[36] http://sunkink.com/contacts.html. 2012.

[37] Devine MK. Detection of Stress in Railroad Steels via Magnetic Property Measurements. Nondestructive Testing and Evaluation. 1994;11:215-34.

[38]http://www.grontmij.com/highlights/transportation-and-mobility/Pages/The-Rail Stress-Test-makes-safety-simple.aspx. 2012.

[39] Tunna J. Vertical Rail Stiffness Equipment (VERSE) Trials. Letter Report for Vortex International: Transportation Technology Center, Inc. (TTCI), Pueblo, CO.; 2000.

[40] Shust W, Read D, Jury FB. A Novel Method for Estimating the Neutral Temperature of Continuously Welded Rail. ASME Conference Proceedings. 2007;2007:105-15.

[41] http://www.erico.com/products/railstress.asp. 2012.

[42] http://railtechnologyltd.com/company.html#. 2012.

[43] Ahlbeck DR, Harrison HD. Monitoring Rail Neutral Temerature and the Long-Term Stability of Track. 1989. p. 135-.

[44] Harrison HD. Wayside system for measuring rail longitudinal force due to thermal expansion of continuous welded rail. SPIE; 1995. p. 225-31.

[45] http://www.lbfoster-salientsystems.com/Rail_Stress_Module.asp. 2012.

[46]http://www.mri.psu.edu/publications/focus_on_materials/fall2010/ultrasonic_waves 2012.

[47] Chree C, Chree C. The Equations of an Isotropic Elastic Solid in Polar and Cylindrical Co-ordinates their Solution and Application. Transactions of the Cambridge Philosophical Society. 1889;14:250.

[48] Ueber die Fortpflanzungsgeschwindigkeiten kleiner Schwingungen in einem unbegrenzten isotropen Kreiscylinder. Journal für die reine und angewandte Mathematik (Crelle's Journal). 2009;1876:324-36.

[49] Gazis DC. Three-Dimensional Investigation of the Propagation of Waves in Hollow Circular Cylinders. I. Analytical Foundation. The Journal of the Acoustical Society of America. 1959;31:568-73.

[50] Zemanek J, Zemanek J. An Experimental and Theoretical Investigation of Elastic Wave Propagation in a Cylinder. Acoustical Society of America Journal. 1972;51:265.

[51] Lamb H. On Waves in an Elastic Plate. Proceedings of the Royal Society of London Series A, Containing Papers of a Mathematical and Physical Character. 1917;93:114-28.

[52] Rayleigh JWS. Scientific papers. Cambridge: University Press; 1899.

[53] Stoneley R. Elastic Waves at the Surface of Separation of Two Solids. Proceedings of the Royal Society of London Series A, Containing Papers of a Mathematical and Physical Character. 1924;106:416-28.

[54] Scholte JG. THE RANGE OF EXISTENCE OF RAYLEIGH AND STONELEY WAVES. Geophysical Journal International. 1947;5:120-6.

[55] Pilant WLP, Walter L. Complex roots of the Stoneley-wave equation. Bulletin of the Seismological Society of America. 1972;62:285-99.

[56] Love AEH. Some problems of geodynamics; being an essay to which the Adams prize in the University of Cambridge was adjudged in 1911. New York: Dover Publications; 1967.

[57] Auld BA. Acoustic Fields and Waves in Solids. Malabar, Fla: R.E. Krieger; 1990.

[58] Achenbach JD. Wave propagation in elastic solids. Amsterdam; New York: North-Holland Pub. Co.; American Elsevier Pub. Co.; 1973.

[59] Graff KF. Wave motion in elastic solids. [Columbus, Oh.]: Ohio State University Press; 1975.

[60] Rose JL. Ultrasonic waves in solid media. Cambridge; New York: Cambridge University Press; 1999.

[61] Mazzotti M, Marzani A, Bartoli I, Viola E. Guided waves dispersion analysis for prestressed viscoelastic waveguides by means of the SAFE method. International Journal of Solids and Structures. 2012;49:2359-72.

[62] Lee U, Oh H. Dynamics of an axially moving viscoelastic beam subject to axial tension. International Journal of Solids and Structures. 2005;42:2381-98.

[63] Bathe K-J. Finite element procedures Prentice Hall; 1996.

[64] Wriggers P. Nonlinear finite element methods. Berlin; Heidelberg: Springer-Verlag; 2008.

[65] Bonet J, Wood RD. Nonlinear continuum mechanics for finite element analysis. Cambridge: Cambridge Univ. Press; 2009.

[66] Bartoli I, Coccia S, Phillips R, Srivastava A, di Scalea FL, Salamone S, et al. Stress dependence of guided waves in rails. In: Kundu T, editor. 1 ed. San Diego, CA, USA: SPIE; 2010. p. 765021-10.

[67] Loveday PW. Semi-analytical finite element analysis of elastic waveguides subjected to axial loads. Ultrasonics. 2009;49:298-300.

[68] Loveday PW, Wilcox PD. Guided wave propagation as a measure of axial loads in rails. 2010:765023-.

[69] Holzapfel GA. Nonlinear solid mechanics : a continuum approach for engineering. Chichester; New York: Wiley; 2000.

[70] Chang YC, Ho B. The poynting theorem of acoustic wave propagating in an inhomogeneous moving medium. Journal of Sound and Vibration. 1995;184:942-5.

[71] Davidovich M. On the electromagnetic energy density and energy transfer rate in a medium with dispersion due to conduction. Technical Physics. 2010;55:630-5.

[72] Treyssède F. Elastic waves in helical waveguides. Wave Motion. 2008;45:457-70.

[73] Bergman RH, Shahbender RA. Effect of Statically Applied Stresses on the Velocity of Propagation of Ultrasonic Waves. Journal of Applied Physics. 1958;29:1736-.

[74] Thurston RN, Brugger K. Third-Order Elastic Constants and the Velocity of Small Amplitude Elastic Waves in Homogeneously Stressed Media. Physical Review. 1964;133:A1604-A.

[75] Crecraft DI. The Use of Ultrasonics in Stress Analysis. Strain. 1965;1:4-8.

[76] Crecraft DI. The measurement of applied and residual stresses in metals using ultrasonic waves. Journal of Sound and Vibration. 1967;5:173-92.

[77] Egle DM. Application of the Acoustoelastic Effect to Rail Stress Measurement. 1980. p. 213-.

[78] Gokhale SA. Determination of applied stresses in rails using the acoustoelastic effect of ultrasonic waves. 2007.

[79] Young Modulus of Elasticity for Metals and Alloys. 2012.

[80] Giurgiutiu V, Zagrai AN. Characterization of Piezoelectric Wafer Active Sensors. Journal of Intelligent Material Systems and Structures. 2000;11:959-76.

[81] Lange YV. Characteristics of the Impedance Method of Inspection and of Impedance Inspection Transducers. The Soviet journal of nondestructive testing. 1978;14:958-66.

[82] Cawley P. The impedance method of non-destructive inspection. NDT International. 1984;17:59-65.

[83] Giurgiutiu V, Rogers CA. Recent advancements in the electromechanical (E/M) impedance method for structural health monitoring and NDE. In: Regelbrugge ME, editor. 1 ed. San Diego, CA, USA: SPIE; 1998. p. 536-47.

[84] Xu J, Yang Y, Soh CK. Electromechanical Impedance-Based Structural Health Monitoring with Evolutionary Programming. Journal of Aerospace Engineering. 2004;17:182-.

[85] Yang Y, Liu H, Annamdas VGM, Soh CK. Monitoring damage propagation using PZT impedance transducers. Smart Materials and Structures. 2009;18:045003-.

[86] Park G, Inman DJ. Structural health monitoring using piezoelectric impedance measurements. Philosophical Transactions of the Royal Society A: Mathematical, Physical and Engineering Sciences. 2007;365:373-92.

[87] Annamdas V, Soh C. Application of Electromechanical Impedance Technique for Engineering Structures: Review and Future Issues. Journal of Intelligent Material Systems and Structures. 2010;21:41-59.

[88] Ong CW, Yang, Y., Naidu, A.S.K., Lu, Y., Soh, C.K. Application of the electro-mechanical impedance method for the identification of in-situ stress in structures. SPIE; 2002. p. 503-14.

[89] Annamdas VGM, Yang Y, Soh CK. Influence of loading on the electromechanical admittance of piezoceramic transducers. Smart Materials and Structures. 2007;16:1888-97.

[90] Annamdas VGM, Rizzo P. Influence of the excitation frequency in the electromechanical impedance method for SHM applications. SPIE; 2009. p. 72930V-V-11-V-V-11.

[91] Yang Y, Liu H, Annamdas VGM. Experimental study on sensing capability of fibre optic and piezoceramic sensors for load monitoring. Proceedings of SPIE. 2009;7292:72923S-S-12-S-S-12.

[92] Lim YY, Soh CK. Effect of Varying Axial Load Under Fixed Boundary Condition on Admittance Signatures of Electromechanical Impedance Technique. Journal of Intelligent Material Systems and Structures. 2012;23:815-26.

[93] Bhalla S, Soh CK. Electromechanical Impedance Modeling for Adhesively Bonded Piezo-Transducers. Journal of Intelligent Material Systems and Structures. 2004;15:955-72.

[94] Bhalla S, Soh CK. Structural Health Monitoring by Piezo-Impedance Transducers. I: Modeling. Journal of Aerospace Engineering. 2004;17:154-.

[95] Sepehry N, Shamshirsaz M, Bastani A. Experimental and theoretical analysis in impedance-based structural health monitoring with varying temperature. Structural Health Monitoring. 2011;10:573-85.

[96] Yang Y, Lim YY, Soh CK. Practical issues related to the application of the electromechanical impedance technique in the structural health monitoring of civil structures: II. Numerical verification. Smart Materials and Structures. 2008;17:035009-.

[97] Yang Y, Miao A. Two-dimensional modeling of the effects of external vibration on the PZT impedance signature. Smart Materials and Structures. 2010;19:065031-.

[98] Zhou S, Liang C, Rogers CA. Integration and Design of Piezoceramic Elements in Intelligent Structures. Journal of Intelligent Material Systems and Structures. 1995;6:733-43.

[99] Giurgiutiu V. Structural health monitoring with piezoelectric wafer active sensors. Amsterdam; Boston: Elsevier/Academic Press; 2008.

[100] Rizzo P, Coccia, S., Bartoli, I. and Lanza di Scalea, F. On-line High-speed Rail Defect Detection – Phase IV: Prototype Assembling and Field Testing, Technical Report No. SSRP- 06/17 to the Federal Railroad Administration. University of California, San Diego; 2006.

[101] Rizzo P, Coccia, S. and Lanza di Scalea, F. On-line High-speed Rail Defect Detection –Phase III, Technical Report No. SSRP-05/04 to the Federal Railroad Administration University of California, San Diego; 2005.

[102] Lanza di Scalea F, Bartoli, I., Rizzo, P. and McNamara, J. On-line High-speed Rail Defect Detection Final Report - Part 1, Technical Report DOT/FRA/ORD-04/16, Department of Transportation/Federal Railroad Administration. University of California, San Diego; 2004.

[103] Coccia S, Bartoli, I., Phillips, R., Salamone, S. and Lanza di Scalea, F. Noncontact Rail Defect Detection: Fourth Field Test,Technical Report No. SSRP-09/04 to the Federal Railroad Administration. University of California, San Diego; 2009.

[104] Coccia S, Bartoli, I., Salamone, S. and Lanza di Scalea, F. Report of Third Field Test of UCSD/FRA Rail Defect Detection Prototype, Gettysburg, PA, March 17-21, 2008, Technical Report No. SSRP-08/02 to the Federal Railroad Administration. University of California, San Diego; 2008.

[105] Coccia S, Bartoli, I., Lanza di Scalea, F. and Rizzo, P. Non-contact Rail Defect Detection: First and Second Field Tests, Technical Report No. SSRP-07/15 to the Federal Railroad Administration. University of California, San Diego 2007.

[106] Lanza di Scalea F. On-line High-speed Rail Defect Detection, Technical Report SSRP-2003/07, Department of Transportation/Federal Railroad Administration. University of California,San Diego; 2003.

[107] Coccia S, Bartoli, I., Phillips, R., Rizzo, P., Salamone, S., and Lanza di Scalea, F. On-lineHigh-speed Rail Defect Detection – Part II, Technical Report No. SSRP-10/03 to the Federal Railroad Administration. University of California, San Diego; 2010.

[108] Park KW, k.worden@sheffield.ac.uk, Charles RF, Graeme M, Gyuhae P, Keith W, et al. The fundamental axioms of structural health monitoring. Proceedings of the Royal Society A: Mathematical, Physical and Engineering Science. 2007;463:1639-64.

[109] Mahalanobis PC. On the Generalized Distance in Statistics. Proceedings of the National Institute of Sciences of India. 1936;2:49-55.

[110] Annamdas VGM, Soh CK. Three-Dimensional Electromechanical Impedance Model. II: Damage Analysis and PZT Characterization. Journal of Aerospace Engineering. 2007;20:63-71.

[111] Annamdas VGM, Soh CK. Three-Dimensional Electromechanical Impedance Model. I: Formulation of Directional Sum Impedance. Journal of Aerospace Engineering. 2007;20:53-62.

[112] Shaker FJ. Effect of axial load on mode shapes and frequencies of beams. Glenn Research Center1975. p. 33-.

[113] Kerr AD. Lateral buckling or railroad tracks due to constrained thermal expansion - a critical survey,. Symposium on Railroad Track, MechanicsTechnology. Oxford: Pergamon; 1978.